Glass transition without quenched disorder: spin-orbital glass transition of a pyrochlore magnet

Kota Mitsumoto

January 31, 2020

Abstract

Frustration is used to describe situations where different constraints imposed on a given system are conflicting with each other so that they cannot be satisfied simultaneously. Frustrated systems are abundant in nature and they exhibit non-trivial phenomena. Glass transition is a representative example. Especially, the spin glass transition, where spin degrees of freedom of electrons randomly freeze cooperatively, has been studied actively by both experimental and theoretical works. It has been established that the spin glass transition is a thermodynamic glass transition. The characteristic features of the spin glass transition are, for example, the negative divergence of the nonlinear magnetic susceptibility and the extraordinary slow dynamics. On the theoretical side, the replica method has been developed. It is known that the concept of replica symmetry breaking (RSB) can explain many experimental observations on spin glasses. In short, the RSB means the appearance of a complex free energy landscape.

In the conventional view, the spin glass transitions occur due to the frustration of random interactions (quenched disorder). On the other hand, it has been known experimentally that spin glass transitions due to purely geometrical frustration without randomness may exist for the last 30 years. However, so far, there are no convincing explanations for the mechanism of this spin glass transition and the issue has remained as an important open problem.

Recently, it was experimentally suggested that lattice distortions play important roles in the spin glass transition on the prototypical geometrically frustrated spin glass $Y_2Mo_2O_7$. This lattice distortion is expected to be a Jahn-Teller distortion resulting from the selection of the electron orbitals. Being motivated by the experiment, we introduced an effective model which includes not only the spin degrees of freedom but also the lattice distortions as dynamical variables. This model doesn't include any quenched disorder but both spins and lattice distortions are strongly frustrated for geometrical reasons. In this thesis, we performed a set of extensive numerical simulations of this effective model. We also developed and analyzed a mean-field theory in the infinite dimension where exact analyses are possible.

In the numerical simulations, we found that spins and lattice distortions simultaneously freeze cooperatively at a common finite temperature. Since the distortions are associated with the electron orbitals, we call this a spin-orbital glass transition. We found numerical evidences that the nonlinear dielectric susceptibility negatively diverges at the transition in addition to the negative divergence of the magnetic one. We believe this is an important suggestion for future experiments.

In the mean-field analysis using the replica method, we found two cases depending on the parameters such as the temperature, the ratio of energy scales associated with the spins and lattice distortions. In one case, the system exhibits the simultaneous spin and lattice glass transition. In the other case, the spin glass transition and lattice glass transitions occur separately. Very interestingly, in both cases, the RSB appears only in the phase where both spins and lattice distortions are frozen. In addition, we found that the glass susceptibilities associated with the nonlinear magnetic and dielectric susceptibilities diverge at the transition temperatures.

From the above results, we clarified that our effective model can explain the glass transitions observed experimentally on $Y_2Mo_2O_7$. Our model is the first theoretical model which exhibits glass transitions without quenched disorder in finite dimensions.

Contents

Chapter 1

INTRODUCTION

In this chapter, we will review some basic aspects of the physics of glasses and geometrical frustration. In this thesis, we will show that the two concepts are very important to understand the spin glass transition of a pyrochlore magnet. At the end of this chapter, we will explain the outline of following chapters.

In physics, *glass* is a generic notion for states where the system under consideration is disordered and frozen. Physics of glasses appears in various fields such as soft matter systems, spin systems, biological systems, information problems and so on. Glassy systems show a variety of interesting phenomena such as aging, memory effect, rejuvenation, dynamic heterogeneity, nonlinear response, etc.

In condensed matter physics, we can find many examples of phase transitions between a disordered liquid state at higher temperatures and a long-ranged ordered crystalline state at lower temperatures. In some cases, however, the long-ranged crystalline ordering can be suppressed or avoided by the *frustration*, giving rise to disordered states even at low temperatures such as supercooled liquids, structural glasses, spin liquids and spin glasses.

In this thesis, we will study theoretically a realization of a spin glass state without quenched disorder, which emerges from a spin liquid state enabled by geometrically frustration. In this chapter, we will review some background of this work.

1.1 Physics of glasses

1.1.1 Glassy systems: two examples

1.1.1.1 Spin glass

Spin glass (SG) is a state in which spins are randomly frozen without any spatial periodicity. The SG transition was found out first in a dilute magnetic metallic alloy, which are sometimes called canonical spin glass, by Cannella and Mydosh [3]. In this metalic system, magnetic ions which are distributed at spatially random positions interact with each other via the Ruderman-Kittel-Kasuya-Yosida (RKKY) interaction [4, 5, 6, 7] given by,

$$J_i j \sim \frac{\cos(k_F r_{ij})}{r_{ij}^3}, \tag{1.1}$$

where k_F is the Fermi wavenumber and r_{ij} is the distance between i-th and j-th magnetic ions. The RKKY interaction is a long-ranged interaction mediated by itinerant electrons and changes the sign with distance in an oscillating fashion, as shown in Fig. 1.1 (a).

Let us briefly summarize some basic features of spin glasses by making comparisons with ferromagnets. At a standard ferromagnetic transition, one usually observes a singularity in the heat capacity and a divergence of the linear magnetic susceptibility χ. The latter is defined as the coefficient of the first order in the expansion

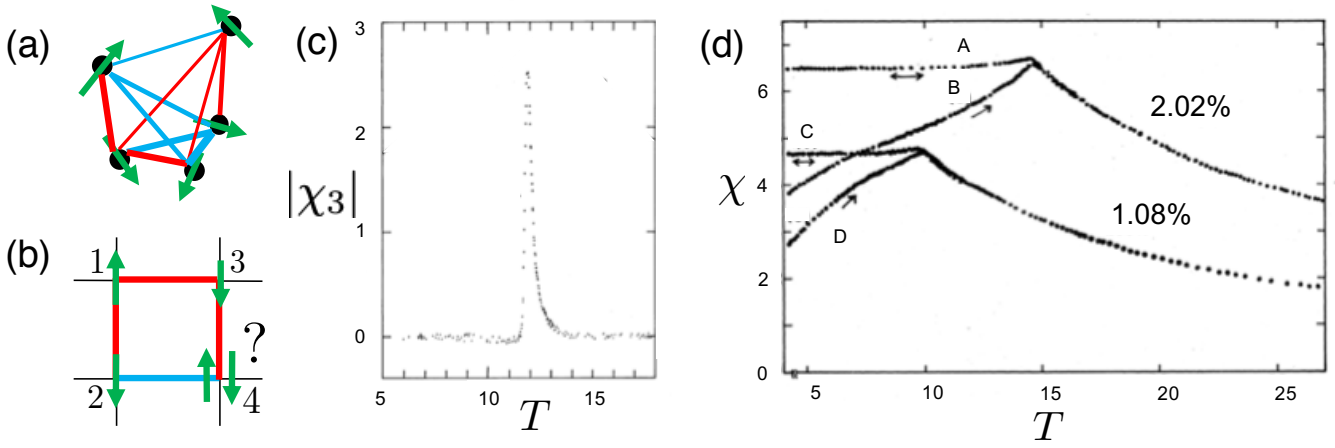

Figure 1.1: **Key features of spin glasses**
Schematic pictures of the canonical spin glass (a) and Edwards-Anderson model (b). Blue and blue bonds represents ferromagnetic and antiferromagnetic interactions, respectively. (c): The temperature dependence of the nonlinear magnetic susceptibility χ_3 of a canonical spin glass $Au_{1-x}Fe_x$ for $x = 0.015$. Taken from [1]. (d): The temperature dependence of the dc linear magnetic susceptibility χ of the canonical spin glass $Cu_{1-x}Mn_x$ for $x = 0.0202, 0.0108$. The curves A and C are the field cooled (FC) susceptibility. The curves B and D correspond to the zero field cooled (ZFC) susceptibility. Taken from [2]

of the magnetization m in the power series of magnetic field h,

$$m = \chi h + \frac{1}{3!}\chi_3 h^3 + O(h^5). \tag{1.2}$$

Here, the even-order terms are absent because of the inversion symmetry of the system. On the other hand, at the spin glass transition, the heat capacity exhibits no singularity but only a broad peak slightly above the transition point [8], and the linear magnetic susceptibility shows only a cusp, while instead, the nonlinear magnetic susceptibility χ_3 diverges negatively at the transition temperature. Fig. 1.1 (c) shows the behavior of the nonlinear susceptibility around the transition temperature. This singular behavior suggests that the spin glass transition is a truly thermodynamic continuous phase transition.

Fig. 1.1 (d) shows the so called FC-ZFC (Field Cooled - Zero Field Cooled) linear magnetic susceptibilities. The top branches marked as A and C are obtained by cooling under magnetic field (FC) while the top branches marked as B and D are obtained in a system cooled without the magnetic field (ZFC) but heated under the magnetic field. Note that the FC and ZFC lines agree at higher temperatures but become different at temperatures below the spin glass transition temperature T_c. It means that the system cannot relax into the true equilibrium state, i.e. the system at temperatures lower than T_c falls out of equilibrium. From the above facts, the spin glass transition can be regard as a thermodynamic phase transition to a glassy phase where the relaxation time is divergingly large.

On the theoretical side, Edwards and Anderson [9] considered that the random signs of the interactions J_{ij} and *frustration* which naturally emerges due to this randomness are essential for the spin glass transition. In order to explain the spin glass transition, they introduced a theoretical lattice model called the Edwards-Anderson (EA) model, with only nearest-neighbor interactions. The Hamiltonian is given by,

$$H = \sum_{<ij>} J_{ij} \boldsymbol{S}_i \cdot \boldsymbol{S}_j, \tag{1.3}$$

where $< ij >$ represents all pairs of the neighboring spins $\{\boldsymbol{S}_i\}$ $(i = 1, 2, ..., N)$. Here, J_{ij} is a random variable which does not evolve with time, i.e. *quenched disorder*.

In this system, the exchange interactions are competing with each other due to the presence of many frustrated loops. An example is shown in Fig. 1.1 (b). Here, let us illustrate the idea of frustration using Ising spins for simplicity. Let us put Ising spins on site 1,2 and 3 so that spins satisfy the antiferromagnetic coupling on 1-2 bond and 1-3 bond. Then if we try to put another spin on site 4, we will find that it cannot satisfy the two couplings on 2-4 bond and 3-4 bond simultaneously. This is a typical situation of frustration. Since there are a lot of such frustrated loops distributed randomly in the system, the system can have a very complex energy landscape with energetically almost degenerate yet significantly different configurations.

Edwards and Anderson introduced an order parameter called the Edwards-Anderson (EA) parameter for the spin glass transition. It is given by,

$$q_{EA} = \frac{1}{N}\sum_{i=1}^{N} \lim_{t\to\infty} \langle \boldsymbol{S}_i(0) \cdot \boldsymbol{S}_i(t) \rangle \,, \tag{1.4}$$

where $\mathbf{S}_i(t)$ is the spin configuration at site i at time t, N is the total number of spins and $\langle \cdots \rangle$ represents the thermal average. The EA order parameter can detect *ergodicity breaking*, i.e. freezing of the spins. It is zero in ergodic phases like the paramagnetic phase and becomes non-zero in non-ergodic states. Interestingly they observed that q_{EA} can also be represented as a static quantity as the following. In equilibrium, the correlation of spin fluctuation becomes decorrelated in the long time limit, which is called "clustering property",

$$\langle (\boldsymbol{S}(0) - \langle \boldsymbol{S} \rangle) \cdot (\boldsymbol{S}(t) - \langle \boldsymbol{S} \rangle) \rangle = \langle \boldsymbol{S}_i(0) \cdot \boldsymbol{S}_i(t) \rangle - \langle \boldsymbol{S} \rangle^2 \xrightarrow[t\to 0]{} 0. \tag{1.5}$$

Then q_{EA} may be rewritten as

$$\overline{q} = \frac{1}{N}\sum_{i=1}^{N} \langle \boldsymbol{S}_i \rangle^2 \,. \tag{1.6}$$

Here, we used a different notation for the order parameter because they may not be precisely the same in the spin glass phase if the so called replica symmetry breaking (RSB) take place, as we discuss later.

1.1.1.2 Structural glass

Structural glass is the state in which positions of particles (molecules, colloids, e.t.c.) are frozen randomly. [10] In sharp contrast to spin glasses, structural glasses are disorder-free, i.e. quenched disorder is absent. The structural glasses have been used by human being from a long time ago and they are indispensable in our daily life. However, physics of structural glasses has never been understood fully microscopically and there remains a lot of open problems. Especially, the most important question is whether a thermodynamic structural glass transition exists or not.

In order to generate a structural glass, we need to obtain at first a supercooled liquid which is a liquid state at temperatures lower than the melting point T_m. Such a supercooled liquid can be obtained by lowering the temperature fast enough to avoid the first-order phase transition toward the crystalline phase at T_m. The viscosity rapidly increases with lowering the temperature and finally the system becomes immobile on our reasonable time scales. This phenomenon is called a "structural glass transition". Then the apparent entropy evaluated by calorimetric measurement deviate from that of the supercooled liquid (Fig. 1.2 (a)) and the heat capacity exhibit a jump. Note that such a transition is not a thermodynamic phase transition. The glass transition temperature T_g is conventionally defined as the temperature where the viscosity η becomes larger than 10^{12} (Pa·s). Indeed, as shown in Fig. 1.2 (a), the transition temperature T_g is changed by the cooling rate, namely if we lower the temperature more slowly, the system falls into the glass at lower temperatures.

Thus, we naturally wonder what happens if we lowered the temperature with an infinitesimal cooling rate, i.e. quasistatic cooling. From Fig. 1.2 (a), it appears that the supercooled liquid line may cross the crystalline line at T_K if it is extrapolated naively. It means that the entropy of the glass state which has the random configuration becomes smaller than that of the ordered crystalline state. This is called Kauzmann

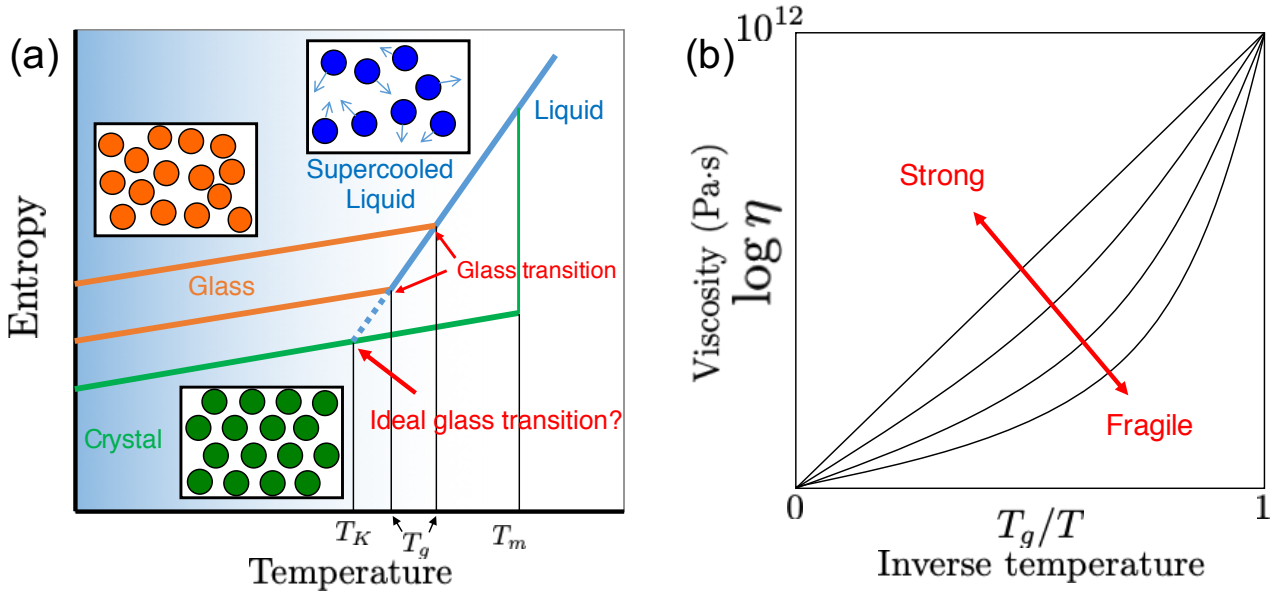

Figure 1.2: **Some key observations in structural glasses**
(a): Schematic picture of entropy vs temperature in a glass forming molecular liquid. (b): Schematic picture of Angell plot of the viscosity. For "strong" liquids, the viscosity increases following the Arrhenius law (Eq. (1.7)) as temperature is decreased. For "fragile" liquids, the curves show non-Arrhenius behavior which can be fitted by Vogel-Fulcher-Tamman law (Eq. (1.8)).

paradox or entropy crisis and T_K is called Kauzmann point. Researchers on glass physics are interested in this paradox and wonder whether an ideal thermodynamic glass transition takes place at T_K. At present, the existence of the Kauzmann transition has not been proved nor disproved.

Nonetheless, the temperature dependence of the viscosity is quite interesting. It is customary to divide the glasses into two groups which are called "strong" and "fragile" glasses by the difference between the temperature dependence of the viscosity as shown in Fig 1.2 (b). For the "strong glass", e.g. SiO_2 glass, the viscosity follows the simple Arrhenius law given by,

$$\log \eta \sim E_0/k_{\rm B}T, \tag{1.7}$$

which means the dynamics is dominated by a simple thermally activated process over a finite energy barrier E_0. In this case the viscosity diverges at $T = 0$. On the other hand, the viscosity of the "fragile glass" grows more rapidly and the temperature dependence of the viscosity is empirically known as,

$$\log \eta \sim 1/(T - T_0), \tag{1.8}$$

which is called the Vogel-Fulcher-Tamman (VFT) law. [11, 12, 13] It suggests that the viscosity diverges at a "critical" temperature T_0. Experimentally this temperature is known to be close to the Kauzmann point estimated by the heat capacity measurement mentioned above in many materials. This observation appears to hint the ideal glass transition but at present there is no satisfactory, microscopic explanation for the VFT law. A candidate scenario in favor of the existence of the thermodynamic glass transition is provided by the so called random first order transition (RFOT) theory. [14, 15, 16]

Recently, replica liquid theory in which the liquid theory [17] and the replica theory (see Sec. 1.1.3 for detail) are combined has been developed. Using this theory, the dense packing of hard spheres in the infinite dimension can be exactly solved and the occurrence of the ideal glass transition has been proved. [18] The establishment of an exact theory is remarkable. It may give some hints to solve the problems in 3-dimensional glassy systems providing some microscopic basis for the RFOT mentioned above.

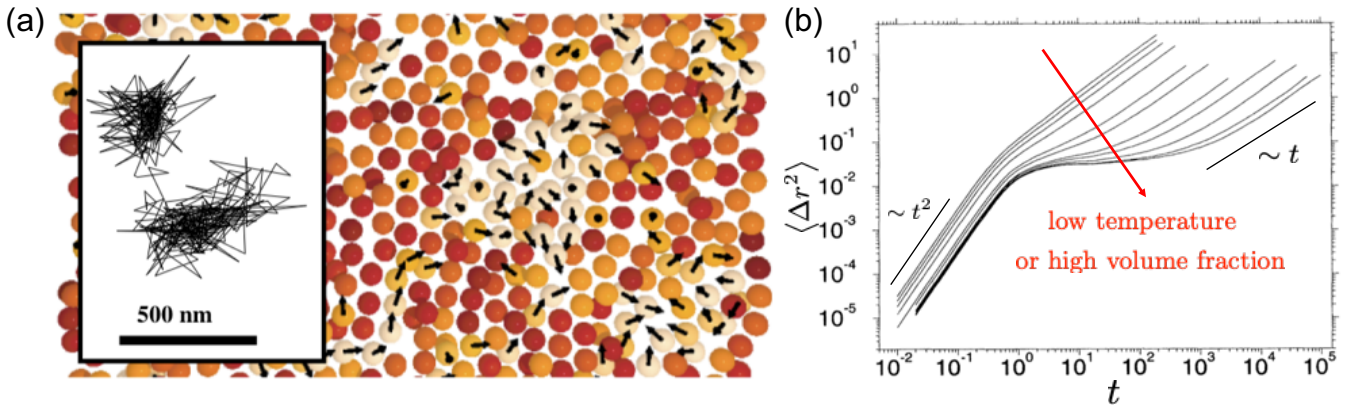

Figure 1.3: **Dynamics in supercooled liquids**
(a): Snapshot of a three dimensional densely packed colloidal system which has the volume fraction $\phi = 0.52$, taken from [19]. The arrows in the main panel indicate the velocity of moving particles. Lighter colors indicate particles with larger displacements. Inset: 120 min trajectory of one tagged particle. (b): Mean squared displacement (MSD) versus time observed in a simulation on a binary mixture of particles with the Lennard-Jones interaction, taken from [20]. The ratio of the particle radius is 1 : 1.4, which is known to be good to avoid crystallization.

It is known empirically that the liquid whose constituent elements have a simple spherical form becomes the fragile glass generally. Hence the fragile glass includes not only molecular glasses and metallic glasses but also colloidal glasses. The colloidal glass is convenient to examine the dynamics because one can observe the movement of the particles directly through optical microscopes. Experiments of the colloidal system are usually performed at room temperature so that the control parameter is the volume fraction ϕ rather than the temperature. Fig. 1.3 (a) shows a snapshot of a three dimensional colloidal system at a high density. [19] We find that dense colloidal system exhibits cooperative, chain like motion of the particles. In addition, focusing on a trajectory of a tagged particle, we find a two-step relaxation such that the particles exhibit vibrational (rattling) motions plus intermittent large displacements. It means that the particle remains trapped inside a "cage" created by the neighboring particles for a long time and moves out of the cages in the even longer time scales. The former and latter are called β and α relaxation, respectively. The α relaxation occurs by changing the configuration of the neighboring particles. Thus the α relaxation enables liquid-like flow and the time scale of motion is related to the viscosity η. The two-step relaxation is observed quantitatively, for example, by the mean square displacement (MSD) as shown in Fig. 1.3 (b). At low temperatures or high volume fractions, the mean square displacement are proportional to the square of the time t^2 at the very initial time scales because the particles behave like free particles (ballistic motion). Then MSD exhibits a plateau which has a height corresponding to the cage size (β-relaxation). During the time scale at the plateau, the system behaves as a piece of solid, i.e. glass. On even longer time scales, MSD finally shows the diffusion, i.e. $\langle \Delta r^2 \rangle \sim t$ (α-relaxation). If the plateau regime is extended to infinity, it means that the system completely stacks in a glass, i.e. the height of the plateau corresponds to the Edwards-Anderson parameter for spin glasses.

1.1.2 Statistical mechanics of glassy systems

Statistical mechanics is a powerful method to understand macroscopic phenomena from microscopic point of views. Especially it allows us to introduce the notion of order parameter which characterize different states of matters. In this section, we review some basic ideas of the statistical mechanics approach for glass transitions but first let us recall a ferromagnetic phase transition for a comparison.

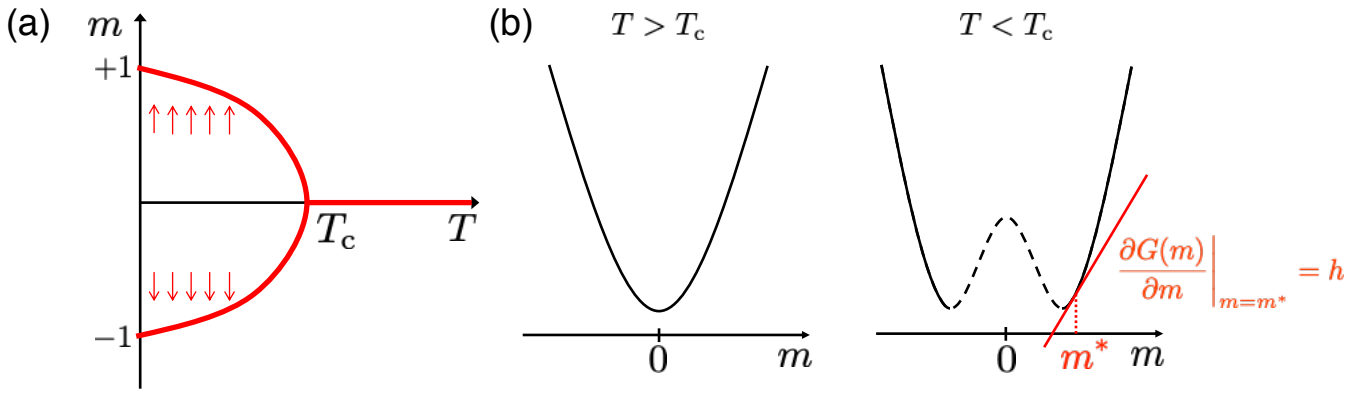

Figure 1.4: **Ferromagnetic phase transition**
(a): Typical behavior of the magnetization by lowering temperature in a ferromagnet. (b): Schematic picture of the free energy $G(m)$ above (left) and below (right) T_c. The slope of the red line represents the external field h and the magnetization $m*(h)$ under the external field is obtained by solving Eq. (1.20).

1.1.2.1 A recap on the ferromagnetic transition

Let us consider a ferromagnetic Ising model on a square lattice. Ising spins $S_i = \pm 1$ $(i = 1, 2, 3, ..., N)$ follow the Hamiltonian given by,

$$H = -J \sum_{<i,j>} S_i S_j, \tag{1.9}$$

where $J > 0$ is the energy scale of the exchange interaction and $< i, j >$ represents all nearest neighboring pairs. The spins exhibits ferromagnetic long-ranged order at low temperatures to satisfy the ferromagnetic couplings. In order to characterize the order quantitatively, we introduce the ferromagnetic order parameter,

$$m = \frac{1}{N} \sum_{i=1}^{N} \langle S_i \rangle \,, \tag{1.10}$$

which is nothing but the magnetization per spin. In a ferromagnetic state, which is realized below a critical temperature T_c, m takes a nonzero value, more precisely $m > 0$ if 'up' spins are dominant and $m < 0$ if 'down' spins are dominant (see Fig. 1.4 (a)). The magnitude of the order parameter follows the power law as $T \to T_c$,

$$m \sim (T - T_c)^{\beta} \tag{1.11}$$

with β being a critical exponent. Thus the spin-reversal symmetry $S_i \to -S_i$ $(\forall i)$ of the Hamiltonian (Eq. (1.9)) is spontaneously broken at temperatures lower than T_c. This spontaneous symmetry breaking can be understood better by considering explicitly the symmetry breaking field, i.e. the external magnetic field h which is conjugate to the order parameter m as,

$$H = -J \sum_{<i,j>} S_i S_j - h \sum_{i=1}^{N} S_i. \tag{1.12}$$

Using the magnetic field h, the order parameter can be calculated as,

$$m(N, h) = -\frac{1}{N} \frac{\partial F(N, h)}{\partial h} = \frac{1}{N} \sum_{i=1}^{N} \langle S_i \rangle_h \,, \tag{1.13}$$

where we introduced the free-energy of the system

$$F(N,h) = (-1/\beta)\log Z(N,h) = (-1/\beta)\log\left[\mathrm{Tr}_S e^{-\beta H}\right]. \tag{1.14}$$

Here, $\langle\cdots\rangle_h$ represents the thermal average in the presence of the magnetic field h. Particularly interesting is the comparison of the following two limits:

$$\lim_{N\to\infty}\lim_{h\to+0} m(N,h) = 0, \tag{1.15}$$

$$m_{\mathrm{s}} = \lim_{h\to+0}\lim_{N\to\infty} m(N,h). \tag{1.16}$$

Although the former is always zero, the later becomes nonzero at temperatures below T_{c} reflecting the spontaneous symmetry breaking. The magnetization m_{s} in Eq. (1.16) is called a spontaneous magnetization m_{s}. Here it is instructive to consider the Legendre transform,

$$G(N,m) = F(N,h^*) + Nmh^* \tag{1.17}$$

to introduce a free-energy $G(N,m)$, where h^* is defined such that

$$m = -\frac{1}{N}\left.\frac{\partial F(N,h)}{\partial h}\right|_{h=h^*(m)}. \tag{1.18}$$

One has equivalently the inverse transformation,

$$F(N,h) = G(N,m^*) - Nm^*h, \tag{1.19}$$

where m^* is defined such that

$$h = \frac{1}{N}\left.\frac{\partial G(N,m)}{\partial m}\right|_{m=m^*(h)}. \tag{1.20}$$

It can be understood that two free-energy minima of $G(m)$ corresponding to ferromagnetic states $m_{\mathrm{s}} > 0$ and $m_{\mathrm{s}} < 0$ are not equivalent under the magnetic field and $m_{\mathrm{s}} > 0$ must be selected if $h > 0$ at temperatures lower than T_c, as shown in Fig. 1.4 (b). Physically this means that by taking the thermodynamic limit $N \to \infty$, the system cannot overcome anymore the free-energy barrier and remains trapped in the $m_{\mathrm{s}} > 0$ state even after switching off the magnetic field $h \to +0$. Therefore, we can detect the symmetry breaking by taking the limit $h \to +0$ *after* thermodynamic limit $N \to 0$. This is equivalent to look for minima of $G(m)$ where $0 = \partial G(m)/\partial m$ holds.

Another important feature of the ferromagnetic phase transition of the Ising model is that it is a second order phase transition with critical phenomena. We have already mentioned that the spontaneous magnetization m_s develops continuously below T_{c}, following the power law Eq. (1.11). The susceptibility which is defined as

$$m = \chi h + O(h^3) \tag{1.21}$$

diverges at the critical point T_{c} as

$$\chi \sim |T - T_{\mathrm{c}}|^{-\gamma} \tag{1.22}$$

with γ being another critical exponent. Here it is instructive to recall that the susceptibility can be expressed by the fluctuation formula,

$$\begin{aligned}\chi = -\frac{1}{N}\left.\frac{\partial^2 F(N,h)}{\partial h^2}\right|_{h=0} &= \frac{\beta}{N}\left(\left\langle\left(\sum_{i=1}^N S_i\right)^2\right\rangle_{h=0} - \left\langle\sum_{i=1}^N S_i\right\rangle_{h=0}^2\right) \\ &= \frac{\beta}{N}\sum_{i,j}\left(\langle S_iS_j\rangle_{h=0} - \langle S_i\rangle_{h=0}\langle S_j\rangle_{h=0}\right).\end{aligned} \tag{1.23}$$

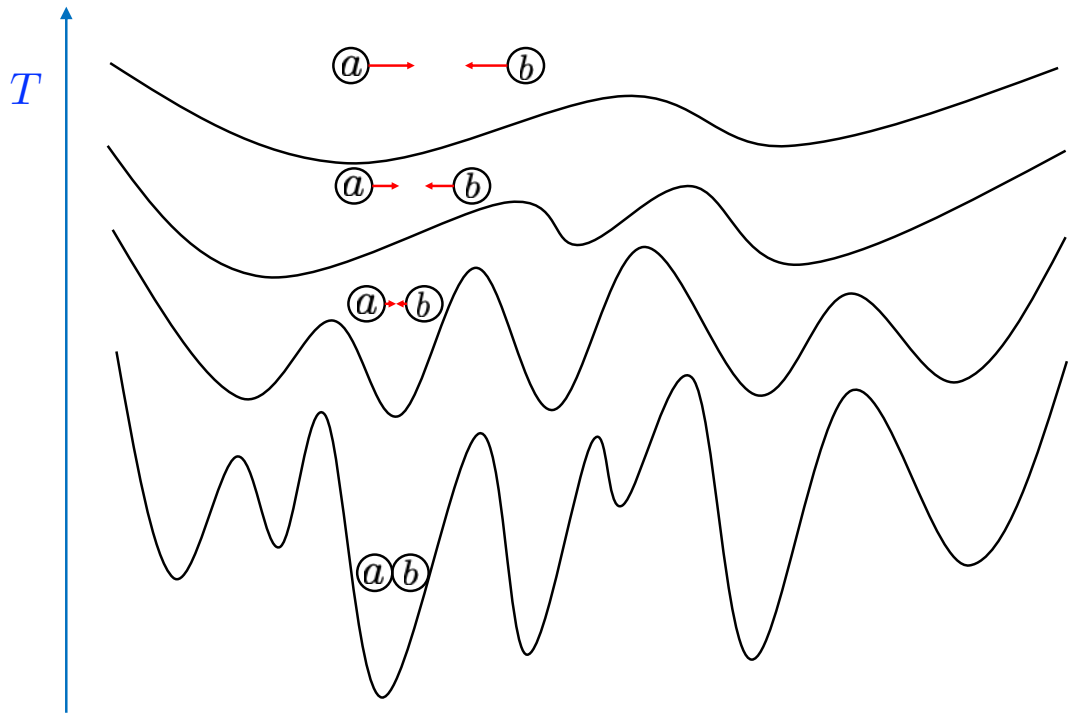

Figure 1.5: **Schematic picture of the free-energy landscape of a glass**
Replicas a and b are symbolized by the circled a and circled b and red arrows represent the externally applied coupling force between two replicas.

From this expression, one can understand that the divergence of the susceptibility χ approaching T_c reflects divergence of the correlation length ξ of the spin fluctuations,

$$\left(\langle S_i S_j \rangle_{h=0} - \langle S_i \rangle_{h=0} \langle S_j \rangle_{h=0}\right) \sim \exp\left(-\frac{r_{ij}}{\xi}\right), \tag{1.24}$$

$$\xi \sim |T - T_c|^{-\nu}, \tag{1.25}$$

where r_{ij} represents the distance between the sites i and j, ν is the critical exponent of the correlation length. The diverging correlation length also means critical slowing down of the dynamics; divergence of the relaxation time

$$\tau \sim \xi^z \tag{1.26}$$

with z being a dynamical critical exponent.

1.1.2.2 Replicas for glasses: detection of ergodicity breaking

Now let us turn to consider the statistical mechanics of glassy systems. For simplicity, I explain it for an Ising spin system as an example. In this case we are interested in the Edwards-Anderson (EA) order parameter $\overline{q}$ introduced in Eq. (1.6) which reflects the breaking of the ergodicity. In order to analyze the behavior of the EA order parameter, we introduce a system of *replicas*: a composite system made of replica a and replica b whose spins S_i^a and S_i^b obey the same form of Hamiltonian $H(S)$. Then we find the EA order parameter can be written as,

$$\overline{q} = \frac{1}{N} \sum_{i=1}^{N} \langle S_i^a \rangle \left\langle S_i^b \right\rangle. \tag{1.27}$$

Now we consider the following extended Hamiltonian for the whole system in which we introduce an additional coupling term between the two replicas,

$$H_{a+b} = H(\{S_i^a\}) + H(\{S_i^b\}) - \lambda \sum_{i=1}^{N} S_i^a S_i^b, \tag{1.28}$$

where $\lambda > 0$ is the strength of the coupling (see Sec. A). Similarly to the magnetic field conjugated to the ferromagnetic order parameter, we can compute the EA order parameter as,

$$\overline{q} = \lim_{\lambda \to +0} \lim_{N \to \infty} Q_{ab}(N, \lambda) \tag{1.29}$$

with

$$Q_{ab}(N, \lambda) = -\frac{1}{N} \frac{\partial F_{a+b}(N, \lambda)}{\partial \lambda} = \frac{1}{N} \sum_{i=1}^{N} \left\langle S_i^a S_i^b \right\rangle_\lambda, \tag{1.30}$$

where

$$F_{a+b}(N, \lambda) = (-1/\beta) \log Z_{a+b}(N, \lambda) = (-1/\beta) \log \left[\mathrm{Tr}_{S^a, S^b} e^{-\beta H_{a+b}} \right]. \tag{1.31}$$

Here, $\langle \cdots \rangle_\lambda$ represents the thermal average under the coupling term. Let us compare the two limits,

$$\lim_{N \to \infty} \lim_{\lambda \to +0} Q_{ab}(N, \lambda) = 0, \tag{1.32}$$

$$\overline{q} = \lim_{\lambda \to +0} \lim_{N \to \infty} Q_{ab}(N, \lambda). \tag{1.33}$$

We assume that the system is symmetric under global spin flip: $H(\{S\}) = H(\{-S\})$. Then we find Eq. (1.32) always vanishes. On the other hand $\overline{q}$ given by Eq. (1.33) can behave differently. It is zero in the paramagnetic phase ($\overline{q} = 0$) and takes a finite value ($\overline{q} > 0$) in the glass phase where the ergodicity is broken. We can understand this by using the schematic picture of the free-energy landscape shown in Fig. 1.28. In the glass phase, the free-energy minima are separated from other minima by high energy barriers because the ergodicity is broken. Obviously the two replica should stay in the same minimum as long as the coupling field λ is on. Now, if we first take thermodynamic limit $N \to \infty$, two replicas will keep close to each other even after turning off the field ($\lambda \to 0$), resulting in $\overline{q} > 0$.

If the system exhibits a second order glass transition, the spin glass susceptibility,

$$\begin{aligned} \chi_{\mathrm{SG}} = -\frac{1}{N} \left. \frac{\partial^2 F_{A+B}(N, \lambda)}{\partial \lambda^2} \right|_{\lambda=0} &= \frac{\beta}{N} \left(\left\langle \left(\sum_{i=1}^{N} S_i^a S_i^b \right)^2 \right\rangle_{\lambda=0} - \left\langle \sum_{i=1}^{N} S_i^a S_i^b \right\rangle_{\lambda=0}^2 \right) \\ &= \frac{\beta}{N} \sum_{i,j} \left(\left\langle S_i^a S_i^b S_j^a S_j^b \right\rangle_{\lambda=0} - \left\langle S_i^a S_i^b \right\rangle_{\lambda=0} \left\langle S_j^a S_j^b \right\rangle_{\lambda=0} \right), \end{aligned} \tag{1.34}$$

would diverge in the limit $N \to \infty$ analogously to the divergence of the linear susceptibility in the ferromagnetic phase transition. In the present case the spin glass susceptibility can be rewritten as

$$\chi_{\mathrm{SG}} = \frac{\beta}{N} \sum_{i,j} \left(\langle S_i S_j \rangle^2 - \langle S_i \rangle^2 \langle S_j \rangle^2 \right). \tag{1.35}$$

Above T_c, $< S_i >= 0$ due to the time-reversal symmetry so that χ_{SG} can be simplified as

$$\chi_{\mathrm{SG}} = \frac{\beta}{N} \sum_{i,j} \langle S_i S_j \rangle^2, \tag{1.36}$$

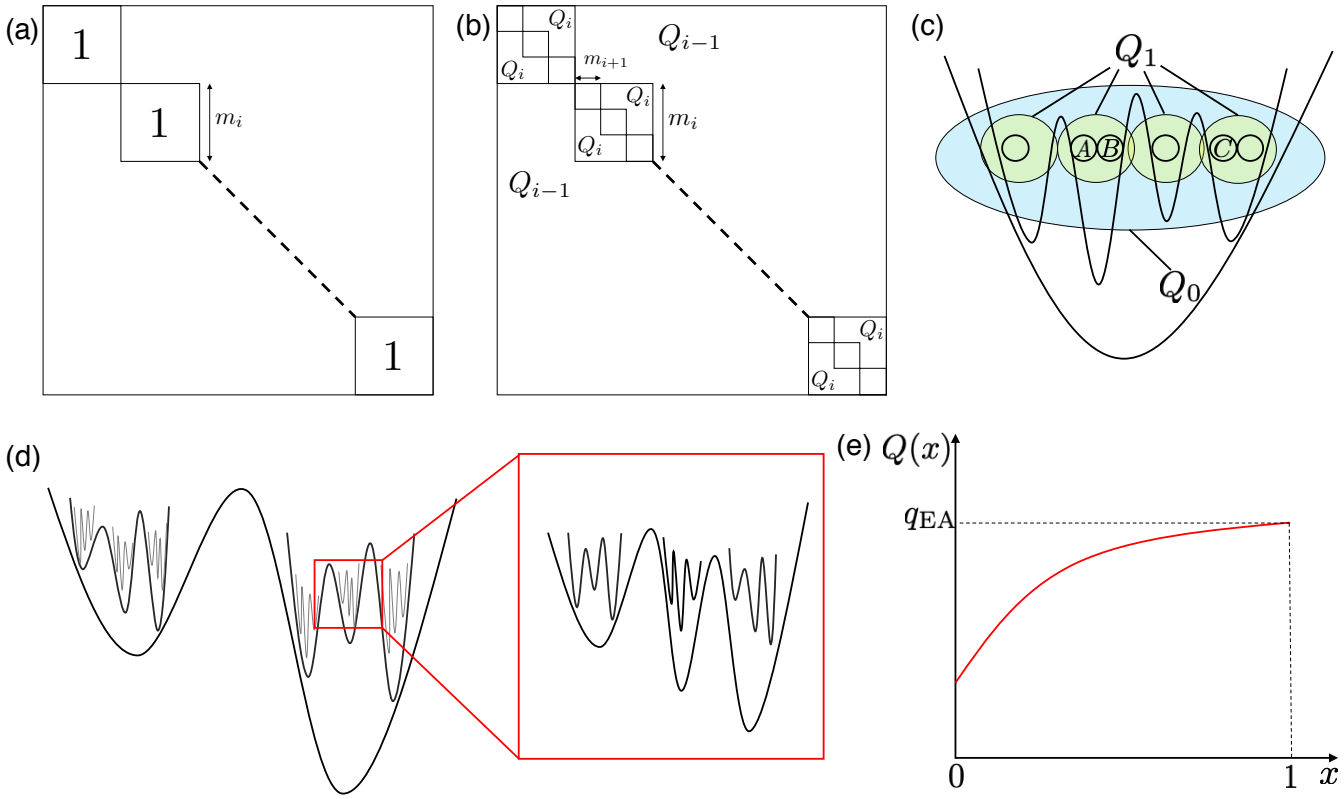

Figure 1.6: **Replica-symmetry breaking**
(a): Generalized identity matrix. (b): Parisi's matrix. (c): Schematic picture of the free-energy in 1-step RSB phase. (d): Hierarchical structure of the free energy in full-RSB phase. (c): Order parameter function $q(x)$ in full-RSB phase.

which can be related to the non-linear susceptibility χ_3,

$$\chi_3 = \left.\frac{\partial^3 m(N,h)}{\partial h^3}\right|_{h\to 0} = \frac{\beta^3}{N}\sum_{i,j,k,l}\left(\langle S_i S_j S_k S_l\rangle - 3\langle S_i S_j\rangle\langle S_k S_l\rangle\right) \tag{1.37}$$

Here, we used again that $\langle S_i\rangle = 0$. Assuming that the four-body correlation is much smaller than the two-body correlation, we find,

$$\chi_3 \sim \sum_{i,j}\langle S_i S_j\rangle^2 \sim -\chi_{\rm SG}. \tag{1.38}$$

Thus, the spin glass susceptibility is negatively proportional to the non-linear susceptibility (see Fig. 1.1 (c)). Above assumption is always correct if the Hamiltonian is gauge invariant with respect to $S_i \to \sigma_i S_i$ with $\sigma_i = \pm 1$.

1.1.3 Replica theory for glasses: basic ideas

Now, let me explain some basic ideas of replica theory which is useful for both systems with/without quenched disorder. In this method, in order to obtain the free energy,

$$f = -\frac{1}{\beta N}\log Z, \tag{1.39}$$

of the system described by the Hamiltonian $H(\{S\})$, we use an identity,

$$\log Z = \lim_{n\to 0} \frac{\partial}{\partial n} Z^n. \tag{1.40}$$

More precisely, as n is an integer, we calculate the partition function of the n-replicated system,

$$Z^n = \left(\prod_{a=1}^{n} \mathrm{Tr}_{S^a} \right) e^{-\beta \sum_{a=1}^{n} H(\{S^a\})} \tag{1.41}$$

and finally take the limit $n \to 0$ by an analytic continuation. Originally, this method was introduced to calculate the random average of quenched disorder [9, 21, 22] (see Sec. B) but it can be naturally used also for systems without quenched disorder [18, 23]. An obvious symmetry of the replicated system is "replica symmetry": we have put the indices $a = 1, 2, ..., n$ but we can permute the indices freely with no physical changes.

The Hamiltonian of the n-replicated system with a coupling term is given by,

$$H = \sum_{a=1}^{n} H(\{\boldsymbol{S}_i^a\}) - \sum_{a<b} \lambda_{ab} \sum_{i=1}^{N} \boldsymbol{S}_i^a \cdot \boldsymbol{S}_i^b, \tag{1.42}$$

where $\lambda_{ab} > 0$ is the strength of the coupling. The additional term explicitly breaks the replica symmetry. In this case, a generalized glass order parameter can be defined as a matrix $\hat{Q}(\{\lambda\})$ whose components are,

$$Q_{ab}(N, \{\lambda\}) = \frac{1}{N} \sum_{i=1}^{N} \left\langle S_i^a S_i^b \right\rangle_{\{\lambda\}}, \tag{1.43}$$

where $\langle \cdots \rangle_{\{\lambda\}}$ represents the thermal average under the coupling term. As before, the spontaneous order parameter can be defined as,

$$Q_{ab}^s = \lim_{\{\lambda\}\to+0} \lim_{N\to\infty} Q_{ab}(\{\lambda\}). \tag{1.44}$$

1.1.3.1 Replica symmetric (RS) case

If we assume $\lambda_{ab} = \lambda$ for all replica pairs, the field do not break the replica symmetry so that we can parametrize the order parameter as

$$Q_{ab}^{\mathrm{RS}} = (1 - Q)\delta_{ab} + Q, \tag{1.45}$$

with a single parameter Q, where $\delta_{ab} = 1$ $(a = b)$, 0 $(a \neq b)$ is Kronecker's delta. $Q_{aa} = 1$ is resulting from the normalization condition $S_i^2 = 1$. The situation is called *replica symmetric* (RS). When Q becomes finite, the ergodicity is broken as we discussed in Sec. 1.1.2.2.

Although it may appear that the RS order parameter can describe the glass transition, in most of the glass models, except for the 2-body spherical spin glass model [24], etc., this assumption causes the unphysical properties after the ergodicity is broken. For example the entropy becomes negative as find in the RS solution of the Sherrington-Kirkpatrick (SK) model [21]. It suggests that the replica symmetry breaking (RSB) takes place.

1.1.3.2 Replica symmetry breaking

More generally, the replica symmetry will be broken. The RSB ansatz for the order parameter was introduced by Parisi [22], which is given by

$$Q_{ab}^{k-\mathrm{RSB}} = Q_0 + \sum_{i=1}^{k+1} (Q_i - Q_{i-1}) I_{ab}^{m_i} = \sum_{i=0}^{k+1} Q_i (I_{ab}^{m_i} - I_{ab}^{m_{i+1}}), \tag{1.46}$$

where $Q_{k+1} = 1$ and $I_{ab}^{m_i}$ is a kind of generalized identity matrix of size $n \times n$ composed of blocks of size $m \times m$. (see Fig. 1.46 (a), (b)) In $I_{ab}^{m_i}$, the matrix elements in the diagonal blocks, are all 1 while those in the off-diagonal blocks are all 0. Here, $\{Q_i\}$ and $\{m_i\}$ are put in order as,

$$1 = Q_{k+1} > Q_k > ... > Q_1 > Q_0, \tag{1.47}$$

$$1 = m_{k+1} < m_k < ... < m_1 < m_0 = n. \tag{1.48}$$

In the limit $n \to 0$, we have,

$$1 = m_{k+1} > m_k > ... > m_1 > m_0 = 0. \tag{1.49}$$

The RSB order parameter can represent the hierarchical structure of the free energy. For example, in the case of $k = 1$ which is called *1-step RSB*, the matrix $\hat{Q}$ is parametrized by two parameters Q_0 and Q_1. This situation can be understood by the free-energy landscape which has two hierarchical levels (see Fig. 1.46 (c)). In this example, all replicas A, B and C are contained in a common big basin but they are grouped differently at the level of smaller basins: replicas A and B are contained the same basin but C is in a different small basin. The order parameters become $Q_{ab} = Q_1$ while $Q_{ac} = Q_{bc} = Q_0$. It is known that hard spheres in infinite dimension ($d = \infty$) [18] and p-body spin glass model ($p \geq 3$) [14] exhibit glass transitions with 1-step RSB.

The free-energy landscape becomes more complicated by increasing k since the number of hierarchical levels increases, as shown in Fig. 1.46 (d). The case in the limit $k \to \infty$ is called *full-RSB* and the order parameter becomes a monotonically increasing continuous function $Q(x)$ $(0 \leq x \leq 1)$ (see Fig. 1.46 (e)). q_{EA} corresponds to the overlap between replicas in the same local minimum and $\overline{q}$ corresponds to the averaged overlap over the whole phase space, namely q_{EA} and $\overline{q}$ are given by,

$$q_{\mathrm{EA}} = Q(1), \tag{1.50}$$

$$\overline{q} = \int dQ P(Q) Q, \tag{1.51}$$

$$P(Q) = \frac{\mathrm{d}x(Q)}{\mathrm{d}Q} \tag{1.52}$$

where $P(Q)$ represents the distribution of the order parameter. RS case corresponds to $Q(x) = \text{const}$ (see Sec. 1.1.3.1).

The full-RSB gives correct results for the spin glass phase of 2-body spin glass model such as SK model which is a representative spin glass model (see Sec. B). The full-RSB successfully describes some non-trivial properties at spin glasses. For example, hysteric behavior observed by the FC-ZFC protocol dependence of the susceptibility (Fig. 1.1 (c)) can be explained as follows. The ZFC susceptibility χ_{ZFC} which is observed by applying magnetic field after the system cooled in the spin glass phase is given by,

$$\chi_{\mathrm{ZFC}} = \beta(1 - q_{\mathrm{EA}}). \tag{1.53}$$

It is interpreted that the ZFC protocol only observe the susceptibility associated with local minimum. On the other hand, the FC susceptibility χ_{FC} which is observed by cooling under magnetic field is given,

$$\chi_{\mathrm{FC}} = \beta(1 - \overline{q}), \tag{1.54}$$

which reflects the susceptibility associated with the whole phase space. Full-RSB phases also appear in hardspheres in infinite dimensions ($d = \infty$) very large densities [18], p-spin Ising spin glass model ($p \geq 3$) at low temperatures [25] (see also [23]).

degree of freedom	quenched disorder	dimension	glass transition
particle	No	3	?
particle	No	∞	◯[18]
spin	Yes	3	◯[26, 27]
spin	Yes	∞	◯[23]
spin	No	3	?
spin	No	∞	◯

Table 1.1: **Summary of previous works and open problems**
In this thesis, we aim to clarify the possibility of a spin glass transition without quenched disorder in 3 dimension.

1.1.4 Is quenched disorder necessary?

Recently, it was established that, in the infinite dimension, disorder-free glass transitions can take place for both particle and spin degrees of freedom [18, 23] (see Table. 1.1). Now, the important question is whether disorder-free glass transition can occur in real *three-dimensional* systems or not. It is difficult for particle systems to clarify this because of the extremely fast growth of the relaxation time (Fig. 1.2 (b)) and crystallization.

Very interestingly, there are experimental reports which suggest that some geometrically frustrated magnets without chemical disorder exhibit the glass transition. In particular experiments performed on a class of pyrochlore magnets including $Y_2Mo_2O_7$ are known to show very clear spin glass transitions which cannot be distinguished from the one of the canonical spin glass as we will discuss in Sec. 1.4. The mechanism of this spin-glass formation has been an important theoretical challenge for some decades. We have constructed a theoretical spin model motivated by a recent experiment on $Y_2Mo_2O_7$ which is a prototypical frustrated magnet showing the spin glass behavior [28]. The model has not only spin degree of freedom but also lattice-displacement degree of freedom that is caused by a dynamical Jahn-Teller effect, i.e. it can be regarded as an orbital degree of freedom. In the following section, I give a short introduction of the geometrically frustrated spin model and then I focus on $Y_2Mo_2O_7$ which is the target material of this thesis.

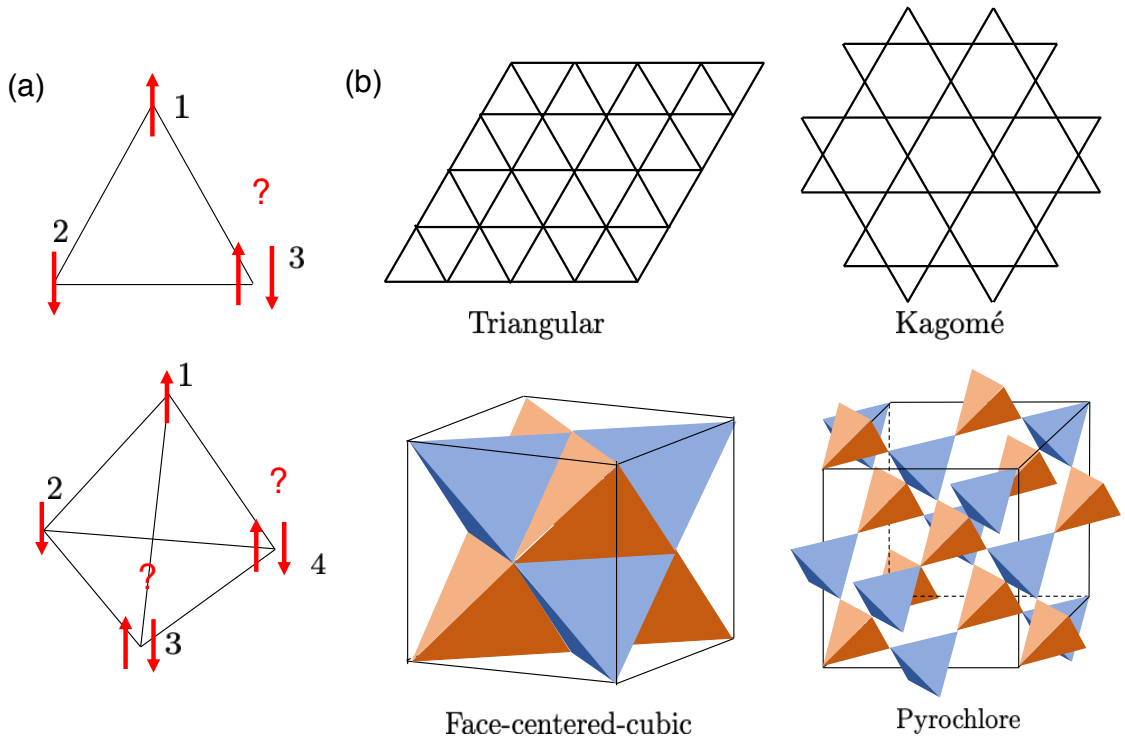

Figure 1.7: **Frustrated lattices**
(a): Ising spins with antiferromagnetic interactions on a triangle (top) and a tetrahedron (bottom). (b): Lattices made of simplexes.

1.2 Geometrical Frustration

In this section, we review some basic aspects of geometrical frustration in some representative magnetic systems [29]. First of all let us note that their thermodynamic properties are unusual. In ordinary systems, the entropy decrease monotonically by lowering the temperature and the system finally reach the ground state where the energy is the lowest and the entropy becomes 0, satisfying the third law of thermodynamics. In this process, a phase transition may take place from a disordered phase to an ordered phase, e.g. ferromagnets and crystals. On the other hand, strongly frustrated systems may not exhibit any long-ranged order even at temperatures lower than the energy scale of the interaction and opens various possibilities of unexpected behaviors at low temperatures. In particular, some geometrically frustrated spin system shows the disorder-free spin glass transition whose microscopic mechanism has not been understood yet. The goal of this thesis is to solve this problem for the case of a pyrochlore magnet $Y_2Mo_2O_7$.

Geometrical frustration in spin systems means a situation where spins in the system cannot find a configuration which fully satisfies all the interactions. The simplest example is the case where three Ising spins on the vertex of a single triangle interact with each other antiferromagnetically (See Fig. 1.7 (a)). If we put an up spin on the site 1 and a down spin on the site 2, the remaining spin on the site 3 cannot satisfy antiferromagnetic couplings 1-3 and 2-3 simultaneously. This frustrated situation can be easily generalized to simplexes including triangles, tetrahedra, e.t.c with spins put on the vertexes and antiferromagnetic interactions along the edges.

Now we can consider extended networks made of such simplexes, such as the triangular lattice, kagomé lattice and pyrochlore lattice with antiferromagnetic coupling on the edges (See Fig. 1.7 (b)). The important common feature is that they are *corner sharing*: adjacent simplexes are connected to each other only through their conners.

The important common feature of the antiferromagnetic model on the corner sharing network made of simplexes is the high degeneracy of the ground state. For example, let us consider an antiferromagnetic model on a triangular lattice, which is exactly solvable. [30] The number of ground states is proportional to $(0.323)^N$ for the number of spin N. According to the third law of thermodynamics, the entropy of a system should approach a constant value as the temperature approaches the absolute zero. Thus, this system breaks the third law of thermodynamics. Because of the degeneracy of the ground state, the system doesn't exhibit any magnetic order even at zero temperature.

In the following, we review two representative frustrated spin models on the pyrochlore lattice. One is a classical antiferromagnetic Heisenberg model and the other is a spin ice model. Both model do not show any ordered phase even at $T = 0$ because of the macroscopic degeneracy. Very interestingly, we will find that the two models put together provide the basis for the development of our effective model for the disorder-free spin glass transition in $Y_2Mo_2O_7$.

1.2.1 Example1: Classical antiferromagnetic Heisenberg model on the pyrochlore lattice

A pyrochlore lattice is a three dimensional network of corner-sharing tetrahedra, which belongs to the spatial symmetry group $Fm\bar{3}d$, which is the same as as a face-centered-cubic lattice. The pyrochlore structure appears in B sites of spinels AB_2O_4 or in A and B sites of pyrochlore oxides $A_2B_2O_7$. As we noted above the simple antiferromagnetic spin model on the pyrochlore lattice is strongly frustrated. Thus the model and its experimental counter part have been examined extensively by theoretical and experimental studies. [31]

First, let us consider the antiferromagnetic classical Heisenberg model on a *single* tetrahedron. [32] The Hamiltonian is given by,

$$H = J\sum_{i<j}^{4} \boldsymbol{S}_i \cdot \boldsymbol{S}_j, \qquad (J > 0). \tag{1.55}$$

When the spin length is normalized as $|\boldsymbol{S}_i| = 1$, the Hamiltonian can be rewritten as,

$$H = \frac{J}{2}\left(\sum_{i=1}^{4} \boldsymbol{S}_i\right)^2 - 2J. \tag{1.56}$$

Thus, the energy of the ground state is $-2J$ and the spins in the ground state must satisfy the condition $\sum_i \boldsymbol{S}_i = \boldsymbol{0}$. Such a spin configuration in the ground state can be parametrized as follows:

$$\begin{aligned}
&\boldsymbol{S}_1 = (0, 0, 1),\\
&\boldsymbol{S}_2 = (\sin\theta_2, 0, \cos\theta_2),\\
&\boldsymbol{S}_3 = (\sin\theta_3\cos\phi_3, \sin\theta_3\sin\phi_3, \cos\theta_3),\\
&\boldsymbol{S}_4 = (-\sin\theta_2 - \sin\theta_3\cos\phi_3, -\sin\theta_3\sin\phi_3, -1 - \cos\theta_2 - \cos\theta_3),
\end{aligned} \tag{1.57}$$

where

$$\cos\phi_3 = \frac{-(\cos\theta_2 + 1)(\cos\theta_3 + 1)}{\sin\theta_2\sin\theta_3} \tag{1.58}$$

and $0 \le \pi - \theta_2 \le \theta_3 \le \pi$. Here, $\boldsymbol{S}_1$ is fixed for convenience. The above expressions mean that the spin configuration in the ground state can be parametrized by two continuous variables θ_2 and θ_3. This can be understood by the following counting argument. The number of degrees of freedom for each spin is 2 because there is spin normalization condition $|\mathbf{S}_i| = 1$. From the constraint of the ground state $\sum_i \boldsymbol{S}_i = \boldsymbol{0}$, we have three constraints $\sum_i S_i^x = \sum_i S_i^y = \sum_i S_i^z = 0$. In addition, there is a global rotational symmetry around three axes x, y and z. Thus, we obtain the number of the remaining internal degrees of freedom as, $2 \times 4 - 3 - 3 = 2$.

Now let us extend the counting argument to the whole system of the pyrochlore lattice. The total number of degrees of freedom is $2N$ for the N-spin system. Each spin is shared by two tetrahedron so that the number of tetrahedra is $2N/4$. Since each tetrahedron gives three constraints, the total number of constraints is $3N/2$. Hence, there are $2N - (2N/4) \times 3 = N/2$ excess degrees of freedom. The macroscopic number of continuous excess degrees of freedom left in the ground state manifold make the system disordered even at zero temperature.

Next let us review the result of a previous Monte Carlo simulation. [33] The Hamiltonian is given by,

$$H = J \sum_{<ij>} \boldsymbol{S}_i \cdot \boldsymbol{S}_j, \qquad (J > 0), \tag{1.59}$$

where $< ij >$ represents all possible nearest neighboring pairs on a pyrochlore lattice. The energy per a spin of the ground state is $-J$. In this system, the dimensionless temperature $\tilde{T} = J/k_B T$ is the only parameter, which we call it simply as T. Fig. 1.8 (a) shows the temperature dependence of the energy per spin $\langle E \rangle_{\rm eq}$, where $\langle \cdots \rangle_{\rm eq}$ represents the Monte Carlo average. By lowering the temperature the energy smoothly converges to the ground state energy $-J$ without any anomaly. Fig. 1.8 (b) shows the specific heat given by,

$$C = \frac{1}{NT^2} \Big(\langle E^2 \rangle_{\rm eq} - \langle E \rangle_{\rm eq}^2 \Big). \tag{1.60}$$

It monotonically increases by lowering the temperature without any singularities. Next, let us look at the spin auto-correlation function,

$$C(t) = \frac{1}{N} \sum_{i=1}^{N} \langle \boldsymbol{S}_i(0) \cdot \boldsymbol{S}_i(t) \rangle_{\rm eq}, \tag{1.61}$$

measured in equilibrium, which is shown in Fig. 1.8 (c). The data implies that the relaxation time monotonically increases lowering the temperature without a sign of phase transition at finite temperatures. The above observations strongly suggests that the system does not exhibit any phase transitions at finite temperatures.

1.2.2 Example2: Spin ice

Next let us review briefly the spin ice problem [29, 34]. The "spin ice" was named due to an analogy to water ice under ordinary pressures. In the water ice, each oxygen atom makes bonds with four nearby hydrogen atoms tetrahedrally (See Fig. 1.9). Two bonds are covalent bonds which create a H_2O molecule. The others are hydrogen bonds where the hydrogens form covalent bonds with other oxygens. In the other words, two hydrogen atoms are close to the oxygen (*in*) and the others are far from it (*out*). This is the so called ice rule: a tetrahedron is said to satisfy the ice rule when the 2-in-2-out structure holds. Note that there are 6 possible configurations which satisfy the ice rule for a tetrahedron. This local degeneracy leads to a macroscopic degeneracy of the energy. Indeed it is known that this system has a finite entropy down to 0 K and it is approximately estimated by Pauling [35] as $S = (N k_{\rm B}/2) \log(3/2)$.

In pyrochlore oxides $Dy_2Ti_2O_7$, $Ho_2Ti_2O_7$, one can realize the same situation. Because of the strong anisotropy in such systems, spins on the pyrochlore lattice become either parallel or anti-parallel to direction toward the center of tetrahedrons which contain them, more precisely the spins (see Fig 1.7 (b)) can be written as,

$$\begin{aligned} \boldsymbol{\sigma}_1 &= \frac{1}{\sqrt{3}} \sigma \begin{pmatrix} +1 \\ +1 \\ +1 \end{pmatrix} \quad \boldsymbol{\sigma}_2 = \frac{1}{\sqrt{3}} \sigma \begin{pmatrix} -1 \\ -1 \\ +1 \end{pmatrix} \\ \boldsymbol{\sigma}_3 &= \frac{1}{\sqrt{3}} \sigma \begin{pmatrix} +1 \\ -1 \\ -1 \end{pmatrix} \quad \boldsymbol{\sigma}_4 = \frac{1}{\sqrt{3}} \sigma \begin{pmatrix} -1 \\ +1 \\ -1 \end{pmatrix}, \end{aligned} \tag{1.62}$$

where σ takes ± 1 representing *in* or *out* . The spins correspond to the displacements of hydrogen atoms in the water ice. We can observe that the inner product between a pair of spins in a tetrahedron $\boldsymbol{\sigma}_i, \boldsymbol{\sigma}_j$ can take only two kinds of values as

$$\boldsymbol{\sigma}_i \cdot \boldsymbol{\sigma}_j = \begin{cases} -1/3 & \text{if both spins are } \textit{in} \text{ or } \textit{out} \\ 1/3 & \text{if one is } \textit{in} \text{ and the other is } \textit{out} \ . \end{cases} \tag{1.63}$$

Thus, spin configurations which satisfy the ice-rule can be realized as the ground states of the following effective ferromagnetic model, which we call as spin ice Hamiltonian,

$$H = -J \sum_{<ij>} \boldsymbol{\sigma}_i \cdot \boldsymbol{\sigma}_j = \frac{J}{3} \sum_{\triangle=1}^{N_\triangle} \sum_{i<j}^{4} \sigma_{i(\triangle)} \sigma_{j(\triangle)}, \tag{1.64}$$

where $\triangle$ represents the indices of tetrahedra and $N_\triangle$ is the number of total tetrahedra in the system.

The macroscopic degeneracy of the ground state is precisely the same as the water-ice problem. The energy landscape of the model should look like Fig. 1.9 (c): there are exponentially large number of degenerate energy minima which are separated by small energy barriers of O(1). However, it is known that the spin fluctuations in the spin ice system exhibit a characteristic short-ranged correlation. Fig. 1.10 (a) and (b) shows the static structure factors obtained by the neutron scattering experiment and the numerical simulation, respectively. There are characteristic features called the pinch points.

1.3 Ordering by lattice distortion

Strongly frustrated system can remain disordered at temperatures lower than the energy scale of interactions. However, some systems show unconventional long-ranged ordered states, e.g. the ordering of a composite degree of freedom such as chirality [38, 39] and magnetic ordering due to thermal fluctuation [40, 41]. The mechanism of the latter is similar to the Alder transition of hardspheres [42] and is called order by disorder. On the other hand, in real materials, perturbative interactions such as second or third nearest neighbor exchange interactions and the dipolar interaction which can be negligible in ordinal systems, quantum fluctuation and lattice distortion often become important in frustrated systems. Therefore, there are many possibilities to observe non-trivial ordering phenomena in frustrated magnets.

Another important player in frustrated magnets, like the pyrochlore antiferromagnets we reviewed in Sec. 1.2.1, is the lattice distortion which can be coupled to the spin degrees of freedom. In the following we review the cases that the spin-lattice coupling induces non-trivial ordering in some pyrochlore antiferromagnetic systems. This effect is called spin-Jahn-Teller effect. To avoid confusion, we must distinguish it from another Jahn-Teller effect that we discuss later, which involves orbital degrees of freedom.

1.3.1 Experiments on $CdCr_2O_4$

As a typical example, let us explain the case of $CdCr_2O_4$. It exhibits a structural phase transition presumably due to a spin-lattice coupling which removes the spin frustration. [43] Cr^{3+} ions have three electrons in their triply degenerate t_{2g} orbitals and form $S = 3/2$ spin effectively, i.e. the spin can be regarded a classical spin. t_{2g} orbitals are half filled and Cr^{3+} ions are *not* Jahn-Teller active so that the orbital angular momentum should be quenching (See Sec. C.3). However, the system shows a structural phase transition from cubic to tetragonal structure at $T_c = 7.8$ K. Spins also show a phase transition simultaneously to the antiferromagnetic Néel state, as shown in Fig. 1.11 (a). This is because the structural phase transition occurs to deform the tetrahedron by which the exchange interactions are changed. This phenomenon is called the spin-Jahn-Teller distortion which is caused not by orbital degeneracy but spin frustration.

Under applied the external magnetic field H below T_c, a gigantic magnetostriction takes place because the magnetic field removes the spin frustration. Fig. 1.11 (b) displays the magnetic field dependence of the magnetization per spin, taken from [43]. The magnetization first grows linearly with the field, then jumps to around $1.5\mu_B$ at 28 T and saturates to a plateau. From Eq. (C.109), we find that $1.5\mu_B$ corresponds to one half of the full moment since $S = 3/2$ in this system. The system falls into a 1/2 magnetization plateau state with three-up and one-down spins out of four spins of each Cr^{3+} tetrahedron. In addition, the inset of Fig. 1.11 (b) shows the magnetostriction along [111] and $[1\bar{1}0]$ with applied field parallel to [111]. The magnetostriction of 4×10^{-4} is clearly observed for both directions. Since the orbital angular momentum is quenching, we can interpret the magnetostriction as a frustration effect.

1.3.2 Theoretical modeling

Now, I review two candidate theoretical models which include some spin-lattice couplings. [44, 45, 46]

1.3.2.1 Bond-phonon model

First one is a "bond-phonon" model [45] which takes into account the elastic energy depending on the distance between two magnetic ions and the exchange interaction is modified due to the distortion. The starting Hamiltonian is given by,

$$H = \sum_{<i,j>} \left[J(1 - \alpha\rho_{ij}) \boldsymbol{S}_i \cdot \boldsymbol{S}_j + \frac{c}{2}\rho_{ij}^2 \right] \tag{1.65}$$

where the summation $< i, j >$ runs over the nearest neighbor pairs of the vertices on the pyrochlore lattice and ρ_{ij} is the change of the distance between neighboring spins $\boldsymbol{S}_i$ and $\boldsymbol{S}_j$ relative to the equilibrium distance. It is assumed that exchange interactions linearly depend on ρ_{ij}. Here, it is convenient to introduce a single dimensionless parameter $b = J\alpha^2/c$ to measure the strength of the spin-lattice coupling. The Hamiltonian can be rewritten as,

$$H = \sum_{<i,j>} \left[J\boldsymbol{S}_i \cdot \boldsymbol{S}_j + \frac{c}{2}\left(\rho_{ij} - \rho_{ij}^*\right)^2 - \frac{c}{2}\rho_{ij}^{*2} \right] \tag{1.66}$$

with

$$\rho_{ij}^* = \frac{b}{\alpha}\boldsymbol{S}_i \cdot \boldsymbol{S}_j. \tag{1.67}$$

By integrating out the displacement ρ_{ij} for all i, one finds a renormalized Hamiltonian,

$$H = J \sum_{<i,j>} \left[\boldsymbol{S}_i \cdot \boldsymbol{S}_j - b(\boldsymbol{S}_i \cdot \boldsymbol{S}_j)^2 \right]. \tag{1.68}$$

The second term is called a bi-quadratic term which favors collinear spin structures. The lattice becomes deformed at lower temperatures by which the symmetry of the lattice is reduced from the cubic symmetry to tetragonal one. By applying a magnetic field h and increasing it up to about $3J$, one finds a first order phase transition accompanying the magnetostriction.

1.3.2.2 Site-phonon model

Another candidate is a "site-phonon" model [46] which assumes that the lattice points can deform elastically independently from each other as in the Einstein model for solids. With the displacement vector $\boldsymbol{u}_i$ at site i from its equilibrium position $\boldsymbol{r}_i^0$, the Hamiltonian is given by,

$$H = \sum_{<i,j>} J_{\rm ex}(|\boldsymbol{r}_{ij}^0 + \boldsymbol{u}_i - \boldsymbol{u}_j|)\boldsymbol{S}_i \cdot \boldsymbol{S}_j + \frac{c}{2}\sum_{i=1}^{N} |\boldsymbol{u}_i|^2, \tag{1.69}$$

where $\boldsymbol{S}_i$ is the classical Heisenberg spin at the site i, $\boldsymbol{r}_{ij}^0 = \boldsymbol{r}_i^0 - \boldsymbol{r}_j^0$, c is an elastic constant, $J_{\rm ex}(r_{ij})$ is the exchange interaction that is assumed to depend only on the distance r_{ij} between the two spins, and the summation $< i, j >$ is taken over all nearest neighboring pairs. By expanding $J_{\rm ex}(|\boldsymbol{r}_{ij}^0 + \boldsymbol{u}_i - \boldsymbol{u}_j|)$ with respect to $\boldsymbol{u}_i/|\boldsymbol{r}_i^0|$, we find,

$$J_{\rm ex}(|\boldsymbol{r}_{ij}^0 + \boldsymbol{u}_i - \boldsymbol{u}_j|) \approx J_{\rm ex}(|\boldsymbol{r}_{ij}^0|) + \left.\frac{{\rm d}J_{\rm ex}}{{\rm d}r}\right|_{r=|\boldsymbol{r}_{ij}^0|} \boldsymbol{e}_{ij} \cdot (\boldsymbol{u}_i - \boldsymbol{u}_j) \tag{1.70}$$

with $\boldsymbol{e}_{ij} = \boldsymbol{r}_{ij}^0/|\boldsymbol{r}_{ij}^0|$. Since $|\boldsymbol{r}_{ij}^0|$ is constant, it is convenient to introduce two parameters defined as

$$J = J_{\rm ex}(|\boldsymbol{r}_{ij}^0|), \tag{1.71}$$

$$b = \frac{1}{cJ}\left[\left.\frac{{\rm d}J_{\rm ex}}{{\rm d}r}\right|_{r=|\boldsymbol{r}_{ij}^0|} \right]^2. \tag{1.72}$$

The Hamiltonian can be rewritten as

$$\begin{aligned} H &\approx J \sum_{<i,j>} \boldsymbol{S}_i \cdot \boldsymbol{S}_j + \sqrt{cJb} \sum_{<i,j>} \boldsymbol{e}_{ij} \cdot (\boldsymbol{u}_i - \boldsymbol{u}_j) \boldsymbol{S}_i \cdot \boldsymbol{S}_j + \frac{c}{2} \sum_{i=1}^{N} |\boldsymbol{u}_i|^2 \\ &\approx J \sum_{<i,j>} \boldsymbol{S}_i \cdot \boldsymbol{S}_j + \frac{c}{2} \sum_{i=1}^{N} \left[|\boldsymbol{u}_i|^2 + \sqrt{cJb} \sum_{j \in \partial i} (\boldsymbol{S}_i \cdot \boldsymbol{S}_j) \boldsymbol{e}_{ij} \cdot \boldsymbol{u}_i \right] \\ &\approx J \sum_{<i,j>} \boldsymbol{S}_i \cdot \boldsymbol{S}_j + \frac{c}{2} \sum_{i=1}^{N} |\boldsymbol{u}_i - \boldsymbol{u}_i^*|^2 - \frac{c}{2} \sum_{i=1}^{N} |\boldsymbol{u}_i^*|^2 \end{aligned} \tag{1.73}$$

with

$$\boldsymbol{u}_i^* = \sqrt{\frac{Jb}{c}} \sum_{j \in \partial i} (\boldsymbol{S}_i \cdot \boldsymbol{S}_j) \boldsymbol{e}_{ij}, \tag{1.74}$$

where ∂i represents the set of nearest neighboring sites of i and $\boldsymbol{u}_i^*$ means the stationary point of the lattice displacement. By integrating out the $\boldsymbol{u}_i$ for all i, we obtain an effective spin Hamiltonian,

$$H_{\text{eff}} = H_0 + H_{\text{SL}} \tag{1.75}$$

with

$$H_0 = J \sum_{<i,j>} \boldsymbol{S}_i \cdot \boldsymbol{S}_j, \tag{1.76}$$

$$H_{\text{SL}} = \frac{c}{2} \sum_{i=1} |\boldsymbol{u}_i^*|^2 = -Jb \sum_{<i,j>} (\boldsymbol{S}_i \cdot \boldsymbol{S}_j)^2 - \frac{Jb}{2} \sum_{j \neq k \in \partial i} \boldsymbol{e}_{ij} \cdot \boldsymbol{e}_{ik} (\boldsymbol{S}_i \cdot \boldsymbol{S}_j)(\boldsymbol{S}_i \cdot \boldsymbol{S}_k). \tag{1.77}$$

H_0 is the classical antiferromagnetic Hamiltonian explained in Sec. 1.2.1 if $J > 0$, and then b is also positive. The first term of H_{SL} favors collinear spin states and tends to induce the spin nematic order similarly to the bond-phonon model. The second term represents effective further-neighbor interactions which is absent in the bond-phonon model (Eq. (1.68)). Since b is proportional to $1/c$, b becomes zero in the limit $c \to 0$ (hard lattice limit), i.e. the model is reduced back to a conventional antiferromagnetic model on the pyrochlore lattice.

This model exhibits periodic patterns for both spin $\boldsymbol{S}_i$ and lattice distortion $\boldsymbol{u}_i^*$ at low temperatures. For the case of the strong lattice coupling b, the system realizes cubic symmetric state characterized by the magnetic $(1/2, 1/2, 1/2)$ Bragg peaks, while the lattice distortion structure exhibits $(1, 1, 0)$ Bragg peaks. Note that the cubic phase is absent in the bond-phonon model. For weak lattice coupling b, by contrast, the ordered phase is tetragonal symmetric with the spin structure exhibiting multiple Bragg peaks at the cubic-symmetry-broken combination of the $(1, 1, 0)$ family and the lattice structure factor shows peaks at the $(1, 1, 1)$ family. This phase is also found in the bond-phonon model. Fig. 1.13 shows the phase diagram of this model. First order phase transitions occur on all phase boundaries.

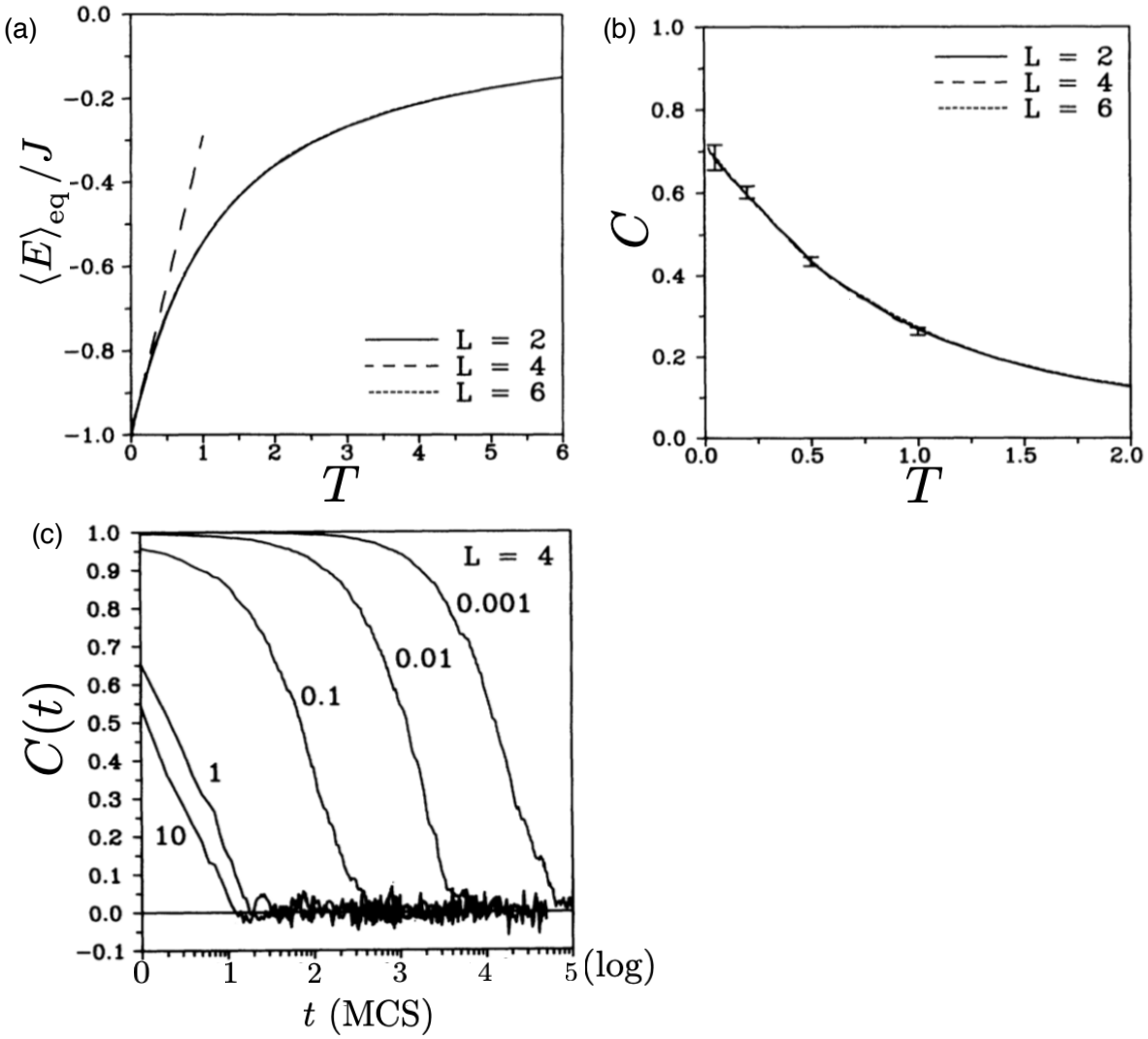

Figure 1.8: **The MC simulation data of the antiferromagnetic Heisenberg model on the pyrochlore lattice, taken from [33]**
(a),(b): Energy and specific heat per spin. (c): Spin auto-correlation function measured at $T/J = 10, 1, 0.1, 0.01$ and 0.001.

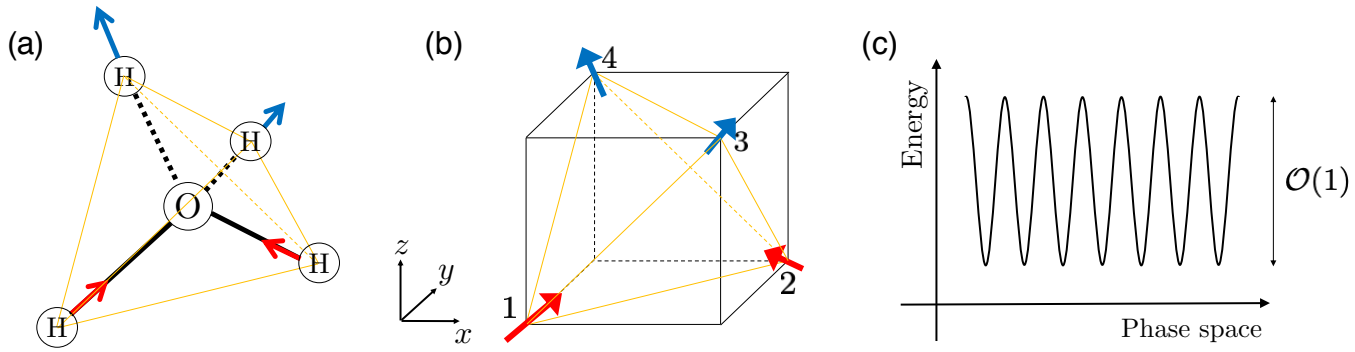

Figure 1.9: **Ice configurations**
(a): Hydrogen configuration of H_2O in water ice. Solid and dash lines correspond to covalent and hydrogen bonds, respectively. (b): 2-*in*-2-*out* structure in spin ice. (c): Energy landscape of ice configurations.

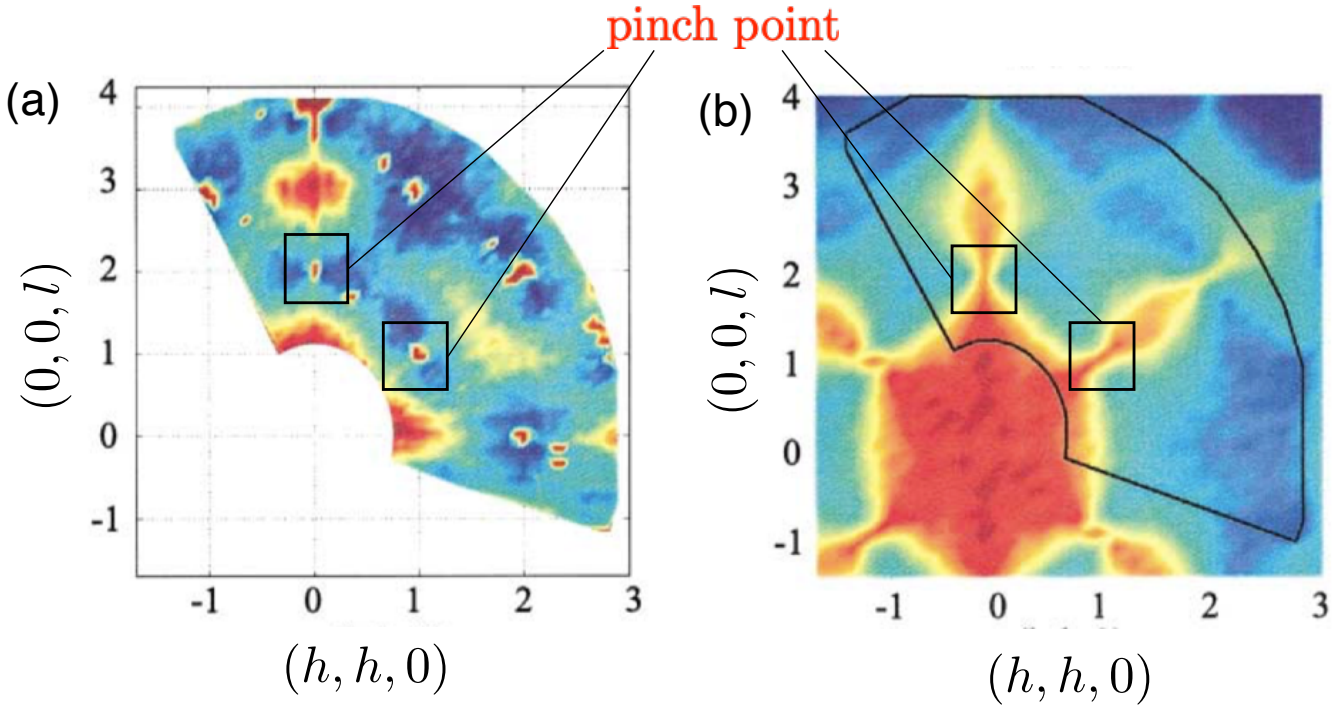

Figure 1.10: **Pinch point structure**
(a): Experimental neutron scattering pattern of $Ho_2Ti_2O_7$ in the (hhl) plane of reciprocal space at $T \sim 50$ mK. Dark blue indicates the lowest intensity and red-brown indicates the highest intensity. (b): Static structure factor for the spin ice model at $T = 0.15J$. (a), (b) are taken from [36, 37].

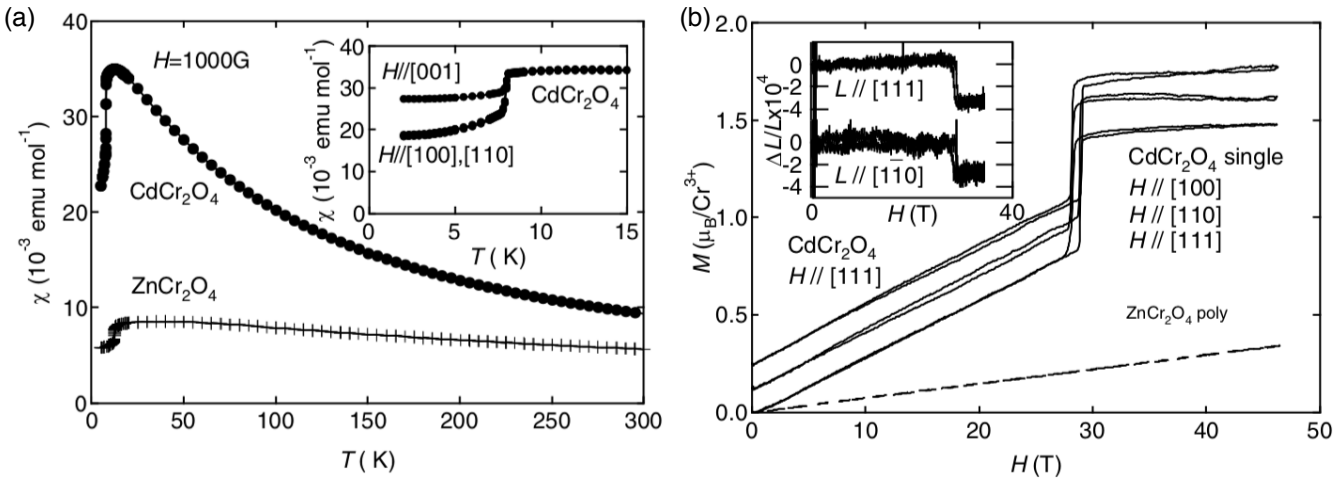

Figure 1.11: **Experimental results of $CdCr_2O_4$ taken from [43]**
(a): Temperature dependence of magnetic susceptibility of $CdCr_2O_4$ single crystal. The inset demonstrates the anisotropy of the magnetic susceptibility in the tetragonal phase. (b): Magnetization curves of $CdCr_2O_4$ single crystal in field of up to 47 T, taken at a temperature of 1.8 K. Magnetic fields are applied along [100], [110], and [111] in cubic indices. The curves are shifted to avoid overlapping. The inset shows longitudinal (along [111]) and transversal (along $[1\bar{1}0]$) magnetostriction measured at 4.2 K, when a magnetic field is applied along the [111] direction of the crystal.

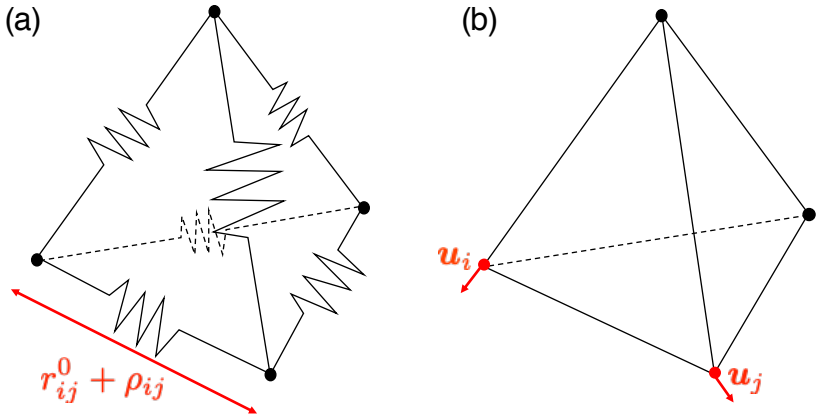

Figure 1.12: **Schematic pictures of the bond-phonon (a) and the site phonon (b) models**

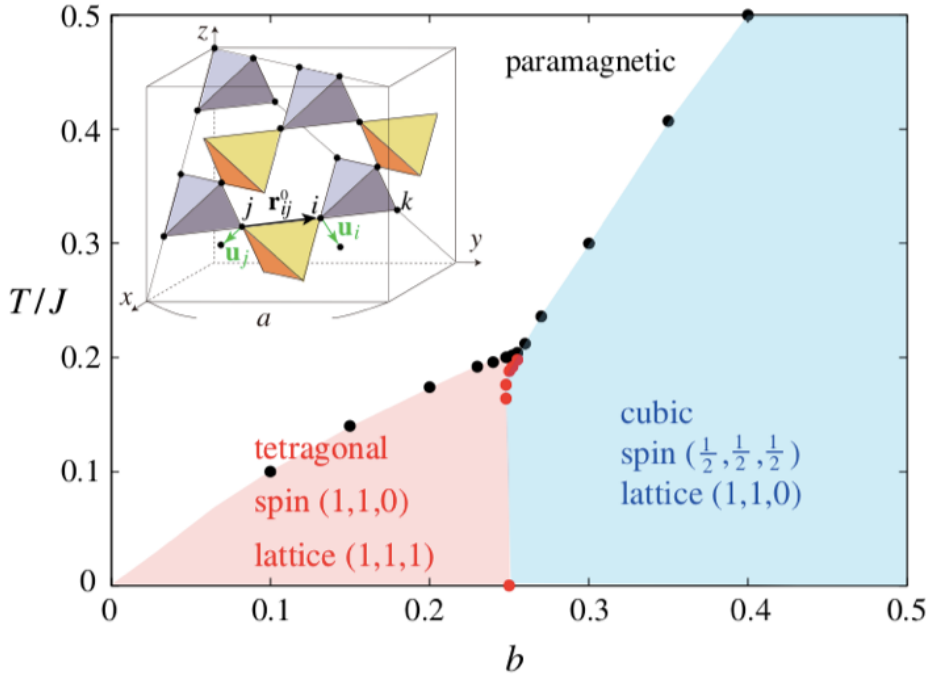

Figure 1.13: **The b-T phase diagram of the pyrochlore magnet with local lattice distortions in the site-phonon model taken from [46]**
The parameter b measures the strength of the spin-lattice coupling. Two types of collinear magnetic long-range-ordered phases with the commensurate lattice distortions are realized. The black dots denote first-order transition points between the paramagnetic and the ordered phases, while the red dots denote those between the ordered phases. The inset shows a cubic unit cell of the side length a, where the lattice distortion vector ui is represented by the green arrow.

1.4 Spin glass transition on disorder-free pyrochlore magnets

In Sec. 1.1.1.1, we reviewed spin glasses in which interactions between spins are quenched and disordered. However it has been known experimentally that some frustrated magnets on kagomé and pyrhoclore lattices exhibit spin glass transition with very little or possibly without any appreciably quenched disorder. The mechanism of the spin glass transitions remain unsolved.

The target of this thesis is the antiferromagnetic system on the pyrochlore lattice such as $Y_2Mo_2O_7$ which is considered as a spin glass without quenched disorder. In Sec. 1.2 we have seen that purely antiferromagnetic spin model on the pyrochlore lattice remain in the paramagnetic phase down to zero temperature. In Sec. 1.3 we recalled some experimental and theoretical results which suggest onset of long-ranged ordering due to spin-lattice coupling. Then the question is what is needed in order to realize the experimentally observed spin glass transition on the pyrochlore magnet.

In this section, we review some key previous results of studies on the pyrochlore magnet $Y_2Mo_2O_7$. We first review previous results on the spin glass transitions by experiments of the material (Sec. 1.4.1) as well as simulations which assumed presence of quenched disorder (Sec. 1.1.1.1). Then we review some important microscopic properties of the $Y_2Mo_2O_7$ magnet in Sec. 1.4.3: the crystalline structure (Sec. 1.4.3.1), electronic properties (Sec. 1.4.3.2) and Jahn-Teller distortion (Sec. 1.4.3.3). Finally in Sec. 1.4.4 we present our effective model for the Y2Mo2O7 magnet which include the two key dynamical degrees of freedom in the system: spins and lattice distortions. Although our model may appear similar to the model discussed in Sec. 1.3, it is distinct in several key points.

1.4.1 Experimental results in $Y_2Mo_2O_7$

In Sec. 1.1.1.1 we reviewed some key experimental features of the spin glass transitions observed in the canonical spin glasses. Quite interestingly many of them are also see in the pyrochlore magnet Y2Mo2O7 as we list below (see Fig. 1.1 and compare it with Fig. 1.14): spin glass transitions on canonical spin glasses with quenched disorder, which we reviewed in Sec. 1.1.1.1, accompany the divergent behavior of the nonlinear magnetic susceptibility χ_3 (see Fig. 1.1 (b)) at the critical point T_c while the linear magnetic susceptibility χ exhibits a cusp (see Fig. 1.1 (c)) and the heat capacity C exhibits no singularity but a broad peak around T_c.

Heat capacity

Fig. 1.14 (a) shows the temperature dependence of the heat capacity. Apparently, we can't find any singularities in this plot but a broad peak.

Nonlinear susceptibility

Fig. 1.14 (b) shows the scaling plot of the nonlinear susceptibility which assumes a scaling form,

$$\chi_3 \sim H^{2/\delta}\mathcal{F}\Big((T/T_c-1)^{\frac{\gamma+\beta}{2}}/H\Big), \tag{1.78}$$

where H is the external magnetic field, δ, γ and β are critical exponents defined as

$$\begin{aligned} \chi_3(T=T_c,H) &\sim H^{2/\delta}, \\ \chi_3(T,H=0) &\sim -|T/T_c-1|^{-\gamma}, \\ Q(T,H=0) &\sim |T/T_c-1|^{\beta}. \end{aligned} \tag{1.79}$$

Here, Q is the spin-glass order parameter. The collapse of the data is convincing and the critical exponents satisfy the scaling relation,

$$\delta = 1+\gamma/\beta, \tag{1.80}$$

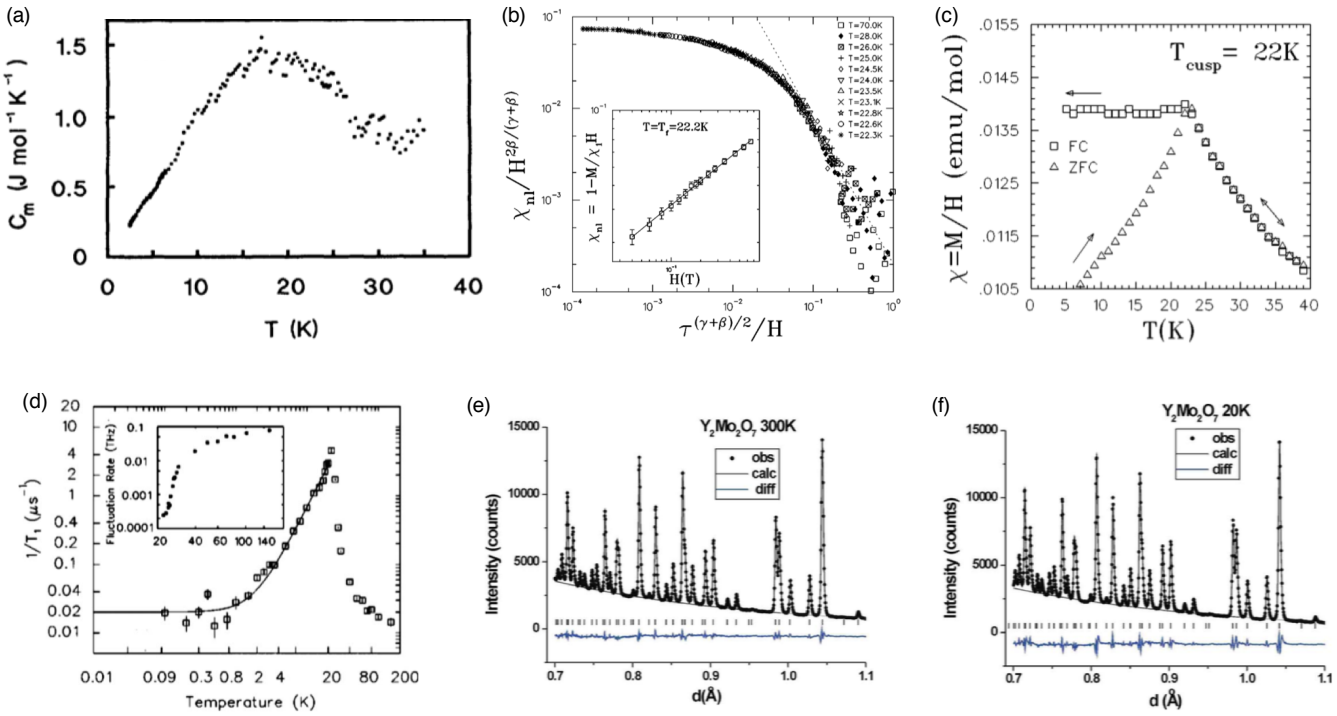

Figure 1.14: **Some key experimental results on $Y_2Mo_2O_7$ spin glass**
(a): Magnetic specific heat, taken from [47]. (b): Nonlinear magnetization analyzed according to a scaling form Eq. (1.78) for a nonzero spin glass transition temperature with choices $T_c = 22$ K, $\gamma = 2.8$, $\beta = 0.75$. The inset shows the log-log plot $\chi_{nl} \approx \chi_3 \sim H^{\delta/2}$ at $T = T_c$ with the value of $\delta = 4.73$ predicted from the scaling relation Eq. (1.80). (c): Field-cooled (FC, squares) and zero field-cooled (ZFC, triangles) susceptibility for $Y_2Mo_2O_7$ in a magnetic field 100 Oe. (b) and (c) are taken from [48]. (d): The muon spin relaxation rate $1/T_1$ vs temperature for $Y_2Mo_2O_7$ in a small applied field of 0.02 T, taken from [49]. The solid line is the best fit to the data assuming a power-law functional form. The Mo^{4+} spin fluctuation rate vs temperature above T_c is shown in the inset. (e),(f): Comparison of neutron diffraction data for $Y_2Mo_2O_7$ at (e) 300 K and (f) 20 K showing the absence of a structural phase transition, taken from [50].

giving $T_c \approx 22$ K, $\gamma = 2.9(5)$, $\beta = 0.8(2)$, and $\delta \approx 4.7$. These critical exponents are closed to ones of canonical spin glasses [51].

FC-ZFC susceptibility

Another notable feature of spin glasses is the FC-ZFC protocol dependence of the magnetic susceptibility (see Fig. 1.1 (c)). The difference of the FC/ZFC susceptibilities mean that the system in the spin glass phase falls out of equilibrium. As shown in Fig. 1.14 (c), we can find that the lines clearly branch off below T_c. Very much similarly as the canonical spin glass with quenched disorder.

Spin relaxation

Strong evidence for spin freezing also comes from studies of spin dynamics studied by muon spin relaxation (see Fig. 1.14 (d)). These data show features typical of disordered spin-frozen systems such as a critical slowing down as T_c is approached from above followed by a sharp decrease.

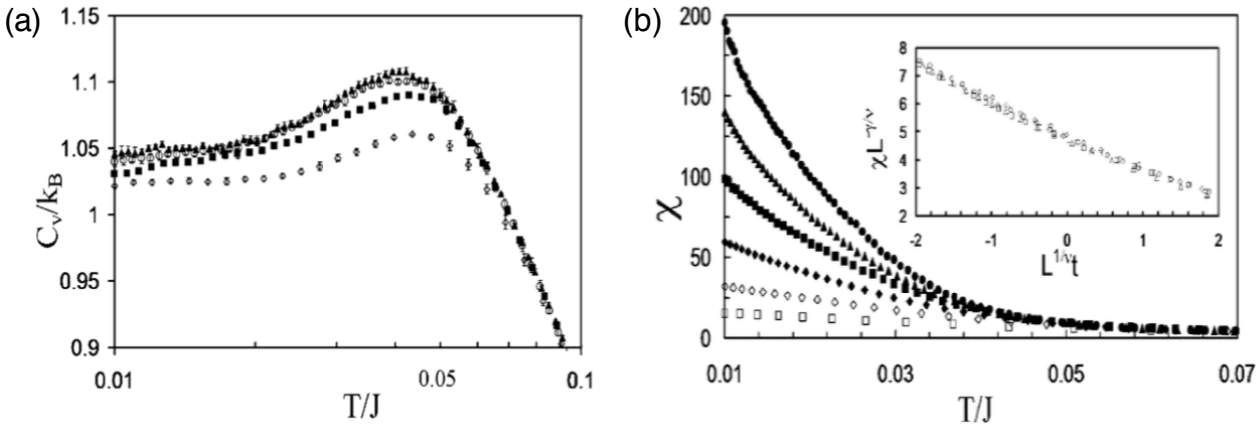

Figure 1.15: **Simulation results of the pyrochlore magnet with quenched disorder taken from [52]**
(a): Heat capacity vs temperature for $\Delta/J = 0.1$ and $L = 3, 4, 5, 6$ (from bottom to top). (b): Spin glass susceptibility vs temperature for $\Delta/J = 0.1$ and $L = 2, 3, 4, 5, 6, 7$ (from bottom to top). Inset: Scaling collapse.

Lattice structure

Finally, I show the neutron diffraction data structures below and above T_c in Fig. 1.14 (e) and (f). Since there are no notable changes between the two data, one can conclude that structural phase transitions do not occur.

1.4.2 Simulation results with quenched disorder

Here we review a previous numerical simulation of the pyrochlore magnet which assumes presence of some quenched disorder. [52, 53] The Hamiltonian is given by,

$$H = \sum_{<ij>} J_{ij} \boldsymbol{S}_i \cdot \boldsymbol{S}_j, \tag{1.81}$$

where J_{ij} is independently and uniformly distributed on the interval $[J - \Delta, J + \Delta]$ with $0.05 \leq \Delta/J \leq 0.2$. Note that all bonds have antiferromagnetic interactions. It has been found that a spin glass transition takes place at Tc which is proportional to the amount to quenched disorder Δ added to the system. The assumption of quenched disorder remain questionable since there are no appreciable chemical disorder in $Y_2Mo_2O_7$.

The heat capacity for $\Delta/J = 0.1$, shown in Fig. 1.15 (a), varies smoothly with T, as in the conventional spin glasses with strong quenched disorder. They also observed the spin glass susceptibility χ_{SG} for $\Delta/J = 0.1$, shown in Fig. 1.15 (b). The rapid increase in χ_{SG} with system size L at low T is clear. In the vicinity of T_c, one can expect a finite-size scaling behavior,

$$\chi_{SG} \sim L^{\gamma/\nu} f(L^{1/\nu}(T/T_c - 1)), \tag{1.82}$$

where ν is the critical exponent for the correlation length. Scaling collapse of the data is shown in the inset of Fig. 1.15 (b), with $T_c = 0.023$, $\nu = 1$ and $\gamma = 1.45$.

1.4.3 Some key microscopic properties of the pyrochlore oxide $A_2Mo_2O_7$

In order to understand the mechanism of the spin glass transition in the $Y_2Mo_2O_7$, we summarize below some important microscopic properties of the family of pyrochlore oxides $A_2Mo_2O_7$.

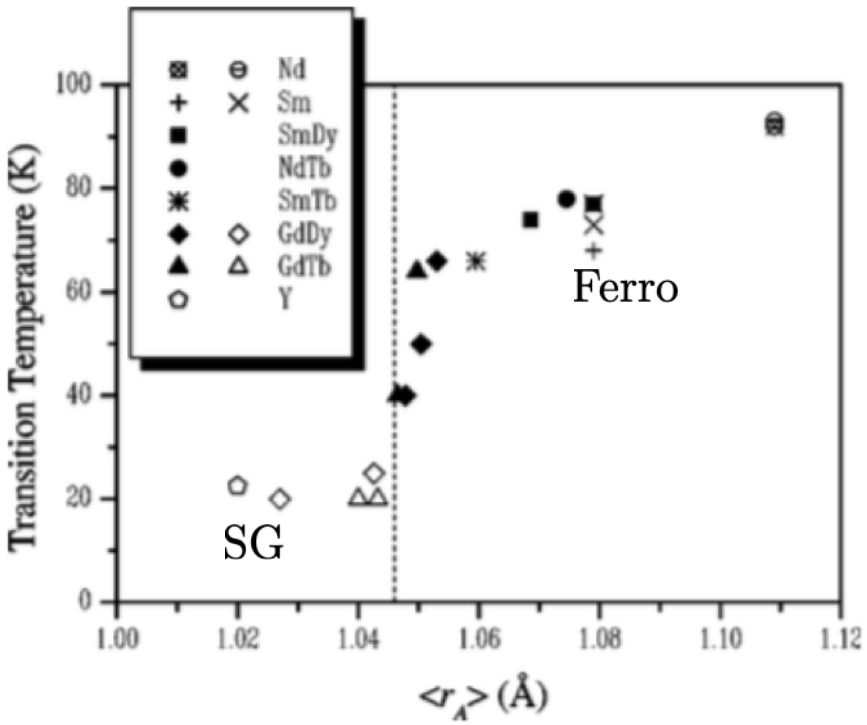

Figure 1.16: **Experimental phase diagram of $A_2Mo_2O_7$: transition temperature T_c vs the averaged ionic radius $\langle r_A \rangle$**
The values for $Nd_2Mo_2O_7$ are taken from [54] ($\otimes$) and [54] ($\ominus$), those for $Sm_2Mo_2O_7$ from [54] (+) and [55] ($\times$), those for $(Sm_{1-x}Dy_x)_2Mo_2O_7$ ($x = 0$ and 0.2), $(Nd_{1-x}Tb_x)_2Mo_2O_7$ ($x = 0.5$), $(Sm_{1-x}Tb_x)_2Mo_2O_7$ ($x = 0.5$), $(Gd_{1-x}Dy_x)_2Mo_2O_7$ ($x = 0$, 0.1, 0.2, 0.4, and 1), and $(Gd_{1-x}Tb_x)_2Mo_2O_7$ ($x = 0.25$, 0.5, 0.75, and 1) from [56], and those for $Y_2Mo_2O_7$ from [57]. The dotted line shows the boundary between ferromagnetic (right) and spin glass (left) behavior. This figure is taken from [58]

1.4.3.1 Lattice structure

In $A_2Mo_2O_7$, each magnetic ion Mo^{4+} has two $4d$ electrons. Mo^{4+} forms the pyrochlore network and each Mo^{4+} is coordinated by 6 oxygen ions O^{2-} (see Fig. 1.17 (a)). This coordination doesn't have the octahedral but trigonal symmetry because the oxygen ions are pushed by A ions. The amount of the difference from the complete octahedral coordination changes depending on the ionic radius r_A of A ion , which results in systematic changes of some physical properties [54, 55, 56, 57, 59]. It is known that large $r_A > R_c \sim 1.047\mathring{A}$ stabilizes the ferromagnetic ground state. Typical examples of ferromagnetic pyrochlores are $Nd_2Mo_2O_7$ and $Gd_2Mo_2O_7$. The origin of the ferromagnetism is the double-exchange mechanism and the compounds show finite conductivity. On the other hand, systems with small $r_A < R_c$ which $Y_2Mo_2O_7$ belongs to gives rise the spin glass behavior. In this regime, the system becomes a Mott insulator. The dominant magnetic interaction is the super-exchange interaction through the mediated oxygen ion. Fig. 1.17 shows the phase diagram as a function of the averaged ionic radius $\langle r_A \rangle$. On the ferromagnetic side $\langle r_A \rangle > R_c$, the Curie temperature (T_c) is around 80 K and slowly increases with $\langle r_A \rangle$. On the other hand, for $\langle r_A \rangle < R_c$, the transition temperature drop down to around 20 K and the system becomes a spin glass.

The pyrochlore oxide $Y_2Mo_2O_7$ crystallizes into a face-centered-cubic structure with the space group $Fm\bar{3}d$. Mo^{4+} ions occupy $16c$ positions and O^{2-} ions coordinated by Mo^{4+} occupy $48f$. There is only one positional parameter u for the O atom in $48f$, as shown in Fig. 1.17 (a) for the single tetrahedron. The four

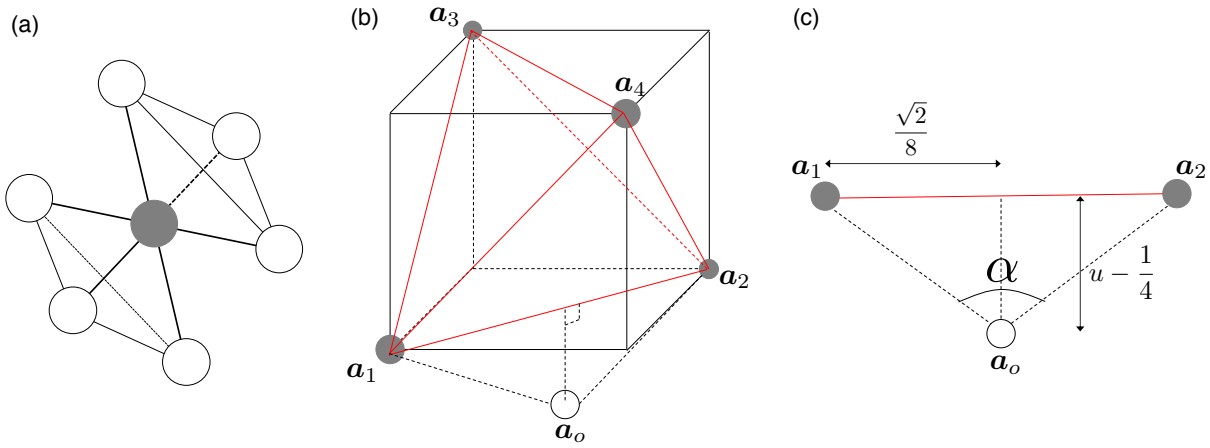

Figure 1.17: **Local structure of $A_2Mo_2O_7$**
(a): Trigonal crystal field of MoO_6. (b): Local coordinate frame in one tetrahedron. Mo^{4+} ions are located on the vertices $\boldsymbol{a}_1, \boldsymbol{a}_2, \boldsymbol{a}_3, \boldsymbol{a}_4$. O^{2-} ions are located, for example, at $\boldsymbol{a}_o$. (c): Relative positions of Mo^{4+} ions at site 1, site 2 and mediated O^{2-} ion $\boldsymbol{a}_o$.

	Compound	a (Å)	u (Å)	$d_{\mathrm{Mo-Mo}}$ (Å)	$d_{\mathrm{Mo-O}}$ (Å)	$\alpha = \angle$ Mo-O-Mo	$\angle$ O-Mo-O
SG	$Y_2Mo_2O_7$	10.21	0.33821	3.6098	2.0171	127.0°	99.5°
Ferro	$Gd_2Mo_2O_7$	10.3356(1)	0.33158	3.6542	2.0123	130.4°	97.2°
Ferro	$Nd_2Mo_2O_7$	10.4836(2)	0.32977	3.7065	2.0332	131.4°	96.6°

Table 1.2: **Structural parameters of $A_2Mo_2O_7$ (A = Y, Gd, Nd) taken from [58]**
Those for $Y_2Mo_2O_7$ from [60, 57], those for $Gd_2Mo_2O_7$ and $Nd_2Mo_2O_7$ from [54].

Mo^{4+} ions are located at

$$\begin{aligned} \boldsymbol{a}_1 &= (0,0,0) \\ \boldsymbol{a}_2 &= (1/4,1/4,0) \\ \boldsymbol{a}_3 &= (0,1/4,1/4) \\ \boldsymbol{a}_4 &= (1/4,0,1/4) \end{aligned} \tag{1.83}$$

in units of the cubic lattice constant. The O^{2-} ion mediated between site 1 and site 2 is located at

$$\boldsymbol{a}_{\mathrm{O}} = (1/8, 1/8, -u + 1/4). \tag{1.84}$$

1.4.3.2 Electric properties

Electric band structure of the family of the compounds $A_2Mo_2O_7$ (A = Y, Gd, Nd) were examined by Solovyev [58]. Structural parameters of $A_2Mo_2O_7$ are listed in Table 1.2. It is important to note that the angle between Mo-O-Mo bond α becomes smaller in the order of Y, Gd, Nd because the transfer integral between Mo($4d$) and O($2p$) orbitals is changed by the direction cosines of the relative vector and the effective exchange interaction through the mediated oxygen depends on the transfer integral. Solovyev performed the band calculation using the local-spin-density approximation (LSDA) which yields the results for three materials shown in Fig. 1.18 (a). In the local coordinate frame, the Mo($4d$) orbitals are split into the triply-degenerate t_{2g} and doubly-degenerate e_g states (see Fig. 1.19 (a)). The splitting is of the order of 4 eV. The triply-degenerate t_{2g} states are located around the Fermi level and the doubly-degenerate e_g are located

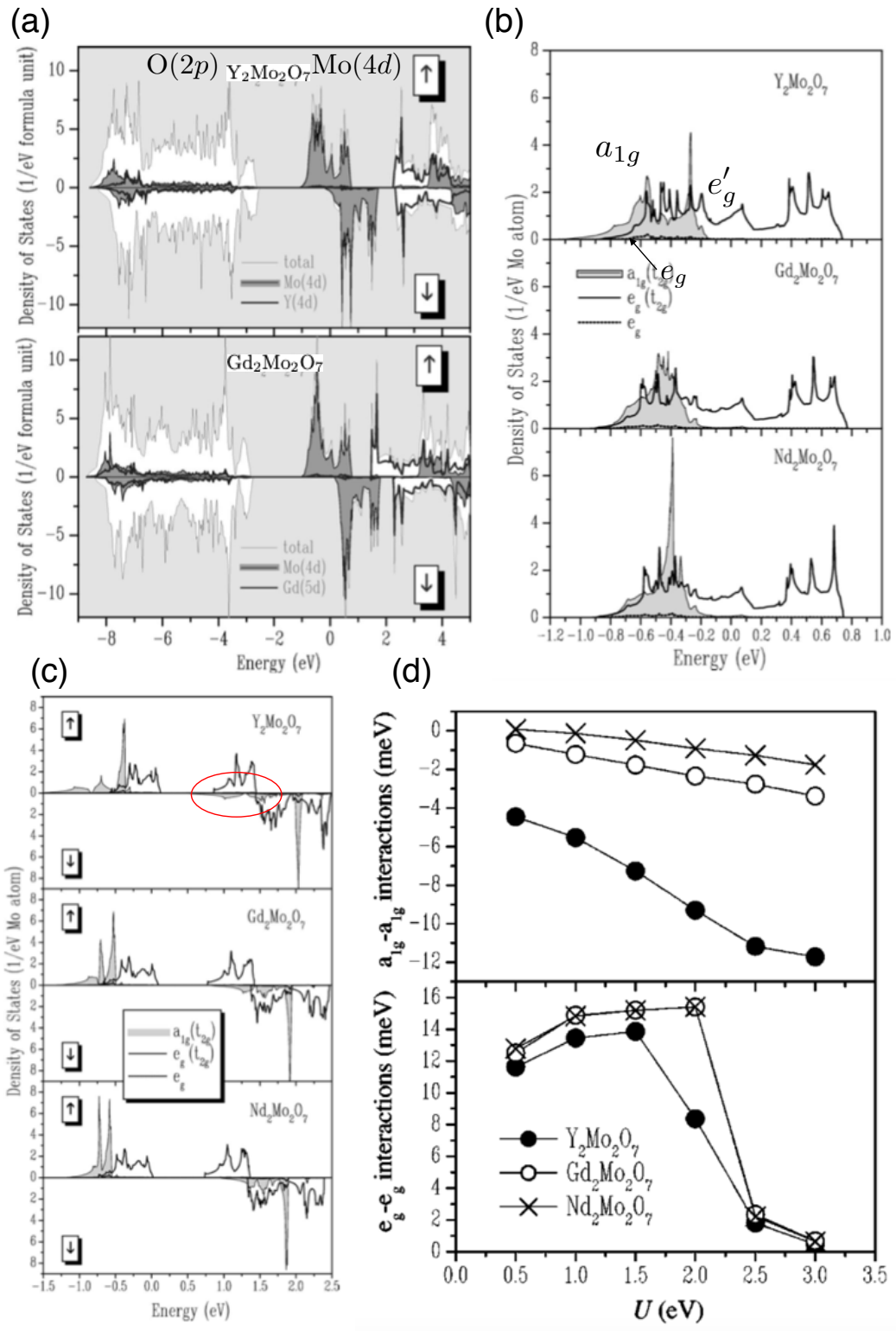

Figure 1.18: **Results of band calculations for $A_2Mo_2O_7$ (A =Y, Gd and Nd) taken from [58]** (a): Total and partial densities of states in the LSDA. The Fermi level is chosen as zero of energy. (b): Mo(t_{2g}) states in the local coordinate frame, split into a_{1g} and e'_g states. (c): Distribution of the Mo($4d$) states for $U = 3.0$ eV. (d): Contributions of a_{1g} and e'_g orbitals to the exchange constant.

Atom pair	σ^2 (Å^2)	R (Å)
Mo-O(1)	0.0045(3)	2.030(2)
Mo-Mo	0.035(1)	3.628(2)
Mo-Y	0.0055(1)	3.628(2)
Y-O(1)	0.0092(3)	2.441(1)
Y-O(2)	0.0036(1)	2.225(1)
Y-Y/Mo	0.0042(1)	3.609(1)

Table 1.3: **Fit results for Y and Mo edge data of XAFS on $Y_2Mo_2O_7$ at $T = 15$ K, taken from [61]**
R represents the pair distances between two atoms. σ^2 is the variance of R.

much higher than t_{2g} states. Thus, we only have to take t_{2g} orbitals into account. The oxygen bands O($2p$) are spreading from -8.5 to -2.5 eV. The trigonal distortion will further split the t_{2g} orbitals into the single a_{1g} and the doubly e'_g orbitals (See Fig. 1.18 (b) and Fig. 1.19 (a)). The a_{1g} state is located below the Fermi level and the doubly e'_g states cross the Fermi level. Thus, we can naturally expect that one electron is in the a_{1g} orbital and the other in e'_g orbital.

In order to investigate the Mott transition in this system, Solovyev also performed LSDA calculation including the on-site Coulomb interactions among the Mo($4d$) electrons as a controlled parameter (LSDA + U). In this calculation, e'_g state open a band gap between $U = 2.0$ and 2.5 eV for each material, i.e. these systems are Mott insulated. Fig. 1.18 (c) shows the densities of states in the insulating phase. It can be seen that the tail of $a_1g(\downarrow)$ state spreads below the unoccupied $e'_g(\uparrow)$ band, which is surrounded by the red loop in Fig. 1.18 (c). It suggests that antiferromagnetic coupling between Mo^{4+} ions is stabilized in the Mott insulating phase of $Y_2Mo_2O_7$. Hence, it is expected that antiferromagnetic interactions become dominant due to $a_{1g}(\uparrow)$-$a_{1g}(\downarrow)$ coupling.

Solovyev also examined the effective exchange interaction: Fig. 1.18 (d) shows the U dependence of the a_{1g}-a_{1g} and e'_g-e'_g exchange interactions. Large α gives rise to the ferromagnetic interaction due to the double-exchange mechanism and small α leads to the antiferromagnetic interaction due to the super-exchange mechanism. Hence, the exchange interaction between Mo^{4+} ions in $Y_2Mo_2O_7$ becomes antiferromagnetic.

1.4.3.3 Jahn-Teller distortion

As we summarized in Sec. 1.2.1, the Heisenberg model model with only the nearest neighboring antiferromagnetic interaction on the pyrochlore lattice does not exhibit the spin glass behavior observed in the experiments. Therefore, we have to look for other factors to understand the spin glass transition on $Y_2Mo_2O_7$. A key ingredient is a characteristic Jahn-Teller distortion uncovered by a recent experiment which we review below.

Some previous experiments have reported lattice distortions which displace Mo^{4+} ions. [61] By using the x-ray-absorption fine-structure (XAFS) technique, Booth et al. found that the Mo-Mo pair distances have significantly large variances (See Table. 2.14), while the variations of the distances between other pairs remain small. In addition, the magnitude of variances turned out to be independent of temperature.

It is suggested by the more recent experiment by Thygesen et al. [62] that the distortion is such that Mo^{4+} ion is distorted towards (*in*) or away from (*out*) the center of the tetrahedron (see Fig. 1.19 (b)). They speculated that this is possibly due to coupling between orbital and lattice. As we discuss more in detail later in Chap. 2, we consider that this is a Jahn-Teller effect which removes the double degeneracy of the e_g orbitals (see Fig. 1.19 (a)) which remained in the undeformed pyrochlore system. Fig. 1.19 (d) shows the fitting of the pair distribution function obtained by the neutron scattering. Thygesen et al. [62] assumed *in* or *out* distortions and succeeded to fit the data successfully (see Fig. 1.19 (c)). The distortions result in the

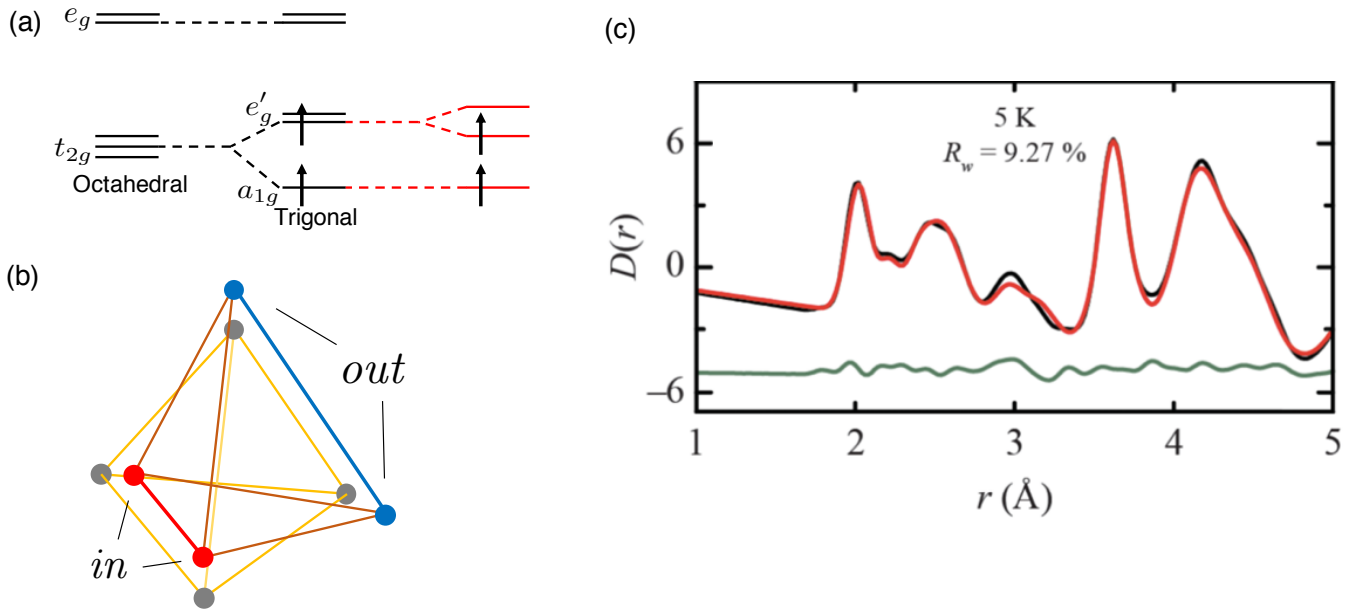

Figure 1.19: **Jahn-Teller distortions on $Y_2Mo_2O_7$**
(a): Schematic picture of the energy splitting of e'_g orbitals by the Jahn-Teller effect. (b): 2-*in*-2-*out* structure of Jahn-Teller distortion. (c): Fit to their neutron PDF data supposing the Jahn-Teller distortion, taken from [62].

variation of the Mo-O-Mo bond angle α (see Fig. 1.17 (c)) from its equilibrium value $\alpha = 127°$ to $\alpha = 116°$ for the *in-in* bond or $\alpha = 139°$ for the *out-out* bond. Hence, we can expect that the effective exchange interaction between Mo^{4+} ions is also modified because the interaction depends on α as we discussed in Sec. 1.4.3.2. Indeed the variation of the bond angle is considered as sufficiently large to vary the effective coupling between ferromagnetic and antiferromagnetic coupling [58]. We consider that this is another key feature of the material and take this into account in our effective model. We will discuss further on this in Sec. 2.3.1.

In [62], it is argued that the *in* and *out* deformations satisfy the ice-rule (see Sec. 1.2.2). Indeed this is plausible since such a deformation is a normal mode of the elastic deformation of a single tetrahedron. This points to a possible scenario for the spin glass transition in the $Y_2Mo_2O_7$ system: if the lattice distortion is frozen in a disordered pattern satisfying the ice-rule, it will be reflected to the effective exchange coupling of each bond, and eventually the spin glass transition may take place. This is also consistent with the fact that the structural phase transition which changes the crystalline symmetry doesnt occur on $Y_2Mo_2O_7$ even under the spin glass transition (see Fig. 1.14 (e) and (f)) unlike the ordering induced by spin-lattice coupling discussed in Sec. 1.3 and the orbital ordering case such as $LaMnO_3$ (see Sec. C.3.2). However we must recall here that the ice-rule structure generally doesnt exhibit any long range order as we discussed in Sec. 1.2.2. Therefore, in our effective model we will regard the distortion as a *dynamical* Jahn-Teller distortion.

1.4.4 An effective model

Being motivated by the experimental results summarized above, we introduce an effective model which includes not only spin degrees of freedom $\boldsymbol{S}_i$ $(i = 1, 2, 3, ..., N)$ but also orbital degrees of freedom which induce the *in* or *out* lattice displacements σ_i $(i = 1, 2, 3, ..., N)$. We regard the Jahn-Teller distortion as the discrete variables in contrast to the vibrational distortion of bond-phonon or site-phonon models discussed

in Sec. 1.3, i.e. $\sigma_i = \pm 1$. Our effective model is given by the following Hamiltonian,

$$H = \sum_{\triangle=1}^{N_\triangle} \sum_{i<j}^{4} \left[J\big(1 + \delta\big(\sigma_{i(\triangle)} + \sigma_{j(\triangle)}\big)\big) \boldsymbol{S}_{i(\triangle)} \cdot \boldsymbol{S}_{j(\triangle)} + \epsilon \sigma_{i(\triangle)} \sigma_{j(\triangle)} \right], \tag{1.85}$$

where $\triangle$ represents the indices of tetrahedra and $N_\triangle$ is the number of total tetrahedra in the system. The first term is the effective interaction which depends on the distortion σ_i and σ_j linearly similarly to the bond-phonon model. The second term represents the elastic energy which takes the same form as the spin ice Hamiltonian (Eq. (1.64)), i.e. the lattice distortion favors the ice-rule structures. Note that the lattice distortions σ_i cannot be integrated out independently of the spin variables unlike bond-phonon or site-phonon models. Thus, we treat both variables as dynamical degrees of freedom in our simulations (Chap. 3) and mean-field theory (Chap. 4). In Chap. 2, we give more precise definition of our effective model and discuss more in detail the microscopic justification of the effective model. Note that if we switch of the coupling between the two degrees of freedom, i.e. $\delta = 0$, the system is decoupled to the purely antiferromagnetic Heisenberg model on the pyrochlore lattice (Sec. 1.2.1) and the spin ice model (Sec. 1.2.2). We have seen that both of them remain distorted down to $T = 0$ because of very strong frustration. In this thesis, we will show by numerical simulations (Chap. 3) and a mean-field theoretical analysis (Chap. 4) that the situation changes dramatically as the coupling $\delta > 0$ is switched on.

1.5 Outline of the following chapters

The rest of this thesis is divided into three chapters, in the next chapter (Chap. 2) we define our effective model precisely and discuss the microscopic background of our effective model introduced above (Eq. (1.85)). Then we analyze the ground state configuration of the system at the level of single tetrahedron. Finally we discuss how the energy landscape changes by $\delta > 0$, i.e. switching on the coupling spins and lattice distortions.

In Chap. 3, we study the static and dynamic properties of our effective model (Eq. (1.85)) by extensive Monte Carlo simulations. We will show that the spin and lattice degrees of freedom exhibit simultaneous 2nd order glass transitions with diverging length and time scales.

In Chap. 4 we construct and analyze an exactly solvable mean-field theory of our effective model. We will find two kinds of glass transitions, namely simultaneous glass transition similar to the result of numerical simulations obtained in Chap. 3 and another one where the spin and lattice degrees of freedom exhibit separated glass transitions.

Finally we summarize our results and discuss future perspectives in the last chapters (Chap. 5 and Chap. 6).

Chapter 2

EFFECTIVE MODEL: microscopic background and its basic properties

In this chapter we introduce our effective model precisely and discuss its microscopic justification concerning the Jahn-Teller distortion and magnetic exchange interaction. Then we analyze the ground states of the model at the level of single tetrahedron. Finally we present a simple numerical analysis on the energy landscape of the model.

2.1 Model

In Sec. 1.4.3.3, we discussed the distortion of the pyrhoclore lattice due to displacements of the Mo^{4+} ions which move towards (*in*) or away from (*out*) the centers of Mo_4 tetrahedra, which appears to play important roles for the disorder-free spin glass transition. As we will discuss in Sec. 2.2, a natural mechanism of distortion is the Jahn-Teller effect that lowers the electrostatic energy of the Mo^{4+} ion lifting the degeneracy of its e_g orbital. We will argue that both from the point of view of the electrostatic energy and elastic energy, distortions following the ice rule, i.e. 2-*in*-2-*out* rule (see Fig. 2.1 (b)), are most relevant. As we discussed in Sec. 1.2.2, the ice-rule constraint allows huge number of configurations. Thus the ice-rule alone will not lead to any long-range structural ordering.

On the other hand it is known as we discussed in Sec. 1.4.3.2 that the exchange interaction may vary significantly and even changes its sign, depending on the degree of the Mo-O-Mo angle α. Indeed, the angle evaluated from the variance of the displacements of the Mo ions distributes in the range $\alpha = 116^\circ$ and $\alpha = 139^\circ$ [62], which is speculated as large enough to change the sign of the spin-spin exchange interaction. We will confirm this in Sec. 2.3.1 based on a microscopic analysis. Then, depending on the configurations of the local lattice distortion, the magnetic exchange interaction may be distributed randomely with finite variances. This can be thought of as follows; If we consider the Jahn-Teller Hamiltonian including only the lattice degrees of freedom, the energy landscape should be such that all the ice-rules give the energy minima of the same height (see Fig. 2.1 (c) and Sec. 1.2.2). In putting spins on the ice-type displaced vertices, its energy landscape is modified to an irregular one with random valley structures, since the variance of the spin interactions from ferro to antiferromagnetic ones add different energies to each ice configuration. We will verify the above picture in Sec. 2.5 by performing numerical analysis of low lying states of our effective model. Furthermore, in Chap 3 we will demonstrate numerically that the spin and lattice distortions simultaneously undergo a glass transition and freeze into aperiodic, irregular types of configurations. Since a randomly frozen lattice distortion corresponds a randomly selected orbital configurations, we call it a *spin-orbital glass*.

As a natural description of the material faithful to the experimental observations, we have introduced in

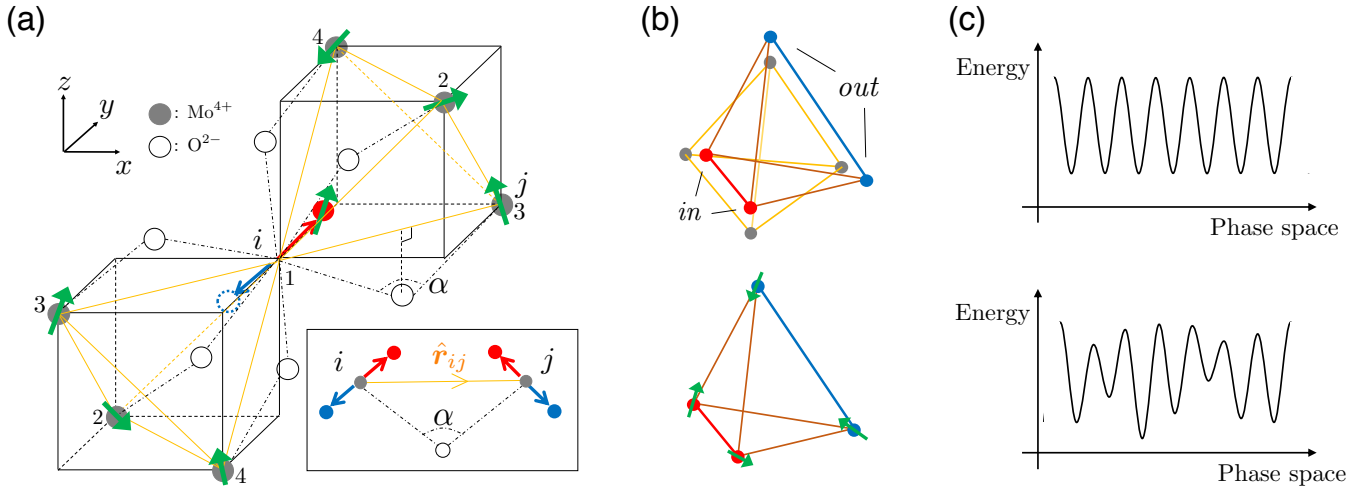

Figure 2.1: **Jahn-Teller distortion in our model**
(a): O^{2-} ions and magnetic Mo^{4+} ions around the i site. The numbers near the Mo^{4+} ions denote the sublattice to which they belong. The red and blue dashed circles represent the positions of the Jahn-Teller distorted i ion. We pick up the i, j ions and the mediated O^{2-} and draw it in the small window. α represents the angle of Mo-O-Mo and $\hat{\boldsymbol{r}}_{ij}$ represents the unit vector from the i site to the j site. (b): Ice-type displacements of the Mo_4 tetrahedron. The different color bonds represent different exchange interactions. (c): Schematic pictures of the energy landscape of ice-type displacements (Top) and modified one by by the coupling between the spin and lattice distortion.

the end of Chap. 1 a disorder-free effective model (Eq. (1.85)). Here let us give more the precise definition. The model consists of not only including not only the classical Heisenberg spins $\boldsymbol{S}_i$ $(i = 1, 2, 3, ..., N)$ for the magnetic moments of the Mo^{4+} ions but also the degree of lattice distortion of the Mo ions $\boldsymbol{\sigma}_i$ represented as vectors taking two discrete values, $\boldsymbol{\sigma}_i = \sigma_i \hat{\boldsymbol{e}}_\nu$. Here, $\sigma_i = \pm 1$ corresponds to either *in* or *out* depending on the direction of $\boldsymbol{e}_\nu$ which is the unit vector in the $[111], [\bar{1}\bar{1}1], [\bar{1}1\bar{1}]$ and $[1\bar{1}\bar{1}]$ directions, respectively for the sublattices $\nu = 1, 2, 3, 4$ which the i-th spin belongs to (See Fig. 2.1.(a)), more precisely,

$$\boldsymbol{\sigma}_{(1)} = \sigma_i \frac{1}{\sqrt{3}} \begin{pmatrix} +1 \\ +1 \\ +1 \end{pmatrix} \quad \boldsymbol{\sigma}_{(2)} = \sigma_i \frac{1}{\sqrt{3}} \begin{pmatrix} -1 \\ -1 \\ +1 \end{pmatrix}$$
$$\boldsymbol{\sigma}_{(3)} = \sigma_i \frac{1}{\sqrt{3}} \begin{pmatrix} +1 \\ -1 \\ -1 \end{pmatrix} \quad \boldsymbol{\sigma}_{(4)} = \sigma_i \frac{1}{\sqrt{3}} \begin{pmatrix} -1 \\ +1 \\ -1 \end{pmatrix}. \tag{2.1}$$

with $\sigma_i = \pm 1$. Both degrees of freedom are normalized as $|\boldsymbol{S}_i| = |\boldsymbol{\sigma}_i| = 1$. The Hamiltonian is given by

$$H = \sum_{<ij>} J_{\boldsymbol{\sigma}_i, \boldsymbol{\sigma}_j} \boldsymbol{S}_i \cdot \boldsymbol{S}_j - \epsilon \sum_{<ij>} \boldsymbol{\sigma}_i \cdot \boldsymbol{\sigma}_j \qquad (\epsilon > 0) \tag{2.2}$$

with

$$J_{\boldsymbol{\sigma}_i, \boldsymbol{\sigma}_j} = J[1 + \delta(\hat{\boldsymbol{r}}_{ij} \cdot \boldsymbol{\sigma}_i + (-\hat{\boldsymbol{r}}_{ij}) \cdot \boldsymbol{\sigma}_j)] \qquad (\delta > 0), \tag{2.3}$$

The first term in Eq. (2.2) represents the exchange interaction whose coupling constant $J_{\boldsymbol{\sigma}_i, \boldsymbol{\sigma}_j}$ depends on the angle of Mo-O-Mo bond. We assume that the coupling constant is determined by the inner products $\hat{\boldsymbol{r}}_{ij} \cdot \boldsymbol{\sigma}_i$ and $\hat{\boldsymbol{r}}_{ij} \cdot \boldsymbol{\sigma}_j$ with the amplitude δ, where $\hat{\boldsymbol{r}}_{ij}$ is the unit vector from i-th site to j-th site. Then the coupling

constant takes 3 kinds of value such that

$$J_{\boldsymbol{\sigma}_i,\boldsymbol{\sigma}_j} = \begin{cases} (1+2\tilde{\delta})J & (in,\ in), \\ J & (in,\ out), \\ (1-2\tilde{\delta})J & (out,\ out), \end{cases} \tag{2.4}$$

where $\tilde{\delta} = \sqrt{6}\delta/3$. The second term of Eq. (2.2), which has the same as the spin-ice Hamiltonian Eq. (1.64), represents the elastic energy of the Mo^{4+} displacement. The elastic energy is minimized if a Mo^{4+} tetrahedron satisfies the ice-rule. More precisely, the elastic energy of each bond takes $\epsilon\boldsymbol{\sigma}_i\cdot\boldsymbol{\sigma}_j = -\epsilon/3$ if both displacements are *out* or *in*, otherwise $+\epsilon/3$. There are three parameters in this system; $\tilde{T} = k_{\rm B}T/J$ is dimensionless temperature, $\tilde{\epsilon} = \epsilon/3J$ the ratio of the energy scales between the exchange interaction and the elastic energy of the displacement, and $\tilde{\delta} = \sqrt{6}\delta/3$ is the amplitude of the displacement (hereafter we call them simply as T, ϵ, δ). At $\epsilon \to \infty$, the lattice distortion becomes static. The model becomes a system with quenched disorder.

2.2 Jahn-Teller mechanism favoring Ice-Rule

2.2.1 Deformation of single tetrahedron

In this section, we discuss the Jahn-Teller mechanism favoring the ice-rule distortion which was reported in the previous experiment [62]. We will define the second term of the Hamiltonian Eq. (2.2) from a microscopic point of view. For a single tetrahedron, it is known that there are six vibrational modes (see Fig. 2.2). The previous experiment [62] suggests that the triplet T_2 mode, i.e. 2-*in*-2-*out* distortion is the dominant one. When a tetrahedron is distorted into the 2-*in*-2-*out* structure, the 3-fold rotational symmetry of the trigonal crystal field is broken, for instance, around [111] direction (see Fig. 2.4 (b)). The doubly-degenerated e'_g orbitals are split and an electron is accommodated in the lower energy orbital (see Fig. 2.3 (a)).

More precisely it is important to note that *in* and *out* motion of one Mo^{4+} ion alone does not directly break the 3-fold rotational symmetry. However, the O^{2-} ions which are ligands of the Mo^{4+} move in conjunction with the Mo^{4+} so that the distances between O^{2-} and Mo^{4+} don't change. Since each O^{2-} bridges two Mo^{4+}, it moves when either of the two Mo^{4+} move. There are three kinds of O^{2-} positions corresponding to three patterns of Mo-O-Mo bonds, *in-in*, *in-out* and *out-out* as shown in Fig. 2.4 (a). The distortion of the O^{2-} breaks the 3-fold rotational symmetry and thus results in the splitting of the e'_g.

Based on the above observations we can write the effective potential for the T_2 mode as,

$$E_{T_2} = \frac{k_{T_2}}{2}u_{T_2}^2 - au_{T_2} \tag{2.5}$$

where the 1st term is the elastic energy with k_{T_2} being the elastic modulus of the T_2 mode. The second term represents the energy gain due to the splitting of the e'_g, which is presumably linearly proportional to the displacement u_{T_2} with some amplitude $a > 0$ (see Fig. 2.3 (a)). The resultant effective potential (Eq. (2.5)) has a minimum at finite amplitude of $u^*_{T_2}$ (see Fig. 2.3 (b)).

We emphasize that this Jahn-Teller effect is very different in nature from the spin-driven Jahn-Teller effect discussed in Sec. 1.3. Most importantly the system is distorted *with finite amplitude in the absence of the spin degrees of freedom*.

Let us finally comment on deformation into other normal modes (see Fig. 2.2). The A_1 mode do not break the 3-fold rotational symmetry so that we can neglect it. The E mode does break the 3-fold rotational symmetry. However this is not observed experimentally. We speculate that it is energetically less favorable in the present system. This point remains to be clarified.

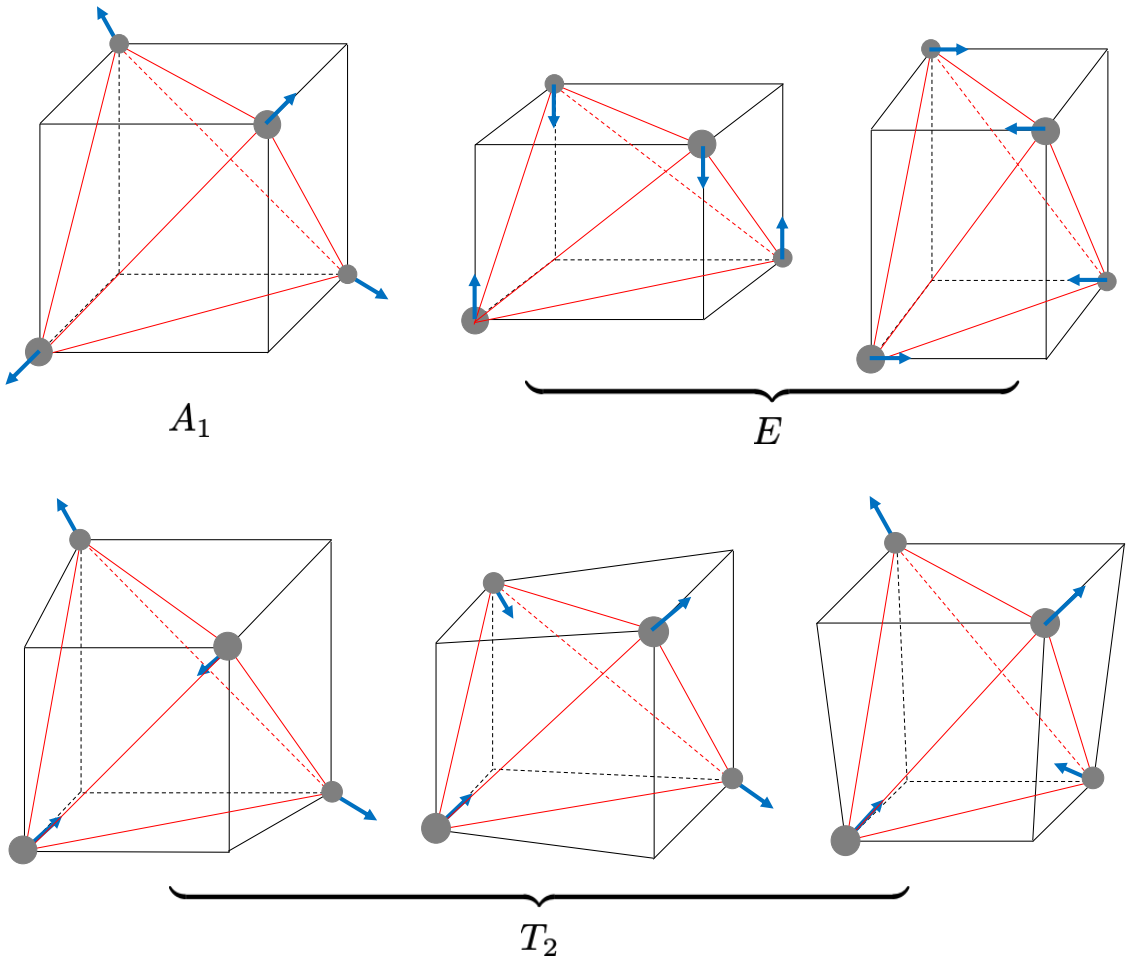

Figure 2.2: **Vibrational normal modes of a tetrahedron**
A singlet A_1 is the breathing vibrational mode where all vertices are distorted into or away from the center of the tetrahedron. A doublet E represent tetragonal and orthorhombic distortions of the tetrahedron. A triplet T_2 represent 2-*in*-2-*out* distortions of the tetrahedron.

2.2.2 Deformation of the whole system

Now let us consider deformations at larger scales than the single tetrahedron. To this end, we limit ourselves to a simplified deformation manifold in which distortions of the Mo^{4+} ions take place only pointing exactly toward or away from the center of tetrahedra which it belongs to. Moreover we assume that the magnitude of the displacement is a *finite* constant u. Apparently this description excludes the E like mode but this assumption considerably simplifies our analysis as we show below.

First let us consider two tetrahedra A and B shown in Fig. 2.4 (b). Here the site i is shared by two tetrahedra A and B which are distorted into 2-*in*-2-*out* structures. One can find that the ligand oxygen 1, which mediates the *in*-*in* pair in A, is displaced outward against the ligands 2 and 3 which mediate the *in*-*out* pairs. In the same manner, the ligand 6 which mediates the *out*-*out* pair in B is displaced inward. Hence, the 3-fold rotational symmetry of the trigonal crystal field is lost in all Mo^{4+} ions in the 2-*in*-2-*out* tetrahedron.

In the whole system, we expect that there are some defects that locally violate the ice-rule, e.g. 3-*in*-1-*out*/1-*in*-3-*out* and all-*in*/all-*out* structures which partially or fully retain the 3-fold rotational symmetry of the trigonal crystal field. These defects can be regarded energy excitation from the ice-rule compatible ground state in terms of the Jahn-Teller energy (electrostatic energy associated with the e'_g orbital).

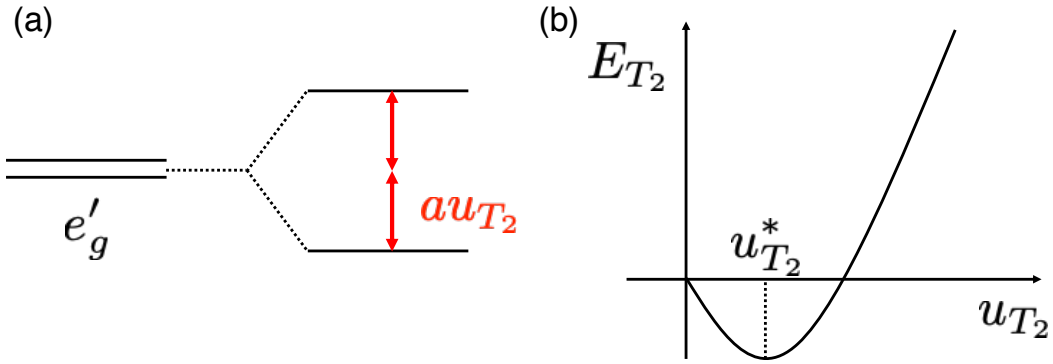

Figure 2.3: **Jahn-Teller energy of 2-*in*-2-out distortion**
(a): Energy gain due to the splitting of the e_g. (b): Jahn-Teller energy vs amplitude of distortion.

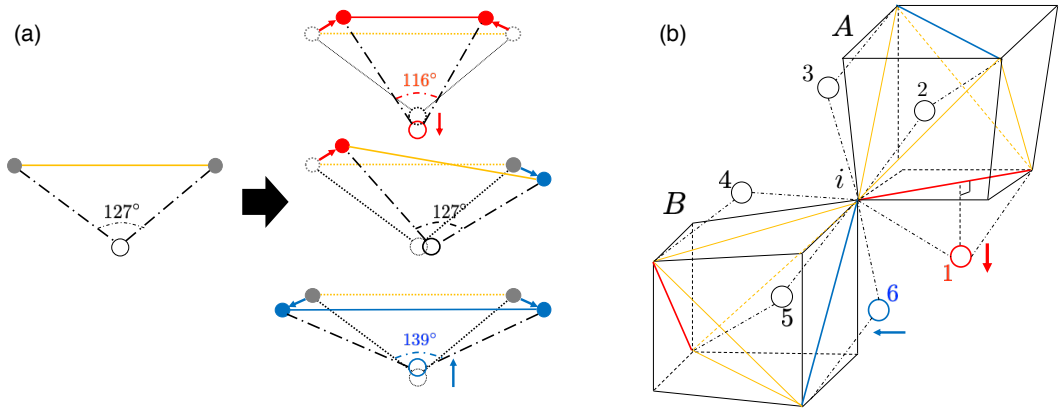

Figure 2.4: **Breaking the trigonal symmetry MoO_6 crystal field**
(a): Three patterns of Mo-O-Mo bonds. (b): Connected tetrahedra A and B. Open circles 1-6 represent the ligands of Mo^{4+} on site i. Red lines, yellow lines and blue lines indicate *in-in*, *in-out* and *out-out* bonds, respectively.

As for the elastic energy, 2-*in*-2-*out* distortion has the lower elastic energy than the 3-*in*-1-*out*/1-*in*-3-*out* and all-*in*/all-*out* structures. Let us consider a single tetrahedron which has the elastic energy between two vertices i and j (see Fig. 4.3 (a)) similarly to the bond-phonon model (see Sec. 1.3.2), more precisely the elastic potential is given by,

$$V(\boldsymbol{r}_i, \boldsymbol{r}_j) = k(r_{ij} - 1)^2, \tag{2.6}$$

where k is an energy scale and $r_{ij} = |\boldsymbol{r}_i - \boldsymbol{r}_j|$ is a distance between two vertices. Note that we normalize the equilibrium distance between the equilibrium positions $\boldsymbol{r}_{i0}$ and $\boldsymbol{r}_{j0}$ as $|\boldsymbol{r}_{i0} - \boldsymbol{r}_{j0}| = 1$. As noted above we assume that each vertex displaces toward or away from the center of the tetrahedron, more precisely we define $\boldsymbol{r}_i$ as

$$\boldsymbol{r}_i = \boldsymbol{r}_{i0} - u\boldsymbol{\sigma_i} \tag{2.7}$$

where δ is length scale of the lattice displacement and σ_i is defined in Eq. (2.1) (see Fig. 4.3 (b)). $\sigma_i = 1$ and

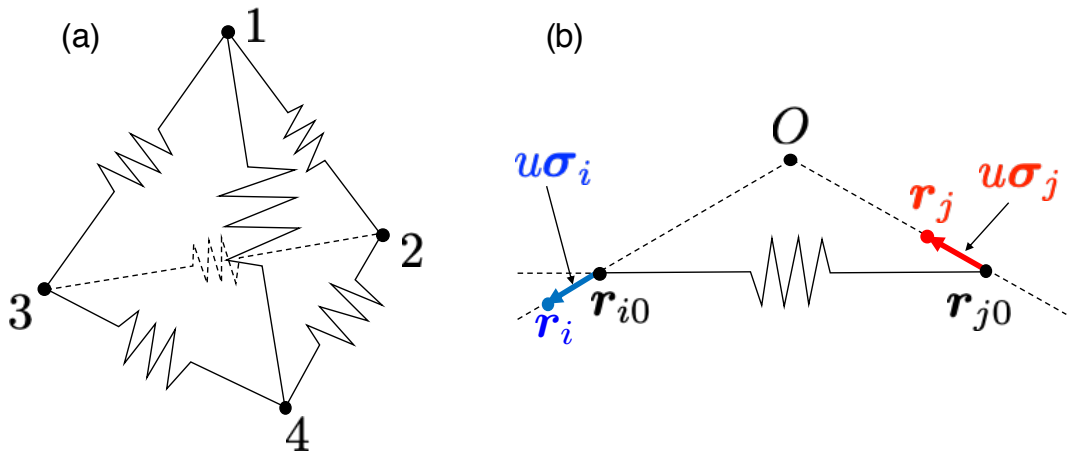

Figure 2.5: **Elastic tetrahedron**
(a): Schematic picture of an elastic tetrahedron. (b): O is the center of the tetrahedron. $\boldsymbol{r}_i$ and $\boldsymbol{r}_j$ represent the positions of the i-th and j-th vertices and $\boldsymbol{r}_{i0}$ and $\boldsymbol{r}_{j0}$ are their equilibrium positions. The i-th vertex is distorted along the vector $\boldsymbol{\sigma}_i$ with amplitude u.

$\sigma_i = -1$ correspond to *in* and *out*, respectively. We find,

$$\begin{aligned} r_{ij} &= |\boldsymbol{r}_{i0} - \boldsymbol{r}_{j0} - u(\boldsymbol{\sigma}_i - \boldsymbol{\sigma}_j)| \\ &= \left\{1 + 2u\sqrt{2/3}(\sigma_i + \sigma_j) + u^2[(\sigma_i - \sigma_j)^2 + 4\sigma_i\sigma_j(2/3)\theta]\right\}^{\frac{1}{2}}. \\ &= 1 + u\sqrt{2/3}(\sigma_i + \sigma_j) + u^2\left[\frac{1}{2}\{(\sigma_i - \sigma_j)^2 + 4\sigma_i\sigma_j(2/3)\} - \frac{1}{8}\{2\sqrt{2/3}(\sigma_i + \sigma_j)\}^2\right] + O(u^3). \end{aligned} \tag{2.8}$$

Assuming that the displacement is small enough ($u \ll 1$), we can rewrite the potential up to the second order of u as

$$V(\sigma_i, \sigma_j) = \frac{2ku^2}{3}(\sigma_i + \sigma_j)^2. \tag{2.9}$$

The total elastic Hamiltonian of the single tetrahedron becomes

$$\begin{aligned} H_{\text{elastic}} &= \frac{2ku^2}{3}\sum_{i<j}(\sigma_i + \sigma_j)^2 \\ &= \frac{4ku^2}{3}\sum_{i<j}\sigma_i\sigma_j + 16ku^2. \end{aligned} \tag{2.10}$$

We find that the lowest energy state is the 2-*in*-2-*out* structure and the other distorted pattern can be regarded as the excitation states. Of course we should take the difference of Jahn-Teller energy among different distorted structures into account, we use this form as the effective Hamiltonian of lattice distortion, which is the second term in Eq. (2.2).

2.3 Origin of magnetic interactions in $Y_2Mo_2O_7$

As we noted in Sec. 1.4.3.2, in the pyrochlore oxide $Y_2Mo_2O_7$, magnetic ion $Mo^{4+}(4d^2)$ is affected by trigonal crystal field, then its triply t_{2g} orbitals are split into a single a_{1g} orbital and doubly e'_g orbitals and a_{1g} has the lower energy than e'_g (see Fig. 1.19 (a)). The spins of two electrons on Mo^{4+} has the same direction and form an effective spin $S = 1$ because of Hund's rule. This is because the magnitude of energy splitting

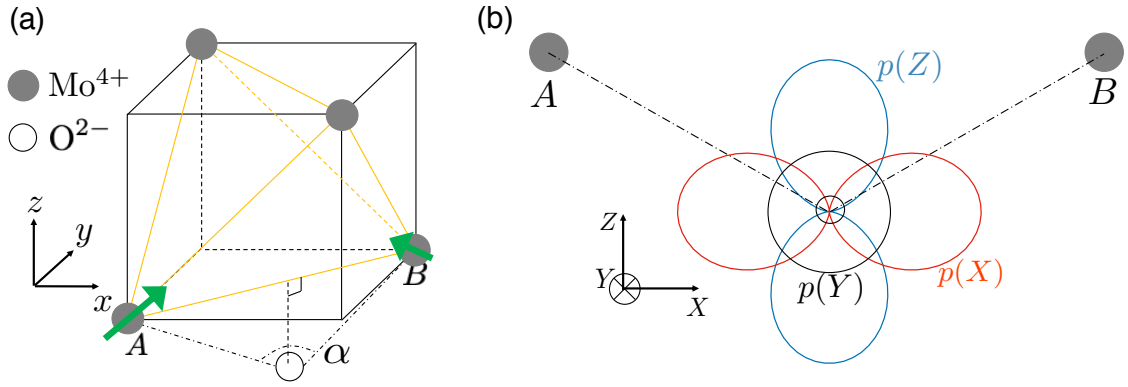

Figure 2.6: **O(2p) orbitals defined by a new coordinates**
(a),(b): We consider the exchange interaction between the two spins on the Mo^{4+} through the O^{2-} ion. Since one can construct three degenerate O(2p) orbitals in an arbitrary combination, we define the new orbitals $|p(X)\rangle, |p(Y)\rangle, |p(Z)\rangle$ using new coordinates (X, Y, Z) given by Eq. (2.18) for convenience.

between a_{1g} and e'_g is smaller than the strength of Hund's coupling. [58] According to the Jahn-Teller theorem [63], the system becomes unstable and lattice distortion takes place because the e'_g orbital is still active (see Sec. C.3). Hence, we should take the lattice distortion into account and indeed it has been already observed experimentally [61, 62]. The reference [62] notably suggested that each Mo^{4+} is distorted into or away from the center of the tetrahedron and the distortion changes the angle of Mo-O-Mo from its equilibrium position 127° to 116° for the in-in bond or 139° for the out-out bond. In the following we clarify that the change of the angle is large enough to change the sign of the exchange interaction theoretically from a microscopic point of view.

2.3.1 Local Hubbard Model

In order to analyze the magnetic exchange interaction between the effective spin degrees of freedom ($S = 1$) on the Mo^{4+} ions through O^{2-} ion, we study a local multi-orbital Hubbard model which is composed of d orbitals $\alpha = |a_{1g}\rangle, |e'_{g+}\rangle, |e'_{g-}\rangle$ of two Mo^{4+} ions A, B and p orbitals $\beta = |p(X)\rangle, |p(Y)\rangle, |p(Z)\rangle$ of the mediated O^{2-} ion. Here, the quantization axis of p orbitals are defined such that it is line symmetric with respect to A and B (See Fig. 2.6 and the following section). We neglect the orbital splitting and Hund's coupling on O(2p) orbitals. The Hamiltonian is given by,

$$\begin{aligned} H_{\text{local}} = &- \sum_{i=A,B} \sum_{\alpha,\beta} \sum_{\sigma} t_{\alpha,\beta} \left(c^\dagger_{i\alpha\sigma} c_{o\beta\sigma} + c^\dagger_{o\beta\sigma} c_{i\alpha\sigma} \right) + \sum_{i=A,B} \sum_{\alpha} \Delta e_\alpha \sum_{\sigma} c^\dagger_{i\alpha\sigma} c_{i\alpha\sigma} \\ &+ \sum_{i=A,B} \sum_{\alpha,\alpha'} \sum_{\sigma,\sigma'} \frac{K(\alpha,\alpha') - \delta_{\sigma,\sigma'} J(\alpha,\alpha')}{2} c^\dagger_{i\alpha\sigma} c_{i\alpha\sigma} c^\dagger_{i\alpha'\sigma'} c_{i\alpha'\sigma'} + \frac{U_o}{2} \sum_{\beta} c^\dagger_{o\beta\sigma} c_{o\beta\sigma} c^\dagger_{o\beta'\sigma'} c_{o\beta'\sigma'}, \end{aligned} \tag{2.11}$$

where $c_{i\alpha\sigma}$ and $c^\dagger_{i\alpha\sigma}$ are the annihilation and creation operators for α-orbital with spin σ in the magnetic ion i and $c_{o\beta\sigma}$ and $c^\dagger_{o\beta\sigma}$ are the annihilation and creation operators for β-orbital with spin σ in the mediated oxygen ion. The first term corresponds to the hopping between Mo(4d) and O(2p) orbitals and $t_{\alpha,\beta}$ is the transfer integral $t_{\alpha,\beta}$ which depends on the relative displacement vector between the two ions [64]. The second term represents the excitation energy from O(2p) to Mo(4d) and we use $\Delta e_{a_{1g}} = 2.0$ (eV) and $\Delta e_{e'_{g\pm}} = 2.5$ (eV) taken from the band calculation given in [58]. The third and fourth terms represent the on-site Coulomb interactions on Mo^{4+} and O^{2-}, respectively. $K(\alpha,\alpha')$ and $J(\alpha,\alpha')$ are the Coulomb and exchange integrations which are represented by using Slater-Condon parameters F^0, F^2 and F^4 (See Sec. C.4).

$-t_{\gamma,\gamma'}(e_x,e_y,e_z)$	Representation by Slater-Koster parameter
$-t_{x,xy}$	$\sqrt{3}e_x^3(pd\sigma)+e_x(1-2e_x^2)(pd\pi)$
$-t_{y,xy}$	$\sqrt{3}e_x^3(pd\sigma)+e_x(1-2e_x^2)(pd\pi)$
$-t_{z,xy}$	$\sqrt{3}e_x^2e_z(pd\sigma)-2e_x^2e_z(pd\pi)$
$-t_{x,yz}$	$\sqrt{3}e_x^2e_z(pd\sigma)-2e_x^2e_z(pd\pi)$
$-t_{y,yz}$	$\sqrt{3}e_x^2e_z(pd\sigma)+e_z(1-2e_x^2)(pd\pi)$
$-t_{z,yz}$	$\sqrt{3}e_z^2e_x(pd\sigma)+e_x(1-2e_z^2)(pd\pi)$
$-t_{x,zx}$	$\sqrt{3}e_x^2e_z(pd\sigma)+e_z(1-2e_x^2)(pd\pi)$
$-t_{y,zx}$	$\sqrt{3}e_x^2e_z(pd\sigma)-2e_x^2e_z(pd\pi)$
$-t_{z,zx}$	$\sqrt{3}e_z^2e_x(pd\sigma)+e_x(1-2e_z^2)(pd\pi)$

Table 2.1: **The transfer integral at general relative positions between O**$(2p)$ (x,y,z) **orbital and Mo**(t_{2g}) (xy,yz,zx) **for the case of** $e_x=e_y$**.** [65]

We adopted $F^2=4.52$ and $F^4/F^2=0.63$ in accordance with [58] and we performed the perturbative calculation treating parameters $F^0=U_{\rm Mo}$ and U_o as unknown parameters.

We performed the perturbative calculation with respect to $t_{\alpha,\beta}$ from the ground state where O$(2p)$ orbitals are fully occupied and both of the magnetic ions A and B have two electrons such that one is in a_{1g} and the other in either e'_{g+} or e'_{g-} (See Fig. 2.7). We neglect the effect of splitting of e'_g orbitals by the Jahn-Teller effect because it amounts the higher order connection. The leading term which gives the effective exchange interaction $J_{\rm eff}\boldsymbol{S}_A\cdot\boldsymbol{S}_B$ appears in the fourth order perturbation, hence we analyzed the fourth order perturbation. The fourth order perturbation energy is given by,

$$E^{(4)}_{mm'}=-\sum_{l,l',l''}\frac{1}{2}E'_{ml}E'_{ll'}E'_{l'l''}E'_{l''m'}\left(\frac{1}{(E_l-E_m)(E_{l'}-E_m)(E_{l''}-E_m)}+\frac{1}{(E_l-E_{m'})(E_{l'}-E_{m'})(E_{l''}-E_{m'})}\right), \tag{2.12}$$

where E_m and E_l are the energies of the ground state m and the excited state l and E'_{ml} is the first order perturbation energy given by the hopping $t_{\alpha,\beta}$.

2.3.2 Transfer integrals

Important ingredient in the following analysis is the values of the transfer integrals to be used in the Hubbard model. The transfer integrals depend on the relative displacement vector between Mo^{4+} and O^{2-} (see Sec. C.5.1). From Eq. (1.84) and Fig. 1.17, the relative vector is given by,

$$(e_x,e_y,e_z)=\frac{1}{\sqrt{64u^2-32u+6}}(1,1,-8u+2), \tag{2.13}$$

where the parameter u is represented by the Mo-O-Mo angle α as,

$$u=\frac{\sqrt{2}}{8\tan\frac{\alpha}{2}}+\frac{1}{4}. \tag{2.14}$$

The transfer integrals are obtained as shown in Table. 2.3.2 in terms of two parameters $(pd\sigma)$ and $(pd\pi)$.

Using $\hbar^2/m\simeq 7.62$ (eV-Å), $r_d\simeq 1.2$ (Å) [64], $d_{\text{Mo - O}}=2.017$ (Å) [60], Eq. (C.132) and Eq. (C.133) we obtain

$$(pd\sigma)\simeq -2.5356(\text{eV}), \tag{2.15}$$
$$(pd\pi)\simeq 1.1684(\text{eV}). \tag{2.16}$$

Now let us evaluate the transfer integral for α =Mo(a_{1g}), Mo(e'_g), β =O($2p$). The wave functions of Mo(a_{1g}) orbital and Mo(e'_g) orbitals are given by

$$\begin{aligned} |a_{1g}\rangle &= \frac{1}{\sqrt{3}}(|xy\rangle + |yz\rangle + |zx\rangle) \\ \left|e'_{g\pm}\right\rangle &= \frac{1}{\sqrt{3}}(e^{\pm\frac{2}{3}\pi i}|xy\rangle + e^{\mp\frac{2}{3}\pi i}|yz\rangle + |zx\rangle), \end{aligned} \tag{2.17}$$

where $|xy\rangle, |yz\rangle, |zx\rangle$ are wave functions of the t_{2g} orbitals. It is convenient to introduce a new coordinate frame which is defined as such that it is line symmetric with respect to A and B (see Fig. 2.6 (b)), i.e.

$$\begin{pmatrix} X \\ Y \\ Z \end{pmatrix} = \begin{pmatrix} 1/\sqrt{2} & 1/\sqrt{2} & 0 \\ 1/\sqrt{2} & -1/\sqrt{2} & 0 \\ 0 & 0 & 1 \end{pmatrix} \begin{pmatrix} x \\ y \\ z \end{pmatrix} \tag{2.18}$$

and then we also define the new orbitals $\beta = p(X), p(Y), p(Z)$ for O^{2-} ion as

$$\begin{pmatrix} |p(X)\rangle \\ |p(Y)\rangle \\ |p(Z)\rangle \end{pmatrix} = \begin{pmatrix} 1/\sqrt{2} & 1/\sqrt{2} & 0 \\ 1/\sqrt{2} & -1/\sqrt{2} & 0 \\ 0 & 0 & 1 \end{pmatrix} \begin{pmatrix} |x\rangle \\ |y\rangle \\ |z\rangle \end{pmatrix}. \tag{2.19}$$

The $|p(X)\rangle$ and $|p(Z)\rangle$ orbitals are lying in the same plane as the triangle composed of the site A, B and the mediated oxygen while the $|p(Y)\rangle$ orbital is orthogonal to it., as shown in Fig. 2.6 (b). In terms of these coordinates, the transfer integrals between these O($2p$) orbitals and Mo(t_{2g}) orbitals are rewritten as

$$\begin{aligned} -t_{p(X),xy} &= \sqrt{6}e_x^3(pd\sigma) + \sqrt{2}e_x(1-2e_x^2)(pd\pi), \\ -t_{p(X),yz} &= -t_{p(X),zx} = \sqrt{6}e_x^2e_z(pd\sigma) + (\frac{1}{\sqrt{2}}e_z - 2\sqrt{2}e_x^2e_z)(pd\pi), \\ -t_{p(Y),xy} &= 0, \\ -t_{p(Y),yz} &= -t_{p(Y),zx} = -\frac{1}{\sqrt{2}}e_z(pd\pi), \\ -t_{p(Z),xy} &= \sqrt{3}e_x^2e_z(pd\sigma) - 2e_x^2e_z(pd\pi), \\ -t_{p(Z),yz} &= -t_{p(Z),zx} = \sqrt{3}e_xe_z^2(pd\sigma) + e_x(1-2e_z^2)(pd\pi), \end{aligned} \tag{2.20}$$

Using Eq. (2.17) and Eq. (2.20), we obtain

$$\begin{aligned} -t_{\beta,a_{1g}} &= \frac{1}{\sqrt{3}}(-t_{\beta,xy} - t_{\beta,yz} - t_{\beta,zx}), \\ -t_{\beta,e'_{g\pm}} &= \frac{1}{\sqrt{3}}(-e^{\pm\frac{2}{3}\pi i}t_{\beta,xy} - e^{\mp\frac{2}{3}\pi i}t_{\beta,yz} - t_{\beta,zx}) \\ &= \frac{1}{2\sqrt{3}}(t_{\beta,xy} + t_{\beta,yz} - 2t_{\beta,zx}) \mp i\frac{1}{2}(t_{\beta,xy} - t_{\beta,yz}). \end{aligned} \tag{2.21}$$

The absolute square of the transfer integral for three angles $\alpha = 116°, 127°, 139°$ are obtained as shown in Table. 2.2. We find that $|t_{p(Y),a_{1g}}|^2$ and $|t_{p(Y),e'_{g\pm}}|^2$ are small enough and does not depend much on α so that we neglect the hopping associated with $p(Y)$. Note that other transfer integrals systematically depend on α strongly suggesting that magnetic interaction can be varied by α.

	$\alpha = 116°$	$\alpha = 127°$	$\alpha = 139°$
$\lvert t_{p(X),a_{1g}}\rvert^2$	0.951913	0.561214	0.151767
$\lvert t_{p(X),e'_{g\pm}}\rvert^2$	1.97879	2.42526	2.69398
$\lvert t_{p(Y),a_{1g}}\rvert^2$	0.255603	0.181218	0.111634
$\lvert t_{p(Y),e'_{g\pm}}\rvert^2$	0.0639006	0.0453044	0.0279085
$\lvert t_{p(Z),a_{1g}}\rvert^2$	0.0580811	0.323847	0.738423
$\lvert t_{p(Z),e'_{g\pm}}\rvert^2$	0.97992	0.572566	0.216754

Table 2.2: **The absolute square $|t|^2$ ($\mathbf{eV}^2$) of the transfer integral for three angles** $\alpha = 116°, 127°, 139°$

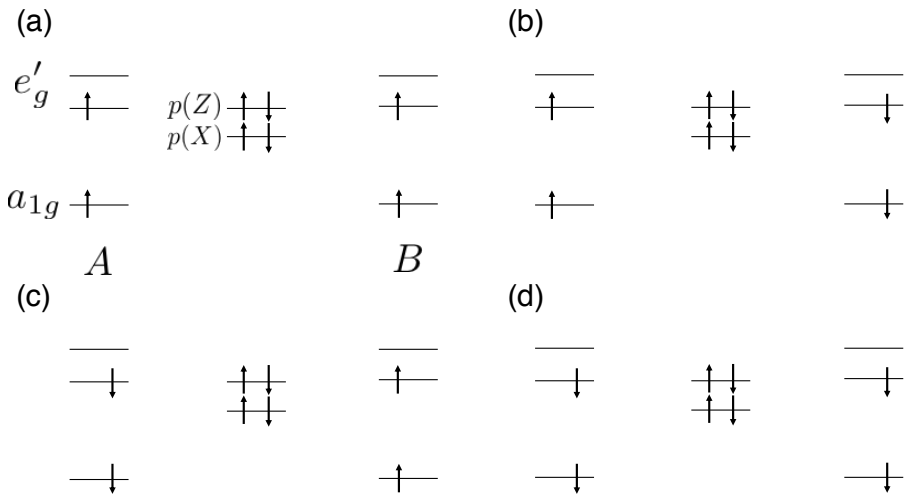

Figure 2.7: **Schematic picture of ground states**
(a),(d): Ferromagnetic alignment. (b),(c): Anti-ferromagnetic alignment.

2.3.3 Fourth order perturbation

Now we start the fourth order perturbation analysis. First we list all possible processes in fourth order perturbation: $m \to l \to l' \to l'' \to m'(= m)$ (see Fig. 2.8). Here the starting point m is a ground state and we will refer to the intermediate states l and l'' as the fist intermediate state and l as he second intermediate state. Next we calculate the energy of first intermediate state (l, l'') and second intermediate state (l') then we evaluate the perturbation energy (Eq. (2.12)). Finally we extract the effective magnetic exchange interaction based on the perturbation energy.

2.3.3.1 Perturbation process

Here we list all relevant perturbation processes which contribute to the effective exchange interactions. There are four ground states of Mo^{4+} ions A, B and O^{2-} ion as shown in Fig. 2.7. We can visualize the fourth order perturbation as a series of electron hoppings such that electrons hop four times from a ground state m and return to the ground state m' (Fig. 2.8). Note that there is no hopping process from a ground state to other ground states in fourth order perturbation, i.e. always $m = m'$. Since the matrix $H_{mm'}$ whose component is given by Eq. (2.12) is a diagonal matrix, we can neglect the quantum effect (see Sec. C.5).

We first consider the case of ferromagnetic ground sate

$$(m) : \left|Aa_{1g}, e'_{g+}, e'_{g-}; O^{2-}p(X), p(Z); Ba_{1g}, e'_{g+}, e_{g-}\right\rangle = |\uparrow, \uparrow, 0; \uparrow\downarrow, \uparrow\downarrow; \uparrow, \uparrow, 0\rangle \tag{2.22}$$

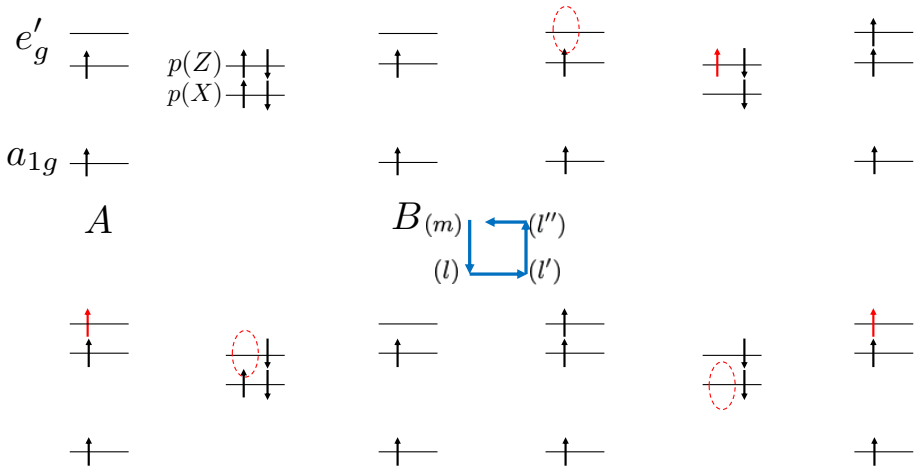

Figure 2.8: **Schematic picture of fourth order perturbation process**

shown in Fig. 2.7(a). It is convenient to consider the candidates of the second intermediate states, which are displayed in Fig. 2.10, hereafter we call these state $F(a)$-$F(e)$. The second intermediate states $F(a)$-$F(d)$ and $F(e)$ realize super-exchange mechanisms and double-exchange mechanisms, respectively. For example, we can explicitly write down the perturbation processes going through $F(a)$ (l') : $|\uparrow,\uparrow,\uparrow;\downarrow,\downarrow;\uparrow,\uparrow,\uparrow\rangle$ as the following. There are 4 possible first intermediate states (l,l''), $|\uparrow,\uparrow,\uparrow;\uparrow\downarrow,\downarrow;\uparrow,\uparrow,0\rangle$, $|\uparrow,\uparrow,0;\uparrow\downarrow,\downarrow;\uparrow,\uparrow,\uparrow\rangle$, $|\uparrow,\uparrow,\uparrow;\downarrow,\uparrow\downarrow;\uparrow,\uparrow,0\rangle$ and $|\uparrow,\uparrow,0;\downarrow,\uparrow\downarrow;\uparrow,\uparrow,\uparrow\rangle$, namely there 4×4 ways to connect the ferromagnetic ground state m (Eq. (2.22)) to the second intermediate state $F(a)$ (l). To evaluate the perturbation energy Eq. (2.12) we need to know the excitation energies, from which we find the excited energy $E_l-E_m, E_{l'}-E_m, E_{l''}-E_m$. To evaluate the latters we take into account of local excitation energy ΔE of Mo^{4-} and Coulomb interactions U_O in O^{2-}, neglecting the difference of energy level of O(2p) and Hund's coupling on O^{2-}. Then the perturbation energy is given by

$$E^{(4)}_{mlF(a)l''m} = -\frac{1}{2}|t_{p(X),e'_{g\pm}}|^2|t_{p(Z),e'_{g\pm}}|^2\frac{16}{(\Delta E_{①}-5U_O)(2\Delta E_{①}-9U_O)(\Delta E_{①}-5U_O)}. \tag{2.23}$$

Here the pre-factor 5 and 9 of U_O is due to the decrease of the number of electron pairs on O^{2-}.

We can similarly study the case to start/end from antiferromagnetic ground state. The candidates of the second intermediate state for the anti-ferromagnetic case are shown in Fig. 2.11, hereafter we call these state $AF(a)$-$AF(f)$. The processes going through $AF(a)$-$AF(e)$ and $AF(f)$ represent super-exchange mechanisms and double-exchange mechanisms, respectively. We find that $E^{(4)}_{mlF(a)l''m} = E^{(4)}_{mlAF(b)l''m}$ in the same way as explained above, so that their effects are cancelled out when we evaluate their contribution to the effective exchange coupling later. Similarly, we find $E^{(4)}_{mlF(c)l''m} = E^{(4)}_{mlAF(e)l''m}$ and $E^{(4)}_{mlF(d)l''m} = E^{(4)}_{mlAF(d)l''m}$. The contributions which will not be canceled out are obtained as the following: $E^{(4)}_{mlF(b)l''m}$, $E^{(4)}_{mlF(e)l''m}$,

$E^{(4)}_{mlAF(a)l''m}$, $E^{(4)}_{mlAF(c)l''m}$ and $E^{(4)}_{mlF(f)l''m}$ given by

$$\begin{aligned}
E^{(4)}_{mlF(b)l''m} =& -\frac{1}{2}\Big(|t_{p(X),e'_{g\pm}}|^4+|t_{p(Z),e'_{g\pm}}|^4\Big)\frac{2}{(\Delta E_{①}+\Delta E_{②}-9U_{\rm O})}\bigg(\frac{1}{\Delta E_{①}-5U_{\rm O}}+\frac{1}{\Delta E_{②}-5U_{\rm O}}\bigg)^2\\
&-\frac{1}{2}\Big(|t_{p(X),e'_{g\pm}}|^4+|t_{p(Z),e'_{g\pm}}|^4\Big)\frac{2}{(\Delta E_{①}+\Delta E_{③}-9U_{\rm O})}\bigg(\frac{1}{\Delta E_{①}-5U_{\rm O}}+\frac{1}{\Delta E_{③}-5U_{\rm O}}\bigg)^2\\
&-\frac{1}{2}\Big(|t_{p(X),e'_{g\pm}}|^2|t_{p(X),a_{1g}}|^2+|t_{p(Z),e'_{g\pm}}|^2|t_{p(Z),a_{1g}}|^2\Big)\\
&\times\frac{2}{(\Delta E_{①}+\Delta E_{④}-9U_{\rm O})}\bigg(\frac{1}{\Delta E_{①}-5U_{\rm O}}+\frac{1}{\Delta E_{④}-5U_{\rm O}}\bigg)^2, \qquad (2.24)
\end{aligned}$$

$$\begin{aligned}
E^{(4)}_{mlF(e)l''m} =& -\frac{1}{2}\Big(|t_{p(X),e'_{g\pm}}|^2+|t_{p(Z),e'_{g\pm}}|^2\Big)^2\frac{2}{(\Delta E_{①}-5U_{\rm O})^2(\Delta E_{①}+\Delta E_{⑤})}\\
&-\frac{1}{2}\Big(|t_{p(X),e'_{g\pm}}||t_{p(X),a_{1g}}|+|t_{p(Z),e'_{g\pm}}||t_{p(Z),a_{1g}}|\Big)^2\frac{2}{(\Delta E_{①}-5U_{\rm O})^2(\Delta E_{①}+\Delta E_{⑥})}, \qquad (2.25)
\end{aligned}$$

$$E^{(4)}_{mlAF(a)l''m} = -\frac{1}{2}\Big(|t_{p(X),e'_{g\pm}}|^4+|t_{p(Z),e'_{g\pm}}|^4\Big)\frac{4}{(\Delta E_{①}-5U_{\rm O})^2(2\Delta E_{①}-9U_{\rm O})}, \qquad (2.26)$$

$$\begin{aligned}
E^{(4)}_{mlAF(c)l''m} =& -\frac{1}{2}\Big(|t_{p(X),e'_{g\pm}}|^4+|t_{p(Z),e'_{g\pm}}|^4\Big)\bigg[\frac{4}{(\Delta E_{②}-5U_{\rm O})^2(2\Delta E_{②}-9U_{\rm O})}\\
&+\frac{4}{(\Delta E_{③}-5U_{\rm O})^2(2\Delta E_{③}-9U_{\rm O})}+\frac{1}{(\Delta E_{②}+\Delta E_{③}-9U_{\rm O})}\\
&\times\bigg(\frac{1}{\Delta E_{②}-5U_{\rm O}}+\frac{1}{\Delta E_{③}-5U_{\rm O}}\bigg)^2\bigg]\\
&-\frac{1}{2}\big(|t_{p(X),a_{1g}}|^4+|t_{p(Z),a_{1g}}|^4\big)\frac{4}{(\Delta E_{④}-5U_{\rm O})^2(2\Delta E_{④}-9U_{\rm O})}\\
&-\frac{1}{2}\Big(|t_{p(X),e'_{g\pm}}|^2|t_{p(X),a_{1g}}|^2+|t_{p(Z),e'_{g\pm}}|^2|t_{p(Z),a_{1g}}|^2\Big)\\
&\times\bigg[\frac{2}{(\Delta E_{②}+\Delta E_{④}-9U_{\rm O})}\bigg(\frac{1}{\Delta E_{②}-5U_{\rm O}}+\frac{1}{\Delta E_{④}-5U_{\rm O}}\bigg)^2\\
&+\frac{2}{(\Delta E_{③}+\Delta E_{④}-9U_{\rm O})}\bigg(\frac{1}{\Delta E_{③}-5U_{\rm O}}+\frac{1}{\Delta E_{④}-5U_{\rm O}}\bigg)^2\bigg], \qquad (2.27)
\end{aligned}$$

$$\begin{aligned}
E^{(4)}_{mlAF(f)l''m} =& -\frac{1}{2}\Big(|t_{p(X),e'_{g\pm}}|^2+|t_{p(Z),e'_{g\pm}}|^2\Big)^2\\
&\times\bigg[\frac{2}{(\Delta E_{②}-5U_{\rm O})^2(\Delta E_{②}+\Delta E_{⑤})}+\frac{2}{(\Delta E_{③}-5U_{\rm O})^2(\Delta E_{③}+\Delta E_{⑤})}\bigg]\\
&-\frac{1}{2}\Big(|t_{p(X),e'_{g\pm}}||t_{p(X),a_{1g}}|+|t_{p(Z),e'_{g\pm}}||t_{p(Z),a_{1g}}|\Big)^2\bigg[\frac{2}{(\Delta E_{②}-5U_{\rm O})^2(\Delta E_{②}+\Delta E_{⑥})}\\
&+\frac{2}{(\Delta E_{③}-5U_{\rm O})^2(\Delta E_{③}+\Delta E_{⑥})}+\frac{2}{(\Delta E_{④}-5U_{\rm O})^2(\Delta E_{④}+\Delta E_{⑤})}\bigg]\\
&-\frac{1}{2}\big(|t_{p(X),a_{1g}}|^2+|t_{p(Z),a_{1g}}|^2\big)^2\frac{2}{(\Delta E_{④}-5U_{\rm O})^2(\Delta E_{④}+\Delta E_{⑥})}, \qquad (2.28)
\end{aligned}$$

respectively. From the above result we can obtain the effective exchange coupling as the following. Using the total spin $\boldsymbol{S}_i$ on an ion i the effective Hamiltonian for the exchange coupling becomes

$$H_{\rm ex} = J_{\rm eff}\boldsymbol{S}_i \cdot \boldsymbol{S}_j + \text{const} \tag{2.29}$$

with

$$J_{\rm eff} = \frac{E_F^{(4)} - E_{AF}^{(4)}}{3}, \tag{2.30}$$

where

$$E_F^{(4)} = E_{mlF(b)l''m}^{(4)} + E_{mlF(e)l''m}^{(4)}, \tag{2.31}$$

$$E_{AF}^{(4)} = E_{mlAF(a)l''m}^{(4)} + E_{mlAF(c)l''m}^{(4)} + E_{mlAF(f)l''m}^{(4)}. \tag{2.32}$$

If $J_{\rm eff} < 0$, the exchange interaction becomes ferromagnetic.

2.3.3.2 Energy of excited states

Now our remaining task is to explicitly evaluate the excitation energies which are needed to evaluate Jeff in Eq. (2.30). We first calculate the interaction energies within Mo^{4+} ions of the ground state, which is given by $K(\phi_{a_{1g}}, \phi_{e'_{g\pm}}) - J(\phi_{a_{1g}}, \phi_{e'_{g\pm}})$. Here, $K(\phi_{a_{1g}}, \phi_{e'_{g\pm}})$ and $J(\phi_{a_{1g}}, \phi_{e'_{g\pm}})$ are given in Eq. (C.87). For convenience we choose [111] direction as quantization axis, then the a_{1g} and $e'_{g\pm}$ orbital wave functions become

$$\begin{aligned}
\phi_{a_{1g}}(\boldsymbol{r}) &= \phi_{420}(\boldsymbol{r}) = R_{42}(r)Y_{20}(\theta,\phi), \\
\phi_{e'_{g\pm}}(\boldsymbol{r}) &= \frac{1}{\sqrt{3}}\Big(\sqrt{2}\phi_{42\mp2}(\boldsymbol{r}) \pm \phi_{42\pm1}(\boldsymbol{r})\Big) = R_{42}(r)\frac{1}{\sqrt{3}}\Big(\sqrt{2}Y_{2\mp2}(\theta,\phi) \pm Y_{2\pm1}(\theta,\phi)\Big),
\end{aligned} \tag{2.33}$$

respectively. Here $R_{nl}(r)$ is the radial wave function and $Y_{lm}(\theta,\phi)$ is the spherical harmonic function. We introduce a short hand notation as

$$\langle m_1, m_2| \left|m_1', m_2'\right\rangle = \int d\boldsymbol{r}_1 \int d\boldsymbol{r}_2 \phi^*_{42m_1}(\boldsymbol{r}_1)\phi^*_{42m_2}(\boldsymbol{r}_2)\frac{e^2}{r_{12}}\phi_{42m_1'}(\boldsymbol{r}_1)\phi_{42m_2'}(\boldsymbol{r}_2). \tag{2.34}$$

Then the Coulomb integral and the exchange integral are calculated as

$$\begin{aligned}
K(\phi_{a_{1g}}, \phi_{e'_{g\pm}}) &= \frac{2}{3}\langle 0,\mp2|\,|0,\mp2\rangle + \frac{\sqrt{2}}{3}(\langle 0,\mp2|\,|0,\pm1\rangle + \langle 0,\pm1|\,|0,\mp2\rangle) + \frac{1}{3}\langle 0,\pm1|\,|0,\pm1\rangle\,, \\
J(\phi_{a_{1g}}, \phi_{e'_{g\pm}}) &= \frac{2}{3}\langle 0,\mp2|\,|\mp2,0\rangle + \frac{\sqrt{2}}{3}(\langle 0,\mp2|\,|\pm1,0\rangle + \langle 0,\pm1|\,|\mp2,0\rangle) + \frac{1}{3}\langle 0,\pm1|\,|\pm1,0\rangle\,.
\end{aligned} \tag{2.35}$$

Using Eq. (C.94), $K(\phi_{a_{1g}}, \phi_{e'_{g\pm}})$ and $J(\phi_{a_{1g}}, \phi_{e'_{g\pm}})$ become

$$\begin{aligned}
K(\phi_{a_{1g}}, \phi_{e'_{g\pm}}) &= \frac{2}{3}\left(F^0 - \frac{4}{49}F^2 + \frac{6}{441}F^4\right) + \frac{1}{3}\left(F^0 + \frac{2}{49}F^2 - \frac{24}{441}F^4\right) \\
&= F^0 - \frac{2}{49}F^2 - \frac{4}{441}F^4
\end{aligned} \tag{2.36}$$

$$\begin{aligned}
J(\phi_{a_{1g}}, \phi_{e'_{g\pm}}) &= \frac{2}{3}\left(\frac{4}{49}F^2 + \frac{15}{441}F^4\right) + \frac{1}{3}\left(\frac{1}{49}F^2 + \frac{30}{441}F^4\right) \\
&= \frac{3}{49}F^2 + \frac{20}{441}F^4.
\end{aligned} \tag{2.37}$$

Using these results we find the interaction energy of the ground state as

$$E_{\rm int}^{\rm GS} = K(\phi_{a_{1g}}, \phi_{e'_{g\pm}}) - J(\phi_{a_{1g}}, \phi_{e'_{g\pm}}) = F^0 - \frac{5}{49}F^2 - \frac{24}{441}F^4. \tag{2.38}$$

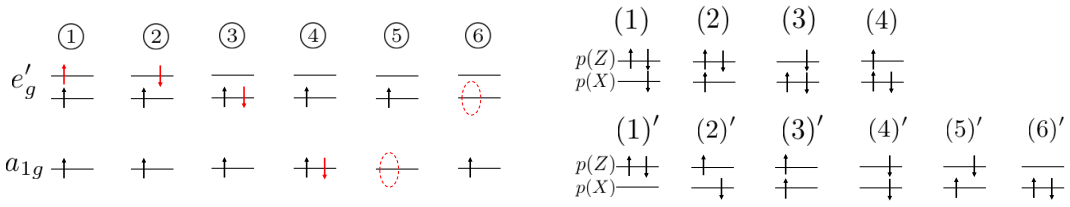

Figure 2.9: **All possible local excitations of Mo^{4+} and O^{2-}**

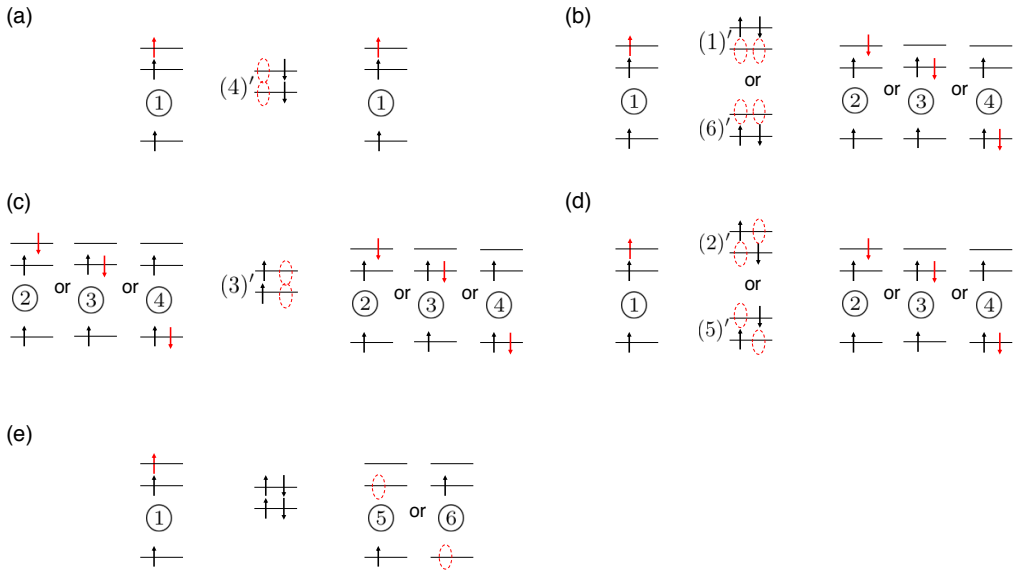

Figure 2.10: **Second excited states with ferromagnetic alignment**
(a)-(d): Super-exchange process. (e): Double-exchange process. Here the notations ⓝ and $(n)'$ represents local states of Mo^{4+} and O^{2-} in Fig .2.9, respectively.

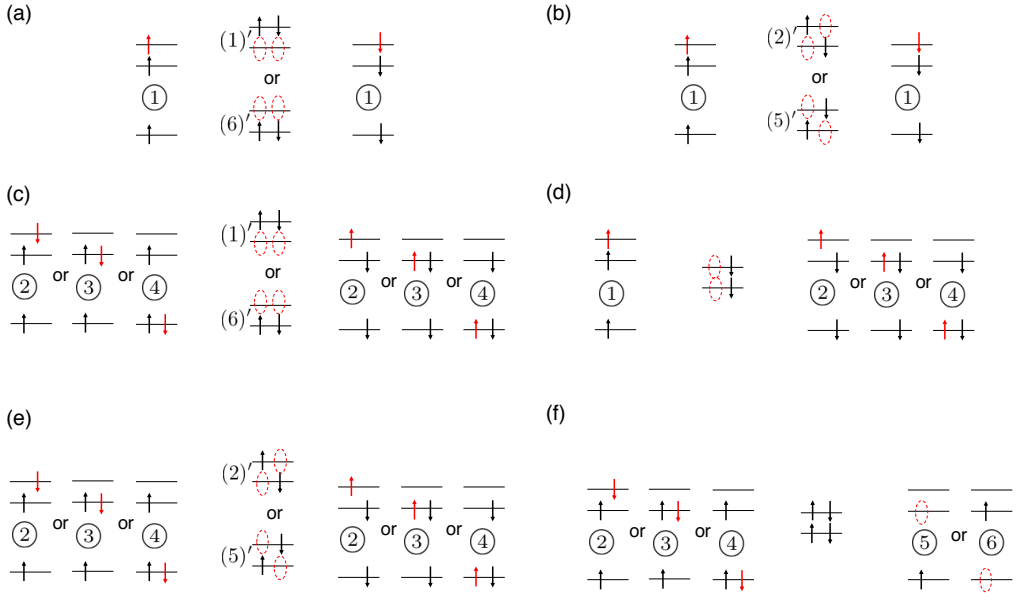

Figure 2.11: **Second excited states with anti-ferromagnetic alignment**
(a)-(e): Super-exchange process. (f): Double-exchange process.

Next we consider the energy of three electrons associated with local excited states ① - ④ in Fig. 2.9. The interaction energies of the states ① - ④ become

$$E^{①}_{\rm int} = 2K(\phi_{a_{1g}}, \phi_{e'_{g\pm}}) + K(\phi_{e'_{g\pm}}, \phi_{e'_{g\mp}}) - 2J(\phi_{a_{1g}}, \phi_{e'_{g\pm}}) - J(\phi_{e'_{g\pm}}, \phi_{e'_{g\mp}}), \tag{2.39}$$

$$E^{②}_{\rm int} = 2K(\phi_{a_{1g}}, \phi_{e'_{g\pm}}) + K(\phi_{e'_{g\pm}}, \phi_{e'_{g\mp}}) - J(\phi_{a_{1g}}, \phi_{e'_{g\pm}}), \tag{2.40}$$

$$E^{③}_{\rm int} = 2K(\phi_{a_{1g}}, \phi_{e'_{g\pm}}) + K(\phi_{e'_{g\pm}}, \phi_{e'_{g\pm}}) - J(\phi_{a_{1g}}, \phi_{e'_{g\pm}}), \tag{2.41}$$

$$E^{④}_{\rm int} = 2K(\phi_{a_{1g}}, \phi_{e'_{g\pm}}) + K(\phi_{a_{1g}}, \phi_{a_{1g}}) - J(\phi_{a_{1g}}, \phi_{e'_{g\pm}}), \tag{2.42}$$

respectively. $K(\phi_{a_{1g}}, \phi_{e'_{g\pm}})$ and $J(\phi_{a_{1g}}, \phi_{e'_{g\pm}})$ are given in Eq. (2.35). Very similarly, we get other Coulomb integrals and exchange integral as

$$K(\phi_{a_{1g}}, \phi_{a_{1g}}) = \langle 0,0|\,|0,0\rangle = F^0 + \frac{4}{49}F^2 + \frac{36}{441}F^4, \tag{2.43}$$

$$\begin{aligned} K(\phi_{e'_{g\pm}}, \phi_{e'_{g\pm}}) &= \frac{4}{9}\langle 2,2|\,|2,2\rangle + \frac{4}{9}\langle 2,\bar{1}|\,|\bar{1},2\rangle + \frac{4}{9}\langle 2,\bar{1}|\,|2,\bar{1}\rangle + \frac{1}{9}\langle 1,1|\,|1,1\rangle \\ &= F^0 + \frac{1}{49}F^2 + \frac{16}{441}F^4, \end{aligned} \tag{2.44}$$

$$\begin{aligned} K(\phi_{e'_{g\pm}}, \phi_{e'_{g\mp}}) &= \frac{4}{9}\langle 2,\bar{2}|\,|2,\bar{2}\rangle - \frac{4}{9}\langle 2,\bar{2}|\,|\bar{1},1\rangle + \frac{4}{9}\langle 2,1|\,|2,1\rangle + \frac{1}{9}\langle 1,\bar{1}|\,|1,\bar{1}\rangle \\ &= F^0 + \frac{1}{49}F^2 + \frac{16}{441}F^4, \end{aligned} \tag{2.45}$$

$$\begin{aligned} J(\phi_{e'_{g\pm}}, \phi_{e'_{g\mp}}) &= \frac{4}{9}\langle 2,\bar{2}|\,|\bar{2},2\rangle - \frac{4}{9}\langle 2,\bar{2}|\,|1,\bar{1}\rangle + \frac{4}{9}\langle 2,1|\,|1,2\rangle + \frac{1}{9}\langle 1,\bar{1}|\,|\bar{1},1\rangle \\ &= \frac{6}{49}F^2 + \frac{40}{441}F^4. \end{aligned} \tag{2.46}$$

2.3.3.3 Fourth perturbation energy

Collecting the above results, we obtain the excitation energies as

$$\begin{aligned} \Delta E_{①} &= E^{①}_{\rm int} - E^{\rm GS}_{\rm int} + \Delta e_{e'_g\text{-}2p} = 2F^0 - \frac{12}{49}F^2 - \frac{38}{441}F^4 + \Delta e_{e'_g\text{-}2p}, \\ \Delta E_{②} = \Delta E_{③} &= E^{②}_{\rm int} - E^{\rm GS}_{\rm int} + \Delta e_{e'_g\text{-}2p} = 2F^0 - \frac{3}{49}F^2 + \frac{22}{441}F^4 + \Delta e_{e'_g\text{-}2p}, \\ \Delta E_{④} &= E^{④}_{\rm int} - E^{\rm GS}_{\rm int} + \Delta e_{a_{1g}\text{-}2p} = 2F^0 + \frac{42}{441}F^4 + \Delta e_{a_{1g}\text{-}2p}, \\ \Delta E_{⑤} &= -E^{\rm GS}_{\rm int} - \Delta e_{e'_g\text{-}2p} \qquad = -F^0 + \frac{5}{49}F^2 + \frac{24}{441}F^4 - \Delta e_{e'_g\text{-}2p}, \\ \Delta E_{⑥} &= -E^{\rm GS}_{\rm int} - \Delta e_{e'_g\text{-}2p} \qquad = -F^0 + \frac{5}{49}F^2 + \frac{24}{441}F^4 - \Delta e_{a_{1g}\text{-}2p}. \end{aligned} \tag{2.47}$$

Finally to evaluate the above results quantitatively we use the Slater-Condon parameter F^2 and F^4 taken from [58], $F^2 = 4.52$ (eV) and $F^4/F^2 = 0.63$. By substituting Eq. (2.47) into Eq. (2.24)-Eq. (2.28), there remain two unknown parameters $U_{\rm Mo} \equiv F^0$ and $U_{\rm O}$. They represent On-site Coulomb energy on Mo^{4+} and O^{-2}, respectively.

First we show the the dependence of the sign of Jeff with respect to variation of $U_{\rm O}$ and $U_{\rm Mo}$ in Fig. 2.12 (a) for the angles $\alpha = 116°, 127°, 139°$. We can see that the smaller angle yields wide anti-ferromagnetic region. For fixed $U_{\rm O} = 0.7$ (eV) the effective exchange energy is changes by $U_{\rm Mo}$ as shown in Fig. 2.12 (b). As shown in Fig. 2.12 (c), the super-exchange energy

$$E^{(4)}_{\rm SE} = E^{(4)}_{mlF(b)l''m} - E^{(4)}_{mlAF(a)l''m} - E^{(4)}_{mlAF(c)l''m} \tag{2.48}$$

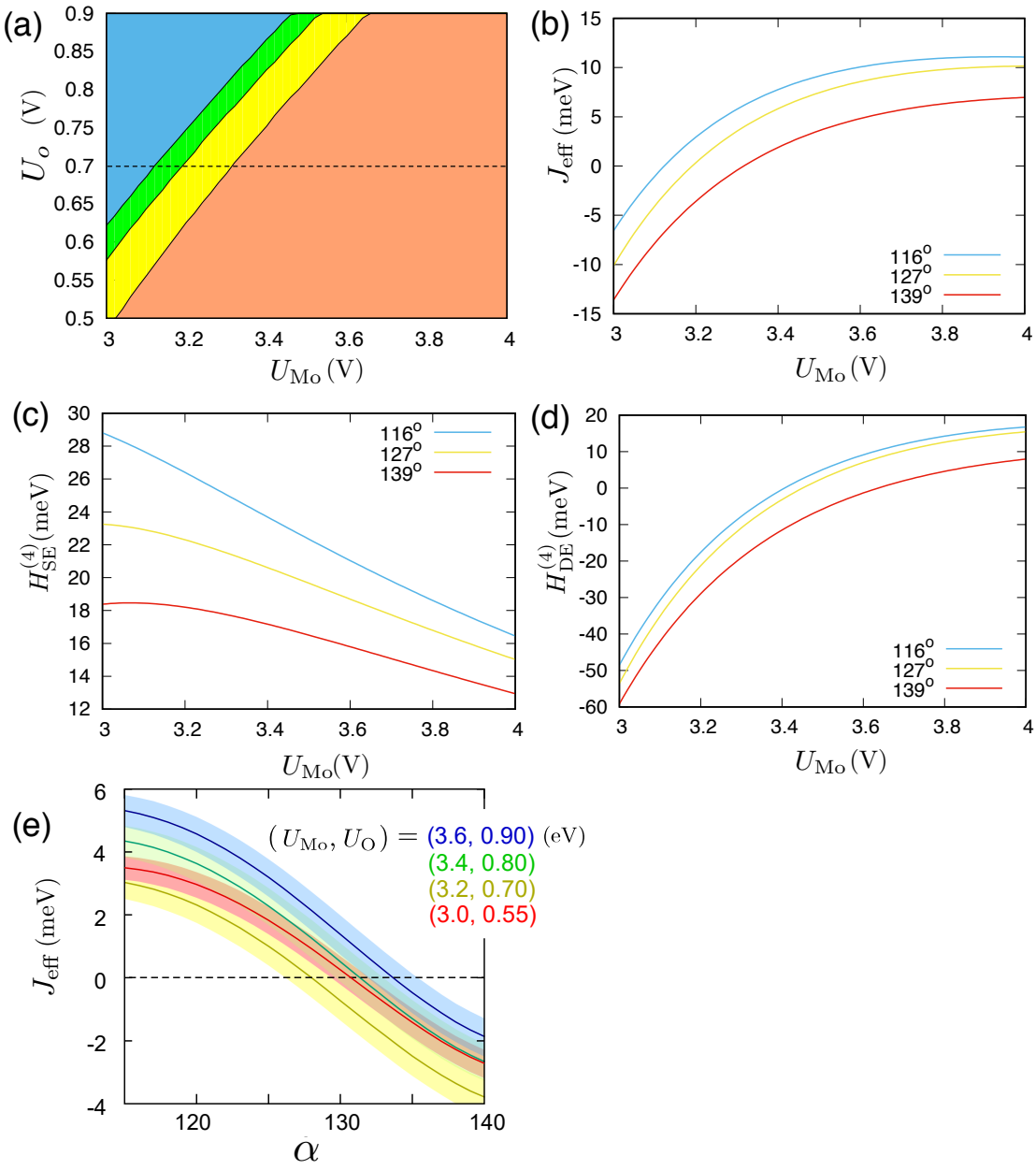

Figure 2.12: **Results of the perturbation calculation**
(a): Diagram of the sign of the exchange interaction $J_{\rm eff}$ for the angles $\alpha = 116°, 127°, 139°$. Here $J_{\rm eff} < 0$ means ferromagnetic coupling. Four colored regions (blue, green, yellow, red) represent different sign sets $\{116°, 127°, 139°\}$. (blue): $\{-,-,-\}$. (green): $\{+,-,-\}$. (yellow): $\{+,+,-\}$. (red): $\{+,+,+\}$. (b): Fourth perturbation energy $H^{(4)}$ (eV) at $U_{\rm O} = 0.7$ (eV). (c): Super-exchange parts $H^{(4)}_{\rm SE}$ (eV) at $U_{\rm O} = 0.7$ (eV). (d): Double-exchange parts $H^{(4)}_{\rm SE}$ (eV) at $U_{\rm O} = 0.7$ (eV). (e): α-dependence of the effective exchange interaction for typical on-site Coulomb interactions on Mo $U_{\rm Mo}$ [58, 66]. Here we determined $U_{\rm O}$ so that the exchange interaction is consistent with the experimental observation (see Fig. 1.16). The shaded regions are the variance of $J_{\rm eff}$ when $U_{\rm O}$ is varied in the range of ± 0.01.

strongly depends on the angle. On the other hand, the double-exchange energy

$$E^{(4)}_{\rm DE} = E^{(4)}_{mlF(e)l''m} - E^{(4)}_{mlAF(f)l''m} \tag{2.49}$$

has a small difference between $\alpha = 116^\circ$ and 127° while it is large between 127° and 139° (Fig. 2.12 (d)). Fig. 2.12 (e) shows α-dependence of the effective exchange interaction $J_{\rm eff}$ for various $U_{\rm Mo}$ and $U_{\rm O}$, where $J_{\rm eff}$ is located around $1 \sim 3$ (meV) for $\alpha = 127^\circ$. Then, $J_{\rm eff}$ takes $3 \sim 5$ and $-1 \sim -3$ for $\alpha = 116^\circ$ and 139°, respectively. In our effective model (Eq. (2.2)), $J_{\rm eff}$ is varied from 1 to $1 + 2\delta$ or $1 - 2\delta$ for the *in-in* bond (116°) and *out-out* bond (139°). Thus we find that by choosing $\delta = 1.5$ in our effective model, we can match the variation of the effective coupling with the one obtained here microscopically. Let us note that according to the ground state at the level of single tetrahedron which we will discuss in the next section (see Fig. 2.13) we can expect the ice-rule lattice structure as the ground state if we take the elastic energy scale as $\epsilon > 17/32 \sim 0.53$.

2.4 Analysis of low energy states

2.4.1 Ground state of single tetrahedron

In the present section, we will examine the ground state at the level of single tetrahedron. In systems on corner sharing lattices such including the pyrochlore lattice, such an analysis often provide useful information. In Sec. 1.2.1, we explained that the ground state of the conventional antiferromagnetic Heisenberg spin model on the pyrochlore lattice has two continuous internal degrees of freedom in the ground state of single tetrahedron.[32] Now, let us perform a similar analysis on our effective model (Eq. (2.2)). The energy of one tetrahedron with 4 spins $(\boldsymbol{S}_1, \boldsymbol{S}_2, \boldsymbol{S}_3, \boldsymbol{S}_4)$ and Mo^{4+} displacements $(\sigma_1, \sigma_2, \sigma_3, \sigma_4)$, $\sigma_i = \pm 1$ $(+ : in, - : out)$, is given by

$$E_\Delta/J = \sum_{i=1}^{4} \sum_{j<i} [(1 + \delta(\sigma_i + \sigma_j))\boldsymbol{S}_i \cdot \boldsymbol{S}_j + \epsilon\sigma_i\sigma_j]. \tag{2.50}$$

The single tetrahedron can takes 5 kinds of distortion patterns, i) all-*in*, ii) all-*out*, iii) 3-*in*-1-*out*, iv) 1-*in*-3-*out* and v) 2-*in*-2-*out* structure. For each of the deformation patterns i)- v), we can find the ground state as the following.

i)**all-in**: Eq. (2.50) becomes

$$\begin{aligned} E_{\Delta(\mathrm{i})}/J &= (1 + 2\delta) \sum_{i=1}^{4} \sum_{j<i} \boldsymbol{S}_i \cdot \boldsymbol{S}_j + 6\epsilon \\ &= \frac{1 + 2\delta}{2} \left(\sum_{i=1}^{4} \boldsymbol{S}_i \right)^2 - 2(1 + 2\delta) + 6\epsilon \end{aligned} \tag{2.51}$$

The lowest energy can be found as

$$E_{\min(\mathrm{i})}/J = -2(1 + 2\delta) + 6\epsilon \tag{2.52}$$

and the associated spin configuration satisfies $\sum_{i=1}^{4} \boldsymbol{S}_i = \boldsymbol{0}$ since all exchange interactions take the same positive (i.e. antiferromagnetic) value. (Note that $\delta > 0$)

ii)**all out**: Eq. (2.50) becomes

$$E_{\Delta(\mathrm{ii})}/J = (1 - 2\delta) \sum_{i=1}^{4} \sum_{j<i} \boldsymbol{S}_i \cdot \boldsymbol{S}_j + 6\epsilon. \tag{2.53}$$

For $\delta > 1/2$ the interaction becomes ferromagnetic and then the system has the lowest energy if $\boldsymbol{S}_1 = \boldsymbol{S}_2 = \boldsymbol{S}_3 = \boldsymbol{S}_4$. For $\delta < 1/2$, the interaction becomes antiferromagnetic and the ground state satisfies $\sum_{i=1}^{4} \boldsymbol{S}_i = \boldsymbol{0}$ similarly to i). The ground state energy is obtained as,,

$$E_{\min(\mathrm{ii})}/J = \begin{cases} 6(1 - 2\delta) + 6\epsilon, & (\delta > 1/2) \\ -2(1 - 2\delta) + 6\epsilon, & (\delta \leq 1/2). \end{cases} \tag{2.54}$$

iii)**3-int-1-out**: Let site 1 be *out* and the others be *in*. The Eq. (2.50) becomes

$$\begin{aligned} E_{\Delta(\mathrm{iii})}/J &= \boldsymbol{S}_1 \cdot (\boldsymbol{S}_2 + \boldsymbol{S}_3 + \boldsymbol{S}_4) + (1 + 2\delta)(\boldsymbol{S}_2 \cdot \boldsymbol{S}_3 + \boldsymbol{S}_3 \cdot \boldsymbol{S}_4 + \boldsymbol{S}_2 \cdot \boldsymbol{S}_4) \\ &= \boldsymbol{S}_1 \cdot \boldsymbol{X} + (1 + 2\delta)\left(\frac{1}{2}\boldsymbol{X}^2 - \frac{3}{2} \right) \\ &= \frac{1 + 2\delta}{2} \left(\boldsymbol{X} + \frac{\boldsymbol{S}_1}{(1 + 2\delta)} \right)^2 - \frac{1}{2(1 + 2\delta)} - \frac{3}{2}(1 + 2\delta), \end{aligned} \tag{2.55}$$

where $\boldsymbol{X} = \boldsymbol{S}_2 + \boldsymbol{S}_3 + \boldsymbol{S}_4$. We find the lowest energy is

$$E_{\min(\mathrm{iii})}/J = -\frac{1}{2(1+2\delta)} - \frac{3}{2}(1+2\delta) \tag{2.56}$$

with the spins in the ground state satisfying the condition $\boldsymbol{S}_1 + (1+2\delta)(\boldsymbol{S}_2 + \boldsymbol{S}_3 + \boldsymbol{S}_4) = \boldsymbol{0}$. We can express such a spin configuration as follows:

$$\begin{aligned}
&\boldsymbol{S}_1 = (0, 0, 1),\\
&\boldsymbol{S}_2 = (\sin\theta_2, 0, \cos\theta_2),\\
&\boldsymbol{S}_3 = (\sin\theta_3\cos\phi_3, \sin\theta_3\sin\phi_3, \cos\theta_3),\\
&\boldsymbol{S}_4 = \left(-\sin\theta_2 - \sin\theta_3\cos\phi_3, -\sin\theta_3\sin\phi_3, -\frac{1}{(1+2\delta)} - \cos\theta_2 - \cos\theta_3\right),
\end{aligned} \tag{2.57}$$

where

$$\cos\phi_3 = \frac{\frac{-2\delta(1+\delta)}{(1+2\delta)^2} - (\cos\theta_2 - \frac{1}{1+2\delta})(\cos\theta_3 - \frac{1}{1+2\delta})}{\sin\theta_2\sin\theta_3} \tag{2.58}$$

and $0 \le \pi - \theta_2 \le \theta_3 \le \pi$. There remain two continuous internal degrees of freedom in the single tetrahedron.

iv)**1-in-3-out**: Let site 1 be *in* and the others be *out*. The Eq. (2.50) becomes

$$\begin{aligned}
E_{\Delta(\mathrm{iv})}/J &= \boldsymbol{S}_1\cdot(\boldsymbol{S}_2 + \boldsymbol{S}_3 + \boldsymbol{S}_4) + (1-2\delta)(\boldsymbol{S}_2\cdot\boldsymbol{S}_3 + \boldsymbol{S}_3\cdot\boldsymbol{S}_4 + \boldsymbol{S}_2\cdot\boldsymbol{S}_4)\\
&= \frac{1-2\delta}{2}\left(\boldsymbol{X} + \frac{\boldsymbol{S}_1}{(1-2\delta)}\right)^2 - \frac{1}{2(1-2\delta)} - \frac{3}{2}(1-2\delta).
\end{aligned}$$

For $\delta > 1/3$, the system takes the ground state if the configuration satisfies $-\boldsymbol{S}_1 = \boldsymbol{S}_2 = \boldsymbol{S}_3 = \boldsymbol{S}_4$, since the couplings between spin 1 and the others are antiferromagnetic and the other couplings are ferromagnetic. For $\delta \le 1/3$, the system has the lowest energy if the spin configuration satisfies the condition $\boldsymbol{S}_1 + (1-2\delta)(\boldsymbol{S}_2 + \boldsymbol{S}_3 + \boldsymbol{S}_4) = \boldsymbol{0}$. The energy minimum is given by,

$$E_{\min(\mathrm{iv})}/J = \begin{cases} -6\delta, & (\delta > 1/3)\\ -\dfrac{1}{2(1-2\delta)} - \dfrac{3}{2}(1-2\delta), & (\delta \le 1/3) \end{cases} \tag{2.59}$$

v)**Ice-rule case 2-in-2-out**: Let site 1, 2 move toward *out* and others move toward *in*. The Eq. (2.50) becomes

$$\begin{aligned}
E_{\Delta(\mathrm{v})}/J &= (1-2\delta)\boldsymbol{S}_1\cdot\boldsymbol{S}_2 + (1+2\delta)\boldsymbol{S}_3\cdot\boldsymbol{S}_4 + (\boldsymbol{S}_1+\boldsymbol{S}_2)\cdot(\boldsymbol{S}_3+\boldsymbol{S}_4) - 2\epsilon\\
&= (1-2\delta)(\frac{1}{2}\boldsymbol{Y}^2 - 1) + (1+2\delta)(\frac{1}{2}\boldsymbol{Z}^2 - 1) + \boldsymbol{Y}\cdot\boldsymbol{Z} - 2\epsilon\\
&= -\left(\frac{1}{2(1+2\delta)} - \frac{1-2\delta}{2}\right)\boldsymbol{Y}^2 + \frac{1+2\delta}{2}\left(\boldsymbol{Z} + \frac{\boldsymbol{Y}}{1+2\delta}\right)^2 - 2 - 2\epsilon,
\end{aligned} \tag{2.60}$$

where $\boldsymbol{Y} = \boldsymbol{S}_1 + \boldsymbol{S}_2$ and $\boldsymbol{Z} = \boldsymbol{S}_3 + \boldsymbol{S}_4$. Note that the pre-factor of $\boldsymbol{Y}^2$ in the third line is negative for any δ, i.e. the first term takes the minimum value if $\boldsymbol{S}_1 = \boldsymbol{S}_2$. Thus the lowest energy is

$$E_{\min(\mathrm{v})}/J = -\frac{8\delta^2 + 4\delta + 2}{1+2\delta} - 2\epsilon \tag{2.61}$$

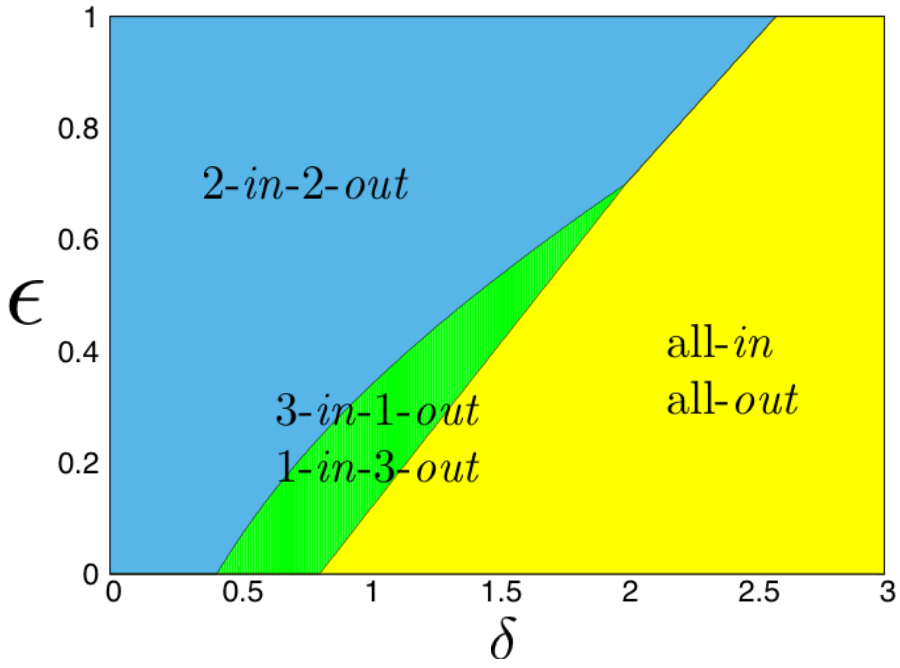

Figure 2.13: **Phase diagram of the ground state for each δ and ϵ**

and then the ground state configuration satisfies the conditions $\boldsymbol{S}_1+\boldsymbol{S}_2+(1+2\delta)(\boldsymbol{S}_3+\boldsymbol{S}_4)=0$ and $\boldsymbol{S}_1=\boldsymbol{S}_2$. Such a spin configuration can be expressed in general as,

$$\begin{aligned}
\boldsymbol{S}_1 &= (0,0,1),\\
\boldsymbol{S}_2 &= (0,0,1),\\
\boldsymbol{S}_3 &= \left(\frac{2\sqrt{\delta(1+\delta)}}{1+2\delta},0,-\frac{1}{1+2\delta}\right),\\
\boldsymbol{S}_4 &= \left(-\frac{2\sqrt{\delta(1+\delta)}}{1+2\delta},0,-\frac{1}{1+2\delta}\right).
\end{aligned} \tag{2.62}$$

In this case, there remains no continuous internal degrees of freedom in the ground state of single tetrahedron.

2.4.2 Low energy states of the total system

It is not clear whether the full pyrochlore system has a unique ground state if all tetrahedra satisfy the ice-rule. We comment on this shortly later. In order to explore the ground state of the full pyrochlore system for each δ and ϵ, we consider the three candidates of the ground state.

- **a) 2-*in*-2-*out***
  The first candidate is the system whose all tetrahedra are distorted into 2-*in*-2-*out* structures. We assume that the spin configurations of all tetrahedra satisfy the above condition. Then the lowest energy per a tetrahedron is

$$e_{2\text{-}2}=E_{\min(\mathrm{v})}/J=-\frac{8\delta^2+4\delta+2}{1+2\delta}-2\epsilon. \tag{2.63}$$

- **b) 3-*in*-1-*out* + 1-*in*-3-*out***
  We next consider the system whose the half of all tetrahedra are distorted into 3-*in*-1-*out* and the others

are distorted into 1-*in*-3-*out* structures. The two kinds of tetrahedra are alternatively connected. Thus the lowest energy per a tetrahedron is calculated as

$$\begin{aligned} e_{3\text{-}1} &= \frac{E_{\Delta(\mathrm{iii})}/J + E_{\Delta(\mathrm{iv})}/J}{2} \\ &= \begin{cases} -\dfrac{9\delta^2+6\delta+1}{1+2\delta}, & (\delta > 1/3), \\ \dfrac{6\delta^2-2}{(1+2\delta)(1-2\delta)}, & (\delta \le 1/3). \end{cases} \end{aligned} \tag{2.64}$$

- **c) all-*in* + all-*out***
  Another candidate is the system whose the half of all tetrahedra are distorted into all-*in* and the others are distorted into all-*out* structures. The two kinds of tetrahedra are also alternatively connected. Thus the lowest energy per a tetrahedron is calculated as

$$\begin{aligned} e_{4\text{-}0} &= \frac{E_{\Delta(\mathrm{i})}/J + E_{\Delta(\mathrm{ii})}/J}{2} \\ &= \begin{cases} 2-8\delta+6\epsilon, & (\delta > 1/2), \\ -2+6\epsilon, & (\delta \le 1/2). \end{cases} \end{aligned} \tag{2.65}$$

  Note that all-*in*/all-*out* structure has the long range order like a breathing pyrochlore structure [67].

Collecting the above results, we show the phase diagram of the ground state for each δ and ϵ in Fig. 2.13. At low δ there is only the 2-*in*-2-*out* phase for any ϵ. The 3-*in*-1-*out*-1-*in*-3-*out* phase appears at $\delta = -1+\sqrt{2}$ and the all-*in*-all-*out* phase appears at $\delta = (1+\sqrt{22})/7$. The 3-*in*-1-*out*-1-*in*-3-*out* phase is vanished at $\delta = 2, \epsilon = 0.7$. While b) and c) are periodic structures, a) may not be so. The spin structure (Eq. (2.62)) cannot be simply periodically. Indeed we will find that generic low energy configuration with 2-*in*-2-*out* structure is disordered as we discuss in the next section. In this respect the phase diagram in Fig. 2.13 is not accurate.

2.5 Complex energy landscape of our effective model

Our effective model (Eq. (2.2)) starts from the two ingredients on the same pyrochlore lattice: antiferromagnetic Heisenberg model for the magnetic moments plus spin-ice model for the lattice distortions. The antiferromagnetic Heisenberg model without the lattice distortions exhibit ground states that have a continuous degeneracy. The lattice distortions without spins put on exhibit ground states compatible with the ice-rule that have also macroscopic degeneracy. Hence, both spins and distortions without coupling ($\delta = 0$) remain liquid states even at $T = 0$.

Once we switch on the coupling $\delta > 0$, we expect that each degree of freedom plays a role of randomness for each other and a glass state can be realized. If this is the case, then the degeneracy of the energy landscape should be removed and the landscape is modified to a complex landscape where the hight of energy minima has a large variance (see Fig. 2.14 (a)). In this section, we numerically verify the above picture by brief Monte Carlo simulations.

We wish to clarify that the variance of energy minima grows with the system size as $O(N^\alpha)$ ($\alpha > 0$). In order to check this, we performed a numerical simulation which consists of the following steps (For the details of the simulation method please refere to the next chapter.):

1. **Preparation of lattice-ice** First we prepare ice configurations of distortions, by quenching the system using only the second term of Eq. (2.2) from $T = \infty$ to $T = 0$. More precisely, we took totally random distortion configurations $\{\boldsymbol{\sigma}_i\}$ as the initial distortion configurations and performed Monte Carlo simulations at $T = 0$: each distortion flip is accepted only if it lowers the energy of the system.

2. **Search for energy minima on the lattice-ice** Next we quenched the spins following only the first term of Eq. (2.2) with the quenched ice configuration of distortions made above. More precisely, we took totally random spin configurations $\{\boldsymbol{S}_i\}$ as the initial spin configuration and performed Monte Carlo simulations at $T = 0$.

In the second step, we performed 100×2^{15} Monte Carlo steps where a unit Monte Carlo step consists of single spin flips for all spins by the Metropolis reflection method and we observed the energy of spins E at final states. We obtained 30 ice configurations of distortions and performed 30 statistically independent runs of spin quenching for each ice configuration of distortions, i.e. 30×30 runs in total. Now, let us consider two kinds of variances defined as,

$$V_{\text{spin}}(E) = \overline{\langle E^2 \rangle - \langle E \rangle^2}, \tag{2.66}$$

$$V_{\text{lattice}}(E) = \overline{\langle E \rangle^2} - \overline{\langle E \rangle}^2, \tag{2.67}$$

where $\overline{\cdots}$ and $\langle \cdots \rangle$ represents averages for 30 ice configurations and 30 independent runs for each ice configurations, respectively. $V_{\text{spin}}(E)$ is related to the change of the spin energy landscape from the flat one for $\delta = 0$ and $V_{\text{lattice}}(E)$ is related to the change of the distortion energy landscape.

Fig. 2.14 (b) and (c) show the system size L dependence of $V_{\text{spin}}(E)$ and $V_{\text{lattice}}(E)$. Both variances monotonically increase with system size L and look depending linearly on L, i.e. they are in the order of $O(N^{1/3})$. These results strongly suggests that the energy landscape becomes complex in the presence of the coupling $\delta > 0$.

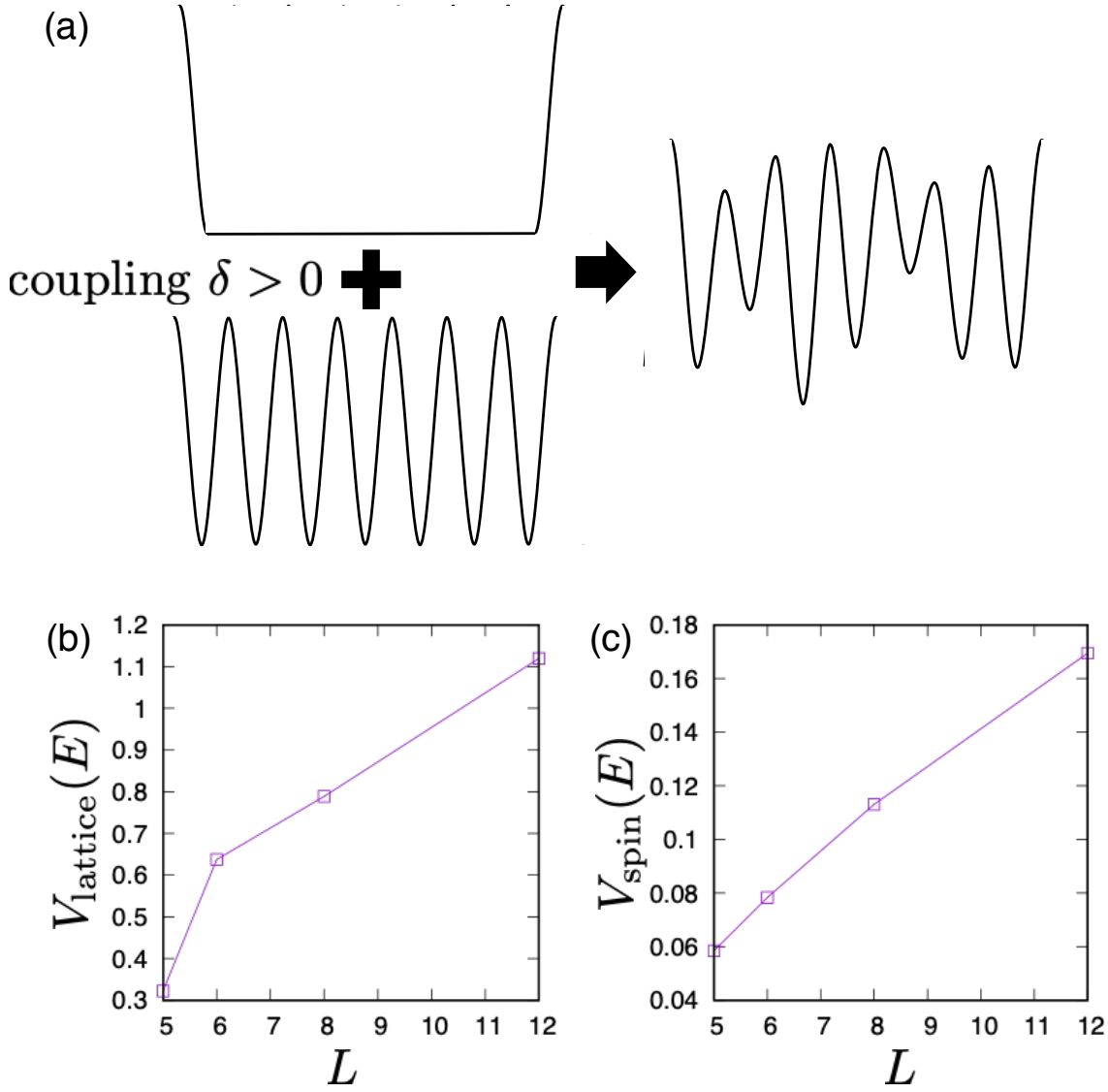

Figure 2.14: **Complex energy landscape of our effective model**
(a): Schematic picture of the energy landscape of our effective model (right) obtained by combining a flat spin energy landscape (left top) and a zigzag but degenerate distortion landscape (left bottom). (b): System size L dependence of $V_{\text{spin}}(E)$ which quantifies the fluctuation of the energy between different energy minima with a common lattice-ice configuration. (c): System size L dependence of $V_{\text{lattice}}(E)$ which quantifies fluctuation of the energy between difference lattice-ice configurations.

Chapter 3

NUMERICAL SIMULATION

In this chapter we study the dynamical and static properties of our effective model by extensive Monte Carlo (MC) simulations focusing on the possibility of the glass transitions. In the following we first explain the method of our MC simulations (Sec. 3.2), the physical observables we study (sec Sec. 3.3). We present our numerical results in Sec. 3.4 and discussions in Sec. 3.5.

3.1 System

We use pyrochlore lattice of size L with periodic boundary condition along all directions. Here L is measuared by the length of the cubic unit cell (see Fig. 1.7 (b:right bottom))

3.2 Method of Monte Carlo simulations

In this section, we explain the method which I used for Monte Carlo simulation. Since it is likely to become harder to equilibrate our system at lower temperatures where we expect glassy behaviors, we adopted various methods in addition to the conventional single-spin-flip method.

3.2.1 Algorithms

3.2.1.1 loop update method

It is hard to sample equilibrium configurations of the ice-type system at low temperatures due to multiple energy minima separated by energy barriers. To overcome this, we adopted a nonlocal update method called the loop update algorithm [68] which goes as follows.

1. Select a loop composed only of *in-out* bonds by constructing a *in-out* chain starting from a randomly chosen initial point and stopping when it overlaps with itself.

2. flip all the lattice distortions $\{\sigma_i\}$ along the loop simultaneously with the acceptance rate determined by the Metropolis rule.

Note that the energy contributed by the second term of the Hamiltonian (Eq. (2.2)) is unchanged in this update because all tetrahedra where the loop passes remain in the 2-*in*-2-*out* structures, while the effective exchange interactions $J_{\boldsymbol{\sigma}_i,\boldsymbol{\sigma}_j}$ in the first term of the Hamiltonian (Eq. (2.2)) are changed. Fig. 3.1 shows an example which is the shortest loop composed of six *in-out* bonds of 2-*in*-2-*out* tetrahedra. If we flip all σ_i $(i = 1, 2, ...)$ along the loop, all tetrahedra still satisfy the ice-rule. Let $\boldsymbol{\sigma}'_i = -\boldsymbol{\sigma}_i$. Using Eq. (2.4), the

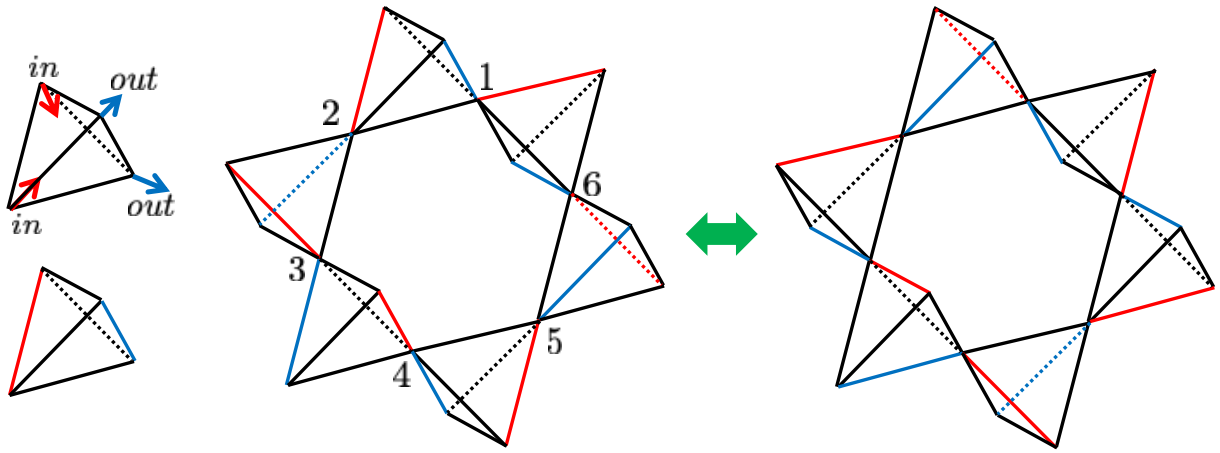

Figure 3.1: **An example of the loop update**
Red and blue bonds correspond to *in-in* and *out-out* bonds, respectively. Two hexagonal loops are composed of only *in-out* bonds of 2-*in*-2-*out* structures. If we flip all the lattice distortions on the left loop simultaneously, the configuration is changed to the one on the right hand side.

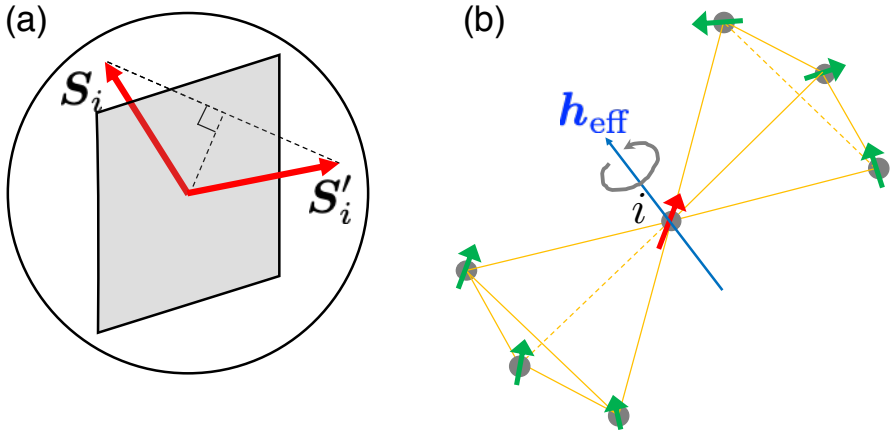

Figure 3.2: **Schematic pictures of metropolis reflection (a) and over relaxation updates (b)**

energy change is obtained as,

$$\begin{aligned}\Delta E &= \frac{1}{2}\sum_{i=1}^{6}\sum_{j\in\partial i}\left(J_{\boldsymbol{\sigma}'_i,\boldsymbol{\sigma}'_j} - J_{\boldsymbol{\sigma}_i,\boldsymbol{\sigma}_j}\right)\boldsymbol{S}_i\cdot\boldsymbol{S}_j \\ &= -J\delta\sum_{i=1}^{6}\sum_{j\in\partial i}(\hat{\boldsymbol{r}}_{ij}\cdot\boldsymbol{\sigma}_i)\boldsymbol{S}_i\cdot\boldsymbol{S}_j, \end{aligned} \tag{3.1}$$

where ∂i represents the set of nearest neighbors around the site i. It can be seen that the energy change is independent of the elastic energy scale ϵ. Therefore, the loop update algorithm can accelerate the equilibration when ϵ is large.

3.2.1.2 Metropolis reflection method

For updating Heisenberg spins $\boldsymbol{S}_i$, we used the Metropolis Reflection method [69]. In the Metropolis Reflection method, we first prepare a plane dividing the spin space into two equal parts. The orientation of the plane

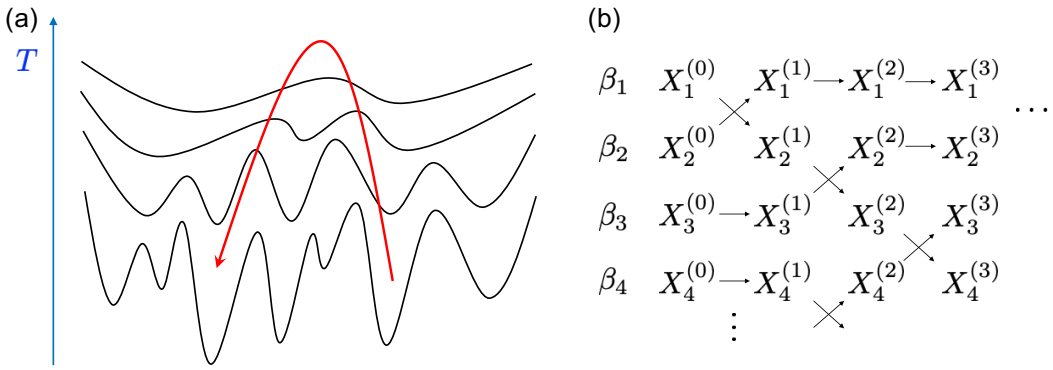

Figure 3.3: **Replica exchange method**
(a): Schematic picture of the free-energy landscape for the replica exchange method. (b): A diagram of exchanges of the spin configurations between replicas at different inverse temperatures.

is chosen randomly. To update a spin $\boldsymbol{S}_i$, a new candidate spin configuration $\boldsymbol{S}_i'$ is created by reflecting $\boldsymbol{S}_i$ by the plane (see Fig. 3.2 (a)). More precisely the sign of the perpendicular component to plane is changed. The reflection is performed with probability determined by the Metropolis rule. In a unit Monte Carlo step (MCS), we try the updates for all spins $\boldsymbol{S}_i$ $(i = 1, 2, 3, ..., N)$ using the same plane. The reflection plane is renewed afterwards.

3.2.1.3 Over relaxation method

We also used the over relaxation method to update the Heisenberg spins. [70] In the over relaxation method, we first calculate the effective magnetic field

$$\boldsymbol{h}_{\text{eff}} = \sum_{j \in \partial i} J_{\boldsymbol{\sigma}_i, \boldsymbol{\sigma}_j} \boldsymbol{S}_j \tag{3.2}$$

on a spin $\boldsymbol{S}_i$, and then rotate the spin around $\boldsymbol{h}_{\text{eff}}$ by an angle of π (see Fig. 3.2 (b)). Note that the energy is not changed by this transformation, i.e. the update is always accepted.

3.2.1.4 Replica exchange method

Definition

Replica exchange method [71] is a useful algorithm and widely used in glassy systems where it is difficult to do sampling the equilibrium states efficiently because of their complicates free-energy landscapes (see Fig. 3.3 (a)). In this method, one considered an extensive ensemble at multiple working temperatures. By allowing the system to explore states at different working temperatures, the equilibration becomes faster. For instance as shown schematically in Fig. 3.3 (a), the system can visit free-energy minima separated by high energy barriers by going to higher temperatures where the landscape is much simpler.

We consider a system of M independent replicas. Let X_m $(m = 1, 2, 3, ..., M)$ specify the spin configuration of m-th replica which obey the common Hamiltonian $H(X_m)$. We prepare a set of M different inverse working temperatures $\beta_1 < \beta_2 < ... < \beta_M$ for replicas $m = 1, 2, ..., M$. The partition function of the extended ensemble is given by,

$$Z = \text{Tr}_{\{X\}} \exp\left(- \sum_{m=1}^{M} \beta_m H(X_m) \right) = \prod_{m=1}^{M} Z(\beta_m), \tag{3.3}$$

where $Z(\beta_m)$ is one for a system at β_m. The probability distribution of the extended system becomes

$$P(X_1, \beta_1; X_2, \beta_2; \cdots; X_M, \beta_M) = \prod_{m=1}^{M} P_{\rm eq}(X_m, \beta_m), \tag{3.4}$$

where

$$P_{\rm eq}(X_m, \beta_m) = \frac{e^{-\beta_m H(X_m)}}{Z(\beta_m)}. \tag{3.5}$$

The replica exchange process goes as follows. Let us consider a trial to exchange configurations X and X' between replicas at nearby inverse temperatures β_m and β_{m+1}. We assume the probability of the exchanging configurations of the m-th and $(m+1)$-th replicas $W(X, \beta_m | X', \beta_{m+1})$ satisfy the detailed balance condition,

$$P(\cdots; X, \beta_m; X', \beta_{m+1}; \cdots) W(X, \beta_m | X', \beta_{m+1}) = P(\cdots; X', \beta_m; X, \beta_{m+1}; \cdots) W(X', \beta_m | X, \beta_{m+1}). \tag{3.6}$$

From Eq. (3.5) we obtain

$$\frac{W(X_m, \beta_m | X_{m+1}, \beta_{m+1})}{W(X_{m+1}, \beta_m | X_m, \beta_{m+1})} = \exp(-\Delta) \tag{3.7}$$

with

$$\Delta = (\beta_{m+1} - \beta_m)(H(X_m) - H(X_{m+1})). \tag{3.8}$$

Adopting the Metropolis rule, the transition probability can be defined as

$$W(X_m, \beta_m | X_{m+1}, \beta_{m+1}) = \begin{cases} 1 & \text{for } \Delta < 0 \\ \exp(-\Delta) & \text{for } \Delta > 0. \end{cases} \tag{3.9}$$

In our work, the procedure of the replica exchange method consists of the following two steps:

1. Each replica is simulated simultaneously and independently for $t_{\rm ex} = 15$ Monte Carlo using other algorithms (see Sec. 3.2.2 for the precise schedule).

2. Make a trial to exchange two configurations X_m and X_{m+1} with the probability $W(X_m, \beta_m | X_{m+1}, \beta_{m+1})$ for $m = 2n - 1$ $(n = 1, 2, ..., M/2)$ if the total Monte Carlo step satisfies $(t \mod 2t_{\rm ex}) = t_{\rm ex}$, for $m = 2n$ $(n = 1, 2, ..., M/2 - 1)$ if $(t \mod 2t_{\rm ex}) = 0$ (see Fig. 3.3 (b)).

We repeat this procedure 1 and 2.

How to design the working temperatures

An important issue is how we determine the temperature set $\{\beta\}$ because the replica exchange will not work efficiently if we do not choose them appropriately. First, we should fix the highest temperature $T_{\rm max} = 1/\beta_1$ which is much higher than the transition point and the lowest temperature $T_{\rm min} = 1/\beta_M$ down to which we desire to equilibrate the system. Next, we select the intervals between neighboring temperatures. The candidate of a suitable temperature set is that all acceptance rates are equal, i.e. $(\beta_{m+1} - \beta_m)(E_m - E_{m+1})$ is independent of m. [72] In order to obtain such a temperature set, we impose a condition,

$$(\beta_{m+1} - \beta_m)(E_m - E_{m+1}) = (\beta_m - \beta_{m-1})(E_{m-1} - E_m) \tag{3.10}$$

whose solution is given as,

$$\beta_m = g(\beta_m) = \frac{1}{E_{m-1} - E_{m+1}} [\beta_{m-1} E_{m-1} - \beta_{m+1} E_{m+1} - E_m(\beta_{m-1} - \beta_{m+1})]. \tag{3.11}$$

Therefore, we obtain a recursion formula,

$$\beta_m(l+1) = \frac{1}{2}[\beta_m(l) + g(\beta_m(l))], \tag{3.12}$$

where l is the iteration step.

In our work, the procedure of updating the temperature set goes as the following:

1. Perform MC simulation for $t_{\rm it} = 1500$ Monte Carlo steps using the replica exchange Monte Carlo and taking the Monte Carlo averages of energy E_m for all m.

2. Update the inverse temperatures β_m using above formula (Eq. (3.11) and Eq. (3.12)) using E_m obtained above for $m = 2n-1$ $(n = 2, ..., M/2)$ if the total Monte Carlo step satisfies $(t \mod 2t_{\rm it}) = t_{\rm it}$, for $m = 2n$ $(n = 1, 2, ..., M/2-1)$ if $(t \mod 2t_{\rm it}) = 0$.

The initial temperature set is defined as a geometric sequence such that

$$\beta_m = \gamma^{m-1}\beta_1 \text{ with } \gamma = \left[\frac{\beta_M}{\beta_1}\right]^{\frac{1}{M-1}}. \tag{3.13}$$

This initial temperature set makes all acceptance rate be equal if the specific heat doesn't depend on the temperature.

3.2.2 Schedule of Monte Carlo simulation

3.2.2.1 Unit Monte Carlo step

A unit Monte Carlo step for equilibration and observation of static quantities consists of the following steps.

1. Perform a sequential single-spin flip for all lattice distortions $\boldsymbol{\sigma}_i$ $(i = 1, 2, ..., N)$ by the conventional Metropolis method.

2. Perform loop updates L times for lattice distortions.

3. Compute coupling constants $J_{\boldsymbol{\sigma}_i, \boldsymbol{\sigma}_j}$.

4. Perform a sequential spin flip for once for all Heisenberg spins $\boldsymbol{S}_i$ $(i = 1, 2, ..., N)$ by the Metropolis Reflection method.

5. Perform sequential spin flips L times for all Heisenberg spins $\boldsymbol{S}_i$ $(i = 1, 2, ..., N)$ by the over-relaxation method.

Here L is the system size defined in Sec. 2.1.

3.2.2.2 Equilibration

To prepare equilibrated systems we used the replica exchange method on top of the other methods.[71, 72] We prepared 48 replicas for $L = 4, 5, 6$ and 72 replicas for $L = 8$. We determined the maximum temperature and the minimum temperature as $T_{\rm max} = 0.400$ and $T_{\rm min} = 0.0625$ respectively. We optimized the temperature set so that the exchange rate is independent of T as explained in Sec. 3.2.1.4 [72]. We performed the trial to exchange the replicas with the interval of 15 (MCS). In every Monte Carlo step the procedures listed in Sec. 3.2.2.1 are done. Initial spin and lattice configuration for each replica were prepared as fully random configurations. The Monte Carlo steps for thermalization is 3.0×10^7 (MCS) for all system sizes we used in this study. We checked equilibration by performing longer simulations. Observations of physical quantities are made during the subsequent 3.0×10^7 (MCS) to evaluate their thermal averages $\langle ... \rangle_{\rm eq}$ by the time averages. We performed 120 statistically independent runs and estimated mean-squared errors of the physical quantities.

3.2.2.3 Simulation to observe relaxational dynamics

To study relaxational dynamics in equilibrium, the initial configurations ($t = 0$ (MCS)) are created by the above equilibration scheme (see Sec. 3.2.2.2). In order to observe the natural time evolution of the system, we apply only the sequential single-spin flip for spin and distortion degrees of freedom. In this case a unit MCS consists of the following steps.

1. Perform a sequential single-spin flip for all lattice distortions σ_i $(i = 1, 2, ..., N)$ by the conventional Metropolis method.
2. Compute coupling constants $J_{\boldsymbol{\sigma}_i, \boldsymbol{\sigma}_j}$.
3. Perform a sequential spin flip for once for all Heisenberg spins $\boldsymbol{S}_i$ $(i = 1, 2, ..., N)$ by the Metropolis Reflection method.

We performed 120 statistically independent runs and estimated mean-squared errors of the physical quantities.

3.3 Physical observables

In this section, we introduce physical observables which we investigate by Monte Carlo simulations and some other related physical quantities.

3.3.1 Dynamical quantities

Auto-correlation function

To investigate the dynamics of the spins and distortions, we examined the auto-correlation functions,

$$C_s(t) = \frac{1}{N}\sum_{i=1}^{N} \langle \boldsymbol{S}_i(t) \cdot \boldsymbol{S}_i(0) \rangle_{\rm eq}\,, \tag{3.14}$$

$$C_\sigma(t) = \frac{1}{N}\sum_{i=1}^{N} \langle \boldsymbol{\sigma}_i(t) \cdot \boldsymbol{\sigma}_i(0) \rangle_{\rm eq}\,, \tag{3.15}$$

where $\boldsymbol{S}_i(t)$ and $\boldsymbol{\sigma}_i(t)$ are the spin and distortion at site i at time t. Here time t is measured in the unit of a Monte Carlo step (MCS). Here the brackets $\langle \cdots \rangle_{\rm eq}$ means to take thermal averages. Note that time 0 in equilibrium can be taken arbitrary since the time translational invariance holds for the two-time quantities such as the auto-correlation functions. In practice, we implement the average $\langle \cdots \rangle_{\rm eq}$ for the equilibrium auto-correlation functions as averages over statistically independent Monte Carlo runs performed in equilibrium. Because of the normalization of the spins $|\mathbf{S}_i(t)| = 1$ and the distortion $|\boldsymbol{\sigma}_i(t)| = 1$, $C_s(0) = C_\sigma(0) = 1$. Because of thermal fluctuations we naturally expect it decays with time t. In the large time limit we can write

$$\lim_{t\to\infty} C_s(t) = \frac{1}{N}\langle \boldsymbol{S}_i \rangle_{\rm eq}^2\,, \tag{3.16}$$

$$\lim_{t\to\infty} C_\sigma(t) = \frac{1}{N}\langle \boldsymbol{\sigma}_i \rangle_{\rm eq}^2\,. \tag{3.17}$$

Note that these are nothing but the Edwards-Anderson (EA) order parameters $q_{\rm EA}$ (see Eq. (1.4)-Eq. (1.6)) for the spin and the corresponding one for the distortion.

At high enough temperatures we naturally expect spins and distortions are disordered so that these EA parameters are zero. Thus the autocorrelation functions should decay down to 0 after some relaxation time (see below). In the glass phases, if they exist, these parameters should become non-zero signaling ergodicity breaking.

Relaxation time

We define the relaxation times $\tau_s(T)$ and $\tau_\sigma(T)$ for each degree of freedom as the timescale such that the auto-correlation functions decrease down to 0.5. If some second order glass transition takes place at a finite temperature $T_{\rm c}$, the critical slowing down should be observed, i.e. τ diverges at $T_{\rm c}$ with power law,

$$\tau = A(T - T_{\rm c})^{-z\nu}. \tag{3.18}$$

where z and ν are critical exponents. The exponent z relates the relaxation time with the spacial correlation length ξ of thermal fluctuation as (Eq. (1.26))

$$\tau \sim \xi^z. \tag{3.19}$$

The exponent ν describes the divergence of the correlation length (Eq. (1.25))

$$\xi \sim |T - T_{\rm c}|^{-\nu}. \tag{3.20}$$

3.3.2 Static quantities

Here we list static quantities we analyze by Monte Carlo simulations.

Structure factor

The static-structure factors of spins and lattice distortions are defined respectively as

$$S_s(\boldsymbol{k}) = \left\langle \frac{1}{N} \left| \sum_{i=1}^{N} e^{-i\boldsymbol{k}\cdot\boldsymbol{r}_i} \boldsymbol{S}_1 \cdot \boldsymbol{S}_i \right| \right\rangle_{\rm eq}, \tag{3.21}$$

$$S_\sigma^{(1)}(\boldsymbol{k}) = \left\langle \frac{1}{N} \left| \sum_{i=1}^{N} e^{-i\boldsymbol{k}\cdot\boldsymbol{r}_i} \sigma_1 \sigma_i \right| \right\rangle_{\rm eq}, \tag{3.22}$$

$$S_\sigma^{(2)}(\boldsymbol{k}) = \left\langle \frac{1}{4N} \left| \sum_{i=1}^{4} \sum_{j=1}^{N} e^{-i\boldsymbol{k}\cdot(\boldsymbol{r}_j - \boldsymbol{r}_i)} \boldsymbol{\sigma}_i \cdot \boldsymbol{\sigma}_j \right| \right\rangle_{\rm eq}, \tag{3.23}$$

where $\boldsymbol{k} = (k_x, k_y, k_z) = \pi/2L(n_1, n_2, n_3)$, $(n_1, n_2, n_3 = -2L, -2L+1, ..., 2L-1, 2L)$ is the wave vector. The brackets $\langle \cdots \rangle_{\rm eq}$ which appear here and below mean to take both time averages and averages over statistically independent MC runs. The last one $S^(2)_\sigma(\boldsymbol{k})$ is useful to compare our result with previous results obtained in spin-ice systems.

Heat capacity

The heat capacity is defined as

$$C = \frac{\beta^2}{N} \Big(\langle E^2 \rangle_{\rm eq} - \langle E \rangle_{\rm eq}^2 \Big), \tag{3.24}$$

where E is the value of the energy (Hamiltonian) defined in Eq. (2.2).

Fraction of 2-*in*-2-*out* structures

The fraction of the 2-*in*-2-*out* structures is defined as,

$$P = \frac{N_{\text{2-in-2-out}}}{8L^3} \tag{3.25}$$

where $N_{\text{2-in-2-out}}$ represent the number of tetrahedra which are distorted into 2-*in*-2-*out* structures. $8L^3$ is the total number of tetrahedra in the whole system.

Nonlinear susceptibilities

If the putative glass transitions of the spins and distortions take place via 2nd order transitions, they should lead to divergence of non-linear susceptibilities. Thus we introduce two non-linear susceptibilities.

- **magnetic nonlinear susceptibility**

  One is the nonlinear magnetic susceptibility (Eq. (1.37)),

$$\chi_3 = \frac{1}{3} \sum_\mu \left. \frac{\partial^3 \langle m_\mu \rangle_{\rm eq}}{\partial h_\mu^3} \right|_{h_\mu \to 0}, \tag{3.26}$$

where

$$m_\mu = \frac{1}{N}\sum_{i=1}^{N} S_{i\mu} \tag{3.27}$$

and h_μ are the magnetization and the magnetic field, respectively, in the μ-direction ($\mu = x, y, z$). From fluctuation formulae, we can rewrite the nonlinear susceptibility by the 4th order cumulant of the magnetization as,

$$\chi_3 = \frac{\beta^3 N^3}{3}\sum_{\mu}\Big(\langle m_\mu^4\rangle_{\rm eq} - 4\langle m_\mu\rangle_{\rm eq}\langle m_\mu^3\rangle_{\rm eq} - 3\langle m_\mu^2\rangle_{\rm eq}^2 + 12\langle m_\mu^2\rangle_{\rm eq}\langle m_\mu\rangle_{\rm eq}^2 - 6\langle m_\mu\rangle_{\rm eq}^4\Big). \tag{3.28}$$

Within our Monte Carlo simulations of finite sized systems at temperatures higher than the glass transition temperature $T_{\rm c}$, odd order moments of the magnetization vanish due to the rotational symmetry, e.g. $\langle m_\mu\rangle_{\rm eq} = \langle m_\mu^3\rangle_{\rm eq} = 0$. Hence we can evaluate simply it as,

$$\chi_3 = \frac{\beta^3 N^3}{3}\sum_{\mu}\Big(\langle m_\mu^4\rangle_{\rm eq} - 3\langle m_\mu^2\rangle_{\rm eq}^2\Big). \tag{3.29}$$

Note that this is not valid below $T_{\rm c}$.

- **dielectric nonlinear susceptibility**

  The other is related to distortions. Note that distortions of the Mo ions should induce electric polarization. Thus we may describe the system in the presence of an electric field E_ν along μ-direction as,

$$H = H_0 - E_\nu p_\nu \tag{3.30}$$

  where H_0 is the Hamiltonian in the absence of the electric field as,

$$p_\nu = \frac{1}{N}\sum_{i=1}^{N} \boldsymbol{\sigma}_i \cdot \hat{\boldsymbol{e}}_\nu \tag{3.31}$$

  is the electric polarization into ν direction. Then similarly to the magnetic case, we can naturally introduce dielectric linear susceptibility as

$$\chi^\sigma = \frac{1}{4}\sum_{\nu}\left.\frac{\partial\langle p_\nu\rangle_{\rm eq}}{\partial E_\nu}\right|_{E_\nu\to 0}, \tag{3.32}$$

  and nonlinear susceptibility as

$$\chi_3^\sigma = \frac{1}{4}\sum_{\nu}\left.\frac{\partial^3\langle p_\nu\rangle_{\rm eq}}{\partial E_\nu^3}\right|_{E_\nu\to 0}. \tag{3.33}$$

  In the same manner as the magnetic case, the nonlinear susceptibility can be rewritten for $T > T_{\rm c}$ as,

$$\chi_3^{(\sigma)} = \frac{\beta^3 N^3}{4}\sum_{\nu}\Big(\langle p_\nu^4\rangle_{\rm eq} - 3\langle p_\nu^2\rangle_{\rm eq}^2\Big). \tag{3.34}$$

The two nonlinear susceptibilities are measurable in laboratories and allow a direct comparison between theories and experiments.

In conventional theoretical and numerical studies [73, 74], one often analyzes the spin glass susceptibility (see Eq. (1.36)), $\chi_{\rm SG}$ (see Eq. (1.38)), which is proportional to χ_3. Although $\chi_{\rm SG}$ is much easier to calculate with better accuracy in the presence of quenched disorder by using the overlap between two independent replicas, it is not convenient for our model, since the Hamiltonian is translationally invariant so that the replicas usually do not overlap.

3.4 Simulation results

Now, we show the result of our extensive Monte Carlo simulation. Here we limit ourselves with $\delta = 1.5$, by which the variation of the effective coupling under lattice distortion become comparable with the result we obtained by the microscopic computation performed as we noted in the end of Sec. 2.3.3.3.

3.4.1 Analysis of the relaxational dynamics

Let us first discuss the result of dynamical observables. We show the result for $\epsilon = 0.6$ and $\epsilon = 0.65$, where the ground state of a single tetrahedron takes the 2-*in*-2*out* lattice structure for $\delta = 1.5$ (see Fig. 2.13).

Auto-correlation function

The behavior of the spin and distortion auto-correlation functions are shown in Fig. 3.4 (a) and Fig. 3.4 (b). It can be seen that the time correlation of each degree of freedom decays with time reflecting the relaxation but the time scale becomes larger by lowering temperatures, which indicates the slowing down of the dynamics.

Relaxation time

As a quantitative measure of dynamics, we extracted $\tau_s(T)$ and $\tau_\sigma(T)$ independently using the least squares method, and obtained results as shown in Fig. 3.4 (c) and Fig. 3.4 (d). Remarkably, both relaxation times tend to diverge at the same temperature $T_c \approx 0.07$ with different exponents, $(z\nu)_s = 2.79(12)$ and $(z\nu)_\sigma = 3.55(4)$. This suggests that spin and orbital undergo phase transitions simultaneously. We checked that there is no finite size effect within the time scale which we analyzed. Fig. 3.4 (e) and Fig. 3.4 (f) we show the scaling plots of auto-correlation functions assuming a scaling form,

$$C(t,T) = \tilde{C}\left(\frac{t}{\tau(T)}\right), \tag{3.35}$$

which is clearly satisfied. The scaling functions turns out to be well fitted by simple exponentials except for the initial part. We note that the relaxation function in the Edwards-Anderson models in the paramagnetic phase is more complicated [26, 75] presumably due to Griffith singularity [76].

ϵ dependence of the dynamical observables

We performed the same analyses for $\epsilon = 0.65$, as shown in Fig. 3.5, the data suggest again a simultaneous glass transitions at $T_c \approx 0.086$. Notably, the exponents $z\nu$ agree with those obtained at $\epsilon = 0.6$ within the numerical accuracy, suggesting a universality. We also show the data of auto-correlation functions for larger ϵ ($\epsilon = 1.2$) in Fig. 3.6. Unfortunately we do not have data of relaxational dynamics in the vicinity of the glass transition temperature at lager ϵ because the dynamics of distortions become too slow to analyze within computationally feasible time scales.

Other scenarios

For clarify let us consider other scenarios.

- **Activated dynamics**

  In this scenario the relaxation time follows the Arrhenius law,

$$\tau = B \exp\left(\frac{E_b}{T}\right), \tag{3.36}$$

where E_b is the typical height of the energy barrier on the activation process. Fig. 3.7 show the Arrhenius plots of the relaxation times $\tau_s(T)$ and $\tau_\sigma(T)$ and the plots tend to be shifted slightly above the Arrhenius law with $B = 25$, $E_\mathrm{b} = 0.77$ for spins and $B = 45$, $E_\mathrm{b} = 0.98$ for lattice distortions. From the plots it can be seen that the relaxation is apparently slower than the Arrhenius law.

- **Power law scaling with $T_\mathrm{c} = 0$**

  In this scenario we assume

  $$\tau = AT^{-z\nu}. \tag{3.37}$$

  We display the double logarithmic plots of the relaxation times $\tau_s(T)$ and $\tau_\sigma(T)$ for $\epsilon = 0.6$ and $\epsilon = 0.65$ in Fig. 3.8. It can be seen that each exponent depends on ϵ. Hence, the exponents become non-universal in this scenario.

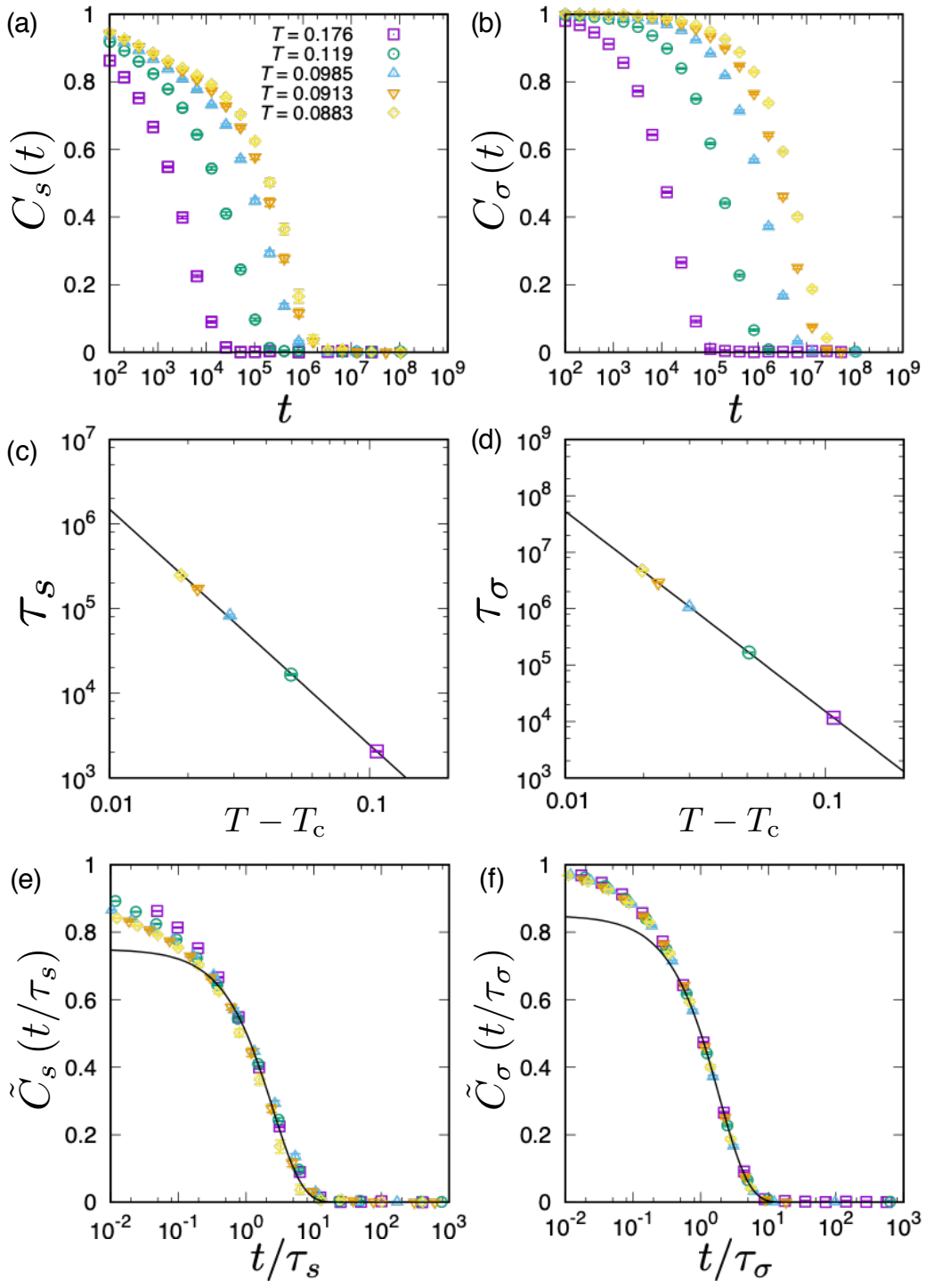

Figure 3.4: **Relaxation of spins and distortions for** $L = 6, \epsilon = 0.6$
(a): Spin auto-correlation function. (b): Orbital auto-correlation function. (c): Typical relaxation time of spins. (d): Typical relaxation time of distortions. The black solid lines in the figure (b) and (d) denote the fits by $\tau = A(T - T_c)^{-z\nu}$ with $(A, T_c, z\nu)_s = (3.99(89), 0.0695(19), 2.79(12))$ and $(A, T_c, z\nu)_\sigma = (4.27(31), 0.0686(5), 3.55(4))$ by using the least squares method. (e), (f): Scaling plots of auto-correlation functions using their relaxation times. The solid lines represent the exponential fits.

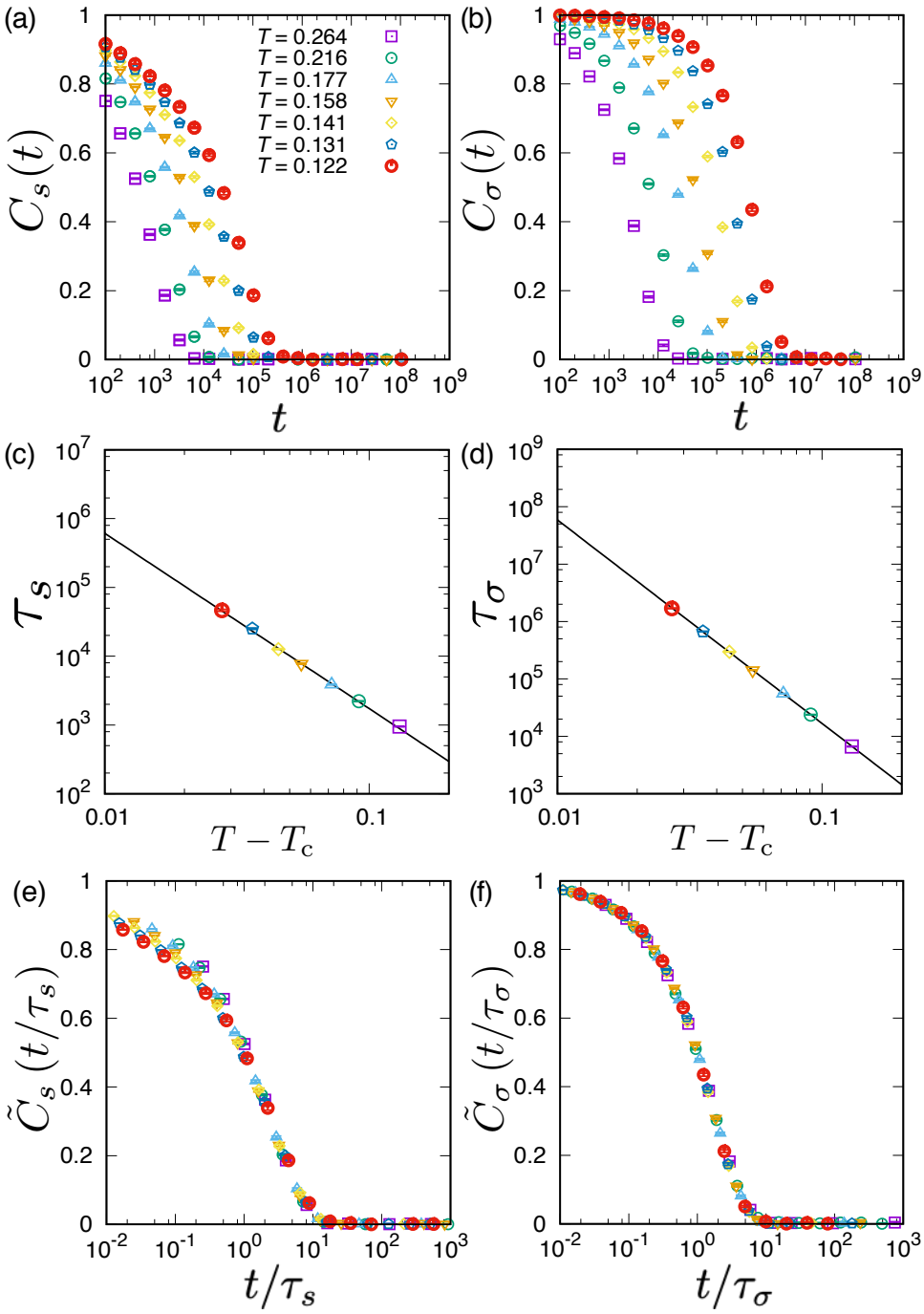

Figure 3.5: **Relaxation of spins and distortions for** $L = 5,\ \epsilon = 0.65$
(a): Spin auto-correlation function. (b): Distortion auto-correlation function. (c): Typical relaxation time of spins. (d): Typical relaxation time of distortions. The black lines in the figure (a) and (b) denote the fits by $\tau = A(T - T_c)^{-z\nu}$ with $(A, T_c, z\nu)_s = (4.91(154), 0.0855(26), 2.55(15))$ and $(A, T_c, z\nu)_\sigma = (4.78(21), 0.0862(5), 3.54(3))$ by using the least squares method. (e), (f): Scaling plots of spin and distortion auto-correlation function, respectively.

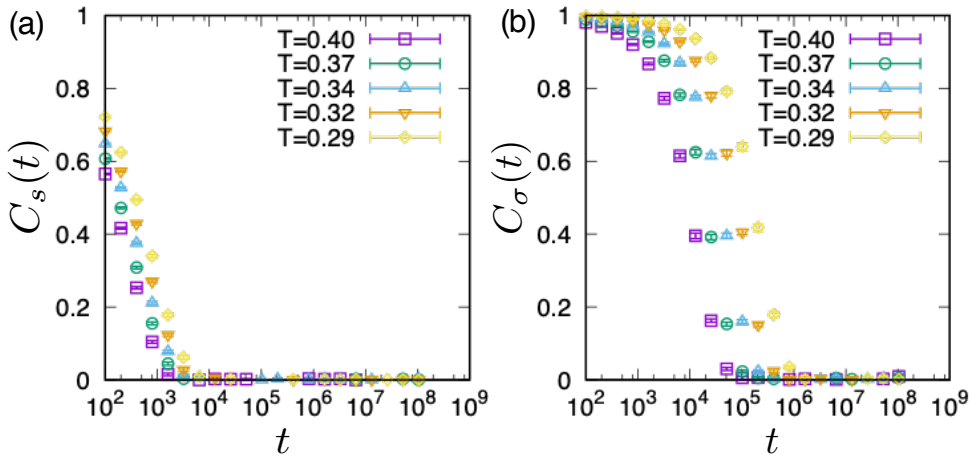

Figure 3.6: **Relaxation of spins and distortions for** $L = 5,\ \epsilon = 1.20$
(a): Spin auto-correlation function. (b): Distortion auto-correlation function.

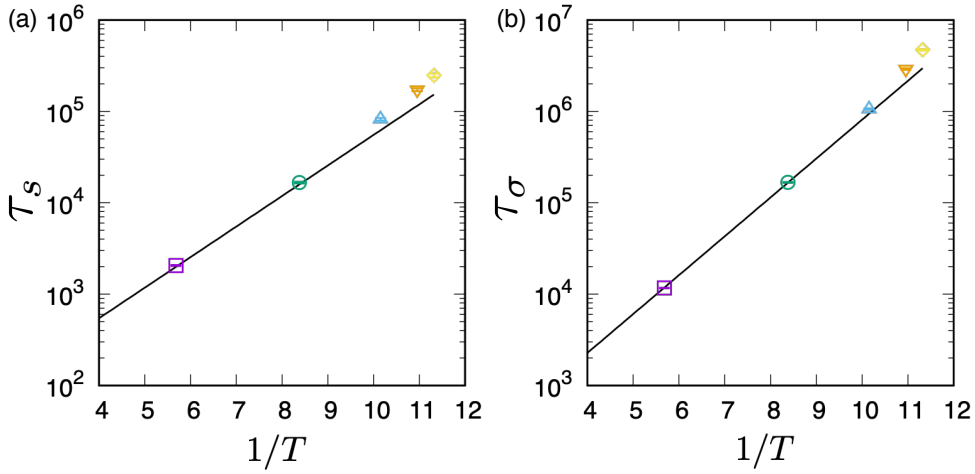

Figure 3.7: **Arrhenius plots of typical relaxation times** $\tau_s(T)$ **(a) and** $\tau_\sigma(T)$ **(b) for** $L = 6,\ \epsilon = 0.60$
The black lines in the figure (a) and (b) denote the Arrhenius law.

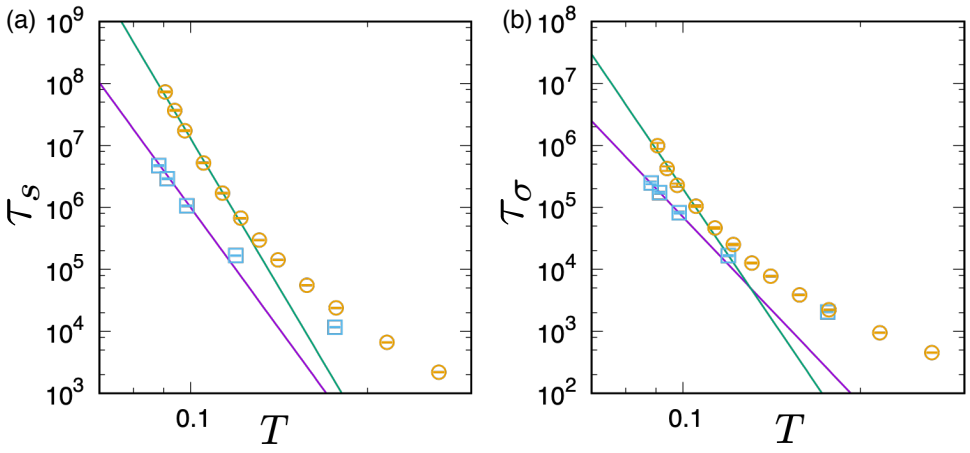

Figure 3.8: **The double logarithmic plots of typical relaxation times for $L = 6,\ \epsilon = 0.60$ (blue) and $L = 5,\ \epsilon = 0.65$ (yellow)**
(a): Spin relaxation time $\tau_s(T)$. The purple and green lines denote $\tau \sim T^{-10}$ and $\tau \sim T^{-14}$, respectively. (b): Distortion relaxation time $\tau_s(T)$. The purple and green lines denote $\tau \sim T^{-13}$ and $\tau \sim T^{-16}$, respectively.

3.4.2 Structural properties and heat capacity

In the previous section, we demonstrated that the critical slowing down occurs approaching a common T_c where spins and distortions freeze simultaneously. Here we analyze static quantities to obtain further insights.

Structure factor

In Fig. 3.9 (a) we show $S_s(0,h,l)$ obtained above and below T_c. Apparently, there are no significant differences between the two. No Bragg peak is observed below T_c, indicating that there is no magnetic long range order. In Fig. 3.9 (b), we also find no sign of long range order in the lattice distortion structure $S_\sigma^{(1)}(0,h,l)$, although the characteristic feature seems to develop at a lower temperature. We find that this feature is similar with the spin structure in spin ice systems, i.e. "pinch-point" like structures can be seen in $S_\sigma^{(2)}(h,h,l)$ (see Fig. 3.9 (d)), which becomes clearer at the lower temperature. These observations strongly suggest the critical slowing down discussed in the previous section is not due to development of some long-ranged ordering but amorphous structure.

Heat capacity and 2-in-2-out structure

In order to obtain more information on the liquid and glass states, let us discuss here how some static quantities depends on the temperature and ϵ. First let us discuss the temperature dependence of the two quantities at $\epsilon = 0.60$ for which we found the simultaneous transition of the spins and distortions at $T_c = 0.069$. The data are displayed in Fig. 1.8.

As can be seen in Fig. 1.8 (a), we find the heat capacity do not show any singularities but a broad peak at around T_c. This is very different from the purely antiferrogagnetic system (Fig. 1.8 (c)) which remain in the paramagnetic phase down to $T = 0$ but similar to the experimental observation (Fig. 1.14 (a)). As we already noted this feature is the same as conventional spin glasses with quenched disorder.

The fraction of the 2-in-2-out structures shown in Fig. 1.14 (b) monotonically increases with lowering temperatures without any singularity. This is consistent with the observation that the structure factor $S_\sigma^{(2)}(\boldsymbol{k})$ show pinch-point pattern clearer at lower temperatures.

Now let us discuss how the above features changes at larger ϵ. As shown in Fig. 3.11 (a), the broad peaks of the heat capacity are shifted to higher temperatures side with increasing ϵ but converge around $T^* = 0.17$. It suggests that the spin glass transition temperature depends on ϵ but saturates above $\epsilon^* = 1.0$. The behavior can be understood from the fraction of the 2-*in*-2-*out* structures, shown in Fig. 3.11 (b). For $\epsilon = 1.0$ and 1.2, most of tetrahedra are distorted into 2-*in*-2-*out* structures at temperatures higher than $T^* = 0.17$. Thus, the behavior of distortions is almost the same above $\epsilon^* = 1.0$.

For even larger ϵ, another broad peak of the heat capacity emerges at higher temperatures (Fig. 3.11 (d)), which can be interpreted as a reflection of the crossover from purely random phase to ice like phase. As shown in Fig. 3.11 (e), the fraction of the 2-*in*-2-*out* structures has a large increase around the temperatures correspondingly. This can be seen clearly in the incremental difference of the fraction (Fig. 3.11 (f)) having a broad peak at the same temperature as that of the heat capacity.

3.4.3 Nonlinear susceptibilities

Fig. 3.12 (a) shows the data of the magnetic nonlinear susceptibility χ_3 as a function of temperature for several system size L at $\epsilon = 0.60$. In overall, it takes the negative value, and from slightly above T_c, its amplitude starts to grow rapidly in lowering the temperature (Fig. 3.12 (c)). This growth is enhanced for larger L, strongly suggesting that the divergence of χ_3 remains in the thermodynamic limit, which is consistent with the experimental observation in $Y_2Mo_2O_7$ (see Fig. 1.14 (b)). Similar behavior is observed also for the dielectric counter part $\chi_3^{(\sigma)}$ (Fig. 3.12 (b) and Fig. 3.12 (d)), indicating the freezing of the lattice distortions into a disordered state.

Finally, let us also show the data for $L = 5$ for various ϵ in Fig. 3.13. we find all plots suggest the divergent behaviors. Unfortunately, the statistical fluctuation of the magnetic nonlinear susceptibility is too large to find ϵ dependence. On the other hand the dielectric nonlinear susceptibility shows clear ϵ dependence that it starts to grow rapidly at higher temperature for larger ϵ and the ϵ dependence disappears for $\epsilon > \epsilon^*$ in Fig. 3.13 (d).

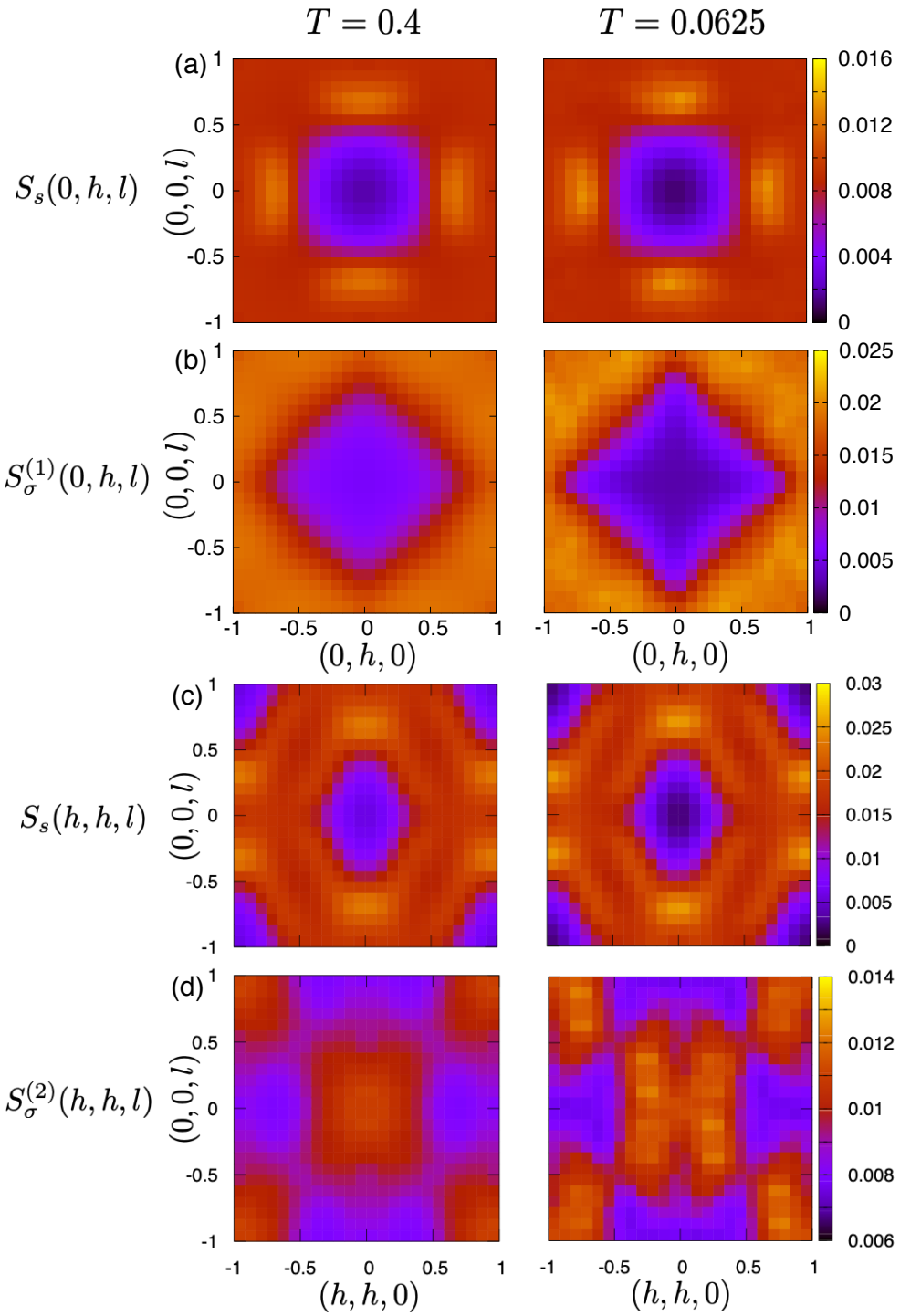

Figure 3.9: **Structure factors for $L = 6, \epsilon = 0.6$ above T_c ($T = 0.4$) in the left side and below T_c ($T = 0.0625$) in the right side**

(a) and (b) show the spin structure factor $S_s(0,h,l)$ and the orbital structure factor $S_\sigma^{(1)}(0,h,l)$, respectively. (c) and (d) show the spin structure factor $S_s(h,h,l)$ and the orbital structure factor $S_\sigma^{(2)}(h,h,l)$, respectively.

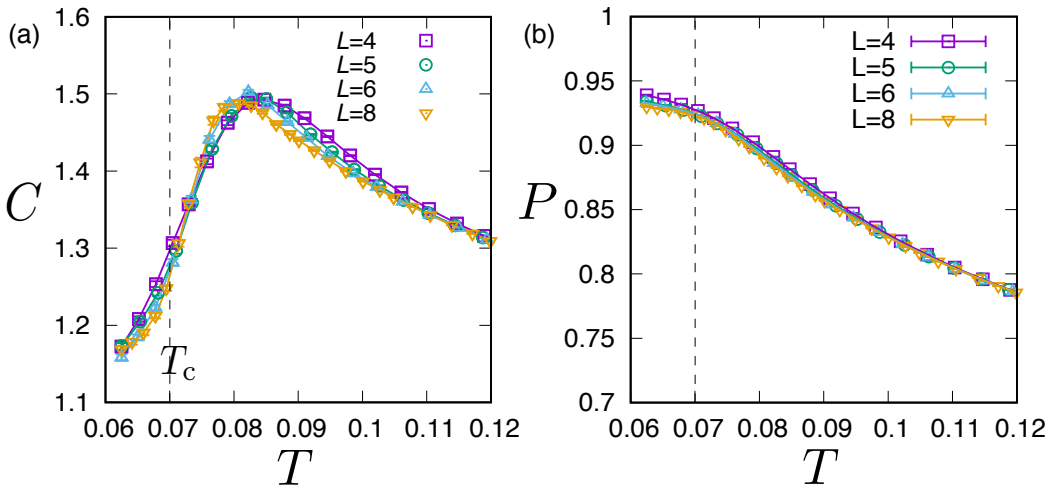

Figure 3.10: **Heat capacity and fraction of 2-*in*-2-*out* structure for** $\epsilon = 0.6$
(a): Size dependence of heat capacity. (b): Size dependence of fraction of 2-*in*-2-*out* structure. The dashed lines represent the freezing temperature $T_c = 0.07$ determined by the analysis on the relaxational dynamics in Sec. 3.4.1.

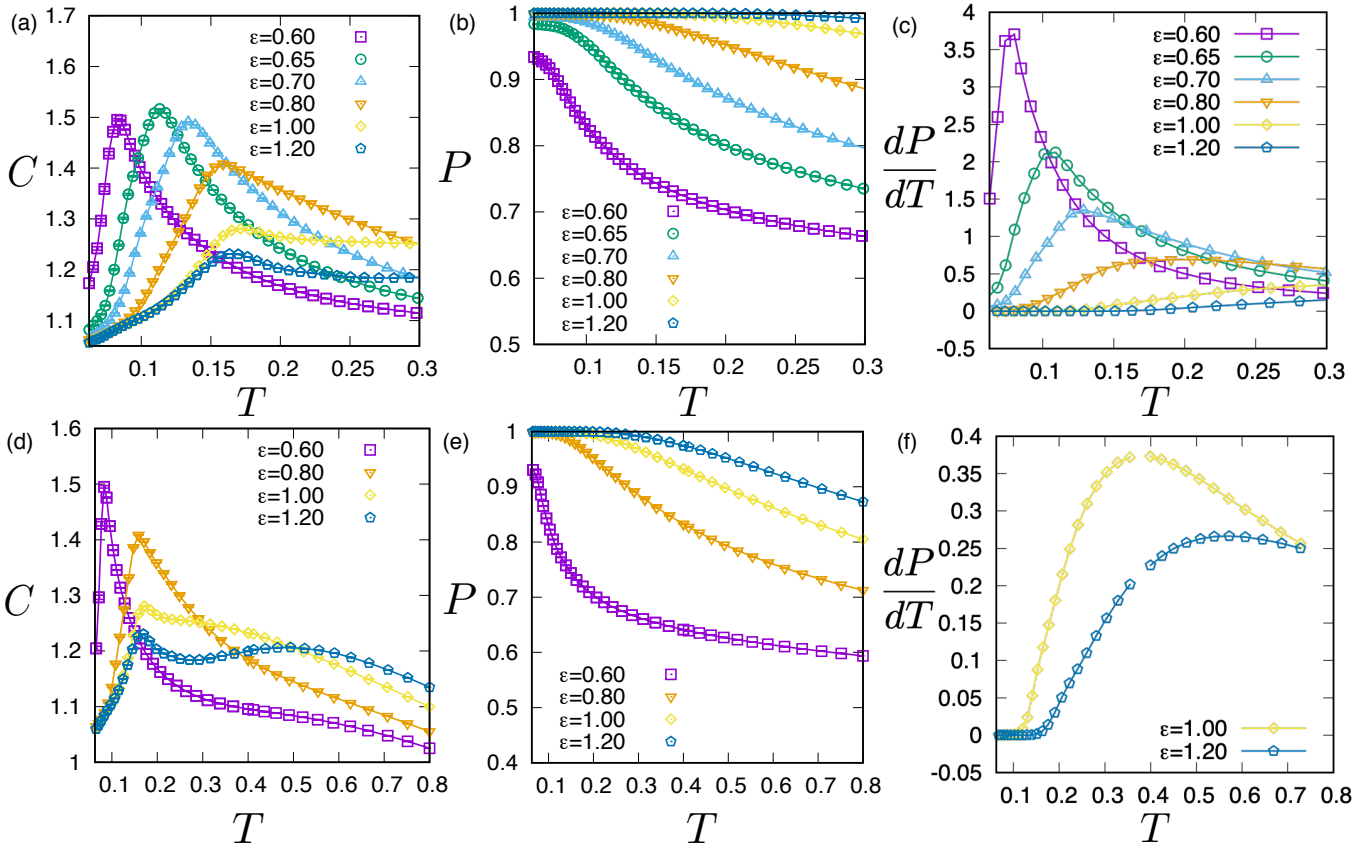

Figure 3.11: ϵ **dependence of heat capacity and fraction of 2-*in*-2-*out* structures for** $L = 5$ (a): Heat capacity in the narrow range of $T = 0.0625$ to $T = 0.3$. (b): Fraction of 2-*in*-2-*out* structures in the narrow range of $T = 0.0625$ to $T = 0.3$. (c): Incremental differences of fractions of 2-*in*-2-*out* structures in the narrow range of $T = 0.0625$ to $T = 0.3$. (d): Heat capacity in the wide range of $T = 0.0625$ to $T = 0.8$. (e): Fraction of 2-*in*-2-*out* structures in the wide range of $T = 0.0625$ to $T = 0.8$. (f): Incremental differences of fractions of 2-*in*-2-*out* structures for $\epsilon = 1.0, 1.2$ in the wide range of $T = 0.0625$ to $T = 0.8$.

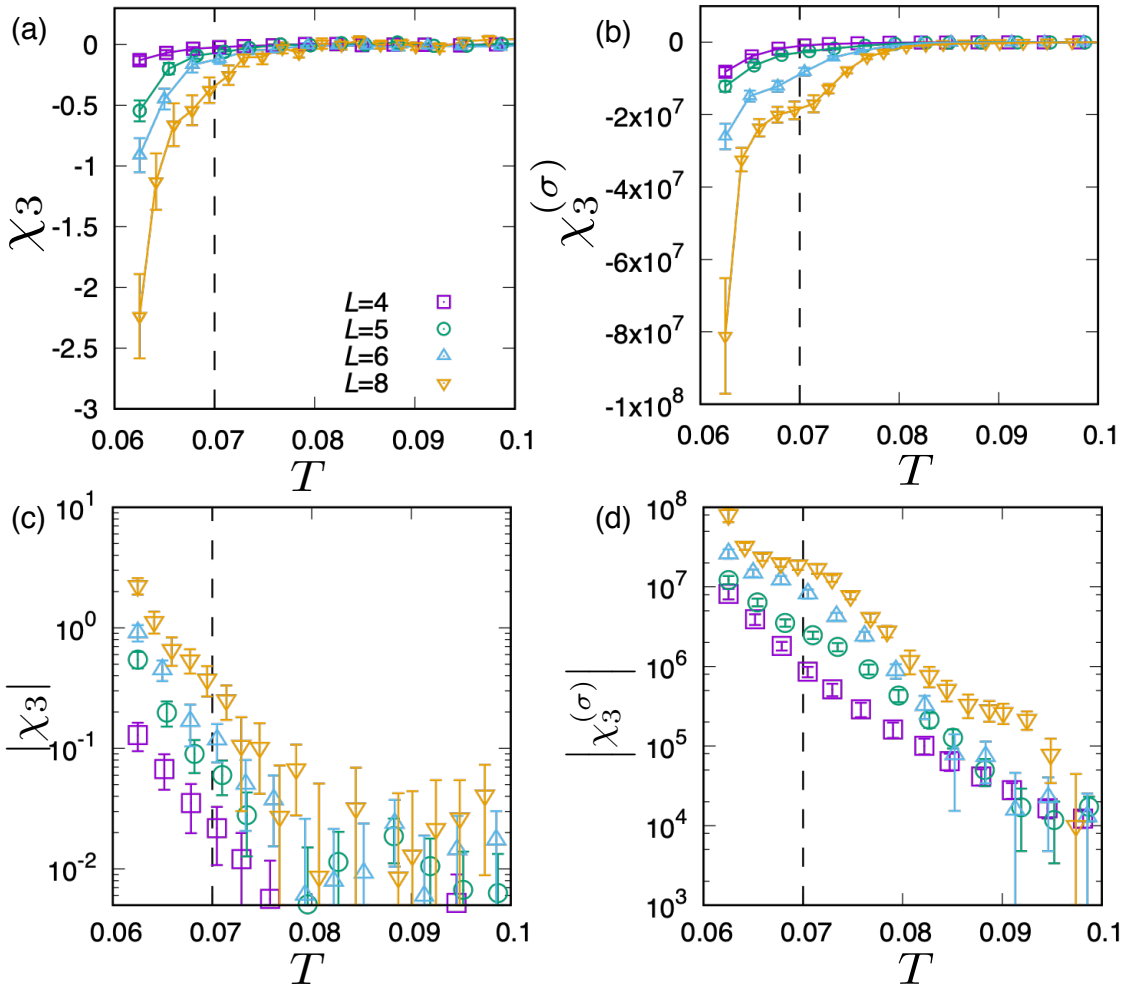

Figure 3.12: **Magnetic and dielectric nonlinear susceptibilities at** $\epsilon = 0.6$
(a), (b): Size dependence of magnetic and dielectric nonlinear susceptibilities. The dashed line represents the freezing temperature $T_c \approx 0.07$ determined by the auto-correlation function. (c), (d): logarithmic scale of the absolute values of the nonlinear susceptibilities.

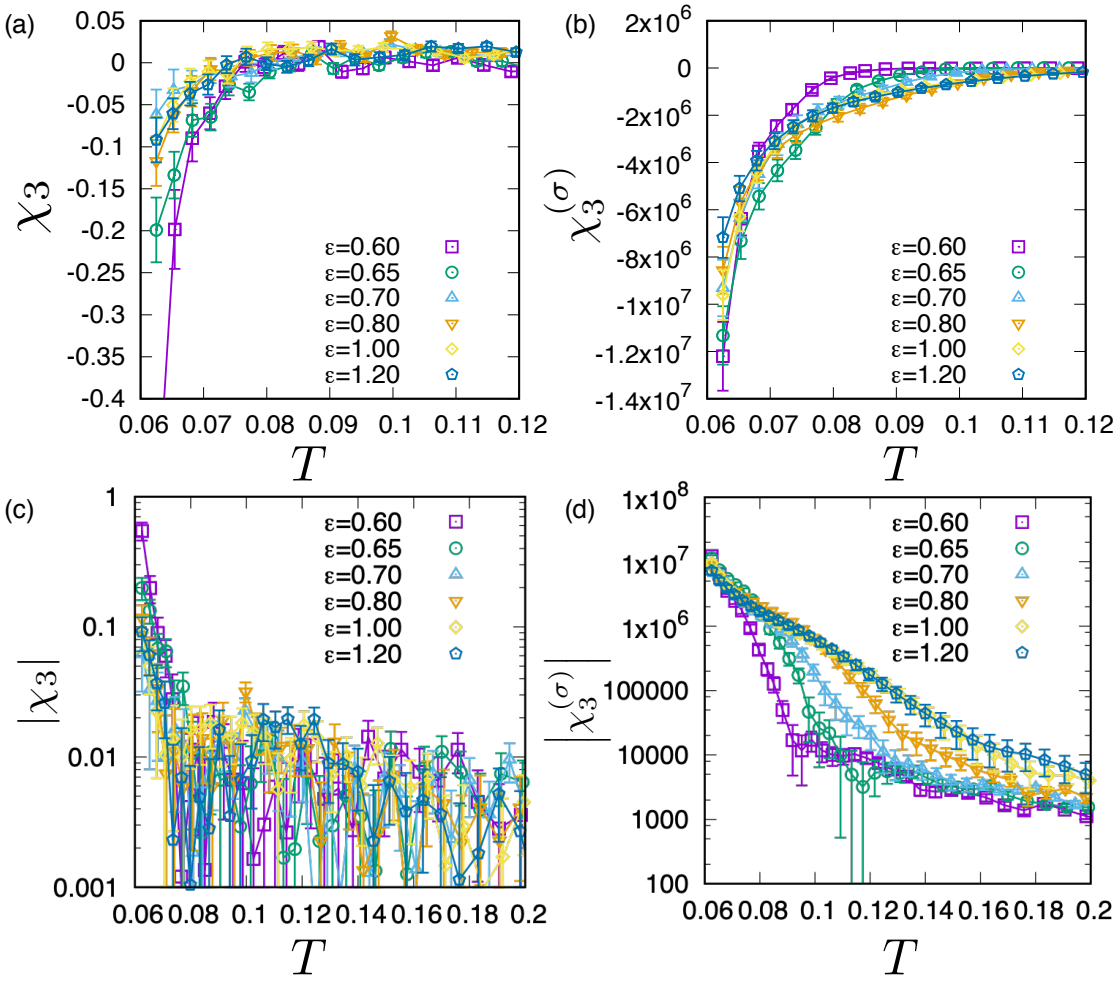

Figure 3.13: **ϵ dependence of magnetic and dielectric nonlinear susceptibilities for $L = 5$** (a): ϵ dependence of the magnetic nonlinear susceptibility. (b): ϵ dependence of the dielectric nonlinear susceptibility. (c), (d): logarithmic scale of absolute values of the nonlinear susceptibilities.

3.5 Discussion and summery on simulation

In this chapter, we presented the results of Monte Carlo simulations for our effective model given in Eq. (2.2) and Eq. (2.3). We equilibrated the system by using various algorithms and observed both dynamical and static properties in equilibrium.

Most importantly, we found evidences that the relaxation times of both spin and lattice distortion variables simultaneously diverge at the temperatures $T_c = 0.069$ for $\epsilon = 0.6$ and $T_c = 0.086$ for $\epsilon = 0.65$ with the universal power laws whose dynamical exponents are $(z\nu)_s \approx 2.7$ for spins and $(z\nu)_\sigma \approx 3.55$ for lattice distortions (Fig. 3.4 and Fig. 3.5). This strongly suggests that the system exhibits simultaneous second order spin and lattice glass transitions at the common glass transition temperature T_c. We found no hints of long-ranged order in the structure factor (Fig. 3.9) and the heat capacity doesn't have any singularities (Fig. 3.10). In addition, we found that the nonlinear magnetic and dielectric susceptibilities negatively and rapidly grow from slightly above T_c (Fig. 3.12). We believe that the nonlinear magnetic and dielectric susceptibilities negatively diverge at T_c because the amplitude of growth is larger by increasing the system size L. However, it is difficult to perform the finite size scaling for them due to their bad statistics of the fourth moment in their definitions (see Eq. (3.29) and Eq. (3.34)). It remains to be clarified whether the nonlinear magnetic and dielectric susceptibilities negatively diverge simultaneously at a common finite temperature or not.

Next, let us discuss the case of larger ϵ. By increasing ϵ, the 2-*in*-2-*out* structures appear at high temperatures. We found that the heat capacity for $\epsilon = 1.2$ has a secondary broad peak around $T = 0.5$ corresponding to the increase of the fraction of the 2-*in*-2-*out* structures (Fig. 3.11), which represents a crossover to the ice state. It is known that a dynamics becomes slow but not completely frozen (liquid) in a conventional ice state. We checked that both spins and lattice distortions in our system do not freeze for $\epsilon = 1.2$ and $T < 0.5$ (see Fig. 3.6). The heat capacity for $\epsilon = 1.2$ has another peak at a lower temperature, which presumably corresponds to the glass transition. This peak can be seen in the heat capacities for the other ϵ, which is shifted to the higher temperatures by increasing ϵ but saturates for ϵ lager than $\epsilon^* = 1.0$. Interestingly, we found that the nonlinear dielectric susceptibilities start to negatively and rapidly grow from slightly above T_c (Fig. 3.13). This strongly suggests that the lattice glass transition for large ϵ occurs at the temperature much lower than the crossover temperature to the ice state. We speculate that the lattice glass transition takes place at the same temperature as that of the spin glass transition in our effective model. This point remains to be clarified by feature studies.

Chapter 4

MEAN-FIELD THEORY

In this chapter, we develop and study a mean-field theory for our effective model. First, in order to construct an exactly solvable model, we extend the pyrochlore lattice to the infinite dimension in Sec. 4.1. We introduce the definition of the simplex which is a generalized notion of triangle or tetrahedron to arbitrary dimensions (Sec. 4.1.1) and then we consider the Bethe lattice of the simplices and the lattice distortions on this lattice (Sec. 4.1.2). Next, in Sec. 4.2, we solve our mean-field model in the spherical limit by using the replica method introduced in Sec. 1.1.3. We first explain how to take the spherical limit and how to trace out the spherical degrees of freedom (Sec. 4.2.1) and then calculate the free energy (Sec. 4.2.2). In Sec. 4.3, we consider the replica symmetric (RS) solution and investigate the ergodicity breaking and obtain the phase diagram. Next, we analyze the stability of the RS solution in Sec. 4.4 and present the behaviors of the physical quantities (Sec. 4.5) such as the internal energy, the heat capacity and the glass susceptibilities that are related to the magnetic and dielectric nonlinear susceptibilities observed by simulations in Chap. 3. Finally, we summarize this chapter in Sec. 4.6.

4.1 Construction of a mean-field model

4.1.1 Simplex

A simplex is a geometrical object such as triangle or tetrahedron generalized to arbitrary dimensions. More formally, let $\boldsymbol{a}_2-\boldsymbol{a}_1, \boldsymbol{a}_3-\boldsymbol{a}_1, ..., \boldsymbol{a}_{d+1}-\boldsymbol{a}_1$ be linearly independent vectors for $d+1$ points $\boldsymbol{a}_1, \boldsymbol{a}_2, \boldsymbol{a}_3, ..., \boldsymbol{a}_{d+1} \in \mathbb{R}^d$. Each point is called a vertex. For example, 0-dimensional simplex is a point, 1-dimensional simplex is a line, 2-dimensional simplex is a triangle, 3-dimensional simplex is a tetrahedron and 4-simplex is a 5-cell. A simplex is called a regular simplex when all distances between its vertices are equal.

In the following we explain how to construct a d-dimensional simplex in a recursive fashion. Let's consider a $(d-1)$-dimensional hyperplane H in $\mathbb{R}^d$. Suppose the we have a set of d points $S_{d-1} = \{\boldsymbol{a}_1, \boldsymbol{a}_2, \boldsymbol{a}_3, ..., \boldsymbol{a}_d\}$ in H with all pairwise distances 1, namely $|\boldsymbol{a}_i - \boldsymbol{a}_j| = 1$ for all i, j pairs. Then

$$\boldsymbol{c}_{d-1} = \frac{1}{d}\sum_{i=1}^{d} \boldsymbol{a}_i \tag{4.1}$$

is a centroid of S_{d-1}. Let $\boldsymbol{b}_{i,d-1} = \boldsymbol{a}_i - \boldsymbol{c}_{d-1}$. Then we find

$$\sum_{i=1}^{d} \boldsymbol{b}_{i,d-1} = 0 \tag{4.2}$$

and

$$|\boldsymbol{b}_{i,d-1} - \boldsymbol{b}_{j,d-1}| = |\boldsymbol{a}_i - \boldsymbol{a}_j| = 1 \tag{4.3}$$

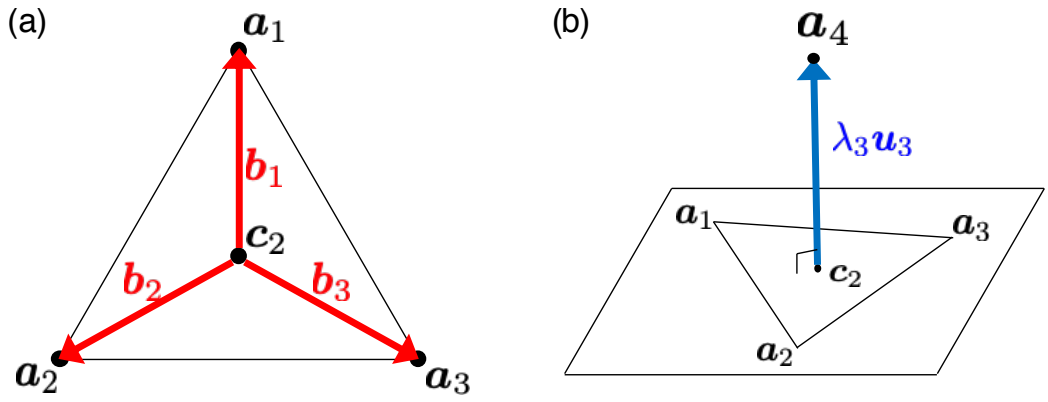

Figure 4.1: **Construction of simplices** (a): 2-dimensional regular simplex. (b): Creating $\boldsymbol{a}_4$ of a 3-dimensional regular simplex from the 2-dimensional regular simplex.

for all $i \neq j$. This implies

$$|\boldsymbol{b}_{i,d-1}|^2 - 2\boldsymbol{b}_{i,d-1} \cdot \boldsymbol{b}_{j,d-1} + |\boldsymbol{b}_{j,d-1}|^2 = 1. \tag{4.4}$$

Taking summation over all j except for fixed i, i.e. $\sum_{j\neq i}$, we obtain

$$\begin{aligned} & (d-1)|\boldsymbol{b}_{i,d-1}|^2 - 2\boldsymbol{b}_{i,d-1} \cdot \sum_{j\neq i} \boldsymbol{b}_{j,d-1} + \sum_{j\neq i} |\boldsymbol{b}_{j,d-1}|^2 \\ = \; & (d-1)|\boldsymbol{b}_{i,d-1}|^2 + 2|\boldsymbol{b}_{i,d-1}|^2 + \sum_{j\neq i} |\boldsymbol{b}_{j,d-1}|^2 \\ = \; & d|\boldsymbol{b}_{i,d-1}|^2 + \sum_{j=1}^{d} |\boldsymbol{b}_{j,d-1}|^2 = d-1. \end{aligned} \tag{4.5}$$

In the derivation of the second line in Eq. (4.5), we replaced $-\boldsymbol{b}_{i,d-1}$ by $\sum_{j\neq i} \boldsymbol{b}_{j,d-1}$ because of Eq. (4.2). We find that the value of $|\boldsymbol{b}_{i,d-1}|^2$ is independent of i, and then we find,

$$|\boldsymbol{b}_{i,d-1}| = \sqrt{\frac{d-1}{2d}}. \tag{4.6}$$

Let $\boldsymbol{u}_d$ be a unit vector orthogonal to H. Then there exists a value $\lambda_d \in \mathbb{R}$ such that $|\lambda_d \boldsymbol{u}_d + \boldsymbol{b}_{i,d-1}| = 1$ for all i. Using $\boldsymbol{u}_d \cdot \boldsymbol{b}_{i,d-1} = 0$ and assuming $\lambda_d > 0$, we find,

$$\lambda_d = \sqrt{\frac{d+1}{2d}}. \tag{4.7}$$

Let us introduce a new vector

$$\boldsymbol{a}_{d+1} = \boldsymbol{c}_{d-1} + \lambda_d \boldsymbol{u}_d. \tag{4.8}$$

Then we find,

$$|\boldsymbol{a}_{d+1} - \boldsymbol{a}_i|^2 = |\lambda_d \boldsymbol{u}_d + \boldsymbol{b}_{i,d-1}|^2 = 1. \tag{4.9}$$

Therefore we now have a set of $d+1$ points $S_d = \{\boldsymbol{a}_1, \boldsymbol{a}_2, \boldsymbol{a}_3, ..., \boldsymbol{a}_{d+1}\} \subset \mathbb{R}^d$ which consists a regular simplex in d-dimension.

There remains the initial point $\boldsymbol{a}_1$ and a vector set $\{\boldsymbol{u}_i\}$ $(i = 1, 2, ..., d)$ to be specified. Now let us choose $\boldsymbol{a}_1$ to be at the origin and $\{\boldsymbol{u}_i\}$ be a standard basis for d-dimensional Euclidean space. Using these

in Eq. (4.1) and Eq. (4.8), we find,

$$\begin{aligned} \boldsymbol{a}_1 &= \boldsymbol{0}, \\ \boldsymbol{a}_{i+1} &= \boldsymbol{c}_{i-1} + \lambda_i \boldsymbol{e}_i, \end{aligned} \tag{4.10}$$

where $\boldsymbol{e}_1 = (1,0,0,...,0), \boldsymbol{e}_2 = (0,1,0,...,0), ..., \boldsymbol{e}_d = (0,0,0,...,1)$. Using Eq. (4.10), we find,

$$\begin{aligned} \boldsymbol{c}_i &= \frac{i\boldsymbol{c}_{i-1} + \boldsymbol{a}_{i+1}}{i+1} \\ &= \boldsymbol{c}_{i-1} + \frac{\lambda_i \boldsymbol{e}_i}{i+1}, \end{aligned} \tag{4.11}$$

which can be solved as

$$\boldsymbol{c}_i = \sum_{j=1}^{i} \frac{\lambda_j}{j+1} \boldsymbol{e}_j. \tag{4.12}$$

Using this in Eq. (4.8), we find

$$\boldsymbol{a}_i = \sum_{j=1}^{i-2} \frac{\lambda_j}{j+1} \boldsymbol{e}_j + \lambda_{i-1} \boldsymbol{e}_{i-1} \quad (i \geq 2). \tag{4.13}$$

Finally, we also obtain a vector from the center to each vertex $\boldsymbol{b}_{i,d} = \boldsymbol{a}_i - \boldsymbol{c}_d$ (hereafter we write $\boldsymbol{b}_i$ for simplicity) as

$$\boldsymbol{b}_i = \begin{cases} -\displaystyle\sum_{j=1}^{d} \frac{\lambda_j}{j+1} \boldsymbol{e}_j & (i=1) \\ \dfrac{(i-1)\lambda_{i-1}}{i} \boldsymbol{e}_{i-1} - \displaystyle\sum_{j=i}^{d} \frac{\lambda_j}{j+1} \boldsymbol{e}_j & (2 \leq i \leq d) \\ \dfrac{d\lambda_d}{d+1} \boldsymbol{e}_d & (i = d+1). \end{cases} \tag{4.14}$$

From Eq. (4.6) we get $|\boldsymbol{b}_i| = \sqrt{d/2(d+1)}$ and the inner product $\boldsymbol{b}_i \cdot \boldsymbol{b}_j$ $(i<j)$ is calculated as

$$\begin{aligned} \boldsymbol{b}_i \cdot \boldsymbol{b}_j &= -\frac{(j-1)\lambda_{j-1}^2}{j^2} + \sum_{k=j}^{d} \left(\frac{\lambda_k}{k+1} \right)^2 \\ &= -\frac{1}{2j} + \frac{1}{2} \left(\frac{1}{j} - \frac{1}{d+1} \right) = -\frac{1}{2(d+1)}. \end{aligned} \tag{4.15}$$

4.1.2 Effective model on Bethe lattice of simplex

Now let us develop a mean-field version of our effective model introduced in Sec. 1.4.4 by building a network of deformable simplices. We first discuss how to construct a generic spin model on the network of regular simplices, which can be regarded as Bethe lattice version of kagomé or pyrochlore lattices. Then we generalize the model on a network of *deformable* simplices.

In order to formalize a mean-field theory of geometrical frustrated spin systems with only nearest-neighbor interactions, we construct a Bethe-like network of simplices. We first consider a regular hypergraph with p-body interactions. The graph is composed of variable nodes ● with c edges and interaction nodes ■ with p edges (Fig. 4.2(a)). We put spin variables or other variables (e.g. lattice distortions) on the variable nodes and p-body interactions are represented by interaction nodes. The relation between the number of variable nodes N and the number of interaction nodes $N_{\blacksquare}$ is

$$N_{\blacksquare} = \frac{Nc}{p}. \tag{4.16}$$

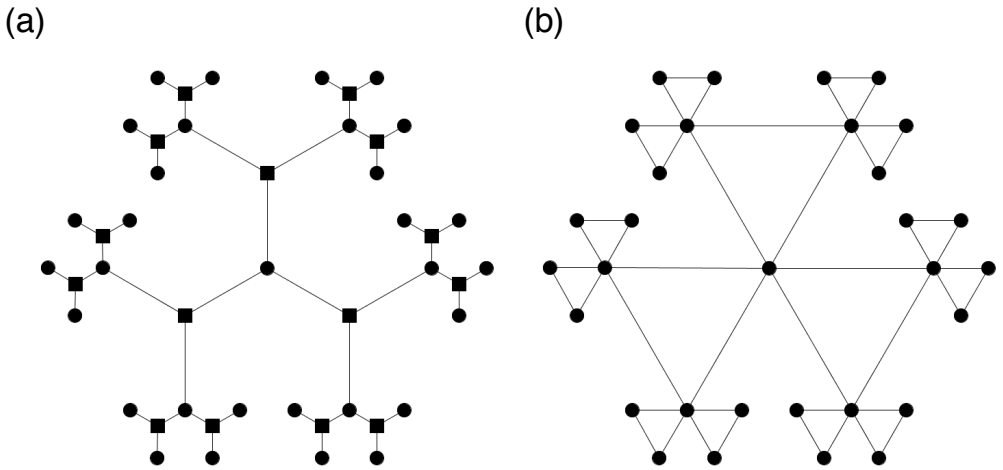

Figure 4.2: **Hypergraph and simplex lattice**
(a): A hypergraph with 3-body interactions and a connectivity $c = 3$. (b): A simplex lattice with $p = 3$ and $c = 3$.

The Hamiltonian of the system defined on such a graph can be written generally as

$$H = \sum_{\blacksquare=1}^{N_\blacksquare} V(\boldsymbol{x}_{1(\blacksquare)}, \boldsymbol{x}_{2(\blacksquare)}, ..., \boldsymbol{x}_{p(\blacksquare)}), \tag{4.17}$$

where $\{\boldsymbol{x}_{i(\blacksquare)}\}_{i=1,2,...p}$ represents variables (represented as variable node ●) participating in an interaction (represented by an interaction node ■). $V(\boldsymbol{x}_{1(\blacksquare)}, \boldsymbol{x}_{2(\blacksquare)}, ..., \boldsymbol{x}_{p(\blacksquare)})$ is a p-body interaction potential. When the p-body interactions can be divided into equivalent 2-body interactions of all possible pairs,

$$V(\boldsymbol{x}_{1(\blacksquare)}, \boldsymbol{x}_{2(\blacksquare)}, ..., \boldsymbol{x}_{p(\blacksquare)}) = \sum_{i=1}^{p-1} \sum_{j=i+1}^{p} \tilde{V}(\boldsymbol{x}_{i(\blacksquare)}, \boldsymbol{x}_{j(\blacksquare)}), \tag{4.18}$$

each interaction node ■ is replaced by a $(p-1)$-dimensional simplex (Fig. 4.2(b)). Hereafter we call the 2-body interaction $\tilde{V}$ simply as V and rewrite the index ■ as △ to distinguish it from the conventional index for factor nodes. Eq. (4.17) becomes

$$H = \sum_{\triangle=1}^{N_\triangle} \sum_{i<j} V(\boldsymbol{x}_{i(\triangle)}, \boldsymbol{x}_{j(\triangle)}), \tag{4.19}$$

here $\sum_{i<j} = \sum_{i=1}^{p-1} \sum_{j=i+1}^{p}$.

Now let us turn to consider a *deformable* simplex lattice defined. At first, we consider the case of c=2 (Fig. 4.3(a)). We suppose that all nearest-neighbor pairs of simplices are connected point symmetrically about the mediated vertex in order to mimic the kagomé and pyrochlore lattices. We assume that the lattice distortions are restricted on the line connecting the centers of the two simplices with the amplitude 1 following the argument in Sec. 2.2. Note that a vertex is "in" for one of two simplices and it is "out" for the other. Therefore, the lattice distortion for each simplex ($\triangle = 1, 2$) around site i can be represented as $\boldsymbol{\sigma}_i = (\sigma_{i(1)}, \sigma_{i(2)}) = (\pm 1, \mp 1)$.

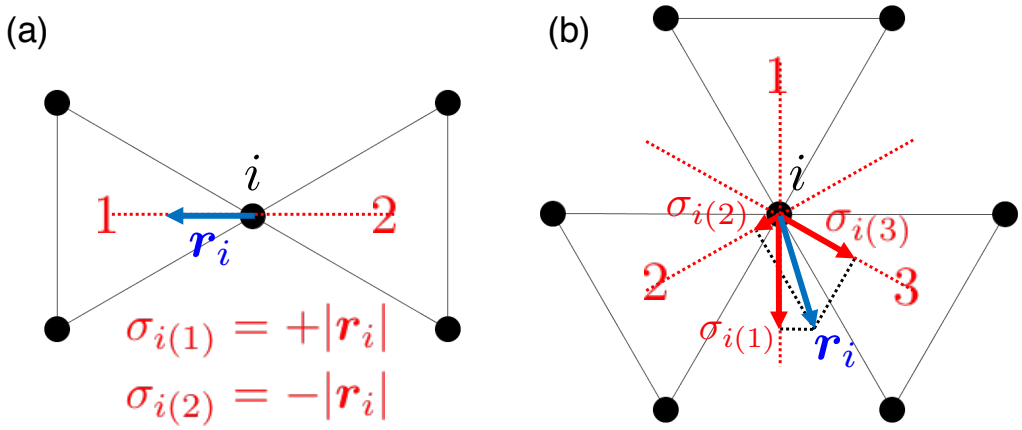

Figure 4.3: **Lattice distortion on a deformable simplex lattice**
(a): Lattice distortion for the connectivity $c = 2$. The vertex i displaces to a center of simplex or the other center. (b): Lattice distortion for the connectivity $c = 3$. The distortion represented by $\boldsymbol{r}_i$ is restricted in 2-dimensional space involving centers of three simplices.

Next, we try to generalize this to lattices with any connectivity c. We suppose that c simplices around site i are *isotropically* connected in $(c-1)$-dimensional space (Fig. 4.3(b)); namely the unit vector from the center of simplex $(\triangle = 1, 2, 3, ..., c)$ to site i can be represented as $\hat{\boldsymbol{b}}_\triangle = \boldsymbol{b}_\triangle/|\boldsymbol{b}_\triangle|$,, where $\boldsymbol{b}_\triangle$ is given in Eq. (4.15). We define the lattice distortion on site i as $(c-1)$-dimensional vector $\boldsymbol{r}_i$ with the amplitude normalized as

$$|\boldsymbol{r}_i|^2 = \sum_{\mu=1}^{c-1} (r_i^\mu)^2 = c - 1 \tag{4.20}$$

and also define its contribution for simplex $\triangle$ as the projection on to the line connecting the vertex and the center of the simplex, more precisely $\boldsymbol{\sigma}_i = (\sigma_{i(1)}, \sigma_{i(2)}, ..., \sigma_{i(c)}) = (\boldsymbol{r}_i \cdot \hat{\boldsymbol{b}}_1, \boldsymbol{r}_i \cdot \hat{\boldsymbol{b}}_2, ..., \boldsymbol{r}_i \cdot \hat{\boldsymbol{b}}_c)$. If $\sigma_{i(\triangle)} > 0$, $i-$th vertex displaces to "in" direction for the simplex $\triangle$.

From Eq. (4.2) we can easily see

$$\sum_{\triangle=1}^{c} \sigma_{i(\triangle)} = 0. \tag{4.21}$$

We can also find the normalization of the distortion $\sigma_{i(\triangle)}$,

$$\sum_{\triangle=1}^{c} \sigma_{i(\triangle)}^2 = \frac{c-1}{2c} \sum_{\triangle=1}^{c} (\boldsymbol{r}_i \cdot \boldsymbol{b}_\triangle)^2. \tag{4.22}$$

From Eq. (4.15) the summation on the right hand side is calculated as

$$\begin{aligned}
\sum_{\mu=1}^{c} (\boldsymbol{r}_i \cdot \boldsymbol{b}_\mu)^2 &= \left[\left(\sum_{\mu=1}^{c-1} \frac{\lambda}{\mu+1} r_i^\mu \right) \right]^2 + \sum_{\mu=1}^{c-2} \left[\left(\frac{\mu\lambda_\mu}{\mu+1} r_i^\mu - \sum_{\nu=\mu+1}^{c-1} \frac{\lambda_\nu}{\nu+1} r_i^\nu \right) \right]^2 + \left[\left(\frac{(c-1)\lambda_{c-1}}{c} r_i^{c-1} \right) \right]^2 \\
&= \sum_{\mu=1}^{c-1} (\mu^2+1) \left(\frac{\lambda_\mu}{\mu+1} \right)^2 (r_i^\mu)^2 + 2 \sum_{\mu<\nu} (1-\mu) \left(\frac{\lambda_\mu}{\mu+1} \right) \left(\frac{\lambda_\nu}{\nu+1} \right) r_i^\mu r_i^\nu + \sum_{\mu=1}^{c-2} \left(\sum_{\nu=\mu+1}^{c-1} \frac{\lambda_\nu}{\nu+1} r_i^\nu \right)^2 .
\end{aligned} \tag{4.23}$$

Using Eq. (4.7), Eq. (4.20) and the identity

$$\sum_{l=1}^{n-1}\left(\sum_{k=l+1}^{n} a_k\right)^2 = \sum_{k=1}^{n}(k-1)a_k^2 + 2\sum_{k<l}(k-1)a_k a_l, \tag{4.24}$$

we obtain

$$\sum_{\mu=1}^{c}(\boldsymbol{r}_i\cdot\boldsymbol{b}_\mu)^2 = \sum_{\mu=1}^{c-1}\mu(\mu+1)\left(\frac{\lambda_\mu}{\mu+1}\right)^2(r_i^\mu)^2 = \frac{1}{2}(c-1). \tag{4.25}$$

Finally we find

$$\sum_{\triangle=1}^{c}\sigma_{i(\triangle)}^2 = c. \tag{4.26}$$

Note that a scalar variable $\sigma_{i(\triangle)}$ takes a discrete value ±1 in the case of $c=2$ due to Eq. (4.21) and Eq. (4.26) while it takes a continuous value for other c.

From Eq. (4.19) and Eq. (D.6), elastic energy associated with the lattice distortions on the simplex network is found as,

$$H = ku^2\cos^2\theta\sum_{\triangle}\sum_{i<j}(\sigma_{i(\triangle)}+\sigma_{j(\triangle)})^2. \tag{4.27}$$

Using Eq. (4.26), this is simplified,

$$H = \epsilon\sum_{\triangle}\sum_{i<j}\sigma_{i(\triangle)}\sigma_{j(\triangle)} + \text{const}, \tag{4.28}$$

where $\epsilon = 2ku^2\cos^2\theta$.

Now we can define a mean-field version of our effective model introduced in Sec. 1.4.4. The dynamical degrees of freedom is M-component spins $\boldsymbol{S}_i$ and c-component distortion vector $\boldsymbol{\sigma}_i$ defined on each vertex i ($i=1,2,3,...,N$). The Hamiltonian is given by

$$H = \sum_{\triangle} V(\vec{\boldsymbol{S}}_{(\triangle)}, \vec{\sigma}_{(\triangle)}), \tag{4.29}$$

with

$$V(\vec{\boldsymbol{S}}_{(\triangle)}, \vec{\sigma}_{(\triangle)}) = \frac{1}{\sqrt{p}}\sum_{i<j}\left[J_{ij}(\sigma_{i(\triangle)},\sigma_{j(\triangle)})\boldsymbol{S}_{i(\triangle)}\cdot\boldsymbol{S}_{j(\triangle)} + \epsilon\sigma_{i(\triangle)}\sigma_{j(\triangle)}\right], \tag{4.30}$$

where $\vec{\boldsymbol{S}}_{(\triangle)} = (\boldsymbol{S}_{1(\triangle)}, \boldsymbol{S}_{2(\triangle)}, ..., \boldsymbol{S}_{p(\triangle)})$, $\vec{\sigma}_{(\triangle)} = (\sigma_{1(\triangle)}, \sigma_{2(\triangle)}, ..., \sigma_{p(\triangle)})$ and $J_{ij}(\sigma_{i(\triangle)},\sigma_{j(\triangle)})$ represents the exchange interaction between spin variables $\boldsymbol{S}_{i(\triangle)}$ and $\boldsymbol{S}_{j(\triangle)}$. The exchange interaction depends linearly on the lattice distortion. More precisely, it is defined as

$$J_{ij}(\sigma_{i(\triangle)},\sigma_{j(\triangle)}) = \frac{J}{\sqrt{M}}[1+\delta(\sigma_{i(\triangle)}+\sigma_{j(\triangle)})], \quad (J>0), \tag{4.31}$$

where δ represents the amplitude of modulation by the lattice distortion. If δ is sufficiently large, the interaction can become both ferromagnetic and antiferromagnetic depending on the distortions $\{\sigma_{i(\triangle)}\}$.

4.2 Replica theory in the spherical limit

4.2.1 Sherical limit

In this section we analyze the effective model defined on the deformable simplex network using the replica approach given by [23]. We consider vectorial spins with M components $\boldsymbol{S}_i = (S_i^1, S_i^2, ..., S_i^M)$ $(i = 1, 2, ..., N)$ normalized such that

$$|\boldsymbol{S}_i|^2 = \sum_{\mu=1}^{M} (S_i^\mu)^2 = M. \tag{4.32}$$

The M-component continuous spin with length $\sqrt{M}$ can rotate in the M-dimensional space. We also consider the lattice displacements satisfying constraints Eq. (4.21) and Eq. (4.26) mentioned in previous section. In order to make the model exactly solvable, we consider the spherical model: we take the limit of large number of spin components $M \to \infty$ independently of the thermodynamic limit $N \to \infty$. We also take the limit of large number of connectivity $c \to \infty$ being proportional to M with the constant ratio α $(= O(1))$, i.e.

$$c = M\alpha. \tag{4.33}$$

The free energy F of the system is given by,

$$-\beta F = \log Z, \tag{4.34}$$

where β is the inverse temperature and Z represents partition function defined as,

$$Z = \left(\prod_i \mathrm{Tr}_{\boldsymbol{S}_i} \mathrm{Tr}_{\boldsymbol{\sigma}_i} \right) e^{-\beta H} \tag{4.35}$$

Here $\mathrm{Tr}_{\boldsymbol{S}}$ and $\mathrm{Tr}_{\boldsymbol{\sigma}}$ represent traces over the spin space of the spin $\boldsymbol{S}$ and the lattice displacement $\boldsymbol{\sigma}$, which can be rewritten as,

$$\begin{aligned}
\mathrm{Tr}_{\boldsymbol{S}} &= \prod_{\mu=1}^{M} \int_{-\infty}^{\infty} \delta\left(M - \sum_{\mu=1}^{M} (S^\mu)^2 \right) dS^\mu \\
&= \left(\prod_{\mu=1}^{M} \int_{-\infty}^{\infty} dS^\mu \right) M \int_{-i\infty}^{i\infty} \frac{d\Omega}{2\pi} \exp\left[\Omega(M - \sum_{\mu=1}^{M} (S^\mu)^2) \right] \\
&= M \int_{-i\infty}^{i\infty} \frac{d\Omega}{2\pi} e^{M\Omega} \prod_{\mu=1}^{M} \int_{-\infty}^{\infty} dS^\mu \exp\left[-\Omega (S^\mu)^2 \right],
\end{aligned} \tag{4.36}$$

$$\begin{aligned}
\mathrm{Tr}_{\boldsymbol{\sigma}} &= \prod_{\triangle=1}^{c} \int_{-\infty}^{\infty} \delta\left(\sum_{\triangle=1}^{c} \sigma_{(\triangle)} \right) \delta\left(c - \sum_{\triangle=1}^{c} (\sigma_{(\triangle)})^2 \right) d\sigma_{(\triangle)} \\
&= \left(\prod_{\triangle=1}^{c} \int_{-\infty}^{\infty} d\sigma_{(\triangle)} \right) c \int_{-i\infty}^{i\infty} \frac{d\omega}{2\pi} \int_{-i\infty}^{i\infty} \frac{d\kappa}{2\pi} \exp\left[\omega(c - \sum_{\triangle=1}^{c} (\sigma_{(\triangle)})^2) + \kappa \sum_{\triangle=1}^{c} \sigma_{(\triangle)} \right] \\
&= c \int_{-i\infty}^{i\infty} \frac{d\omega}{2\pi} e^{c\omega} \int_{-i\infty}^{i\infty} \frac{d\kappa}{2\pi} \prod_{\triangle=1}^{c} \int_{-\infty}^{\infty} d\sigma_{(\triangle)} \exp\left[-\omega (\sigma_{(\triangle)})^2 + \kappa \sigma_{(\triangle)} \right].
\end{aligned} \tag{4.37}$$

4.2.2 Replicated system

In order to study the glass transitions we use the replica method. We consider n-replicated system of our model given by,

$$\beta H = \sum_{a=1}^{n} \sum_{\triangle} \beta V(\vec{\boldsymbol{S}}^a_{(\triangle)}, \vec{\sigma}^a_{(\triangle)}). \tag{4.38}$$

The free energy of the replicated system can be obtained as

$$-\beta F = \log Z = \lim_{n\to 0} \partial_n Z^n. \tag{4.39}$$

Here the replicated partition function is given by,

$$Z^n = \left(\prod_i \prod_a \mathrm{Tr}_{\boldsymbol{S}_{i,a}} \right) \prod_{\triangle} e^{-\sum_{a=1}^{n} \beta V(\vec{\boldsymbol{S}}^a_{(\triangle)}, \vec{\sigma}^a_{(\triangle)})}. \tag{4.40}$$

In order to observe the glass transition with spontaneous ergodicity and replica symmetry breaking, we explicitly put the coupling between replicas into the Hamiltonian as (see Sec. 1.1.3),

$$\beta H = \sum_{a=1}^{n} \sum_{\triangle} \beta V(\vec{\boldsymbol{S}}^a_{(\triangle)}, \vec{\sigma}^a_{(\triangle)}) - \sum_{a<b} \left[\Lambda_{ab} \sum_i \sum_\mu (S^a)^\mu_i (S^b)^\mu_i + \lambda_{ab} \sum_i \sum_{\triangle} \sigma^a_{i(\triangle)} \sigma^b_{i(\triangle)} \right], \tag{4.41}$$

and then study the behavior of the glass order parameter matrices of the spins and lattice distortions,

$$Q_{ab} = \lim_{\Lambda_{ab}\to 0} \lim_{\lambda_{ab}\to 0} \lim_{N\to\infty} \frac{1}{NM} \sum_{i=1}^{N} \sum_{\mu=1}^{M} \left\langle (S^a)^\mu_i (S^b)^\mu_i \right\rangle_{\Lambda,\lambda}, \tag{4.42}$$

$$q_{ab} = \lim_{\Lambda_{ab}\to 0} \lim_{\lambda_{ab}\to 0} \lim_{N\to\infty} \frac{1}{Nc} \sum_{i=1}^{N} \sum_{\triangle=1}^{c} \left\langle \sigma^a_{i(\triangle)} \sigma^b_{i(\triangle)} \right\rangle_{\Lambda,\lambda}. \tag{4.43}$$

Here $\langle ... \rangle_{\Lambda,\lambda}$ represents the thermal average in the presence of the symmetry breaking field which are eventually switched off $\lambda \to 0$ and $\Lambda \to 0$. For convenience, we extend the matrices to include the diagonal elements,

$$Q_{aa} = 1, \tag{4.44}$$

$$q_{aa} = 1, \tag{4.45}$$

to include the normalization condition of the spins and lattice distortions Eq. (4.32) and Eq. (4.26). Since we take the large number limits of the spin components $M \to \infty$ ($c = M\alpha \to \infty$), we can also define the *local* glass order parameters as

$$(Q_{ab})_i = \lim_{\Lambda_{ab}\to 0} \lim_{\lambda_{ab}\to 0} \lim_{M\to\infty} \frac{1}{M} \sum_{\mu=1}^{M} \left\langle (S^a)^\mu_i (S^b)^\mu_i \right\rangle_{\Lambda,\lambda}, \tag{4.46}$$

$$(q_{ab})_i = \lim_{\Lambda_{ab}\to 0} \lim_{\lambda_{ab}\to 0} \lim_{c\to\infty} \frac{1}{c} \sum_{\triangle=1}^{c} \left\langle \sigma^a_{i(\triangle)} \sigma^b_{i(\triangle)} \right\rangle_{\Lambda,\lambda}. \tag{4.47}$$

To obtain a free-energy functional in terms of the order parameters, one can do the Legendre transforms like Eq. (1.17) for the ferromagnetic case. This can be done by making use of the following identities [23],

$$
\begin{aligned}
1 &= \int_{-\infty}^{\infty} d(Q_{ab})_i \delta\left(M(Q_{ab})_i - \sum_{\mu=1}^{M} (S^a)_i^\mu (S^b)_i^\mu \right) \\
&= M \int_{-i\infty}^{i\infty} \frac{d(\Lambda_{ab})_i}{2\pi} \int_{-\infty}^{\infty} d(Q_{ab})_i \exp\left[(\Lambda_{ab})_i \left(M(Q_{ab})_i - \sum_{\mu=1}^{M} (S^a)_i^\mu (S^b)_i^\mu \right) \right] \qquad (4.48) \\
1 &= \int_{-\infty}^{\infty} d(q_{ab})_i \delta\left(c(q_{ab})_i - \sum_{\triangle=1}^{c} \sigma^a_{i(\triangle)} \sigma^b_{i(\triangle)} \right) \\
&= c \int_{-i\infty}^{i\infty} \frac{d(\lambda_{ab})_i}{2\pi} \int_{-\infty}^{\infty} d(q_{ab})_i \exp\left[(\lambda_{ab})_i \left(c(q_{ab})_i - \sum_{\triangle=1}^{c} \sigma^a_{i(\triangle)} \sigma^b_{i(\triangle)} \right) \right] \qquad (4.49)
\end{aligned}
$$

for $a < b$. Then the traces of spin can be expressed formally as,

$$
\prod_{a'=1}^{n} \mathrm{Tr}_{\boldsymbol{S}^{a'}} [\cdots] = \left(\frac{1}{2^n} \prod_{a \le b} M \int_{-i\infty}^{i\infty} \frac{d\Lambda_{ab}}{2\pi} \int_{-\infty}^{\infty} dQ_{ab} \right) \exp\left[\frac{M}{2} \sum_{a,b=1}^{n} \Lambda_{ab} Q_{ab} + M \log Z_\Lambda \right] \prod_{\mu=1}^{M} \langle \cdots \rangle_\mu , \qquad (4.50)
$$

where

$$
Z_\Lambda = \left(\prod_{a'=1}^{n} \int_{-\infty}^{\infty} dS^{a'} \right) \exp\left[-\frac{1}{2} \sum_{a,b=1}^{n} \Lambda_{ab} S^a S^b \right] = \left(\frac{(2\pi)^n}{\det(\hat{\Lambda})} \right)^{\frac{1}{2}} \qquad (4.51)
$$

and

$$
\langle \cdots \rangle_\mu = \frac{1}{Z_\Lambda} \left(\prod_{a'=1}^{n} \int_{-\infty}^{\infty} d(S^{a'})^\mu \right) \exp\left[-\frac{1}{2} \sum_{a,b=1}^{n} \Lambda_{ab} (S^a)^\mu (S^b)^\mu \right] [\cdots]. \qquad (4.52)
$$

Here we replaced Ω_a by $\Lambda_{aa}/2$. $\prod_{\mu=1}^{M} \langle \cdots \rangle_\mu$ means averages for all components μ. In the limit $M \to \infty$, we can use a saddle-point method to integrate out Λ_{ab}. and the saddle point equation which determines the saddle point $\Lambda^*_{ab}(\hat{Q})$ is given by,

$$
Q_{ab} = \frac{1}{M} \sum_{\mu=1}^{M} \left. \frac{\left(\prod_{a'=1}^{n} \int_{-\infty}^{\infty} d(S^{a'})^\mu \right) \exp\left[-\frac{1}{2} \sum_{a,b=1}^{n} \Lambda_{ab} (S^a)^\mu (S^b)^\mu \right] (S^a)^\mu (S^b)^\mu}{\left(\prod_{a'=1}^{n} \int_{-\infty}^{\infty} d(S^{a'})^\mu \right) \exp\left[-\frac{1}{2} \sum_{a,b=1}^{n} \Lambda_{ab} (S^a)^\mu (S^b)^\mu \right]} \right|_{\Lambda_{ab} = \Lambda^*_{ab}(\hat{Q})} = (\Lambda^*)^{-1}_{ab} \qquad (4.53)
$$

and we find,

$$
\prod_{a'=1}^{n} \mathrm{Tr}_{\boldsymbol{S}^{a'}} [\cdots] \propto \left(\prod_{a \le b} \int_{-\infty}^{\infty} dQ_{ab} \right) e^{M s^{(s)}_{\mathrm{ent}}[\hat{Q}]} \prod_{\mu=1}^{M} \langle \cdots \rangle_\mu , \qquad (4.54)
$$

where $s^{(s)}_{\mathrm{ent}}[\hat{Q}]$ represents the entropic contribution of spins to the free energy, which is given by

$$
s^{(s)}_{\mathrm{ent}}[\hat{Q}] = \sum_{a,b=1}^{n} \frac{1}{2} \Lambda^*_{ab} Q_{ab} + \frac{1}{2} \log \left(\frac{(2\pi)^n}{\det(\hat{\Lambda}^*)} \right) = \frac{n}{2}(1 + \log(2\pi)) + \frac{1}{2} \log\det \hat{Q}. \qquad (4.55)
$$

Similarly, the trace of lattice displacement is formally obtained as,

$$\prod_{a'=1}^{n} \mathrm{Tr}_{\boldsymbol{\sigma}^{a'}}[\cdots] = \left(\frac{1}{2^n}\prod_{a\le b} c\int_{-i\infty}^{i\infty}\frac{d\lambda_{ab}}{2\pi}\int_{-\infty}^{\infty} dq_{ab}\right)\left(\prod_{a'=1}^{n}\int_{-i\infty}^{i\infty}\frac{d\kappa_a}{2\pi}\right)\exp\left[\frac{c}{2}\sum_{a,b=1}^{n}\lambda_{ab}q_{ab}+\sum_{\triangle=1}^{c}\log Z_\lambda\right]\prod_{\triangle=1}^{c}\langle\cdots\rangle_\triangle\,, \tag{4.56}$$

where

$$Z_\lambda = \left(\prod_{a'=1}^{n}\int_{-\infty}^{\infty} d\sigma^{a'}\right)\exp\left[-\frac{1}{2}\sum_{a,b=1}^{n}\lambda_{ab}\sigma^a\sigma^b-\sum_{a=1}^{n}\kappa_a\sigma^a\right] = \left(\frac{(2\pi)^n}{\det(\hat{\lambda})}\right)^{\frac{1}{2}}\exp\left[\frac{1}{2}\sum_{a,b=1}^{n}\lambda^{-1}_{ab}\kappa_a\kappa_b\right] \tag{4.57}$$

and

$$\langle\cdots\rangle_\triangle = \frac{1}{Z_\lambda}\left(\prod_{a'=1}^{n}\int_{-\infty}^{\infty} d\sigma^{a'}_{(\triangle)}\right)\exp\left[-\frac{1}{2}\sum_{a,b=1}^{n}\lambda_{ab}\sigma^a_{(\triangle)}\sigma^b_{(\triangle)}-\sum_{a=1}^{n}\kappa_a\sigma^a_{(\triangle)}\right][\cdots]. \tag{4.58}$$

Here we replaced ω_a by $\lambda_{aa}/2$. In the limit $c\to\infty$, we use the saddle point method to integrate out κ_a and λ_{ab}. The saddle point equations are given by,

$$\begin{aligned} 0 &= \frac{1}{c}\sum_{\triangle=1}^{c}\left.\frac{\left(\prod_{a'=1}^{n}\int_{-\infty}^{\infty}d\sigma^{a'}_{(\triangle)}\right)\exp\left[-\frac{1}{2}\sum_{a,b=1}^{n}\lambda_{ab}\sigma^a_{(\triangle)}\sigma^b_{(\triangle)}-\sum_{a=1}^{n}\kappa_a\sigma^a_{(\triangle)}\right]\sigma^a_{(\triangle)}}{\left(\prod_{a'=1}^{n}\int_{-\infty}^{\infty}d\sigma^{a'}_{(\triangle)}\right)\exp\left[-\frac{1}{2}\sum_{a,b=1}^{n}\lambda_{ab}\sigma^a_{(\triangle)}\sigma^b_{(\triangle)}-\sum_{a=1}^{n}\kappa_a\sigma^a_{(\triangle)}\right]}\right|_{\lambda_{ab}=\lambda^*_{ab}(\hat{q}),\kappa_a=\kappa^*_a(\hat{q})} \\ &= \sum_{b=1}^{n}(\lambda^*)^{-1}_{ab}\kappa^*_b \end{aligned} \tag{4.59}$$

and

$$\begin{aligned} q_{ab} &= \frac{1}{c}\sum_{\triangle=1}^{c}\left.\frac{\left(\prod_{a'=1}^{n}\int_{-\infty}^{\infty}d\sigma^{a'}_{(\triangle)}\right)\exp\left[-\frac{1}{2}\sum_{a,b=1}^{n}\lambda_{ab}\sigma^a_{(\triangle)}\sigma^b_{(\triangle)}-\sum_{a=1}^{n}\kappa_a\sigma^a_{(\triangle)}\right]\sigma^a_{(\triangle)}\sigma^b_{(\triangle)}}{\left(\prod_{a'=1}^{n}\int_{-\infty}^{\infty}d\sigma^{a'}_{(\triangle)}\right)\exp\left[-\frac{1}{2}\sum_{a,b=1}^{n}\lambda_{ab}\sigma^a_{(\triangle)}\sigma^b_{(\triangle)}-\sum_{a=1}^{n}\kappa_a\sigma^a_{(\triangle)}\right]}\right|_{\lambda_{ab}=\lambda^*_{ab}(\hat{q}),\kappa_a=\kappa^*_a(\hat{q})} \\ &= (\lambda^*)^{-1}_{ab} + \left(\sum_{c=1}^{n}(\lambda^*)^{-1}_{ac}\kappa^*_c\right)\left(\sum_{c'=1}^{n}(\lambda^*)^{-1}_{bc'}\kappa^*_{c'}\right) = (\lambda^*)^{-1}_{ab}. \end{aligned} \tag{4.60}$$

We find,

$$\prod_{a'=1}^{n}\mathrm{Tr}_{\boldsymbol{\sigma}^{a'}}[\cdots] \propto \left(\prod_{a\le b}\int_{-\infty}^{\infty}dq_{ab}\right)e^{cs^{(\sigma)}_{\mathrm{ent}}[\hat{q}]}\prod_{\triangle=1}^{c}\langle\cdots\rangle_\triangle\,, \tag{4.61}$$

where $s^{(\sigma)}_{\mathrm{ent}}[\hat{q}]$ represents entropic contribution of spins to the free energy, which is given by

$$s^{(\sigma)}_{\mathrm{ent}}[\hat{q}] = \sum_{a,b=1}^{n}\frac{1}{2}\lambda^*_{ab}q_{ab}+\frac{1}{2}\log\left(\frac{(2\pi)^n}{\det(\hat{\lambda}^*)}\right) = \frac{n}{2}(1+\log(2\pi))+\frac{1}{2}\log(\det\hat{q}). \tag{4.62}$$

Using Eq. (4.54) and Eq. (4.61) we find, for example,

$$\begin{aligned} &\prod_{a'=1}^{n}\left(\mathrm{Tr}_{\boldsymbol{S}^{a'}}\mathrm{Tr}_{\boldsymbol{\sigma}^{a'}}\right)(S^a)^\mu = 0 \qquad &&\prod_{a'=1}^{n}\left(\mathrm{Tr}_{\boldsymbol{S}^{a'}}\mathrm{Tr}_{\boldsymbol{\sigma}^{a'}}\right)(S^a)^\mu(S^b)^\mu = Q_{ab} \\ &\prod_{a'=1}^{n}\left(\mathrm{Tr}_{\boldsymbol{S}^{a'}}\mathrm{Tr}_{\boldsymbol{\sigma}^{a'}}\right)\sigma^a_{(\triangle)} = 0 \qquad &&\prod_{a'=1}^{n}\left(\mathrm{Tr}_{\boldsymbol{S}^{a'}}\mathrm{Tr}_{\boldsymbol{\sigma}^{a'}}\right)\sigma^a_{(\triangle)}\sigma^b_{(\triangle)} = q_{ab} \end{aligned} \tag{4.63}$$

4.2.3 Evaluation of free energy

Now the replicated partition function can be rewritten as,

$$Z^n \propto \left(\prod_i \prod_{a \le b} \int_{-\infty}^{\infty} d(Q_{ab})_i \int_{-\infty}^{\infty} d(q_{ab})_i \right) e^{M \sum_{i=1}^{N} \left(s_{\rm ent}^{(s)}[\hat{Q}_i] + \alpha s_{\rm ent}^{(\sigma)}[\hat{q}_i] \right) + NM\mathcal{F}_{\rm int}}, \tag{4.64}$$

where

$$\begin{aligned} & NM\mathcal{F}_{\rm int} \\ &= \log \left(\prod_i \prod_\mu \prod_{\triangle \in \partial i} \left\langle \prod_{\triangle=1}^{N_\triangle} e^{-\sum_{a=1}^{n} \beta V(\vec{\boldsymbol{S}}^a_{(\triangle)}, \vec{\sigma}^a_{(\triangle)})} \right\rangle_{i,\mu,\triangle} \right) \\ &= \sum_{\triangle=1}^{N_\triangle} \log \left(\prod_i \prod_\mu \left\langle \exp \left[\frac{\beta}{\sqrt{p}} \sum_{a=1}^{n} \sum_{i<j}^{p} A^a_{ij(\triangle)} \right] \right\rangle_{i,\mu,\triangle} \right). \end{aligned} \tag{4.65}$$

with

$$A^a_{ij} = \frac{J}{\sqrt{M}} \Big(1 + \delta(\sigma^a_{i(\triangle)} + \sigma^a_{j(\triangle)}) \Big) \sum_{\mu=1}^{M} (S^a_{i(\triangle)})^\mu (S^a_{j(\triangle)})^\mu + \epsilon \sigma^a_{i(\triangle)} \sigma^a_{j(\triangle)}. \tag{4.66}$$

In the derivation of the third line from the second line, we used the fact that the average can be performed independently for different $\triangle$. Noting that the average can be decoupled also different site i and spin component μ, we can evaluate $\mathcal{F}_{\rm int}$ using the cumulant expansion,

$$\log \left\langle e^{\frac{\beta}{\sqrt{p}} \sum_a \sum_{i<j} A^a_{ij}} \right\rangle = \frac{\beta}{\sqrt{p}} \sum_a \sum_{i<j} \left\langle A^a_{ij} \right\rangle + \frac{1}{2!} \left(\frac{\beta}{\sqrt{p}} \right)^2 \sum_{a,b} \sum_{i<j} \left(\left\langle A^a_{ij} A^b_{ij} \right\rangle - \left\langle A^a_{ij} \right\rangle \left\langle A^b_{ij} \right\rangle \right) + \cdots \tag{4.67}$$

with

$$\left\langle A^a_{ij} \right\rangle = 0, \tag{4.68}$$

$$\left\langle A^a_{ij} A^b_{ij} \right\rangle = \frac{J^2}{M} \big(1 + \delta^2 ((q_{ab})_i + (q_{ab})_j) \big) \sum_{\mu=1}^{M} (Q_{ab})_i (Q_{ab})_j + \epsilon^2 (q_{ab})_i (q_{ab})_j. \tag{4.69}$$

In the limit $p \to \infty$ we find,

$$\begin{aligned} \mathcal{F}_{\rm int}[\hat{Q}, \hat{q}] &= \frac{1}{NM} \frac{\beta^2}{2p} \sum_{a,b} \sum_{\triangle=1}^{N_\triangle} \sum_{i<j} \left[\frac{J^2}{M} \big(1 + \delta^2 ((q_{ab})_{i(\triangle)} + (q_{ab})_{j(\triangle)}) \big) \sum_{\mu=1}^{M} (Q_{ab})_{i(\triangle)} (Q_{ab})_{j(\triangle)} + \epsilon^2 (q_{ab})_{i(\triangle)} (q_{ab})_{j(\triangle)} \right] \\ &= \frac{1}{NM} \frac{\beta^2}{2p} \sum_{a,b} \sum_{\triangle=1}^{N_\triangle} \frac{p(p-1)}{2} \Big[J^2 \big(1 + 2\delta^2 (q_{ab})_{(\triangle)} \big) (Q_{ab})^2_{(\triangle)} + \epsilon^2 (q_{ab})^2_{(\triangle)} \Big] \\ &= \frac{\alpha \beta^2}{4} \sum_{a,b} \left[J^2 \big(1 + 2\delta^2 q_{ab} \big) Q^2_{ab} + \epsilon^2 q^2_{ab} \right] \end{aligned} \tag{4.70}$$

The integrations over each $(Q_{ab})_i$ can be performed in the limit $N \to \infty$ and $M \to \infty$ by the saddle point method. We assume $\hat{Q}_i = \hat{Q}$ and $\hat{q}_i = \hat{q}$ for any i since in our system every vertex is equivalent to each other.

Finally, we can rewrite the replicated partition function (Eq. (4.40)) as,

$$Z^n \propto \left(\prod_{a \leq b} \int_{-\infty}^{\infty} dQ_{ab} \int_{-\infty}^{\infty} dq_{ab} \right) e^{NMs_n[\hat{Q},\hat{q}]}, \tag{4.71}$$

where we defined

$$s_n[\hat{Q},\hat{q}] = s_{\text{ent}}^{(s)}[\hat{Q}] + \alpha s_{\text{ent}}^{(\sigma)}[\hat{q}] + \mathcal{F}_{\text{int}}. \tag{4.72}$$

The saddle point equations are given by,

$$0 = \left. \frac{\partial s_n[\hat{Q},\hat{q}]}{\partial Q_{ab}} \right|_{\hat{Q}=\hat{Q}^*,\hat{q}=\hat{q}^*}, \tag{4.73}$$

$$0 = \left. \frac{\partial s_n[\hat{Q},\hat{q}]}{\partial q_{ab}} \right|_{\hat{Q}=\hat{Q}^*,\hat{q}=\hat{q}^*}. \tag{4.74}$$

The stability condition is also required, namely the eigenvalues of the $\left(\frac{n-1}{2}\right) \times \left(\frac{n-1}{2}\right)$ Hessian matrix,

$$H_{Q_{ab},Q_{cd}} \equiv -\frac{\partial^2 s_n[\hat{Q},\hat{q}]}{\partial Q_{ab}\partial Q_{cd}} \qquad H_{Q_{ab},q_{cd}} \equiv -\frac{\partial^2 s_n[\hat{Q},\hat{q}]}{\partial Q_{ab}\partial q_{cd}} \qquad H_{q_{ab},q_{cd}} \equiv -\frac{\partial^2 s_n[\hat{Q},\hat{q}]}{\partial q_{ab}\partial q_{cd}} \quad (a<b, c<d) \tag{4.75}$$

in the $n \to 0$ limit, must be non negative. The resultant free energy functional reads,

$$-\beta f[\hat{Q}^*,\hat{q}^*] = \frac{-\beta F[\hat{Q}^*,\hat{q}^*]}{NM} = \frac{1}{NM} \lim_{n\to 0} \frac{\partial}{\partial n} \log Z^n[\hat{Q}^*,\hat{q}^*] = \left. \frac{\partial s_n[\hat{Q}^*,\hat{q}^*]}{\partial n} \right|_{n=0}. \tag{4.76}$$

4.3 Replica symmetric ansatz

Now our task is to solve the above problem with the simplest ansatz called the replica symmetric (RS) ansatz (see Sec. 1.1.3.1). In the replica symmetric (RS) ansatz we assume that the overlap matrices Q_{ab} and q_{ab} are given by,

$$\begin{aligned} Q_{ab} &= (1-Q)\delta_{ab} + Q, \\ q_{ab} &= (1-q)\delta_{ab} + q. \end{aligned} \tag{4.77}$$

Using Eq. (4.77) we find,

$$\log\det \hat{Q}^{\mathrm{RS}} = \log[1+(n-1)Q] + (n-1)\log(1-Q). \tag{4.78}$$

so that the entropic part of the free energy is obtained as

$$\begin{aligned} s_{\mathrm{ent}}^{(s)}[\hat{Q}^{\mathrm{RS}}] + \alpha s_{\mathrm{ent}}^{(\sigma)}[\hat{q}^{\mathrm{RS}}] = \frac{n(1+\alpha)}{2}(1+\log(2\pi)) + \frac{1}{2}\{\log[1+(n-1)Q] + (n-1)\log(1-Q)\} \\ + \frac{\alpha}{2}\{\log[1+(n-1)q] + (n-1)\log(1-q)\}. \end{aligned} \tag{4.79}$$

The interaction part of the free energy is obtained as,

$$\mathcal{F}_{\mathrm{int}}[\hat{Q}^{\mathrm{RS}}, \hat{q}^{\mathrm{RS}}] = \frac{\alpha\beta^2}{4}\big\{n\big[J^2(1+2\delta^2)+\epsilon^2\big] + n(n-1)\big[J^2(1+2\delta^2 q)Q^2 + \epsilon^2 q^2\big]\big\}. \tag{4.80}$$

Then the free energy within RS ansatz is calculated as

$$\begin{aligned} -\beta f^{\mathrm{RS}}(Q,q) &= \left.\frac{\partial s_n[\hat{Q}^{\mathrm{RS}}, \hat{q}^{\mathrm{RS}}]}{\partial n}\right|_{n=0} \\ &= \frac{1+\alpha}{2}(1+\log(2\pi)) + \frac{1}{2}\left(\frac{Q}{1-Q} + \log(1-Q)\right) + \frac{\alpha}{2}\left(\frac{q}{1-q} + \log(1-q)\right) \\ &+ \frac{\alpha\beta^2}{4}\big\{J^2(1+2\delta^2) + \epsilon^2 - \big[J^2(1+2\delta^2 q)Q^2 + \epsilon^2 q^2\big]\big\} \end{aligned} \tag{4.81}$$

The saddle point equations for the order parameters Q and q are obtained as,

$$0 = \frac{\partial(-\beta f^{\mathrm{RS}}(Q,q))}{\partial Q} = \frac{Q}{2}\left[\frac{1}{(1-Q)^2} - \alpha(\beta J)^2(1+2\delta^2 q)\right] \tag{4.82}$$

$$0 = \frac{\partial(-\beta f^{\mathrm{RS}}(Q,q))}{\partial q} = \frac{\alpha}{2}\left[\frac{q}{(1-q)^2} - (\beta\epsilon)^2 q - (\beta J\delta)^2 Q^2\right]. \tag{4.83}$$

We find that $Q=0, q=0$ is always a solution which represents the paramagnetic (disordered) phase. From Eq. (4.83) we also notice that Q becomes 0 if $q=0$, which is responsible for the simultaneous spin and lattice glass transition, as we will see below.

4.3.1 Separated glass transition

For $\epsilon > \sqrt{\alpha}J$, we find a finite q solution,

$$q = 1 - \frac{T}{\epsilon}, \tag{4.84}$$

at temperatures lower than $T^* = \epsilon$ while $Q=0$. Thus only the lattice is in a glassy phase while the spin remains paramagnetic. below another transition temperature T_c lower than T^*, a finite Q solution emerges.

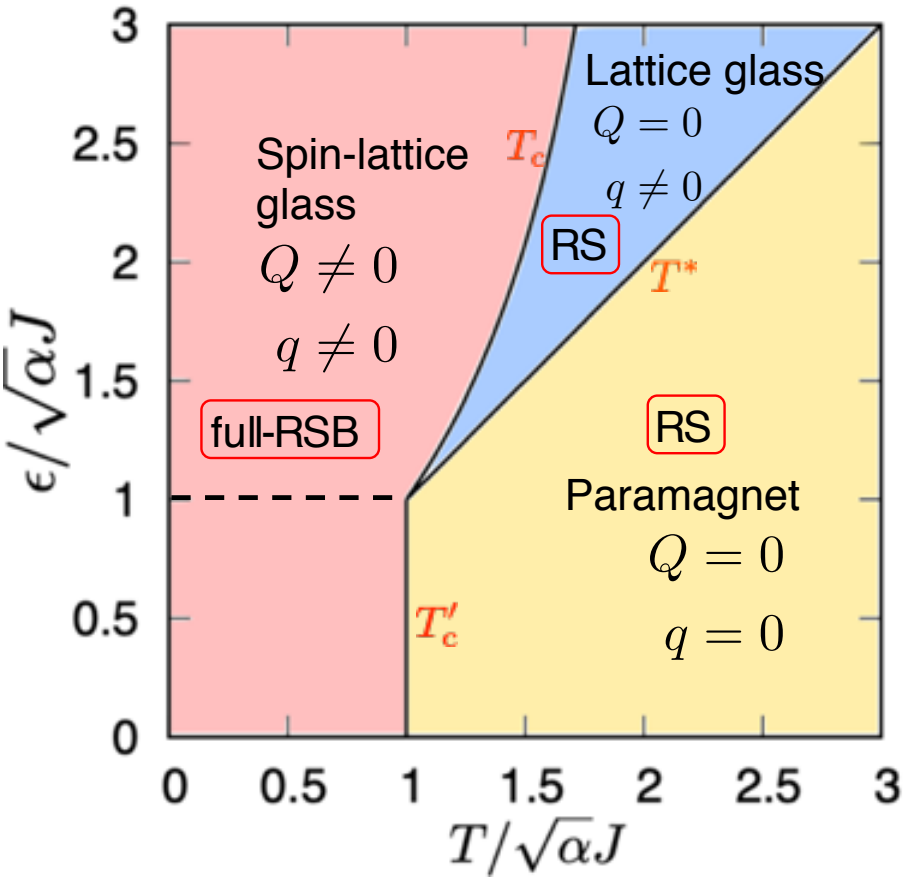

Figure 4.4: **Mean-field phase diagram**
Here $\delta = 1.5$. In the case of $\epsilon/\sqrt{\alpha}J > 1$, the lattice glass transition occurs on the line $T^* = \epsilon$ and the spin glass transition occurs on the line $T_c/\sqrt{\alpha}J = (\sqrt{\alpha}J/\epsilon)(\sqrt{\delta^4 + (\epsilon/\sqrt{\alpha}J)^2(2\delta^2+1)} - \delta^2)$. In the case of $\epsilon/\sqrt{\alpha}J < 1$, the simultaneous spin and lattice glass transition takes place on the line $T_c' = \sqrt{\alpha}J$.

Now, let us focus on a temperature slightly above T_c. Here the order parameter Q is small enough, namely $Q \ll 1$. It is useful to introduce a small parameter $u = q - (1 - T/\epsilon)$, $(u \ll 1)$. Then Eq. (4.82) and Eq. (4.83) become

$$1 + 2Q + 3Q^2 + O(Q^3) - \alpha(\beta J)^2\left(1 + 2\delta^2\left(1 - \frac{1}{\beta\epsilon} + u\right)\right) = 0, \tag{4.85}$$

$$u = \left(\frac{J\delta}{\epsilon}\right)\frac{Q^2}{2(\beta\epsilon - 1)} + O(Q^3). \tag{4.86}$$

Noting that u is proportional to Q^2, from the Eq. (4.85) up to $O(1)$, we find,

$$\frac{T_c}{\sqrt{\alpha}J} = \frac{\sqrt{\alpha}J}{\epsilon}\left(\sqrt{\delta^4 + \left(\frac{\epsilon}{\sqrt{\alpha}J}\right)^2(2\delta^2+1)} - \delta^2\right). \tag{4.87}$$

If $\epsilon = \sqrt{\alpha}J$ or the interaction between spins and lattice distortions are decoupled, namely $\delta = 0$, the transition temperature becomes $T_c = \sqrt{\alpha}J$. It can also be seen that the the phase boundary given by Eq. (4.87) is shifted to higher temperatures by increasing δ and it converges to another phase boundary

$$T^* = \epsilon$$

in the limit $\delta \to \infty$, i.e. the lattice glass phase disappears. A dimensionless temperature which measures the distance to the transition temperature can be defined as

$$t = \frac{T_c - T}{T_c} \tag{4.88}$$

and then we can write $\beta = \beta_c/(1-t)$. Using the dimensionless temperature, we can calculate the order parameter Q and the small parameter u as

$$Q = \alpha(\beta_c J)^2(1+2\delta^2)t + O(t^2), \tag{4.89}$$

$$u = \left(\frac{J\delta}{\epsilon}\right)\frac{\left[\alpha(\beta_c J)^2(1+2\delta^2)\right]^2}{2(\beta_c\epsilon - 1)}t^2 + O(t^3). \tag{4.90}$$

4.3.2 Simultaneous glass transition

For $\epsilon < \sqrt{\alpha}J$ the situation changes: a simultaneous spin and lattice glass transition takes place at the common transition temperature T_c'. Similarly to the separated case, let us focus on the order parameters near the critical point, namely $Q, q \ll 1$. From Eq. (4.83), we notice that q is much smaller than Q, more precisely $q \sim Q^2$. Dividing the saddle point equation Eq. (4.82) by Q and then expanding of the equation up to second order in Q, we find,

$$1 + 2Q + 3Q^2 - \alpha(\beta J)^2(1+2\delta^2 q) = 0. \tag{4.91}$$

We can easily find the critical temperature as $T_c' = \sqrt{\alpha}J$ which doesn't depend on the elastic energy scale ϵ nor the amplitude δ. This means that the spin degrees of freedom are primary for the simultaneous glass transition in this case.

Using the dimensionless temperature,

$$t' = \frac{T_c' - T}{T_c'}, \tag{4.92}$$

the order parameters Q and q become

$$Q = t' + \delta^2\frac{(\beta_c' J\delta)^2}{1-(\beta_c'\epsilon)^2}t'^2 + O(t'^3) = t' + \delta^2 q + O(t'^3), \tag{4.93}$$

$$q = \frac{(\beta_c' J\delta)^2}{1-(\beta_c'\epsilon)^2}t'^2 + O(t^3). \tag{4.94}$$

In this case, the order parameter of the spins Q is modified by that of the lattice distortions q.

4.4 Stability of the replica symmetric solution

In the previous section, we derived the free energy under the RS ansatz. Now, let us investigate the stability of the replica symmetric solution. The necessary condition of the RS solution to be stable is that the eigenvalues of Hessian matrix $\mathcal{H}$ given by,

$$\hat{\mathcal{H}} = \begin{bmatrix} H_{QQ} & H_{Qq} \\ H_{qQ} & H_{qq} \end{bmatrix}, \tag{4.95}$$

are all non-negative, where the submatrices H_{QQ}, $H_{Qq} = H_{qQ}$ and H_{qq} are given by Eq. (4.75). To analyze these matrices we need the first and second derivatives of the functional $s_n[\hat{Q}, \hat{q}]$, which are obtained as,

$$\frac{\partial s_n}{\partial Q_{ab}} = \frac{1}{2} Q_{ab}^{-1} + \alpha(\beta J)^2(1 + 2\delta^2 q_{ab})Q_{ab} \tag{4.96}$$

$$\frac{\partial s_n}{\partial q_{ab}} = \alpha\left[\frac{1}{2} q_{ab}^{-1} + (\beta J\delta)^2 Q_{ab}^2 + (\beta\epsilon)^2 q_{ab}\right] \tag{4.97}$$

$$\frac{\partial^2 s_n}{\partial Q_{ab}\partial Q_{cd}} = -\left(Q_{ac}^{-1}Q_{bd}^{-1} + Q_{ad}^{-1}Q_{bc}^{-1}\right) + \delta_{ac}\delta_{bd}\alpha(\beta J)^2(1 + 2\delta^2 q_{ab}) \tag{4.98}$$

$$\frac{\partial^2 s_n}{\partial Q_{ab}\partial q_{cd}} = 2\delta_{ac}\delta_{bd}\alpha(\beta J\delta)^2 Q_{ab} \tag{4.99}$$

$$\frac{\partial^2 s_n}{\partial q_{ab}\partial q_{cd}} = \alpha\left[-\left(q_{ac}^{-1}q_{bd}^{-1} + q_{ad}^{-1}q_{bc}^{-1}\right) + \delta_{ac}\delta_{bd}(\beta\epsilon)^2\right], \tag{4.100}$$

where $a < b, c < d$. For the RS solution, the components of inverse matrix $\hat{Q_n}^{-1}$ and $\hat{q_n}^{-1}$ are obtained as,

$$\left\{Q_n^{\mathrm{RS}}\right\}^{-1}_{a\neq b} = -\frac{\det \hat{\Delta}^Q_{n-1}}{\det \hat{Q}_n^{\mathrm{RS}}} = -\frac{Q}{(1 + (n-1)Q)(1-Q)}, \tag{4.101}$$

$$\left\{Q_n^{\mathrm{RS}}\right\}^{-1}_{a=b} = \frac{\det \hat{Q}^{\mathrm{RS}}_{n-1}}{\det \hat{Q}_n^{\mathrm{RS}}} = \frac{1 + (n-2)Q}{(1 + (n-1)Q)(1-Q)}, \tag{4.102}$$

$$\left\{q_n^{\mathrm{RS}}\right\}^{-1}_{a\neq b} = -\frac{\det \hat{\Delta}^q_{n-1}}{\det \hat{q}_n^{\mathrm{RS}}} = -\frac{q}{(1 + (n-1)q)(1-q)}, \tag{4.103}$$

$$\left\{q_n^{\mathrm{RS}}\right\}^{-1}_{a=b} = \frac{\det \hat{q}^{\mathrm{RS}}_{n-1}}{\det \hat{q}_n^{\mathrm{RS}}} = \frac{1 + (n-2)q}{(1 + (n-1)q)(1-q)}, \tag{4.104}$$

where $\hat{\Delta}^Q_{n-1}$ and $\hat{\Delta}^q_{n-1}$ are $(n-1)$-dimensional matrices whose components are obtained as,

$$\{\hat{\Delta}^Q_{n-1}\} = (1-Q)(\delta_{ab} - \delta_{a1}\delta_{b1}) + Q, \tag{4.105}$$

$$\{\hat{\Delta}^q_{n-1}\} = (1-q)(\delta_{ab} - \delta_{a1}\delta_{b1}) + q, \tag{4.106}$$

respectively. Then the submatrices of the Hessian matrix in the limit $n \to 0$ are rewritten as

$$\{H_{QQ}\}_{ab,cd} = M_1^Q \frac{\delta_{ac}\delta_{bd} + \delta_{ad}\delta_{bc}}{2} + M_2^Q \frac{\delta_{ac} + \delta_{ad} + \delta_{bc} + \delta_{bd}}{4} + M_3^Q \tag{4.107}$$

$$\{H_{Qq}\}_{ab,cd} = -2\delta_{ac}\delta_{bd}\alpha(\beta J\delta)^2 Q \tag{4.108}$$

$$\{H_{qq}\}_{ab,cd} = M_1^q \frac{\delta_{ac}\delta_{bd} + \delta_{ad}\delta_{bc}}{2} + M_2^q \frac{\delta_{ac} + \delta_{ad} + \delta_{bc} + \delta_{bd}}{4} + M_3^q, \tag{4.109}$$

where

$$M_1^Q = \frac{2}{(1-Q)^2} - 2\alpha(\beta J)^2(1 + 2\delta^2 q) \qquad M_2^Q = -\frac{4Q}{(1-Q)^3} \qquad M_3^Q = -\frac{2Q^2}{(1-Q)^4} \tag{4.110}$$

$$M_1^q = \frac{2\alpha}{(1-q)^2} - 2\alpha(\beta\epsilon)^2 \qquad M_2^q = -\frac{4\alpha q}{(1-q)^3} \qquad M_3^q = -\frac{2\alpha q^2}{(1-q)^4}. \tag{4.111}$$

Note that H_{Qq} can be written as

$$H_{Qq} = c\hat{I} \tag{4.112}$$

where $\hat{I}$ represents an identity matrix and

$$c = -2\alpha(\beta J\delta)^2 Q. \tag{4.113}$$

Next, we analyze the eigenvalues of the submatrices H_{QQ} and H_{qq}. Let us write the eigenvalue equation in the form

$$H\boldsymbol{\mu} = \lambda\boldsymbol{\mu}, \tag{4.114}$$

where $\boldsymbol{\mu} = (\mu_{(1,2)}, \mu_{(1,3)}, ..., \mu_{(1,n)}, \mu_{(2,3)}, \mu_{(2,4)}, ..., \mu_{(n-1,n)})$ represents an $\{n(n-1)/2\}$-dimensional eigenvector and λ represents an eigenvalue. We define the first eigenvector $\boldsymbol{\mu}_L$ whose all components are a_L and then the eigenvalue λ_L becomes,

$$\lambda_L = \frac{1}{2}M_1 + \frac{(n-1)}{2}M_2 + \frac{n(n-1)}{2}M_3 \xrightarrow[n\to 0]{} \frac{1}{2}(M_1 - M_2). \tag{4.115}$$

The second eigenvector $\boldsymbol{\mu}_A^\theta$ for a specific replica θ is defined as the components $\mu_{A(a,b)}^\theta = a_A$ when a or b is equal to θ and $\mu_{A(a,b)}^\theta = b_A$ otherwise. The eigenvector has $(n-1)$-fold degeneracy and should be orthogonal to the first eigenvector $\boldsymbol{\mu}_L$. Thus, the components a_A and b_A satisfy the condition $a_A = -\{(m/2) - 1\}b_A$. The eigenvalue λ_A becomes,

$$\lambda_A = \frac{1}{2}M_1 + \frac{n-2}{4}M_2 \xrightarrow[n\to 0]{} \frac{1}{2}(M_1 - M_2), \tag{4.116}$$

which is also degenerate with λ_L. The third and final eigenvector $\boldsymbol{\mu}_R^{\theta,\phi}$ for two specific replicas θ, ϕ has the components $\mu_{R(a,b)}^{\theta,\phi} = a_R$ when (a,b) is equal to (θ,ϕ) and $\mu_{R(a,b)}^{\theta,\phi} = b_R$ when a or b is equal to θ or ϕ and $\mu_{R(a,b)}^{\theta} = c_R$ otherwise. Since it should be orthogonal to the first and second eigenvectors, the components satisfy the conditions $a_R = -(n-2)b_R$ and $b_R = -\{(n-3)/2\}c_R$. Then the eigenvalue called a replicon mode is,

$$\lambda_R = \frac{1}{2}M_1, \tag{4.117}$$

which is the minimum one among three eigenvalues if the order parameters Q and q are positive. Therefore replica symmetry breaking takes place when the replicon mode λ_R becomes negative. Hereafter, we use a label k $(k = 1, 2, ..., n(n-1)/2)$ such that

$$\lambda_k^\alpha = \begin{cases} \lambda_L^\alpha & (k = 1) \\ \lambda_A^\alpha & (2 \le k \le n) \\ \lambda_R^\alpha & (n+1 \le k \le n(n-1)/2), \end{cases} \tag{4.118}$$

where $\alpha = Q, q$.

In the case of our system, the eigenvalues of H_{QQ} and H_{qq} are obtained as

$$\lambda_L^Q = \lambda_A^Q = \frac{1+Q}{(1-Q)^3} - \alpha(\beta J)^2(1 + 2\delta^2 q) \quad \lambda_R^Q = \frac{1}{(1-Q)^2} - \alpha(\beta J)^2(1 + 2\delta^2 q), \tag{4.119}$$

$$\lambda_L^q = \lambda_A^q = \alpha\left[\frac{1+q}{(1-q)^3} - (\beta\epsilon)^2\right] \qquad \lambda_R^q = \alpha\left[\frac{1}{(1-q)^2} - (\beta\epsilon)^2\right]. \tag{4.120}$$

Note that H_{QQ} and H_{qq} are diagonalized by the same orthogonal matrix

$$P = (\boldsymbol{\mu}_L, \underbrace{\boldsymbol{\mu}_A^1, ..., \boldsymbol{\mu}_A^{n-1}}_{n-1}, \underbrace{\boldsymbol{\mu}_R^{1,2}, ...}_{n(n-3)/2}), \tag{4.121}$$

namely we find the relation,

$$\begin{bmatrix} P^{-1} & O \\ O & P^{-1} \end{bmatrix} \begin{bmatrix} H_{QQ} & H_{Qq} \\ H_{qQ} & H_{qq} \end{bmatrix} \begin{bmatrix} P & O \\ O & P \end{bmatrix} = \begin{bmatrix} \lambda_1^Q & & & c & & \\ & \ddots & & & \ddots & \\ & & \lambda_{n(n-1)/2}^Q & & & c \\ c & & & \lambda_L^q & & \\ & \ddots & & & \ddots & \\ & & c & & & \lambda_{n(n-1)/2}^q \end{bmatrix} \equiv \hat{\Xi}, \tag{4.122}$$

where c is defined in Eq. (4.113) The determinant of the matrix $\Xi - \lambda \hat{I}$ which should be zero is calculated as

$$\det\left[\hat{\Xi} - \lambda \hat{I}\right] = \prod_k \left[(\lambda_k^Q - \lambda)(\lambda_k^q - \lambda) - c^2\right] = 0 \tag{4.123}$$

and the eigenvalue of the Hessian matrix is obtained as

$$\lambda_{k\pm} = \frac{\lambda_k^Q + \lambda_k^q \pm \sqrt{(\lambda_k^Q - \lambda_k^q)^2 + 4c^2}}{2}. \tag{4.124}$$

Note that $\lambda_{k\pm} = \lambda_k^Q, \lambda_k^q$ ($\lambda_{k+} > \lambda_{k-}$) if $c = -2\alpha(\beta J\delta)^2 Q = 0$, which means that each degree of freedom doesn't affect the stability of another degree of freedom. Thus, in the paramagnetic phase (see Fig. 4.4), all eigenvalues are positive,

$$\lambda_{L-} = \lambda_{A-} = \lambda_{R-} = \begin{cases} \alpha(1 - (\beta\epsilon)^2) = \alpha(1 + T^*/T)(1 - T^*/T) & (\epsilon > \sqrt{\alpha}J), \\ 1 - \alpha(\beta J)^2 = (1 + T_c'/T)(1 - T_c'/T) & (\epsilon < \sqrt{\alpha}J), \end{cases} \tag{4.125}$$

and then the RS solutions are stable.

4.4.1 Separated glass transition

For $\epsilon > \sqrt{\alpha}J$, the lattice glass transition occurs at the transition temperature T^* and λ_{i-} for all k become 0. below T^*, i.e. in the lattice glass phase, $\lambda_{L-} = \lambda_{A-}$ becomes positive again,

$$\lambda_{\mathrm{L}-} = \lambda_{\mathrm{A}-} = \frac{2\alpha q}{(1-q)^3}, \tag{4.126}$$

but λ_{R-} remains 0. It means that the system becomes marginally stable in the lattice glass phase similarly to the spherical SK model. [24] below another glass transition temperature T_c, noting that λ_R^Q and λ_R^q can be calculated as

$$\lambda_R^Q = 0 \tag{4.127}$$

$$\lambda_R^q = 2\alpha(\beta\epsilon)^3 u + O(t^3) \sim O(t^2), \tag{4.128}$$

we can evaluate the replicon mode as,

$$\lambda_{R-} = \frac{\lambda_R^q - \sqrt{\left(\lambda_R^q\right)^2 + 4c^2}}{2} = -c + O(t^2) \sim -t. \tag{4.129}$$

Therefore, the continuous replica symmetry breaking should take place at T_c.

4.4.2 Simultaneous glass transition

For $\epsilon < \sqrt{\alpha}J$, the simultaneous spin and lattice glass transition occurs at T_c' and λ_{k-} for all k becomes 0. below T_c', $\lambda_{A-} = \lambda_{L-}$ becomes positive again,

$$\lambda_{A-} = \lambda_{L-} = \frac{2Q}{(1-Q)^3}. \tag{4.130}$$

From Eq. (4.93), Eq. (4.94), Eq. (4.119) and Eq. (4.119), λ_R^Q and λ_R^q can be calculated as

$$\lambda_R^Q = 0, \tag{4.131}$$

$$\lambda_R^q = \alpha(\beta J\delta)^2 \frac{Q^2}{q}. \tag{4.132}$$

The replicon mode becomes

$$\begin{aligned} \lambda_{R-} &= \frac{\lambda_R^q - \sqrt{\left(\lambda_R^q\right)^2 + 4c^2}}{2} \\ &= -\frac{c^2}{\lambda_R^q} = -4\frac{\alpha\beta^2 J^4\delta^4}{T^2-\epsilon^2}t'^2 \sim -t'^2. \end{aligned} \tag{4.133}$$

Therefore, the continuous replica symmetry breaking should take place at T_c'.

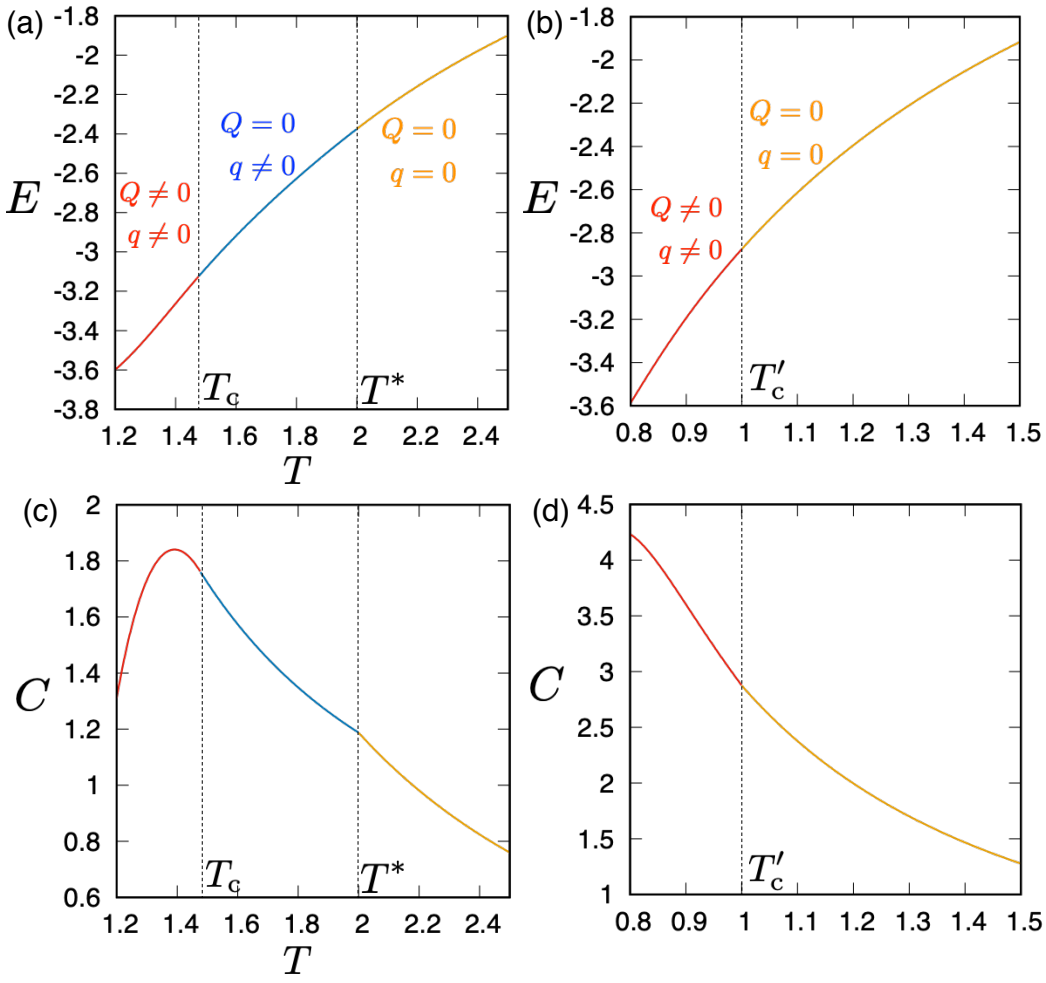

Figure 4.5: **Internal energy and heat capacity**
(a), (b): Internal energy and heat capacity in the separated case ($\delta = 1.5, J\sqrt{\alpha} = 1, \epsilon = 2$). (c), (d): Internal energy and heat capacity in the simultaneous case ($\delta = 1.5, J\sqrt{\alpha} = 1, \epsilon = 0.5$). T^*, T_c and T'_c are the glass transition temperatures obtained above.

4.5 Physical quantities

Having established the phase diagram in Fig. 4.4, let us study some basic physical quantities of the model.

4.5.1 Energy, Heat capacity

The internal energy is given by,

$$\frac{\langle E \rangle}{NM} = -\frac{\partial(-\beta f)}{\partial \beta} = -\frac{\alpha\beta}{2}\left\{J^2(1+2\delta^2) + \epsilon^2 - \left[J^2(1+2\delta^2 q)Q^2 + \epsilon^2 q^2\right]\right\}. \tag{4.134}$$

Fig. 4.5 (a) and (b) show typical behaviors of the temperature dependence of the energy in the case of (a) separated ($\delta = 1.5, \sqrt{\alpha}J = 1, \epsilon = 2$) and (b) simultaneous ($\delta = 1.5, \sqrt{\alpha}J = 1, \epsilon = 0.5$) glass transitions, respectively. Note that we are using the RS solutions for both Q and q which is incorrect below T_c and T'_c, however it is useful to check whether there are any singularities or not. We find that the internal energy monotonically decrease and it doesn't exhibit any singularities for both the separated and the simultaneous cases.

The heat capacity is calculated as,

$$\frac{C}{NM} = \frac{1}{NM}\frac{\partial \langle E \rangle}{\partial T}. \tag{4.135}$$

Fig. 4.5 (c) and (d) display the temperature dependence of the heat capacity for the same parameter as above. We also find that there are any singularities.

4.5.2 Glass susceptibility

The glass susceptibility is given by the inverse matrix of the Hessian matrix $\hat{\mathcal{H}}$, i.e.

$$\hat{\chi} = \begin{bmatrix} \chi_{QQ} & \chi_{Qq} \\ \chi_{qQ} & \chi_{qq} \end{bmatrix} = \begin{bmatrix} H_{QQ} & H_{Qq} \\ H_{qQ} & H_{qq} \end{bmatrix}^{-1}. \tag{4.136}$$

In order to obtain the components χ_{ij}, let us consider the matrix $\hat{S}$ defined such that

$$\hat{S}^{-1}\hat{\mathcal{H}}\hat{S} = \begin{bmatrix} \lambda_{1+} & & & & & & \\ & \ddots & & & & & \\ & & \lambda_{m+} & & & & \\ & & & \lambda_{1-} & & & \\ & & & & \ddots & & \\ & & & & & \lambda_{m-} \end{bmatrix}, \tag{4.137}$$

$$\hat{S}^{-1}\hat{\chi}\hat{S} = \begin{bmatrix} 1/\lambda_{1+} & & & & & & \\ & \ddots & & & & & \\ & & 1/\lambda_{m+} & & & & \\ & & & 1/\lambda_{1-} & & & \\ & & & & \ddots & & \\ & & & & & 1/\lambda_{m-} \end{bmatrix}, \tag{4.138}$$

where $m = n(n-1)/2$. Using matrix $\hat{S}$, we find,

$$\chi_{ij} = \sum_l \frac{s_{il}s_{jl}}{\lambda_l} \tag{4.139}$$

where s_{ij} is the components of the matrix and λ_l is a short hand notation defined such that

$$\lambda_l = \begin{cases} \lambda_{l+} & (l \le m) \\ \lambda_{(l-m)-} & (m < l). \end{cases} \tag{4.140}$$

Using Eq. (4.121) and Eq. (4.122), we notice that $\hat{S}$ can be factorized as

$$\hat{S} = \begin{bmatrix} P & O \\ O & P \end{bmatrix}\hat{T}, \tag{4.141}$$

where $\hat{T}$ is a matrix which diagonalize $\hat{\Xi}$ (Eq. (4.122)), i.e.

$$\hat{T}^{-1}\hat{\Xi}\hat{T} = \hat{T}^{-1}\begin{bmatrix} \lambda_1^Q & & & c & & & \\ & \ddots & & & \ddots & & \\ & & \lambda_m^Q & & & c & \\ c & & & \lambda_L^q & & & \\ & \ddots & & & \ddots & & \\ & & c & & & \lambda_m^q \end{bmatrix}\hat{T} = \begin{bmatrix} \lambda_{1+} & & & & & & \\ & \ddots & & & & & \\ & & \lambda_{m+} & & & & \\ & & & \lambda_{1-} & & & \\ & & & & \ddots & & \\ & & & & & \lambda_{m-} \end{bmatrix}, \tag{4.142}$$

whose c is defined in Eq. (4.113), λ_k^Q and λ_k^q are given by Eq. (4.118), Eq. (4.119) and Eq. (4.120). Here, each eigenvector is normalized as

$$\sum_{i=1}^{2m} t_{ij}^2 = 1 \quad \text{for all } j, \tag{4.143}$$

where t_{ij} is the component of the matrix $\hat{T}$. If $c = 0$ (see Eq. (4.113)), i.e. in the paramagnetic phase ($Q = q = 0$) or the lattice glass phase ($Q = 0, q > 0$), $\hat{T}$ becomes an identity matrix $\hat{I}$. In the spin-lattice glass phase ($Q, q > 0$), we find that the component t_{ij} can be calculated as

$$t_{kj} = \begin{cases} t_{(k+m)j} = 0 & \text{if } (\lambda_k^Q - \lambda_j)(\lambda_k^q - \lambda_j) - c^2 \neq 0 \quad \Leftrightarrow \quad \lambda_j \neq \lambda_{k\pm} \\ -\dfrac{\lambda_k^q - \lambda_j}{c} t_{(k+m)j} & \text{if } (\lambda_k^Q - \lambda_j)(\lambda_k^q - \lambda_j) - c^2 = 0 \quad \Leftrightarrow \quad \lambda_j = \lambda_{k\pm} \end{cases} \tag{4.144}$$

for $k = 1, 2, ..., m$.

Now let us consider the inverse matrix of $\hat{\Xi}$ whose components are obtained as,

$$\left\{\hat{\Xi}^{-1}\right\}_{ij} = \sum_l \frac{t_{il} t_{jl}}{\lambda_l}, \tag{4.145}$$

because we have

$$\hat{\chi} = \begin{bmatrix} P^{-1} & O \\ O & P^{-1} \end{bmatrix} \hat{\Xi}^{-1} \begin{bmatrix} P & O \\ O & P \end{bmatrix} \tag{4.146}$$

and all components of P are in the order of $O(1)$. Here, it is convenient to decompose $\hat{\Xi}^{-1}$ as

$$\hat{\Xi}^{-1} = \begin{bmatrix} \Xi_{QQ}^{-1} & \Xi_{Qq}^{-1} \\ \Xi_{qQ}^{-1} & \Xi_{qq}^{-1} \end{bmatrix}, \tag{4.147}$$

since the components of $\chi_{\alpha\beta}$ ($\alpha, \beta = Q, q$) are associated with only the components of $\Xi_{\alpha\beta}$.

We show the schematic picture of the temperature dependences of $\chi_{\alpha\beta}$ ($\alpha, \beta = Q, q$) in Fig. 4.6. In the following, we present the detail of the calculation to obtain this.

4.5.2.1 Separated glass transitions

For $\epsilon > \sqrt{\alpha} J$, the system exhibits the lattice glass transition at T^* and the spin glass transition at T_c which is lower than T^* (see Fig. 4.4). Slightly above T^* the system is in the paramagnetic phase ($Q = q = 0$) and $1/\lambda_k^q$ for all k proportional to $1/|t^*|$ (see Eq. (4.124) and Eq. (4.125)) where we introduced

$$t^* = (T^* - T)/T^*. \tag{4.148}$$

The components of χ_{qq}^{-1} diverge at T^*,

$$\{\chi_{qq}\}_{ij} \sim O(|t^*|^{-1}) \quad (T > T^*), \tag{4.149}$$

while χ_{QQ}^{-1} and χ_{Qq}^{-1} have no singularity.

Slightly above T_c the system is in the lattice glass phase ($Q = 0, q \neq 0$) and $1/\lambda_k^Q$ for all k proportional to $1/|t|$ (see Eq. (4.119) and Eq. (4.124)) where $t = (T_c - T)/T_c$ (Eq. (4.88)). The components of χ_{QQ}^{-1} diverge at T_c,

$$\{\chi_{QQ}\}_{ij} \sim O(|t|^{-1}) \quad (T > T_c), \tag{4.150}$$

while χ_{Qq}^{-1} remains 0.

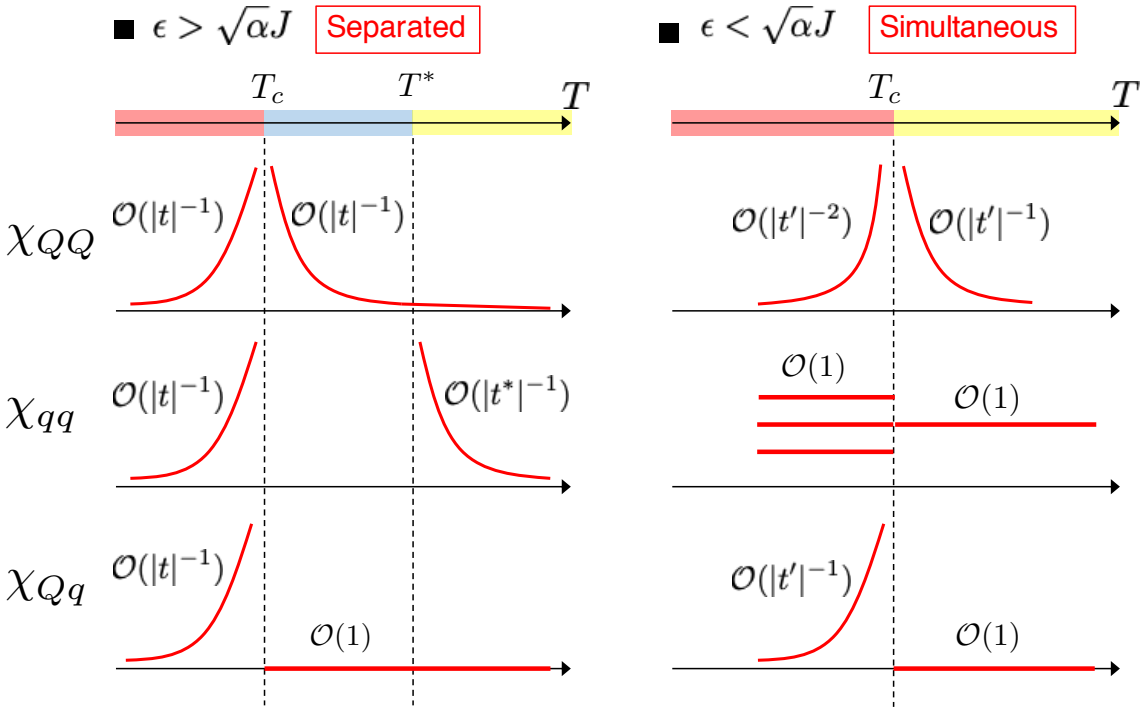

Figure 4.6: **Schematic picture of temperature dependence of the glass susceptibilities**

In the spin-lattice glass phase, c becomes finite, namely $\hat{T}$ is not an identity matrix. Now let us consider the components of $\hat{\Xi}^{-1}$ related to $\lambda_{R\pm}$ because they are relevant to the divergent features of the components of $\hat{\chi}$. Using Eq. (4.144) and Eq. (4.145) and noting $(\lambda_R^q - \lambda_{R\pm})/c \sim O(1)$, we find the magnitude of the components of $\hat{T}$ are,

$$\hat{T} = \begin{bmatrix} O(1) & O(1) \\ O(1) & O(1) \end{bmatrix}. \tag{4.151}$$

Here each block size is $m \times m$. Since $\frac{1}{\lambda_{R-}} \sim |t|^{-1}$, the components of $\hat{\Xi}^{-1}_{ij}$ become

$$\left\{\Xi^{-1}_{QQ}\right\}_{ij} \sim \left\{\Xi^{-1}_{Qq}\right\}_{ij} \sim \left\{\Xi^{-1}_{qq}\right\}_{ij} \sim O(|t|^{-1}). \tag{4.152}$$

Therefore, the components of $\hat{\chi}$ slightly below T_c are obtained as

$$\{\chi_{QQ}\}_{ij} \sim \{\chi_{Qq}\}_{ij} \sim \{\chi_{qq}\}_{ij} \sim O(|t|^{-1}) \quad (T < T_c). \tag{4.153}$$

4.5.2.2 Simultaneous glass transition

For $\epsilon < \sqrt{\alpha}J$, the system exhibits the simultaneous spin and lattice glass transitions at T_c' (see Fig. 4.4). Slightly above T_c' the system is in the paramagnetic phase ($Q = q = 0$) and $1/\lambda_k^Q$ for all k proportional to $1/|t'|$ (see Eq. (4.119) and Eq. (4.124)) where $t = (T_c - T)/T_c$ (Eq. (4.88)). The components of χ^{-1}_{QQ} diverge at T_c',

$$\{\chi_{QQ}\}_{ij} \sim O(|t'|^{-1}) \quad (T > T_c'), \tag{4.154}$$

while χ^{-1}_{Qq} and χ^{-1}_{qq} remain finite.

Similarly to the case of separated glass transitions (Sec. 4.5.2.1), in the spin-lattice glass phase, it is convenient to consider the components of $\hat{\Xi}^{-1}$ related to the only $\lambda_{R\pm}$. Using Eq. (4.144) and Eq. (4.145)

and noting $(\lambda_R^q - \lambda_{R-})/c \sim O(|t'|^{-1})$ and $(\lambda_R^q - \lambda_{R+})/c \sim O(|t'|)$, we find the magnitude of the components of $\hat{T}$ are evaluated as,

$$\hat{T} = \begin{bmatrix} O(|t'|) & O(1) \\ O(1) & O(|t'|) \end{bmatrix}. \tag{4.155}$$

Since $1/\lambda_{R-} \sim |t|^{-2}$, the components of $\hat{\Xi}_{ij}^{-1}$ become

$$\left\{\Xi_{QQ}^{-1}\right\}_{ij} \sim O(|t'|^{-2}), \tag{4.156}$$

$$\left\{\Xi_{Qq}^{-1}\right\}_{ij} \sim O(|t'|^{-1}), \tag{4.157}$$

$$\left\{\Xi_{qq}^{-1}\right\}_{ij} \sim O(1). \tag{4.158}$$

Therefore, the components of $\hat{\chi}$ slightly below $T_{\rm c}$ are obtained as

$$\{\chi_{QQ}\}_{ij} \sim O(|t'|^{-2}), \tag{4.159}$$

$$\{\chi_{Qq}\}_{ij} \sim O(|t'|^{-1}), \tag{4.160}$$

$$\{\chi_{qq}\}_{ij} \sim O(1). \tag{4.161}$$

The notable fact is that the glass susceptibility of lattice distortions $\{\chi_{qq}\}_{ij}$ does not diverge by approaching the simultaneous glass transition temperature $T_{\rm c}'$ from both sides due to the pre-factor t_{ij} while the glass order parameter q becomes finite.

4.6 Discussion and summary of the mean-field theory

In this chapter, we constructed the exactly solvable mean-field model of our effective model in the spherical limit. This model is defined on the Bethe lattice made of the $(p-1)$-dimensional simplices. We analyzed this model in the limit $p \to \infty$ using the replica method. As a result, we found that the system exhibits the separated spin and lattice glass transitions if the energy scale of the lattice distortion is larger than one of the exchange interaction, more precisely $\epsilon > \sqrt{\alpha}J$. On the other hand, in the case of $\epsilon < \sqrt{\alpha}J$, spin and lattice glass transitions simultaneously take place.

In the case of the separated glass transition, the lattice distortion are firstly frozen. The transition temperature T^* does not depend on the amplitude of the spin-lattice coupling δ and this glass transition can occur without the spin-lattice coupling. We speculate this is a pathology of the mean-field theory which is absent in finite dimensional systems. At T^*, only the lattice glass susceptibility χ_{qq} exhibits the divergent behavior. In the lattice glass phase, the RS solution remains marginally stable, which is the same as the spherical SK model. At $T_{\rm c}$ lower than T^*, the spin glass transition takes place. Here, $T_{\rm c}$ depends on δ. Interestingly, the system falls into a full-RSB state due to the spin-lattice coupling ($\delta > 0$). In addition, the spin glass susceptibility χ_{QQ} diverges at $T_{\rm c}$ and the cross glass susceptibility χ_{Qq} between spin and lattice distortion also diverges at $T_{\rm c}$.

In the case of the simultaneous glass transition, the transition temperature $T_{\rm c}'$ doesn't depend on the spin lattice coupling δ nor the energy scale of the lattice distortion but depends on the exchange interaction between spins. The lattice glass order parameter q becomes non-zero as $q \sim |t'|^2$ when the spin glass order parameter appears. This is due to the coupling term formed as $\sigma \boldsymbol{S}_i \cdot \boldsymbol{S}_j$. In the Hamiltonian Eq. (4.29)-Eq. (4.31) we can find that the inner product $\boldsymbol{S}_i \cdot \boldsymbol{S}_j$ can be regarded as the random field for lattice distortion variable σ while the lattice distortion can be regarded as the randomness in the exchange interaction for spin variable $\boldsymbol{S}_i$ and $\boldsymbol{S}_j$. The situation is similar to the random field spin model, where the order parameter is always finite. Thus, in our model, if the spin glass order parameter becomes finite, the lattice glass order parameter automatically become finite. At $T_{\rm c}'$, the lattice glass susceptibility doesn't diverge because of the vanishing pre-factor while the spin glass susceptibility diverges. below $T_{\rm c}'$, the system falls into the full-RSB state in similarly to the case of separated glass transitions.

Chapter 5

DISCUSSIONS

Relevance of our effective model for experiments

Let us discuss the relevance of our effective model for experiments. The existence of the spin glass transition itself is already established in $Y_2Mo_2O_7$ and its families. A recent analysis showed that the lattice distortions possibly plays a certain role in the glass transition [**?**, 62]. Our model introduced in Sec. 1.4.4 is constructed motivated by this finding so that it includes the direct coupling between the lattice distortion and the spin. In three dimension, the two degrees of freedom simultaneously undergo a glass transition (Chap. 3), indicating that they generate an effect of dynamical randomness to each other. We also found that our mean-field model in the infinite dimension exhibits the glass transition accompanying with the full-RSB due to the couplings between spins and lattice distortions (Chap. 4). Experiments can test our scenario by examining whether the nonlinear dielectric susceptibility diverges in the vicinity of T_c, where already the nonlinear magnetic susceptibility shows the divergence (see Fig. 1.14 (b)). Previously, the orbital-glass transition was observed in the $FeCr_2S_4$, where the dielectric spectroscopy measurement played a major role, detecting the slowing down of orbital dynamics [77]. Similar techniques shall be applied to the pyrochlore materials.

Comparison between the cases of $d = 3$ and $d = \infty$

In our mean-field theory in $d = \infty$, we assumed that every ordered state is suppressed by the frustration and we analyzed only the glass transition. As a result, we found that spins and lattice distortions separately frozen for large ϵ and simultaneously frozen for small ϵ (see Fig. 4.4). On the other hand, in the numerical simulation of our effective model on a pyrochlore lattice ($d = 3$), the system exhibits long-ranged ordered distortion pattern such as a breathing all-*in*-all-*out* pattern for small ϵ (see Sec. 2.13) while the simultaneous spin and glass transition occurs at $T_c^{(d=3)}$ even for large ϵ. It appers that the results of the numerical simulation in the three dimension and the mean-field analysis are not consistent with each other in this respect. In the following, let us discuss the consistency between the results of $d = 3$ (Chap. 3) and $d = \infty$ (Chap. 4).

On the mean-field model, the lattice glass transition at $T^{*(d=\infty)} = \epsilon$ for $\epsilon > \sqrt{\alpha}J$ exists without the spin-lattice coupling δ (see Eq. (4.83)) because of the spherical limit $M \to \infty$. This is simply a phase transition resulting from the temperature becoming lower than the energy scale of the elastic energy ϵ. This would mean "spin-ice glass transition" which we consider as an artifact in $d = \infty$. We rather consider that the "lattice glass transition" corresponds to the crossover from the lattice liquid state to the lattice ice state in the three dimension (see Fig. 3.11 (d)-(f)). The spin glass transition at $T_c^{(d=\infty)}$ being lower than T^* accompanies with the full-RSB as long as the coupling δ is non-zero and the spin glass transition temperature $T_c^{(d=\infty)}$ depends on ϵ, δ and $\sqrt{\alpha}J$. We expect that the spin glass transition temperature $T_c^{(d=\infty)}$ corresponds to the simultaneous spin and lattice glass transition temperature $T_c^{(d=3)}$. $T_c^{(d=\infty)}$ is shifted to higher temperatures by increasing ϵ and converge to $J\sqrt{\alpha(2\delta^2+1)}$. We speculate that this corresponds to the ϵ dependence of the peak temperature of the heat capacity in the three dimension (see Fig. 3.11 (a)).

Scenario of effectively quenched distortions

Let us comment on the scenario often posed experimentally, which expects that the freezing of the orbital degrees of freedom occurs at a higher temperature than the spin glass transition [61, 62]. In a sence this corresponds to the case of separated glass transition found in the mean-field theory discussed above.

Once the orbital configuration is frozen, our model is reduced to the standard Edwards-Anderson model of Heisenberg spins with quenched randomness on a pyrochlore lattice, which is known to exhibit a spin glass transition. [52, 53] Actually, if we increase ϵ, the ice-rule configuration of orbitals is selected at the higher temperature, which is detected by the broad peak in the heat capacity (see Fig. 3.11 (d)). However, this peak does not mean the transition but a crossover; Below that temperature, the orbitals are still dynamically fluctuating among huge numbers of quasi-degenerate ice-rule configurations. In lowering the temperature, the orbital dynamics naturally slows down but without any thermodynamic anomaly much as usual spin ices [78]. Interestingly, at a lower temperature the heat capacity shows a second peak which should be attributed to coupling between the spin and lattice distortions. In our scenario, we anticipate the thermodynamic spin-orbital glass transition at around that temperature.

Effects of other type interaction

Some other effect such as the spin-orbit interaction [66], the spin-phonon coupling [53, 79] and longer range interactions [80, 81], which are not included in our model, may play a secondary role to reproduce more precisely the experimental measurements, e.g. its universality class, whereas our findings proved that the interplay of nearest-neighbor interactions and the dynamical JT distortions can solely drive the system to the glass transition.

Chapter 6

CONCLUSION

Possibility of disorder-free spin glass is a long-standing, challenging issue in glass physics and frustrated magnetism. In a previous work [82], we examined the possibility of a disorder-free orientational glass in a soft-matter system and concluded that it is absent there. In the case of the pyrochlore magnet $Y_2Mo_2O_7$, there were convincing experimental results yet no theoretical explanations.

In this thesis, we showed theoretically that spin and orbital degrees of freedom in the pyrochlore oxide $Y_2Mo_2O_7$, which is free of quenched disorder, can exhibit a simultaneous glass transition driven by the interplay of the two degrees of freedom. Historically, the spin models on the periodic lattices without quenched randomness have failed to realize the thermodynamic glass transition in any finite dimensions. Our model overcomes this long-standing issue by including the effect of lattice distortions that selects the choice of orbitals the spins are living on, which can then vary the sign of the spin exchange interactions, properly reflecting the experimental observations (Chap. 2). Because of the geometrical frustration effect of the pyrochlore lattice, the lattice distortions follow the so-called ice-rule, generating macroscopic numbers of different patterns with the same elastic Jahn-teller energy. Through the couplings of the lattice distortion and the spin, the two degrees of freedom work as dynamical randomness to each other giving rise to a modified glassy energy landscape. Our Monte Carlo simulations show the simultaneous spin and orbital glass transition at the same temperature, which can be detected by the negative divergence of the nonlinear susceptibility in both the magnetic and dielectric measurements (Chap. 3). Our mean-field theory using the replica theory also show that the full-RSB due to the spin-lattice coupling can occur (Chap. 4). To conclude our effective model exhibit disorder-free glass transitions of the spin and distortions. We believe there are many possibilities of further theoretical, numerical and experimental works based on our results.

Acknowledgement

We would like to thank Professor H. Yoshino who is my adviser for fruitful discussions and his continuous support. Without his guidance and invaluable advices, I couldn't complete this thesis. I also thank Professor C. Hotta from the University of Tokyo for helpful advices and discussions. I also owe a very important debt to Prof. Kikuchi, Prof. Kawamura, Prof. Akutsu and Prof. Hanasaki whose meticulous comments were an enormous help to me. I would also like to express my gratitude to my family for their moral support and warm encouragements. This work was supported by KAKENHI (No. 19H01812, 17K05533, 17K05497,18H01173,17H02916) from MEXT, Japan. The computation in this work has been done using the facilities of the Supercomputer Center, the Institute for Solid State Physics, the University of Tokyo, OCTOPUS and supercomputer system SX-ACE at the Cybermedia Center, Osaka University.

Appendix A

Correspondence between random field and replica coupling

Let us consider a common random field $\{h_i\}$ for two replicas a and b of Ising spin systems $\{S_i^a\}$ and $\{S_i^b\}$ with the same Hamiltonian $H(\{S_i\})$, namely we consider the following extended Hamiltonian,

$$H_{a+b} = H(\{S_i^a\}) + H(\{S_i^b\}) - \sum_{i=1}^{N} h_i\Big(S_i^a + S_i^b\Big). \tag{A.1}$$

Now let $\{h_i\}$ follow the Gaussian distribution with the mean 0 and the variance $2\lambda/\beta$, i.e.

$$P(h_i) = \sqrt{\frac{\beta}{4\pi\lambda}} e^{\frac{\beta h_i^2}{4\lambda}}. \tag{A.2}$$

In this case, the averaged partition function with respect to $\{h_i\}$ is obtained as,

$$\begin{aligned} Z_\lambda &= \mathrm{Tr}_{\{S_i^a\},\{S_i^b\}} \left(\prod_i \int P(h_i) \right) e^{-\beta(H(\{S_i^a\})+H(\{S_i^b\})-\sum_{i=1}^N h_i\left(S_i^a+S_i^b\right))} \\ &= \mathrm{Tr}_{\{S_i^a\},\{S_i^b\}} e^{-\beta(H(\{S_i^a\})+H(\{S_i^b\}))} \prod_i \left(e^{\beta\sum_{i=1}^N h_i\left(S_i^a+S_i^b\right)} \right) \\ &= \mathrm{Tr}_{\{S_i^a\},\{S_i^b\}} e^{-\beta H_\lambda} \end{aligned}$$

with

$$H_\lambda = H(\{S_i^a\}) + H(\{S_i^b\} - \lambda \sum_{i=1}^{N} S_i^a S_i^b + 2. \tag{A.3}$$

This effective Hamiltonian has the same form as Eq. (1.28) except for the constant term. Thus, $\lambda \to +0$ in Eq. (1.33) corresponds to the zero limit of the random field $h_i \to 0$.

Appendix B

Replica theory for the system with quenched disorder

The replica theory was introduced first by Edwards-Anderson [9] to study the Edwards-Anderson (EA) model for spinglasses (Eq. (1.3)) which has the quenched disorder in the interaction J_{ij} between the spins. It is important to notice that thermodynamic quantities are self-averaging. For example the free-energy per spin $-\beta F_{\rm J}/N$, which depends on specific realizations of the quenched disorder J_{ij} if the system size N is finite, becomes independent of the disorder in the thermodynamic limit $N \to \infty$. This means that we are allowed to take average over the quenched disorder $\overline{\cdots}$ of the free-energy.

$$-\beta F = \overline{\log Z}, \tag{B.1}$$

where $\beta = 1/k_B T$ is the inverse temperature, Z is the partition function in the canonical ensemble and $\overline{\cdots}$ represents the random average of quenched disorder $\{J_{ij}\}$. Using the replica method (see Eq. (1.40) and Eq. (1.41)) we can write

$$\overline{\log Z} = \lim_{n\to 0} \frac{\partial}{\partial n} \overline{Z^n}. \tag{B.2}$$

When n is integer, Z^n can be interpreted as the partition function of n-replicated system $\{\boldsymbol{S}_i^a\}$ $(a = 1, 2, ..., n)$ with common $\{J_{ij}\}$. For example, for the case of Ising EA model (Eq. (1.3)), the replicated Hamiltonian is given by

$$\overline{Z^n} = \overline{{\rm Tr}_{\{S_i^a\}} \exp\left(-\beta \sum_{a=1}^{n} H_a\right)} = \overline{{\rm Tr}_{\{S_i^a\}} \exp\left(-\beta \sum_{a=1}^{n} \sum_{<ij>} J_{ij} S_i^a S_j^a\right)}. \tag{B.3}$$

Hence we can take the random average easily. Assuming that the random quenched variables $\{J_{ij}\}$ follow Gaussian distribution with mean 0 and variance J,

$$P(J_{ij}) = \frac{1}{\sqrt{2\pi J^2}} \exp\left[\frac{1}{2J^2} J_{ij}^2\right]. \tag{B.4}$$

Then the random average of the partition function is calculated as

$$\overline{Z^n} = \left(\prod_{i\le j} \int dJ_{ij} P_{ij}\right) Z^n = {\rm Tr}_{\{S_i^a\}} \exp\left(\frac{(\beta J)^2}{2} \sum_{a,b=1}^{n} \sum_{<ij>} (S_i^a S_i^b)(S_j^a S_j^b)\right). \tag{B.5}$$

Therefore the partition function can be regarded as one of the uniform system.

Appendix C

Summary of magnetism

Magnetism is one of the most fundamental field in condensed matter physics. The microscopic origin of the magnetism is the spin degrees of freedom of the electrons. Macroscopic number of spins interact with each other and exhibits various cooperative phenomena such as ferromagnetism, antiferromagnetism, ferrimagnetism, chiral magnetism and so on. In addition, in frustrated magnets, we can find cooperative phenomena where not only spins but also lattice distortions play important roles.

In this section, we review some basic principles of magnetism from microscopic point of views. I first summarize the single electron problem. Then I summarize the properties of magnetic ion in condensed matter and magnetic interactions. Especially, I will focus on insulated magnets whose electrons are localized on the periodic lattices. Moreover, I will review Jahn-Teller distortions cased by the instability of the degenerated electrons.

C.1 Single electron state in a free magnetic ion

At first, I will recall the orbital states of a single electron around a nucleus. The electron moves in a spherically symmetric potential

$$u(r) = -\frac{Ze^2}{r} \tag{C.1}$$

resulting from the nucleus, where r is the distance between the electron and the nucleus. The Schrödinger equation for the electron is given by,

$$H\phi(\boldsymbol{r}) = \left[-\frac{\hbar^2}{2m}\nabla^2 + u(r)\right]\phi(\boldsymbol{r}) = E\phi(\boldsymbol{r}), \tag{C.2}$$

where m is the mss of the electron, $H = -\frac{\hbar^2}{2m}\nabla^2 + u(r)$ is the Hamiltonian, E is the eigenvalue (energy) and $\nabla = (\frac{\partial}{\partial x}, \frac{\partial}{\partial y}, \frac{\partial}{\partial z})$. It is convenient to use the angular momentum in order to specify the electron state. The angular momentum $\boldsymbol{l} = (l_x, l_y, l_z)$ of the electron is given by,

$$\boldsymbol{l} = \boldsymbol{r} \times \boldsymbol{p}, \tag{C.3}$$

where $\boldsymbol{r}$ and $\boldsymbol{p} = -i\hbar\nabla$ represent the position and the momentum of the electron, respectively. The angular momentum satisfies the following commutation relations,

$$[l_y, l_z] = il_x, \quad [l_z, l_x] = il_y, \quad [l_x, l_y] = il_z, \quad \left[\boldsymbol{l}^2, l_k\right] = 0, \quad (k = x, y, z). \tag{C.4}$$

In quantum mechanics, the angular momentum is measured in the unit of Plank constant $\hbar$. Hereafter we regard $\hbar$ as a unit of the angular momentum for simplicity.

Using the angular momentum operator the Lapracian ∇^2 can be rewritten as,

$$\nabla^2 = \frac{\partial 2}{\partial r} + \frac{2}{r}\frac{\partial}{\partial r} - \frac{\boldsymbol{l}^2}{r^2}. \tag{C.5}$$

Now, we assume that the wave function can be written as,

$$\phi(\boldsymbol{r}) = R(r)Y(\theta, \varphi), \tag{C.6}$$

where (r, θ, φ). Then the Schrödinger can also be divided into the radial part and the angular part,

$$\left[-\frac{\hbar^2}{2m}\left(\frac{\partial 2}{\partial r} + \frac{2}{r}\frac{\partial}{\partial r}\right) + \frac{l(l+1)\hbar^2}{2mr^2} + u(r)\right]R(r) = ER(r), \tag{C.7}$$

$$\boldsymbol{l}^2 Y(\theta, \varphi) = l(l+1)Y(\theta, \varphi), \tag{C.8}$$

where $Y(\theta, \varphi)$ satisfies,

$$l_z Y(\theta, \varphi) = mY(\theta, \varphi), \tag{C.9}$$

because $\boldsymbol{l}^2$ and l_z are commutative (Eq. (C.4)). Eq. (C.8) and Eq. (C.9) are well-known differential equations of spherical harmonics which are defined as,

$$Y_{lm}(\theta, \varphi) = \Theta_{lm}(\theta)\Phi_m(\varphi) \tag{C.10}$$

with

$$\Theta_{lm}(\theta) = (-1)^{\frac{m+|m|}{2}}\sqrt{\frac{2l+1}{2}\frac{(l-|m|)!}{(l+|m|)!}}P_l^m(\cos\theta), \tag{C.11}$$

$$\Phi_m(\varphi) = \frac{1}{\sqrt{2\pi}}e^{im\varphi}. \tag{C.12}$$

$P_l^m(\cos\theta)$ is called the associated Legendre polynomial and defined as,

$$P_l^m(z) = \frac{(1-z^2)^{\frac{|m|}{2}}}{2^l l!}\frac{\mathrm{d}^{|m|+l}}{\mathrm{d}z^{|m|+l}}\left(z^2-1\right)^l. \tag{C.13}$$

From Eq. (C.12), we find that m must be an integer and, from $\boldsymbol{l}^2 - l_z^2 = l_x^2 + l_y^2$, m takes $m = -l, -l+1, ...l-1, l$. l and m are called the azimuthal quantum number and the magnetic quantum number, respectively.

Assuming the binding condition $\lim_{r\to\infty} R(r) \to 0$, we can derive the eigenvalue as,

$$E_n = -\frac{me^2}{2\hbar^2 n^2}, \qquad n = 1, 2, 3, \cdots, \tag{C.14}$$

where n is called the principal quantum number. Note that the eigenvalue doesn't depend on the azimuthal quantum number l and l takes values $l = 0, 1, 2, ..., n-1$. Since m takes $2l+1$ kinds of integers for l, the eigenstate has n^2-degeneracy for a given n. According to the convention in spectroscopy, the state for $l = 0, 1, 2, 3, 4, \cdots$ are represented as $s, p, d, f, g, \cdots$, e.g. $3d$ orbital is the state for $n = 3$ and $l = 2$. Here we are neglecting interactions with other electrons. We know that the orbitals for larger l have the higher energies.

Let us turn to summarize the spin angular momentum. The spin has the dimension of the angular momentum, which is the same as that of the orbital degree of freedom, namely the angular moment is quantized in the unit of the Planck constant $\hbar$. The spin angular moment $\boldsymbol{s} = \hbar\boldsymbol{s}' = \hbar(s_x, s_y, s_z)$ of a single

electron takes $\pm\hbar/2$ in the arbitrary direction (hereafter we call $\boldsymbol{s}'$ simply as $\boldsymbol{s}$). The components s_x, s_y, s_z are represented as the matrices,

$$s_x = \frac{1}{2}\sigma_x = \frac{1}{2}\begin{bmatrix} 0 & 1 \\ 1 & 0 \end{bmatrix}, \qquad s_y = \frac{1}{2}\sigma_y = \frac{1}{2}\begin{bmatrix} 0 & -i \\ i & 0 \end{bmatrix}, \qquad s_z = \frac{1}{2}\sigma_z = \frac{1}{2}\begin{bmatrix} 1 & 0 \\ 0 & -1 \end{bmatrix}, \tag{C.15}$$

where $\sigma_x, \sigma_y, \sigma_z$ are called Pauli's matrix. Similarly to the orbital angular momentum $\boldsymbol{l}$, the components s_x, s_y, s_z satisfies commutation relations,

$$[s_y, s_z] = is_x, \quad [s_z, s_x] = is_y, \quad [s_x, s_y] = is_z, \quad \left[\boldsymbol{s}^2, s_k\right] = 0, \quad (k = x, y, z). \tag{C.16}$$

Let σ be the spin coordinate. Since $\boldsymbol{s}^2 = s_x^2 + s_y^2 + s_z^2 = 3/4$, it is convenient to introduce the spin-state function $\theta_{sm_s}(\sigma)$ $(s = 1/2)$ as follows,

$$\boldsymbol{s}^2\theta_{sm_s}(\sigma) = s(s+1)\theta_{sm_s}(\sigma), \tag{C.17}$$

$$s_z\theta_{sm_s}(\sigma) = m_s\theta_{sm_s}(\sigma), \tag{C.18}$$

where m_s takes $\pm 1/2$ and is called the spin quantum number. $\theta_{\frac{1}{2}\frac{1}{2}}(\sigma)$ is called the up-spin state and $\theta_{\frac{1}{2}-\frac{1}{2}}(\sigma)$ is called the down-spin state, more precisely

$$\begin{aligned} \theta_{\frac{1}{2}\frac{1}{2}}(\uparrow) &= 1, \qquad \theta_{\frac{1}{2}\frac{1}{2}}(\downarrow) = 0, \\ \theta_{\frac{1}{2}-\frac{1}{2}}(\uparrow) &= 0, \qquad \theta_{\frac{1}{2}-\frac{1}{2}}(\downarrow) = 1, \end{aligned} \tag{C.19}$$

The state of a single electron is represented by the direct product between the orbital state and the spin state, namely

$$\psi_k(\boldsymbol{r}, \sigma) = \phi_{nlm}(\boldsymbol{r})\theta_{\frac{1}{2}m_s}(\sigma), \tag{C.20}$$

where the quantum number is $k = (n, l, m, m_s)$. According to Pauli's principle, each state can accommodate only one electron. Then in general, the electron state becomes filled from the lowest energy state up to higher states successively, e.g. the helium atom has $(1s)^2$ and the lithium atom has $(1s)^2(2s)$. However it is not necessarily that the lower energy states are filled up in the order of $1s, 2s, 2p, 3s, 3p, 3d, 4s, \cdots$. For example, the energy of the $3d$ state is mostly equal to the one of the $4s$ state and the potassium atom has $(1s)^2(2s)^2(2p)^6(3s)^2(3p)^6(4s)$. Subsequentially, Ca, Sc and Ti have $(4s)^2, (4s)^2(4p), (4s)^2(3d)^2$. Elements in which some d states are occupied are called transition metals. In addition, elements in which some f states are occupied are called rare earths. Transition metal ions and rare earth ions show fascinating properties such as magnetic properties because of its incomplete d and f sub-shell.

C.2 Crystal Field

Magnetic ion in the ion crystal is affected by the electric field produced by the coordinated anions, which is called the crystal field. The typical coordinations of anions are the octahedral coordination where 6 anions surround the magnetic ion and the tetrahedral coordination where 4 anions surround the magnetic ion, as shown in Fig. C.1. Here, the spatial symmetry of the magnetic ion is lowered from the spherical symmetry. In this section, I recall how the symmetry lowering makes the degenerated d orbitals split in the cases where one electron exists in the d orbital.

C.2.1 Cubic crystal field

Let us consider the case that the magnetic ion is affected by the cubic crystal field and 6 anions are located in the equal distances from the magnetic ion (See Fig. C.1 (a)). If the magnetic ion is located at the origin

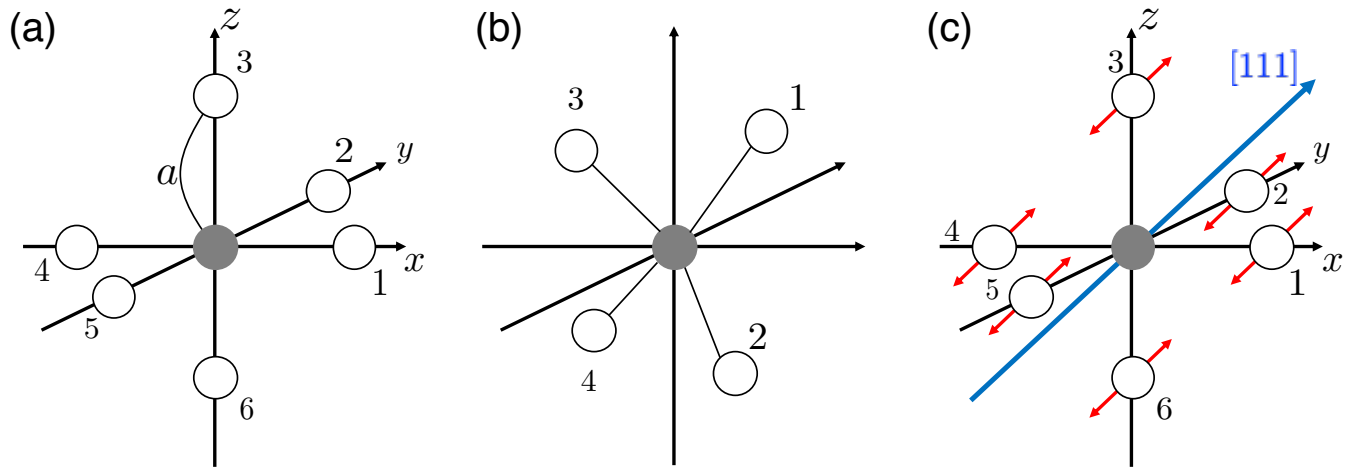

Figure C.1: **Examples of crystal fields**
Filled circle and open circle represent the magnetic ion and the coordinated anions, respectively. (a): Octahedral coordination. (b): Tetrahedral coordination. (a) and (b) have the cubic symmetry. (c): Octahedral coordination with the trigonal symmetry, which is distorted in the [111] direction.

and the electron of the magnetic ion is at $\boldsymbol{r}$ and the anions with the charge $-Ze$ are at $R_1 = (a, 0, 0), R_2 = (0, a, 0), R_3 = (0, 0, a), R_4 = (-a, 0, 0), R_5 = (0, -a, 0), R_6 = (0, 0, -a)$, the Schrödinger equation and the Hamiltonian for the electron become,

$$H\phi(\boldsymbol{r}) = E\phi(\boldsymbol{r}), \tag{C.21}$$

$$H = H_0 + v_{\rm cry}(\boldsymbol{r}), \tag{C.22}$$

with

$$H_0 = -\frac{\hbar^2}{2m}\nabla^2 + u(\boldsymbol{r}) \tag{C.23}$$

and the crystal field,

$$v_{\rm cry}(\boldsymbol{r}) = \sum_{i=1}^{6} \frac{Ze^2}{|\boldsymbol{R}_i - \boldsymbol{r}|}. \tag{C.24}$$

In the previous section, we have derived the eigenvalue and the eigenstate of the unperturbed Hamiltonian H_0.

Now, we consider $v_{\rm cry}(\boldsymbol{r})$ as the perturbation for H_0. Assuming $r \ll a$, we make use of the multipole expansion,

$$\frac{1}{|\boldsymbol{R}_i - \boldsymbol{r}|} = \frac{1}{a}\sum_{k=0}^{\infty}\left(\frac{r}{a}\right)^k P_k(\cos\omega_i), \tag{C.25}$$

where ω_i represents the angle between $\boldsymbol{r}$ and $\boldsymbol{R}_i$. Converting $\boldsymbol{r}$ and $\boldsymbol{R}_i$ to the poler coordinate system, $\boldsymbol{r} = (r, \theta, \varphi)$ and $\boldsymbol{R}_i = (a, \theta_i, \varphi_i)$ and using the addition formula,

$$P_k(\cos\omega_i) = \frac{4\pi}{2k+1}\sum_{m=-k}^{k} Y_{km}(\theta, \varphi)Y_{km}^*(\theta_i, \varphi_i), \tag{C.26}$$

the crystal-field potential becomes,

$$v_{\rm cry}(\boldsymbol{r}) = \sum_{k=0}^{\infty}\sum_{m=-k}^{k} A_{km}r^k C_m^{(k)}(\theta, \varphi), \tag{C.27}$$

with

$$A_{km}^{\rm cub} = \sqrt{\frac{4\pi}{2k+1}} \frac{Ze^2}{a^{k+1}} \sum_{i=1}^{6} Y_{km}^*(\theta_i, \phi_i), \tag{C.28}$$

$$C_m^{(k)}(\theta, \varphi) = \sqrt{\frac{4\pi}{2k+1}} Y_{km}(\theta, \varphi). \tag{C.29}$$

We can obtain $A_{km}^{\rm cub}$ just by substituting the positions of anions into $\{\theta_i, \phi_i\}$. Note that $A_{km}^{\rm cub}$ vanishes for $m = \pm 1, \pm 2, \pm 3$ or $k = 2$ or $k =$ (odd) because of the cubic symmetry. Thus, the crystal-field potential becomes,

$$v_{\rm cry}(r, \theta, \phi) = \frac{6Ze^2}{a} + \frac{7Ze^2}{2a^5} r^4 \left\{ C_0^{(4)}(\theta, \varphi) + \sqrt{\frac{5}{14}} \left[C_4^{(4)} + C_{-4}^{(4)} \right] \right\} + \cdots . \tag{C.30}$$

Here, the first term,

$$A_{00}^{\rm cub} = \frac{6Ze^2}{a}, \tag{C.31}$$

is just the simple electrostatic energy as if the electron is at (0,0,0) and the following terms,

$$v_{\rm cub} = \frac{7Ze^2}{2a^5} r^4 \left\{ C_0^{(4)}(\theta, \varphi) + \sqrt{\frac{5}{14}} \left[C_4^{(4)} + C_{-4}^{(4)} \right] \right\} + \cdots , \tag{C.32}$$

reflect the cubic symmetry of the system. It is worth to mention that the second order terms with r^2 vanish because of the cubic symmetry.

In order to examine the energy difference given by the crystal-field potential, we expand the wave function $\phi(\boldsymbol{r})$ with the unperturbed eigenstate of the single electron subjected to the spherical symmetric potential (Eq. (C.1)),

$$\phi(\boldsymbol{r}) = \sum_{nlm} a_{nlm} \phi_{nlm}(\boldsymbol{r}) = \sum_{nlm} a_{nlm} \left| nlm \right\rangle . \tag{C.33}$$

Substituting Eq. (C.33) into Eq. (C.21) and multiplying $\langle nlm|$, we find,

$$(E_n - E) a_{nlm} + \sum_{n'l'm'} \left\langle nlm \right| v_{\rm cry} \left| n'l'm' \right\rangle = 0 \tag{C.34}$$

with

$$H_0 \phi_{nlm}(\boldsymbol{r}) = E_n \phi_{nlm}(\boldsymbol{r}), \tag{C.35}$$

$$\left\langle nlm \right| v_{\rm cry} \left| n'l'm' \right\rangle = \int d^3\boldsymbol{r} \phi_{nlm}^*(\boldsymbol{r}) v_{\rm cry}(\boldsymbol{r}) \phi_{n'l'm'}(\boldsymbol{r}). \tag{C.36}$$

Using Eq. (C.6) and rewriting Eq. (C.36), we find that we need to calculate the integral,

$$\begin{aligned} \left\langle l'm' \right| C_m^{(k)} \left| l''m'' \right\rangle &= \int Y_{l'm'}(\theta, \varphi) C_m^{(k)}(\theta, \varphi) Y_{l''m''}(\theta, \varphi) \sin\theta d\theta d\varphi \\ &= \sqrt{\frac{4\pi}{2k+1}} \int \Theta_{l'm'}(\theta) \Theta_{km}(\theta) \Theta_{l''m''}(\theta) \left(\frac{1}{2\pi} \right)^{\frac{3}{2}} e^{i(-m'+m+m'')\varphi} \sin\theta d\theta d\varphi \\ &= \frac{1}{\sqrt{2k+1}} \int \Theta_{l'm'}(\theta) \Theta_{km}(\theta) \Theta_{l''m''}(\theta) \delta_{m,m'-m''} \sin\theta d\theta. \end{aligned} \tag{C.37}$$

Here, we see that $\langle l'm'| C_m^{(k)} |l''m''\rangle$ takes non-zero value if $m = m' - m''$. Thus, we just need

$$\left\langle lm \right| C_{m-m'}^{(k)} \left| l'm' \right\rangle = c^k(lm, l'm'), \tag{C.38}$$

m	m'	c^0	c^2	c^4
±2	±2	1	$-2/7$	$+1/21$
±2	±1	0	$+\sqrt{6}/7$	$-\sqrt{5}/21$
±2	0	0	$-2/7$	$+\sqrt{15}/21$
±1	±1	1	$+1/7$	$-4/21$
±1	0	0	$+1/7$	$+\sqrt{30}/21$
0	0	1	$+2/7$	$+6/21$
±2	∓2	0	0	$+\sqrt{70}/21$
±2	∓1	0	0	$-\sqrt{35}/21$
±1	∓1	0	$-\sqrt{6}/7$	$-2\sqrt{10}/21$

Table C.1: **The values of** $c^k(2,m|2,m')$
They can be calculated by substituting Eq. (C.11) into Eq. (C.37).

which has important properties such that

$$k+l+l' = \text{even number}, \tag{C.39}$$
$$|l-l'| \le k \le l+l', \tag{C.40}$$
$$c^k(lm,l'm') = (-1)^{m-m'}c^k(l'm',lm). \tag{C.41}$$

Note that, for the case of d electron ($l=l'=2$), thus $c^k(lm,l'm')$ becomes 0 for $k \le 4$ and the values of $c^k(2m,2m')$ are listed in Table. C.1.

Now, we assume that the matrix elements between different n and l states in Eq. (C.34) can be neglected, more precisely we assume,

$$(E'_n - E)a_{n2m} + \sum_{m'=-2}^{2} \langle n2m|\, v_{\text{cub}}\, |n2m'\rangle = 0, \qquad (m=-2,-1,0,1,2), \tag{C.42}$$

where

$$E'_n = E_n + A_{00}. \tag{C.43}$$

From Table. C.1, we can easily calculate $\langle n2m|\, v_{\text{cub}}\, |n2m'\rangle$ as

$$\begin{aligned}
\langle n2\pm2|\, v_{\text{cub}}\, |n2\pm2\rangle &= Dq,\\
\langle n2\pm1|\, v_{\text{cub}}\, |n2\pm1\rangle &= -4Dq,\\
\langle n20|\, v_{\text{cub}}\, |n20\rangle &= 6Dq,\\
\langle n2\pm2|\, v_{\text{cub}}\, |n2\mp2\rangle &= 5Dq,
\end{aligned} \tag{C.44}$$

with

$$D = \frac{35Ze}{4a^5}, \tag{C.45}$$
$$q = \frac{2e}{105}, \tag{C.46}$$
$$\bar{r^4} = \int |R_{n2}(r)| r^4 r^2 dr. \tag{C.47}$$

If a_{n2m} in Eq. (C.42) has a non-zero solution, the following determinant must be zero, i.e.

$$\begin{vmatrix} E'_n + Dq - E & 0 & 0 & 0 & 5Dq \\ 0 & E'_n - 4Dq - E & 0 & 0 & 0 \\ 0 & 0 & E'_n + 6Dq - E & 0 & 0 \\ 0 & 0 & 0 & E'_n - 4Dq - E & 0 \\ 5Dq & 0 & 0 & 0 & E'_n + Dq - E \end{vmatrix} = 0. \tag{C.48}$$

The eigenvalues are obtained as,

$$E(t_{2g}) = E'_n - 4Dq, \quad \text{(degeneracy 3)}, \tag{C.49}$$
$$E(e_g) = E'_n + 6Dq, \quad \text{(degeneracy 2)}, \tag{C.50}$$

and the eigenstates are obtained as,

$$\begin{aligned} t_{2g}: \quad \varphi_\xi &= \frac{i}{\sqrt{2}}(\varphi_{n21} + \varphi_{n2-1}) = \sqrt{\frac{15}{4\pi}}\frac{yz}{r^2}R_{n2}(r), \\ \varphi_\eta &= -\frac{1}{\sqrt{2}}(\varphi_{n21} - \varphi_{n2-1}) = \sqrt{\frac{15}{4\pi}}\frac{zx}{r^2}R_{n2}(r), \\ \varphi_\zeta &= -\frac{i}{\sqrt{2}}(\varphi_{n22} - \varphi_{n2-2}) = \sqrt{\frac{15}{4\pi}}\frac{xy}{r^2}R_{n2}(r), \end{aligned} \tag{C.51}$$

$$\begin{aligned} e_g: \quad \varphi_u &= \varphi_{n20} = \sqrt{\frac{5}{16\pi}}\frac{3z^2 - r^2}{r^2}R_{n2}(r), \\ \varphi_v &= \frac{1}{\sqrt{2}}(\varphi_{n22} + \varphi_{n2-2}) = \sqrt{\frac{15}{16\pi}}\frac{x^2 - y^2}{r^2}R_{n2}(r), \end{aligned} \tag{C.52}$$

These states are called t_{2g} and e_g according to the convention of the group theory. We show these wave functions in Fig. C.2. Although the total energy of three t_{2g} and two e_g orbitals did't change by the perturbation, t_{2g} has the lower energy than before. This implies the system is stabilized by lowering the symmetry if there are unfilled orbitals.

Similarly, in the case of the tetrahedral coordination (see Fig. C.1 (b)), d orbitals are split into three t_{2g} and two e_g orbitals because the system has also the cubic symmetry. However, in this case e_g orbitals become the lower energy state instead of t_{2g} orbitals, i.e. $D < 0$ (see Eq. (C.49) and Eq. (C.50)).

C.2.2 Trigonal crystal field

In real materials, the ligands of the magnetic ion can be located at positions with even lower symmetry such as tetragonal, trigonal and so on. For such a lower symmetry, t_{2g} and e_g orbitals can be split further.

Now, let me explain the effect of the trigonal crystal field, of which the schematic picture is drawn in Fig. C.1 (c). Let us consider an infinitesimal displacement δ for each ligand, more precisely the positions of ligands are shifted from the cubic case as $\boldsymbol{R}_1 = (a + \delta, \delta, \delta), \boldsymbol{R}_2 = (\delta, a + \delta, \delta), \boldsymbol{R}_3 = (\delta, \delta, a + \delta), \boldsymbol{R}_4 = (-a - \delta, -\delta, -\delta), \boldsymbol{R}_5 = (-\delta, -a - \delta, -\delta), \boldsymbol{R}_6 = (-\delta, -\delta, -a - \delta)$. If $\delta > 0$, the system is expanded along [111] axis, otherwise it is compressed.

It is convenient to regard the [111] direction as the quantization axis of $C_m^{(k)}(\theta, \varphi)$. Thus, we define a new

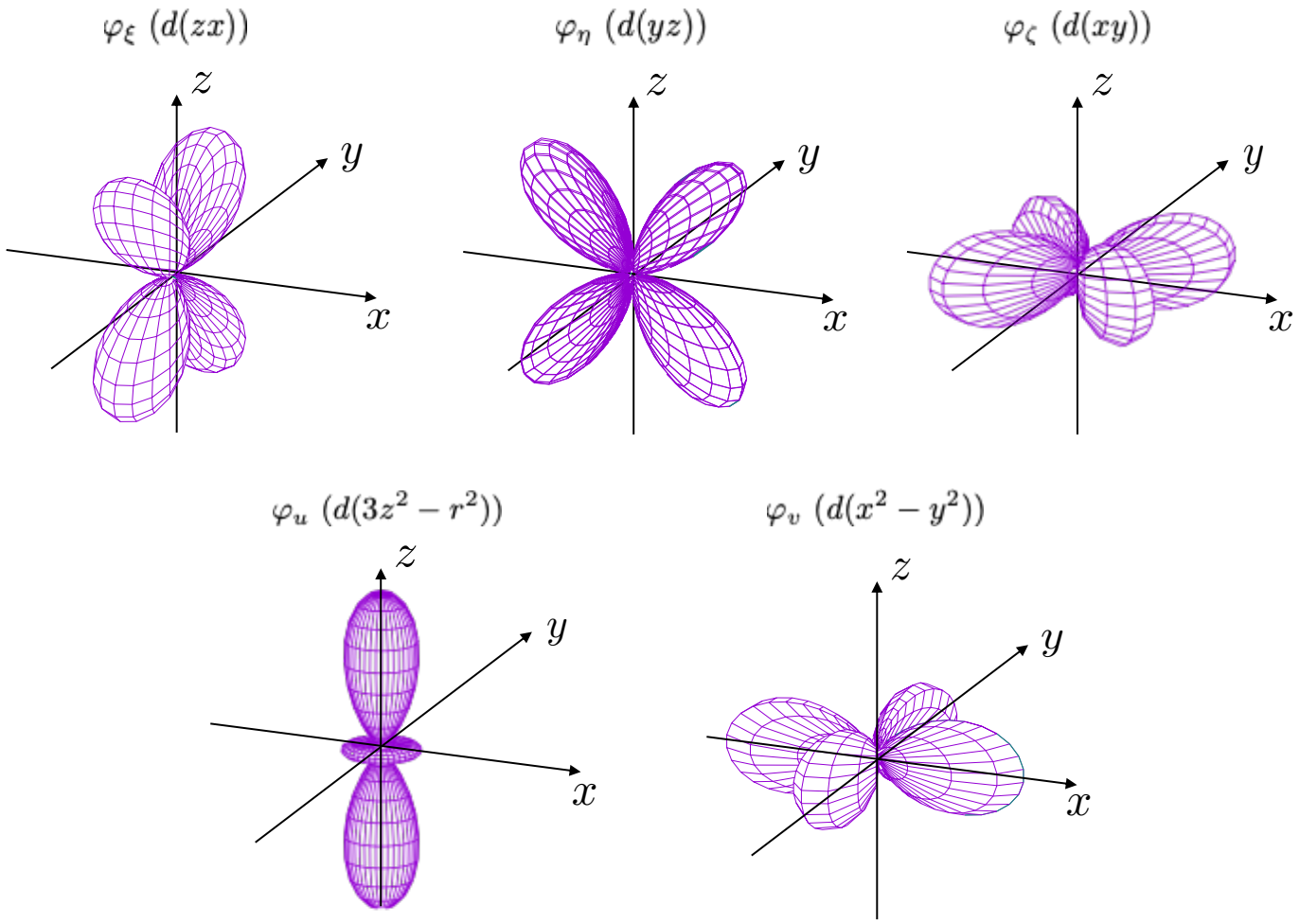

Figure C.2: **Orbital states of a d-electron subjected to cubic crystal field**
3 tops and 2 bottoms correspond to t_{2g} and e_g orbitals, respectively.

coordinate (X, Y, Z) as,

$$X = \frac{1}{\sqrt{6}}(-x - y + 2z), \tag{C.53}$$

$$Y = \frac{1}{\sqrt{2}}(x - y), \tag{C.54}$$

$$Z = \frac{1}{\sqrt{3}}(x + y + z). \tag{C.55}$$

In this coordination, from Eq. (C.9), $C_m^{(k)}(\theta, \varphi)$ is found to satisfy,

$$l_Z C_m^{(k)}(\theta, \varphi) = m C_m^{(k)}(\theta, \varphi) \tag{C.56}$$

with

$$l_Z = \frac{1}{\sqrt{3}}(l_x + l_y + l_z). \tag{C.57}$$

In the same manner as in the cubic case, the trigonal-crystal-field potential can be written as,

$$v_{\rm cry}(\boldsymbol{r}) = \sum_{k,m} A_{km}^{\rm tri} r^k C_m^{(k)}(\theta, \varphi). \tag{C.58}$$

Some coefficients $A_{km}^{\rm tri}$ vanish because of the trigonal symmetry such as the 3-fold rotational symmetry around Z axis, the inversion symmetry and the reflection symmetry with respect to the Y-Z plane.

The potential must be invariant with respect to the trigonal-symmetry operation. Let $R_\alpha(Z)$ the rotational operation which rotates the system by an angle α around Z axis. From Eq. (C.12), we find,

$$R_\alpha(Z)C_m^{(k)}(\theta,\varphi) = e^{-im\alpha}C_m^{(k)}(\theta,\varphi). \tag{C.59}$$

For $\alpha = \frac{2\pi}{3}$, the potential must be invariant, thus we find $A_{km}^{\rm tri} = 0$ for $m = \pm1, \pm2, \pm4$. For the inversion operator I which gives the transformation of coordinate, $(X, Y, Z) \to (-X, -Y, -Z)$, thus $C_m^{(k)}(\theta,\varphi)$ must satisfy,

$$IC_m^{(k)}(\theta,\varphi) = (-1)^k C_m^{(k)}(\theta,\varphi). \tag{C.60}$$

Moreover, for the reflection in the Y-Z plane, here called I_{YZ} which gives the transformation of coordinate $\varphi \to -\varphi$, $A_{km}^{\rm tri}$ must satisfy,

$$I_{YZ}A_{km}^{\rm tri} = (-1)^m A_{km}^{\rm tri}. \tag{C.61}$$

Therefore the trigonal-crystal-field potential is obtained as,

$$v_{\rm cry}(\boldsymbol{r}) = A_{00}^{\rm tri} + A_{20}^{\rm tri}r^2C_0^{(2)}(\theta,\varphi) + A_{40}^{\rm tri}r^4C_0^{(4)}(\theta,\varphi) + A_{43}^{\rm tri}r^4\Big[C_3^{(4)}(\theta,\varphi) - C_{-3}^{(4)}(\theta,\varphi)\Big]. \tag{C.62}$$

On the other hand, the cubic symmetry includes the trigonal symmetry, more precisely the system is invariant with respect to the trigonal-symmetry operation if the system has the cubic symmetry. Thus we can expect that the potential can be divided into the cubic-symmetric term and the correction term which has only the trigonal symmetry, i.e.

$$v_{\rm cry}(\boldsymbol{r}) = A_{00}^{\rm tri} + v'_{\rm cub}(\boldsymbol{r}) + v_{\rm tri}(\boldsymbol{r}), \tag{C.63}$$

where $v'_{\rm cub}(\boldsymbol{r})$ is not exactly equal but proportional to $v_{\rm cub}$ given by Eq. (C.32) because the distance between the electron and anions are shifted: $v'_{\rm cub}(\boldsymbol{r}) = \tilde{D}/D v_{\rm cub}(\boldsymbol{r})$. If the quantization axis is the Z axis, the cubic-crystal-field potential $v'_{\rm cub}$ changes the form as,

$$v'_{\rm cub}(\boldsymbol{r}) = fr^4\left[C_0^{(4)}(\theta,\varphi) + \sqrt{\frac{10}{7}}\Big[C_3^{(4)}(\theta,\varphi) - C_{-3}^{(4)}(\theta,\varphi)\Big]\right] \tag{C.64}$$

with

$$f = -\frac{7Ze^2}{3a^5} = -\frac{4e}{15}\tilde{D}. \tag{C.65}$$

The trigonal symmetric term $v_{\rm tri}(\boldsymbol{r})$ must be orthogonal to $v'_{\rm cub}(\boldsymbol{r})$ and be represented as,

$$v_{\rm tri}(\boldsymbol{r}) = A_{20}^{\rm tri}r^2C_0^{(2)}(\theta,\varphi) + Br^4\left[C_0^{(4)}(\theta,\varphi) - \frac{1}{2}\sqrt{\frac{7}{10}}\Big[C_3^{(4)}(\theta,\varphi) - C_{-3}^{(4)}(\theta,\varphi)\Big]\right]. \tag{C.66}$$

The sign of $A_{20}^{\rm tri}$ is important to determine the lowest energy state. We can obtain $A_{20}^{\rm tri}$ by substituting the positions of anions into Eq. (C.28). Now, we expand $A_{20}^{\rm tri}$ in power series of (δ/a). Since $\cos\theta_1 = \cos\theta_2 = \cos\theta_3 = \frac{1}{\sqrt{3}} + \frac{2\delta}{3a}$ and $\cos\theta_4 = \cos\theta_5 = \cos\theta_6 = -\frac{1}{\sqrt{3}} - \frac{2\delta}{3a}$, we find,

$$A_{20}^{\rm tri}(\delta) = \frac{6\sqrt{10}Ze^2}{a^3}\frac{\delta}{a} + O((\delta/a)^2). \tag{C.67}$$

Here we used Eq. (C.28) and $\Theta_{20}(\theta) = \sqrt{\frac{5}{8}}(3\cos^2\theta - 1)$. We find that $A_{20}^{\rm tri}(\delta)$ becomes positive if the anions are distorted so that they are extended in [111] direction, i.e. $\delta > 0$.

Next, we consider the eigenstates of $v(\boldsymbol{r})$. These must be represented as the linear combination of t_{2g} orbitals and e_g orbitals. In addition, it is convenient to take them to be eigenstates of l_Z. The wave functions of the t_{2g} orbitals (Eq. (C.51)) are,

$$\varphi_{x_+} = -\frac{1}{\sqrt{3}}(\omega\varphi_\xi + \omega^2\varphi_\eta + \varphi_\zeta), \tag{C.68}$$

$$\varphi_{x_0} = \frac{1}{\sqrt{3}}(\varphi_\xi + \varphi_\eta + \varphi_\zeta), \tag{C.69}$$

$$\varphi_{x_-} = \frac{1}{\sqrt{3}}(\omega^2\varphi_\xi + \omega\varphi_\eta + \varphi_\zeta), \tag{C.70}$$

where $\omega = e^{\frac{2\pi}{3}i}$. By using $Y_{lm}(\theta, \phi)$ with [111] quantization axis, they can be rewritten as,

$$\varphi_{x_+} = -\frac{1}{\sqrt{3}}(\sqrt{2}Y_{2-2}(\theta,\phi) + Y_{21}(\theta,\phi)), \tag{C.71}$$

$$\varphi_{x_0} = Y_{20}(\theta,\phi), \tag{C.72}$$

$$\varphi_{x_-} = \frac{1}{\sqrt{3}}(\sqrt{2}Y_{22}(\theta,\phi) - Y_{2-1}(\theta,\phi)). \tag{C.73}$$

Then we can easily find,

$$\langle\varphi_{x_+}|\, l_Z\, |\varphi_{x_+}\rangle = -1, \tag{C.74}$$

$$\langle\varphi_{x_0}|\, l_Z\, |\varphi_{x_0}\rangle = 0, \tag{C.75}$$

$$\langle\varphi_{x_-}|\, l_Z\, |\varphi_{x_-}\rangle = +1. \tag{C.76}$$

If we choose e_g orbitals to be orthogonal to $\varphi_{x_\pm}$, they are represented as,

$$\varphi_{u_+} = -\frac{1}{\sqrt{2}}(\varphi_u + i\varphi_v) = -\frac{1}{\sqrt{3}}(Y_{2-2}(\theta,\phi) - \sqrt{2}Y_{21}(\theta,\phi)), \tag{C.77}$$

$$\varphi_{u_-} = -\frac{1}{\sqrt{2}}(\varphi_u - i\varphi_v) = \frac{1}{\sqrt{3}}(Y_{22}(\theta,\phi) + \sqrt{2}Y_{2-1}(\theta,\phi)). \tag{C.78}$$

Using Table. C.1, the diagonal terms of the matrix $\langle\varphi|\, v_{\rm tri}(\boldsymbol{r})\, |\varphi\rangle$ with $\varphi = \varphi_{x_\pm}, \varphi_{x_0}, \varphi_{u_\pm}$ are calculated as,

$$\langle\varphi_{x_+}|\, v_{\rm tri}(\boldsymbol{r})\, |\varphi_{x_+}\rangle = \langle\varphi_{x_-}|\, v_{\rm tri}(\boldsymbol{r})\, |\varphi_{x_-}\rangle = -\frac{1}{7}A_{20}^{\rm tri}\bar{r^2} - \frac{1}{7}B\bar{r^4}, \tag{C.79}$$

$$\langle\varphi_{x_0}|\, v_{\rm tri}(\boldsymbol{r})\, |\varphi_{x_0}\rangle = \frac{2}{7}A_{20}^{\rm tri}\bar{r^2} + \frac{2}{7}B\bar{r^4}, \tag{C.80}$$

$$\langle\varphi_{u_+}|\, v_{\rm tri}(\boldsymbol{r})\, |\varphi_{u_+}\rangle = \langle\varphi_{u_-}|\, v_{\rm tri}(\boldsymbol{r})\, |\varphi_{u_-}\rangle = 0, \tag{C.81}$$

and all off-diagonal terms are 0 since all bases are orthogonal to each other. Therefore, the t_{2g} orbitals are split into two degenerated states called the e_g' orbitals and a non-degenerated state called the a_{1g} orbital, and e_g orbitals aren't split. If the system is compressed along [111] direction, $A_{20}^{\rm tri}$ becomes negative. Then the a_{1g} orbital becomes the lowest energy state as shown in Fig. C.3. There is what happens for the orbitals of Mo^{4+} ions in the pyrochlore magnet (see Fig. 1.19 (a)).

C.3 Jahn-Teller distortion

C.3.1 Static Jahn-Teller distortion

In the previous section, I explained the energy level splitting by the crystal field. The new ground state has lower energy than before lowering the symmetry. In other words, the energy state is unstable if the ground

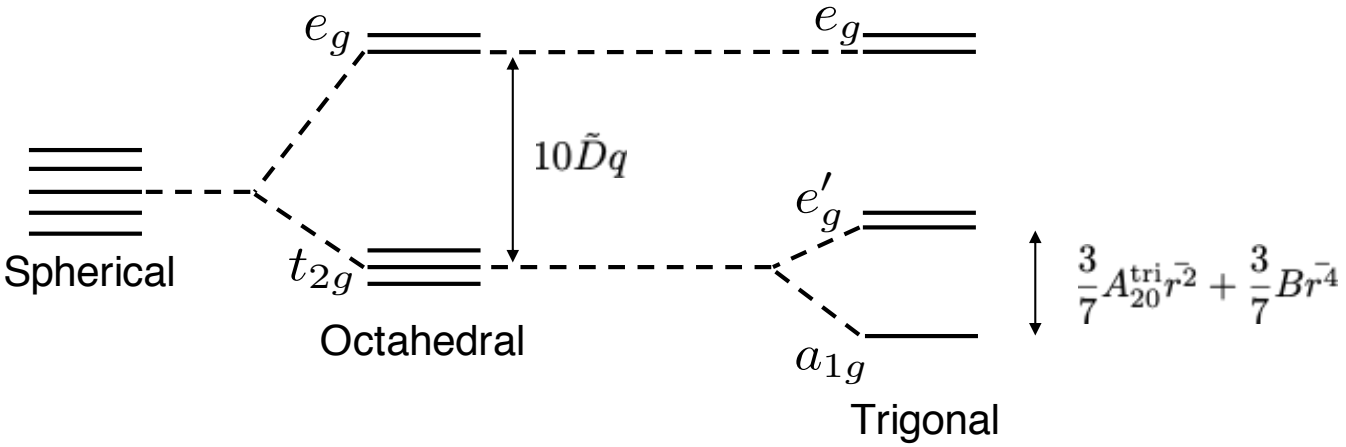

Figure C.3: **Energy level splitting of d orbitals by the trigonal-crystal field**
I show the case of the system shrinking in [111] direction, i.e. $A_{20}^{\rm tri} < 0$.

state is degenerated. It is generally known that the structure becomes unstable against distortion if the ground state of electron has degeneracy. This is the so called the Jahn-Teller theorem. For example, if the number of d electron is not 3, 5 and 8 for the case of the octahedral coordination, the ground state is degenerated. Hence, the system is unstable and tends to be distorted to the lower symmetry. The phenomenon is generally called the Jahn-Teller effect and the distortion is called the Jahn-Teller distortion.

Here, I give the intuitive explanation for the Jahn-Teller distortion. Let δ be the amount of the distortion. As mentioned above, the crystal-field potential with the low symmetry is generated by the distortion and it can be expanded in power series of δ. The leading term of the difference of ground state energy would be proportional to δ, i.e. $\Delta E_{\rm orbital} = -a\delta$. In addition, the elastic energy of the lattice distortion is quadratic, i.e. $\Delta E_{\rm elastic} = \frac{1}{2}k\delta^2$. The total change of the energy becomes

$$\Delta E = \Delta E_{\rm orbital} + \Delta E_{\rm elastic} = \frac{k}{2}\Big(\delta - \frac{a}{k}\Big)^2 - \frac{a^2}{4k^2}. \tag{C.82}$$

Therefore the system will be stabilized by deforming up to $\delta^* = a/k$.

The lattice will be transformed to the lower symmetry until the degeneracy of the ground state is removed. In this situation, the expectation value of the orbital angular momentum must be zero, which is called the *quenching of orbital angular momentum*. This is because the orbital angular momentum operator is a pure imaginary number, $\boldsymbol{l} = -i\hbar\boldsymbol{r} \times \nabla$, while the wave function $|0\rangle$ of the ground state is a real function. From $\boldsymbol{l}^* = -\boldsymbol{l}$, the expectation value must satisfy $\langle 0|\,\boldsymbol{l}\,|0\rangle = -\langle 0|\,\boldsymbol{l}\,|0\rangle^*$ but $\langle 0|\,\boldsymbol{l}\,|0\rangle$ is a real vector. Thus $\langle 0|\,\boldsymbol{l}\,|0\rangle$ becomes zero.

C.3.2 Dynamical Jahn-Teller distortion

In many cases, there are no orbital degeneracies left in the ground state and the orbital degrees of freedom disappear. In such cases it would be appear that we only have to consider the spin degree of freedom as the origin of the magnetism. However the reality can be more complex. Note that we didn't take into account the kinetic energy of the lattice distortion in above discussion. In addition, we have to consider the direction of the lattice distortions. For example, in the case where the system is distorted to the trigonal symmetry, there are four possible axes for the distortions, regarded as Z-axis. If the kinetic effect is large enough, tunneling takes place between four equivalent directions of the distortion. This orbital fluctuation is called the dynamical Jahn-Teller effect.

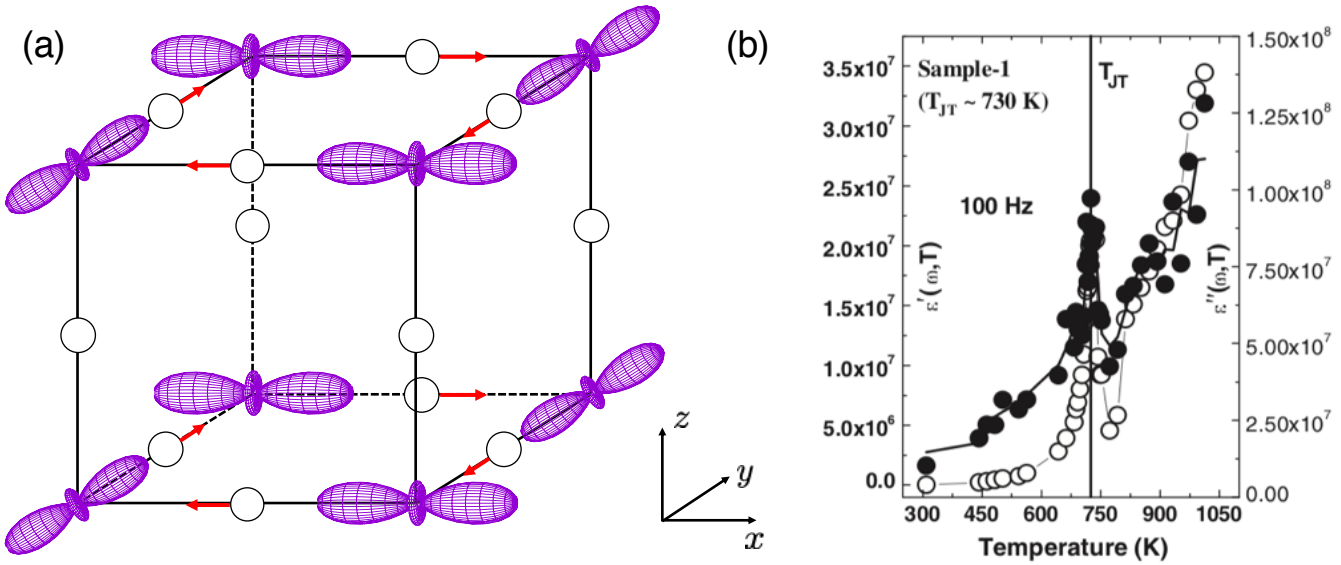

Figure C.4: **Orbital ordering**
(a): Crystal structure in the orbital ordered phase of $LaMnO_3$. The open circles and the red arrows represent the oxygen ions and the directions of lattice distortions, respectively. Then the d orbitals are ordered with antiparallel in xy plane and parallel in the z direction. (b): The real part (open circle) and the imaginary part (solid circle) of the dielectric permittivity for $LaMnO_3$, taken from [83].

The orbital fluctuation can be controlled by changing temperatures. At low temperatures, the directions of Jahn-Teller distortions are ordered in order to optimize the total elastic energy of the whole system. Thus, the structural transition can occur because of the cooperative Jahn-Teller distortion, which is known as orbital ordering.

An example of the cooperative Jahn-Teller distortion can be found in $LaMnO_3$. It can be detected by the neutron-diffraction study [84] since the crystal symmetry changes as shown in Fig. C.4 (a). In addition, the dielectric property exhibits a singularity at the transition temperature of the orbital ordering $T_{\rm JT}$ because the ion displacement behaves like a dipole moment. [83, 85] Fig. C.4 (b) shows the measurements of complex dielectric permittivity $\epsilon = \epsilon' - i\epsilon''$. There are clear anomalies for both part of them near the transition temperature $T_{\rm JT}$.

If the energy scale of the Jahn-Teller energy is near the energy scale of the interactions between spins, more complicated phenomena can occur, for example, multiferroics. [86, 87] And if there is a frustration for the elastic energy, the system exhibits a disordered orbital state such as orbital liquid [88, 89] or orbital glass state, at low temperatures.

C.4 Hund's rule

So far, we have limited to discuss the case for only one electron in the d orbitals. Now, we explain the case for electrons more than two. In this case the lower energy levels are not simply filled in sequence because of the Coulomb interactions between electrons.

The wave function of the n-electron system is represented as the Slater determinant,

$$|\psi^{(1)},\psi^{(2)},...,\psi^{(n)}|(\boldsymbol{r}_1,\sigma_1,\boldsymbol{r}_2,\sigma_2,...,\boldsymbol{r}_n,\sigma_n)=\frac{1}{\sqrt{n!}}\begin{vmatrix}\psi^{(1)}(\boldsymbol{r}_1,\sigma_1) & \psi^{(2)}(\boldsymbol{r}_1,\sigma_1) & \cdots & \psi^{(n)}(\boldsymbol{r}_1,\sigma_1)\\ \psi^{(1)}(\boldsymbol{r}_2,\sigma_2) & \psi^{(2)}(\boldsymbol{r}_2,\sigma_2) & \cdots & \psi^{(n)}(\boldsymbol{r}_2,\sigma_2)\\ \vdots & \vdots & \ddots & \vdots\\ \psi^{(1)}(\boldsymbol{r}_n,\sigma_n) & \psi^{(2)}(\boldsymbol{r}_n,\sigma_n) & \cdots & \psi^{(n)}(\boldsymbol{r}_n,\sigma_n)\end{vmatrix}, \tag{C.83}$$

where $\psi^{(k)}(\boldsymbol{r}_k,\sigma_k)$ is the wave function of k-th electron. The use of Slater determinants ensures compatibility to Pauli's principle because it is an antisymmetric function with respect to exchanging two particle positions. The Hamiltonian of the n-electrons is given by,

$$H=\sum_{i=1}^{n}H^{(i)}(\boldsymbol{r}_i)+\sum_{i<j}v_{\rm c}(r_{ij}) \tag{C.84}$$

with

$$v_{\rm c}(r_{ij})=\frac{e^2}{r_{ij}}, \tag{C.85}$$

where $H^{(i)}(\boldsymbol{r}_i)$ is the single electron Hamiltonian given in Eq. (C.22) and r_{ij} represents the distance between i-th and j-th electrons.

C.4.1 Strong crystal field

Let us consider the case that the crystal field is strong enough so that the Coulomb energy can be regarded as a perturbation. This situation often appears in the $4d$ and $5d$ electron systems. Then lower energy states are obtained by simply filling the lower orbitals.

Now, we consider the case of two electrons in t_{2g} orbitals, hereafter we call the case t_{2g}^2 Considering the spin state, there are 3×2 t_{2g}-orbital state, $\psi^{(i)}(\boldsymbol{r}_i,\sigma_i)=\varphi_\alpha^{(i)}(\boldsymbol{r}_i)\theta^{(i)}_{\frac{1}{2}m_s}(\sigma_i)$, $(\alpha=\xi,\eta,\zeta,\ m_s=\pm\frac{1}{2})$. Hereafter we write $\varphi_\alpha^{(i)}\theta^{(i)}_{\frac{1}{2}\frac{1}{2}}$ and $\varphi_\alpha^{(i)}\theta^{(i)}_{\frac{1}{2}-\frac{1}{2}}$ simply as $\varphi_\alpha^{(i)}$ and $\overline{\varphi_\alpha}^{(i)}$. Thus, if the Coulomb interaction between two electrons is switched off, the state has ${}_6C_2=15$ degeneracy. In order to investigate the wave functions and energy states, we regard $v_{\rm c}(r_{12})$ as the perturbation for $H^{(1)}(\boldsymbol{r}_1)+H^{(2)}(\boldsymbol{r}_2)$. The perturbation energy is calculated as,

$$\begin{aligned}E_{\rm c}(\psi^{(1)},\psi^{(2)})&=\sum_{\sigma_1,\sigma_2}\int d^3\boldsymbol{r}_1\int d^3\boldsymbol{r}_2|\psi^{(1)},\psi^{(2)}|^*(\boldsymbol{r}_1,\sigma_1,\boldsymbol{r}_2,\sigma_2)\frac{e^2}{r_{12}}|\psi^{(1)},\psi^{(2)}|(\boldsymbol{r}_1,\sigma_1,\boldsymbol{r}_2,\sigma_2)\\&=K(\varphi^{(1)},\varphi^{(2)})-\delta_{m_{\rm s}^1,m_{\rm s}^2}J(\varphi^{(1)},\varphi^{(2)})\end{aligned} \tag{C.86}$$

with

$$\begin{aligned}K(\varphi^{(1)},\varphi^{(2)})&=\int d^3\boldsymbol{r}_1\int d^3\boldsymbol{r}_2\varphi^{(1)*}(\boldsymbol{r}_1)\varphi^{(2)*}(\boldsymbol{r}_2)\frac{e^2}{r_{12}}\varphi^{(1)}(\boldsymbol{r}_1)\varphi^{(2)}(\boldsymbol{r}_2),\\J(\varphi^{(1)},\varphi^{(2)})&=\int d^3\boldsymbol{r}_1\int d^3\boldsymbol{r}_2\varphi^{(1)*}(\boldsymbol{r}_1)\varphi^{(2)*}(\boldsymbol{r}_2)\frac{e^2}{r_{12}}\varphi^{(1)}(\boldsymbol{r}_2)\varphi^{(2)}(\boldsymbol{r}_1).\end{aligned} \tag{C.87}$$

$K(\varphi^{(1)},\varphi^{(2)})$ is called the Coulomb integration and $J(\varphi^{(1)},\varphi^{(2)})$ is called the exchange integration. The latter exists if two spins align the same direction. Using the Fourier transformation for e^2/r_{12}, we find,

$$\begin{aligned}J(\varphi^{(1)},\varphi^{(2)})&=\int d^3\boldsymbol{r}_1\int d^3\boldsymbol{r}_2\varphi^{(1)*}(\boldsymbol{r}_1)\varphi^{(2)*}(\boldsymbol{r}_2)\frac{1}{V}\sum_{\boldsymbol{k}}\frac{4\pi e^2}{k^2}e^{i\boldsymbol{k}\cdot(\boldsymbol{r_1}-\boldsymbol{r_2})}\varphi^{(1)}(\boldsymbol{r}_2)\varphi^{(2)}(\boldsymbol{r}_1),\\&=\frac{1}{V}\sum_k\frac{4\pi e^2}{k^2}\left|\int d^3\boldsymbol{r}e^{i\boldsymbol{k}\cdot\boldsymbol{r_1}}\phi\varphi^{(1)*}(\boldsymbol{r}_1)\varphi^{(2)}(\boldsymbol{r}_1)\right|^2>0,\end{aligned} \tag{C.88}$$

where V is the volume of the system and $\boldsymbol{k}$ is the wave number. This means that the energy becomes lower if two spins have the same direction. Generally, if the total spin quantum number for the electrons in the open subshell $\boldsymbol{S} = \sum_i \boldsymbol{s}_i$ are maximized, the energy of the atomic state becomes minimized, which is called the Hund's first rule and $J(\varphi^{(1)}, \varphi^{(2)})$ is called the Hund's coupling.

Let us calculate the integrals Eq. (C.87) for t_{2g}^2 orbitals by using Eq. (C.51). From the symmetry, we find,

$$\begin{aligned} K(\varphi_\xi, \varphi_\xi) &= K(\varphi_\eta, \varphi_\eta) = K(\varphi_\zeta, \varphi_\zeta), \\ K(\varphi_\xi, \varphi_\eta) &= K(\varphi_\eta, \varphi_\zeta) = K(\varphi_\zeta, \varphi_\xi), \\ J(\varphi_\xi, \varphi_\eta) &= J(\varphi_\eta, \varphi_\zeta) = J(\varphi_\zeta, \varphi_\xi). \end{aligned} \tag{C.89}$$

It is convenient to introduce a short hand notation,

$$\langle m_1, m_2 | \, | m_1', m_2' \rangle = \int d^3\boldsymbol{r}_1 \int d^3\boldsymbol{r}_2 \varphi^*_{n2m_1}(\boldsymbol{r}_1)\varphi^*_{n2m_2}(\boldsymbol{r}_2)\frac{e^2}{r_{12}}\varphi_{n2m_1'}(\boldsymbol{r}_1)\varphi_{n2m_2'}(\boldsymbol{r}_2). \tag{C.90}$$

Using the expansion

$$\frac{1}{r_{12}} = \sum_k \frac{4\pi}{2k+1}\frac{r_<^k}{r_>^{k+1}}\sum_q (-1)^q Y_{kq}(\theta_1, \phi_1)Y_{k-q}(\theta_2, \phi_2), \tag{C.91}$$

where $r_<$ ($r_>$) is the smaller (larger) one of r_1 and r_2, we can rewrite Eq. (C.90) as

$$\begin{aligned} \langle m_1, m_2 | \, | m_1', m_2' \rangle &= \sum_{k,q} (-1)^q c^k(2, m_1|2, m_1')c^k(2, m_2|2, m_2')\delta_{q+m_1', m1}\delta_{-q+m_2', m_2}F^k(n, 2|n, 2) \\ &= \delta_{m_1+m_2, m_1'+m_2'}(-1)^{m_1-m_1'}\sum_k c^k(2, m_1|2, m_1')c^k(2, m_2|2, m_2')F^k(n, 2|n, 2) \end{aligned} \tag{C.92}$$

with

$$F^k(n, l|n', l') = e^2 \int r_1^2 dr_1 \int r_2^2 dr_2 R_{nl}^2(r_1)R_{n'l'}^2(r_2)\frac{r_<^k}{r_>^{k+1}}, \tag{C.93}$$

Here, $F^k(n, l|n', l')$ is called Slater-Condon parameter, hereafter we write it as F^k for simplicity. Note that $\langle m_1, m_2 | \, | m_1', m_2' \rangle$ takes a non-zero value if $m_1 + m_2 = m_1' + m_2'$. Let us write down all elements of

$\langle m_1, m_2| \, |m_1', m_2'\rangle$ below,

$$
\begin{aligned}
\langle 2,2| \, |2,2\rangle = \langle 2,\bar{2}| \, |2,\bar{2}\rangle &= F^0 + \frac{4}{49}F^2 + \frac{1}{441}F^4, \\
\langle 2,\bar{2}| \, |\bar{2},2\rangle &= \frac{70}{441}F^4, \\
\langle 2,1| \, |2,1\rangle = \langle 2,\bar{1}| \, |2,\bar{1}\rangle = \langle 1,2| \, |1,2\rangle = \langle 1,\bar{2}| \, |1,\bar{2}\rangle &= F^0 - \frac{2}{49}F^2 - \frac{4}{441}F^4, \\
\langle 2,1| \, |1,2\rangle = \langle 1,2| \, |2,1\rangle &= \frac{6}{49}F^2 + \frac{5}{441}F^4, \\
\langle 2,\bar{2}| \, |1,\bar{1}\rangle = \langle 1,\bar{1}| \, |2,\bar{2}\rangle &= -\frac{6}{49}F^2 - \frac{5}{441}F^4, \\
\langle 2,\bar{1}| \, |\bar{1},2\rangle = \langle 1,\bar{2}| \, |\bar{2},1\rangle &= \frac{35}{441}F^4, \\
\langle 2,\bar{2}| \, |\bar{1},1\rangle = \langle 1,\bar{1}| \, |\bar{2},2\rangle &= -\frac{35}{441}F^4, \\
\langle 2,0| \, |2,0\rangle = \langle 0,2| \, |0,2\rangle &= F^0 - \frac{4}{49}F^2 + \frac{6}{441}F^4, \\
\langle 2,0| \, |0,2\rangle = \langle 0,2| \, |2,0\rangle &= \frac{4}{49}F^2 + \frac{15}{441}F^4, \\
\langle 1,1| \, |1,1\rangle = \langle 1,\bar{1}| \, |1,\bar{1}\rangle &= F^0 + \frac{1}{49}F^2 + \frac{16}{441}F^4, \\
\langle 1,\bar{1}| \, |\bar{1},1\rangle &= \frac{6}{49}F^2 + \frac{40}{441}F^4, \\
\langle 1,0| \, |1,0\rangle = \langle 0,1| \, |0,1\rangle &= F^0 + \frac{2}{49}F^2 - \frac{24}{441}F^4, \\
\langle 1,0| \, |0,1\rangle = \langle 0,1| \, |1,0\rangle &= \frac{1}{49}F^2 + \frac{30}{441}F^4, \\
\langle 0,0| \, |0,0\rangle &= F^0 + \frac{4}{49}F^2 + \frac{36}{441}F^4.
\end{aligned}
\tag{C.94}
$$

where we omitted the signs of m_1 and m_2. Here the bar represents different sign, i.e. $|m_1, m_2\rangle = |\pm m_1, \pm m_2\rangle$ and $|m_1, \overline{m}_2\rangle = |\pm m_1, \mp m_2\rangle$. Then the Coulomb integration and the exchange integration are obtained as,

$$
\begin{aligned}
K(\varphi_\zeta, \varphi_\zeta) &= \langle 2,2| \, |2,2\rangle + \frac{1}{2}\langle 2,\bar{2}| \, |\bar{2},2\rangle = F^0 + \frac{4}{49}F^2 + \frac{36}{441}F^4, \\
K(\varphi_\zeta, \varphi_\xi) &= \langle 2,1| \, |2,1\rangle = F^0 - \frac{2}{49}F^2 - \frac{4}{441}F^4, \\
J(\varphi_\zeta, \varphi_\xi) &= \frac{1}{2}(\langle 2,1| \, |1,2\rangle + \langle 2,\bar{1}| \, |\bar{1},2\rangle) = \frac{3}{49}F^2 + \frac{20}{441}F^4.
\end{aligned}
\tag{C.95}
$$

In order to obtain the eigenstates, we diagonalize the 15×15 matrix whose elements are given in Eq. (C.86). It is easy to calculate it using the group theory but we leave out the explanation. As the result of the

calculation, the eigenstates are obtained as,

$$a_1: \quad \Psi_{a_1} = \frac{1}{\sqrt{3}}\big\{|\phi_\xi, \overline{\phi}_\xi| + |\phi_\eta, \overline{\phi}_\eta| + |\phi_\zeta, \overline{\phi}_\zeta|\big\}, \tag{C.96}$$

$$\begin{aligned} e: \quad \Psi_{e_u} &= \frac{1}{\sqrt{6}}\big\{-|\phi_\xi, \overline{\phi}_\xi| - |\phi_\eta, \overline{\phi}_\eta| + 2|\phi_\zeta, \overline{\phi}_\zeta|\big\}, \\ \Psi_{e_v} &= \frac{1}{\sqrt{2}}\big\{|\phi_\xi, \overline{\phi}_\xi| - |\phi_\eta, \overline{\phi}_\eta|\big\}, \end{aligned} \tag{C.97}$$

$$\begin{aligned} t_1: \quad & \Psi_{t_1\alpha(M=1)} = |\phi_\eta, \phi_\zeta|,\ \Psi_{t_1\alpha(M=0)} = \frac{1}{\sqrt{2}}\big\{|\phi_\eta, \overline{\phi}_\zeta| - |\phi_\zeta, \overline{\phi}_\eta|\big\},\ \Psi_{t_1\alpha(M=-1)} = |\overline{\phi}_\eta, \overline{\phi}_\zeta|, \\ & \Psi_{t_1\beta(M=1)} = |\phi_\zeta, \phi_\xi|,\ \Psi_{t_1\beta(M=0)} = \frac{1}{\sqrt{2}}\big\{|\phi_\zeta, \overline{\phi}_\xi| - |\phi_\xi, \overline{\phi}_\zeta|\big\},\ \Psi_{t_1\beta(M=-1)} = |\overline{\phi}_\zeta, \overline{\phi}_\xi|, \\ & \Psi_{t_1\gamma(M=1)} = |\phi_\xi, \phi_\eta|,\ \Psi_{t_1\gamma(M=0)} = \frac{1}{\sqrt{2}}\big\{|\phi_\xi, \overline{\phi}_\eta| - |\phi_\eta, \overline{\phi}_\xi|\big\},\ \Psi_{t_1\gamma(M=-1)} = |\overline{\phi}_\xi, \overline{\phi}_\eta|, \end{aligned} \tag{C.98}$$

$$\begin{aligned} t_2: \quad \Psi_{t_2\xi} &= \frac{1}{\sqrt{2}}\big\{|\phi_\eta, \overline{\phi}_\zeta| + |\phi_\zeta, \overline{\phi}_\eta|\big\}, \\ \Psi_{t_2\eta} &= \frac{1}{\sqrt{2}}\big\{|\phi_\zeta, \overline{\phi}_\xi| + |\phi_\xi, \overline{\phi}_\zeta|\big\}, \\ \Psi_{t_2\zeta} &= \frac{1}{\sqrt{2}}\big\{|\phi_\xi, \overline{\phi}_\eta| + |\phi_\eta, \overline{\phi}_\xi|\big\}. \end{aligned} \tag{C.99}$$

The t_1 state has the lowest energy $K(\varphi_\zeta, \varphi_\xi) - J(\varphi_\zeta, \varphi_\xi)$ since it has the highest spin $S = 1$ and M represents the eigenvalue of $S_z = s_z^1 + s_z^2$. In the same manner, we can obtain the eigenstates for the cases where t_{2g} and e_g orbitals have one electron for each ($t_{2g}e_g$) or e_g orbital has two electrons (e_g^2).

For the case of more than three electrons, the Laplace expansion for the Slater determinant is useful to calculate the Coulomb interaction energy, namely we can divide the wave function into the Slater determinant for the particle 1,2 and others,

$$\begin{aligned} & |\psi^{(1)}, \psi^{(2)}, ..., \psi^{(n)}|(\boldsymbol{r}_1, \sigma_1, \boldsymbol{r}_2, \sigma_2, ..., \boldsymbol{r}_n, \sigma_n) \\ &= \left[\frac{n(n-1)}{2}\right]^{-\frac{1}{2}} \sum_{i<j} (-1)^{3+i+j} |\psi^{(i)}, \psi^{(j)}|(\boldsymbol{r}_1, \sigma_1, \boldsymbol{r}_2, \sigma_2) \\ &\times |\psi^{(1)}, ..., \psi^{(i-1)}, \psi^{(i+1)}, ..., \psi^{(j-1)}, \psi^{(j+1)}, \psi^{(n)}|(\boldsymbol{r}_3, \sigma_3, ..., \boldsymbol{r}_n, \sigma_n). \end{aligned} \tag{C.100}$$

Then we can rewrite the expectation value of the Coulomb interactions as,

$$\begin{aligned} E_{\rm c}(\psi^{(1)}, \psi^{(2)}, ..., \psi^{(n)}) &= \sum_{\sigma_1, ..., \sigma_n} \int d^3\boldsymbol{r}_1 \cdots \int d^3\boldsymbol{r}_n |\psi^{(1)}, \psi^{(2)}, ..., \psi^{(n)}|^* \sum_{i<j} v_{\rm c}(r_{ij}) |\psi^{(1)}, \psi^{(2)}, ..., \psi^{(n)}| \\ &= \frac{n(n-1)}{2} \sum_{\sigma_1, ..., \sigma_n} \int d^3\boldsymbol{r}_1 \cdots \int d^3\boldsymbol{r}_n |\psi^{(1)}, \psi^{(2)}, ..., \psi^{(n)}|^* v_{\rm c}(r_{12}) |\psi^{(1)}, \psi^{(2)}, ..., \psi^{(n)}| \\ &= \sum_{i<j} \sum_{k<l} (-1)^{i+j+k+l} \Big[\Big\langle \psi^{(i)}, \psi^{(j)} \Big| v_{\rm c}(r_{12}) \Big| \psi^{(k)}, \psi^{(l)} \Big\rangle - \Big\langle \psi^{(i)}, \psi^{(j)} \Big| v_{\rm c}(r_{12}) \Big| \psi^{(l)}, \psi^{(k)} \Big\rangle \Big] S_{ij,kl} \end{aligned} \tag{C.101}$$

with

$$\begin{aligned} S_{ij,kl} = \sum_{\sigma_3, ..., \sigma_n} \int d^3\boldsymbol{r}_3 \cdots \int d^3\boldsymbol{r}_n & |\psi^{(1)}, ..., \psi^{(i-1)}, \psi^{(i+1)}, ..., \psi^{(j-1)}, \psi^{(j+1)}, \psi^{(n)}|^* \\ & \times |\psi^{(1)}, ..., \psi^{(k-1)}, \psi^{(k+1)}, ..., \psi^{(l-1)}, \psi^{(l+1)}, \psi^{(n)}|. \end{aligned} \tag{C.102}$$

If two Slater determinant in the integration, $S_{ij,kl} = 1$, otherwise $S_{ij,kl} = 0$. Therefore, we find,

$$E_{\rm c}(\psi^{(1)}, \psi^{(2)}, ..., \psi^{(n)}) = \sum_{i<j} \Big[K(\varphi^{(i)}, \varphi^{(j)}) - \delta_{m_{\rm s}^i, m_{\rm s}^j} J(\varphi^{(i)}, \varphi^{(j)}) \Big]. \tag{C.103}$$

C.4.2 Week crystal field

In the above discussion, we assumed that the crystal field is large enough, i.e. t_{2g} energy levels is far from e_g energy levels. If they become closer, we can't neglect the interactions between t_{2g}^2 and $t_{2g}e_g$, or t_{2g}^2 and e_g^2. Now, we consider the case where the Coulomb energy is large enough compared with the crystal field energy. This situation appears in the $3d$ electron system. Then the crystal field is regarded as the perturbation for the Coulomb interactions.

At first, we apply the Hund's first rule because the rule is completely resulting from the Coulomb interactions. In addition, it is empirically known that the Coulomb energy becomes lower if the state has the larger total angular momentum $\boldsymbol{L} = \sum_i \boldsymbol{l}_i$, which is called the Hund's second rule. Intuitively, this is because the wave function is spatially spread when the angular momentum is large.

For example, in the case of two electrons, the total spin becomes $S = 1$ and the total orbital angular momentum becomes $L = 2 + 1 = 3$ because of Pauli's principle. The ground state has 7-fold degeneracy: $M = -3, -2, -1, 0, 1, 2, 3$, and the wave functions are given by,

$$\begin{aligned}
\Phi_3 &= |\varphi_{n22}, \varphi_{n21}|, \\
\Phi_2 &= |\varphi_{n22}, \varphi_{n20}|, \\
\Phi_1 &= \frac{1}{\sqrt{5}} \Big(\sqrt{2} |\varphi_{n21}, \varphi_{n20}| + \sqrt{3} |\varphi_{n22}, \varphi_{n2-1}| \Big), \\
\Phi_0 &= \frac{1}{\sqrt{5}} (2|\varphi_{n21}, \varphi_{n2-1}| + |\varphi_{n22}, \varphi_{n2-2}|), \\
\Phi_{-1} &= \frac{1}{\sqrt{5}} \Big(\sqrt{2} |\varphi_{n20}, \varphi_{n2-1}| + \sqrt{3} |\varphi_{n21}, \varphi_{n2-2}| \Big), \\
\Phi_{-2} &= |\varphi_{n22}, \varphi_{n21}|,
\end{aligned} \tag{C.104}$$

which is obtained by applying the lowering operator L^- sequentially. Calculating the crystal-field energy $V_{\rm cub} = v_{\rm cub}(\boldsymbol{r}_1) + v_{\rm cub}(\boldsymbol{r}_2)$ for these 7-degenerated states and diagonalizing the 7×7 matrix, we obtain the eigenstates and eigenvalues for the two-electron problem. As a result of calculation, 7-degenerated states are split into the 3-degenerated t_1 state, the 3-degenerated t_2 state and the single a_2 state, more precisely

$$\begin{aligned}
t_1 : \quad & \Phi_{t_1\alpha} = \frac{1}{\sqrt{8}} (\sqrt{5}\Phi_3 + \sqrt{3}\Phi_{-1}), \\
& \Phi_{t_1\beta} = \frac{1}{\sqrt{8}} (\sqrt{5}\Phi_{-3} + \sqrt{3}\Phi_1), \\
& \Phi_{t_1\gamma} = \Phi_1,
\end{aligned} \tag{C.105}$$

$$\begin{aligned}
t_2 : \quad & \Phi_{t_2\xi} = \frac{1}{\sqrt{8}} (\sqrt{3}\Phi_3 - \sqrt{5}\Phi_{-1}), \\
& \Phi_{t_2\eta} = \frac{1}{\sqrt{8}} (\sqrt{3}\Phi_{-3} - \sqrt{5}\Phi_1), \\
& \Phi_{t_2\zeta} = \frac{1}{\sqrt{2}} (\Phi_2 + \Phi_{-2}),
\end{aligned} \tag{C.106}$$

$$a_2 : \quad \Phi_{a_2} = \frac{1}{\sqrt{2}} (\Phi_2 - \Phi_{-2}). \tag{C.107}$$

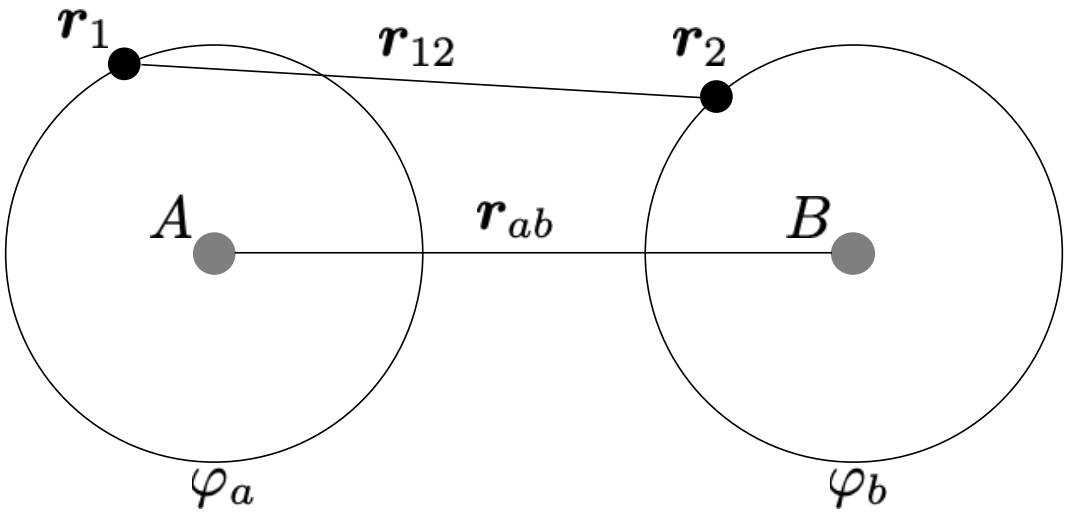

Figure C.5: **Schematic picture of the interaction between electrons 1 in φ_a and 2 in φ_b**

The eigenvalues corresponding to t_1, t_2 and a_2 states are

$$E_{t_1} = -6Dq, \quad E_{t_2} = 2Dq, \quad , E_{a_2} = -12Dq, \tag{C.108}$$

respectively (see Eq. (C.49) and Eq. (C.50)). Note that the energy must be $2 \times (-4Dq) = -8Dq$ if both two electrons are in t_{2g} orbital. However, t_1 state which is the ground state has $-6Dq$. This means that the ground state is mixed by t_{2g} and e_g states in order to satisfy the Hund's rule.

To sum up we considered two extreme cases, (Crystal field $\gg$ Coulomb interaction (Sec. C.4.1), Crystal field $\ll$ Coulomb interaction (this section)). Of course, in real materials, an intermediate cases also exist and Tanabe-Sugano diagram is well-known as the way to discuss it [90].

C.5 Magnetic interactions

Magnetically ordered states result from interactions between the atomic magnetic moments,

$$\boldsymbol{\mu} = -\mu_{\mathrm{B}}(g\boldsymbol{S} + \boldsymbol{L}), \tag{C.109}$$

where $\mu_{\mathrm{B}} = e\hbar/2mc = 9.27... \times 10^{-21}$ is the Bohr magneton, $g \approx 2$ is called g-factor, $\boldsymbol{S}$ and $\boldsymbol{L}$ are the total spin and orbital angular momenta. The interaction that we expect at first is the magnetic dipole-dipole interaction given by,

$$\frac{\boldsymbol{\mu}_1 \cdot \boldsymbol{\mu}_2}{r_{12}^2} - 3\frac{(\boldsymbol{\mu}_1 \cdot \boldsymbol{r}_{12})(\boldsymbol{\mu}_1 \cdot \boldsymbol{r}_{12})}{r_{12}^5}, \tag{C.110}$$

where $\boldsymbol{r}_{12}$ represents the vector from $\boldsymbol{\mu}_2$ to $\boldsymbol{\mu}_1$. This interaction is too much small to explain the Curie or Néel temperature where the phase transitions from disordered states to ordered states take place. For example, if the distance is $1\mathring{A}$, the energy of the interaction becomes around 1K. Thus, in order to account for the origin of magnetic ordering in real materials, we have to consider the effect of the quantum mechanics and the key factors are Pauli's principle and the Coulomb interaction.

C.5.0.1 Direct Exchange interaction

First, we consider two magnetic ions A and B of the same kind whose orbitals φ_a and φ_b are far enough from each other so that they do not overlap. When φ_a and φ_b accommodate electron 1 and 2 (see Fig.

C.5), they satisfy the Schrödinger equations given in Eq. (C.2). Then, if they have the same energy level, the two-electron states $\Psi_{ab}(\boldsymbol{r}_1, \sigma_1, \boldsymbol{r}_2, \sigma_2) = |\varphi_a\varphi_b|, |\varphi_a\overline{\varphi}_b|, |\overline{\varphi}_a\varphi_b|, |\overline{\varphi}_a\overline{\varphi}_b|$ are degenerated. The degeneracy is broken by the Coulomb interaction between two electrons. The matrix element of the Coulomb energy is given by,

$$\langle \Psi_{ab}| \, e^2/r_{12} \, |\Psi'_{ab}\rangle = \sum_{\sigma_1,\sigma_2} \int\int d^3\boldsymbol{r}_1 d^3\boldsymbol{r}_2 \Psi^*_{ab} \frac{e^2}{r_{12}} \Psi'_{ab}, \tag{C.111}$$

and we can diagonalize the matrix represented by the bases $|\varphi_a\varphi_b|, |\varphi_a\overline{\varphi}_b|, |\overline{\varphi}_a\varphi_b|$ and $|\overline{\varphi}_a\overline{\varphi}_b|$,

$$\begin{vmatrix} K(\varphi_a,\varphi_b) - J(\varphi_a,\varphi_b) & 0 & 0 & 0 \\ 0 & K(\varphi_a,\varphi_b) & -J(\varphi_a,\varphi_b) & 0 \\ 0 & -J(\varphi_a,\varphi_b) & K(\varphi_a,\varphi_b) & 0 \\ 0 & 0 & 0 & K(\varphi_a,\varphi_b) - J(\varphi_a,\varphi_b) \end{vmatrix}, \tag{C.112}$$

where $K(\varphi_a, \varphi_b)$ and $J(\varphi_a, \varphi_b)$ are the Coulomb and the exchange integrations given in Eq. (C.87). Then the eigenstates are obtained as,

$$\begin{aligned} (S=1): \quad & |\varphi_a\varphi_b| \\ & \frac{1}{\sqrt{2}}(|\varphi_a\overline{\varphi}_b| + |\overline{\varphi}_a\varphi_b|) \\ & |\overline{\varphi}_a\overline{\varphi}_b| \end{aligned} \tag{C.113}$$

$$(S=0): \quad \frac{1}{\sqrt{2}}(|\varphi_a\overline{\varphi}_b| - |\overline{\varphi}_a\varphi_b|), \tag{C.114}$$

where S is the magnitude of the total spin $\boldsymbol{S} = \boldsymbol{s}_1 + \boldsymbol{s}_2$. The former is called the triplet state and latter is called singlet state. The triplet state has the energy $K(\varphi_a, \varphi_b) - J(\varphi_a, \varphi_b)$ and the singlet state has the energy $K(\varphi_a, \varphi_b) + J(\varphi_a, \varphi_b)$, thus the triplet state becomes the ground state. Using

$$\boldsymbol{S}^2 = \boldsymbol{s}_1^2 + \boldsymbol{s}_2^2 + 2\boldsymbol{s}_1 \cdot \boldsymbol{s}_2 = 3/2 + 2\boldsymbol{s}_1 \cdot \boldsymbol{s}_2 = S(S+1), \tag{C.115}$$

we find $\boldsymbol{s}_1 \cdot \boldsymbol{s}_2 = 1/4$ for the triplet state and $\boldsymbol{s}_1 \cdot \boldsymbol{s}_2 = -3/4$ for the singlet state. Therefore we can obtain the effective spin Hamiltonian as,

$$H_{\text{ex}} = -2J(\varphi_a, \varphi_b)\boldsymbol{s}_1 \cdot \boldsymbol{s}_2. \tag{C.116}$$

If φ_a and φ_b are orthogonal to each other, $J(\varphi_a, \varphi_b)$ becomes positive, as above, and the interaction prefers to align the spins, i.e. ferromagnetic. This interaction is called the exchange interaction and the spin Hamiltonian which has the form of Eq. (C.116) is called the Heisenberg model.

When the two magnetic ions become closer to each other, we have to consider the electron hopping between two orbitals. In this case, it is convenient to introduce the Hubbard model given by,

$$H = -\sum_{<i,j>}\sum_{\sigma} t_{i,j}\left(c^\dagger_{i\sigma}c_{j\sigma} + c^\dagger_{j\sigma}c_{i\sigma}\right) + U\sum_i c^\dagger_{i\uparrow}c_{i\uparrow}c^\dagger_{i\downarrow}c_{i\downarrow}, \tag{C.117}$$

where $c_{i\sigma}$ represents the second-quantized fermion such that it satisfies anti-commutative relations,

$$\begin{aligned} c^\dagger_{i\sigma}c_{j\sigma'} + c_{j\sigma'}c^\dagger_{i\sigma} &= \delta_{ij}\delta_{\sigma\sigma'}, \\ c^\dagger_{i\sigma}c^\dagger_{j\sigma'} + c^\dagger_{j\sigma'}c^\dagger_{i\sigma} &= 0, \\ c_{i\sigma}c_{j\sigma'} + c_{j\sigma'}c_{i\sigma} &= 0, \end{aligned} \tag{C.118}$$

and $c^\dagger_{i\sigma}$ creates an electron with spin σ at cite i and $c_{i\sigma}$ annihilates an electron. The wave function is represented by applying the creation and annihilation operators to vacuum $|0\rangle$. The first term of Eq. (C.117)

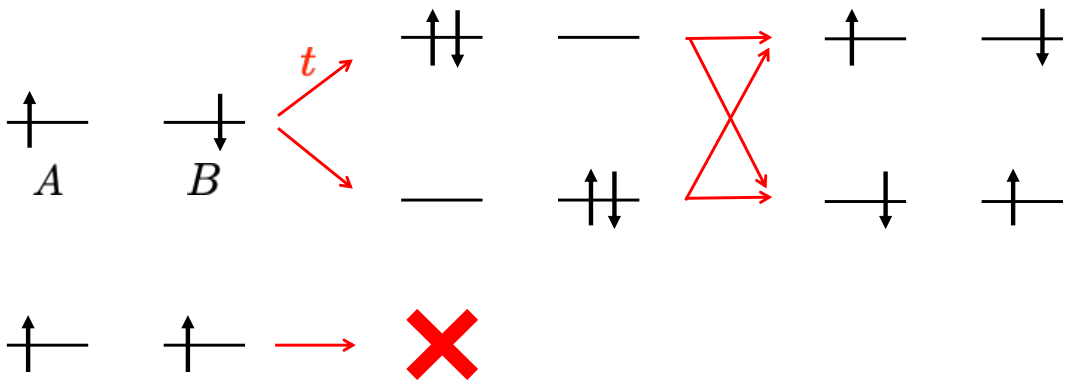

Figure C.6: **Schematic picture of second perturbative process of Eq. (C.120)**

represents the electron hopping from site j to site i and the second term represents the Coulomb interaction on site i. $t_{i,j}$ is the transfer integral represented as,

$$t_{i,j} = \int d^3\boldsymbol{r}\varphi_i^*(\boldsymbol{r})H_{\rm hop}\varphi_j(\boldsymbol{r}), \tag{C.119}$$

where $H_{\rm hop}$ is the Hamiltonian for the hopping electron and is given by the sum of the kinetic energy and the periodic potential of the crystal. On-cite Coulomb energy U exists if two spins are different because of Pauli's principle. Now, we suppose that the number of electrons is the same as the number of sites and the Coulomb energy is larger than the hopping energy such that we can treat the hopping as a perturbation. In this situation, the system becomes the Mott insulator where all sites have only one electron to minimize the Coulomb energy.

For simplicity, let us consider two magnetic ions A and B in order to discuss the exchange interaction cased by the electron hopping. More precisely the local Hamiltonian is defined as,

$$H_{\rm local} = -\sum_{\sigma} t\left(c_{a\sigma}^\dagger c_{b\sigma} + c_{b\sigma}^\dagger c_{a\sigma}\right) + U\sum_{i=a,b} c_{i\uparrow}^\dagger c_{i\uparrow} c_{i\downarrow}^\dagger c_{i\downarrow}. \tag{C.120}$$

If the hopping effect is absent, the ground states are $c_{a\uparrow}^\dagger c_{b\uparrow}^\dagger\left|0\right\rangle, c_{a\uparrow}^\dagger c_{b\downarrow}^\dagger\left|0\right\rangle, c_{a\downarrow}^\dagger c_{b\uparrow}^\dagger\left|0\right\rangle, c_{a\downarrow}^\dagger c_{b\downarrow}^\dagger\left|0\right\rangle$ and the excited states are $c_{a\uparrow}^\dagger c_{a\downarrow}^\dagger\left|0\right\rangle, c_{b\uparrow}^\dagger c_{b\downarrow}^\dagger\left|0\right\rangle$. Hereafter we write them simply as $\left|\uparrow;\uparrow\right\rangle, \left|\uparrow;\downarrow\right\rangle, \left|\downarrow;\uparrow\right\rangle, \left|\downarrow;\downarrow\right\rangle, \left|\uparrow\downarrow;0\right\rangle, \left|0;\uparrow\downarrow\right\rangle$. The perturbation process where the electron hops to another orbital and returns to the original orbital, shown in Fig. C.6, gives the leading term of the perturbation. The energy is given by,

$$E_{mm'}^{(2)} = -\sum_l \frac{1}{2}E'_{ml}E'_{lm'}\left(\frac{1}{E_l - E_m} + \frac{1}{E_l - E_{m'}}\right), \tag{C.121}$$

where m, m' are the indices of the ground states, l is the index of the excited state, E_k is the energy of the state k and $E'_{kk'}$ is the first order perturbation between states k and k'. For example, $H^{(2)}_{\left|\uparrow;\downarrow\right\rangle,\left|\downarrow;\uparrow\right\rangle}$ is calculated as,

$$\begin{aligned}
E^{(2)}_{\left|\uparrow;\downarrow\right\rangle,\left|\downarrow;\uparrow\right\rangle} &= -\frac{t^2}{U}\Big(\left\langle\uparrow\downarrow;0\right| c_{a\downarrow}^\dagger c_{b\downarrow}\left|\uparrow;\downarrow\right\rangle\left\langle\downarrow;\uparrow\right| c_{b\uparrow}^\dagger c_{a\uparrow}\left|\uparrow\downarrow;0\right\rangle + \left\langle 0;\uparrow\downarrow\right| c_{b\uparrow}^\dagger c_{a\uparrow}\left|\uparrow;\downarrow\right\rangle\left\langle\downarrow;\uparrow\right| c_{a\uparrow}^\dagger c_{b\downarrow}\left|0;\uparrow\downarrow\right\rangle\Big) \\
&= -\frac{2t^2}{U}\left\langle\uparrow\downarrow;0\right| c_{a\downarrow}^\dagger c_{b\downarrow}\left|\uparrow;\downarrow\right\rangle\left\langle\downarrow;\uparrow\right| c_{b\uparrow}^\dagger c_{a\uparrow}\left|\uparrow\downarrow;0\right\rangle \\
&= \frac{2t^2}{U} = J.
\end{aligned} \tag{C.122}$$

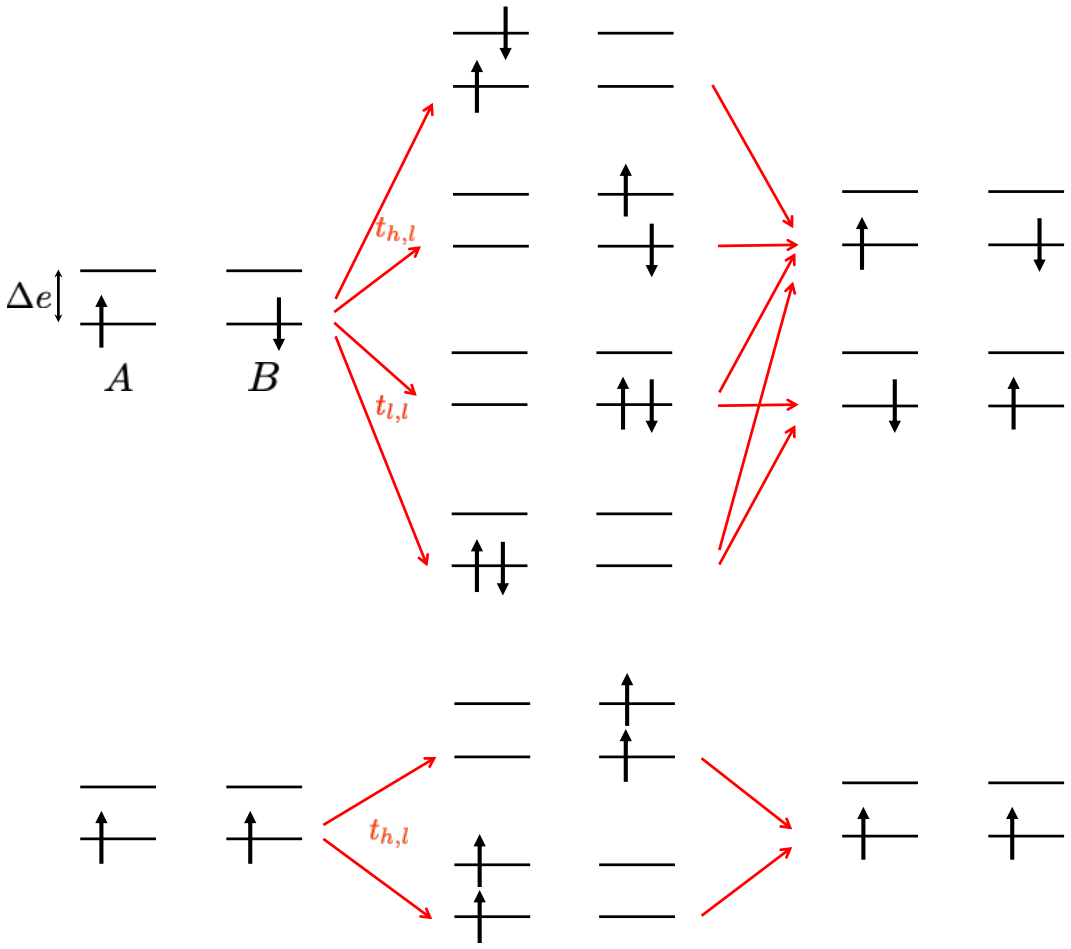

Figure C.7: **Schematic picture of second perturbative process of Eq. (C.125)**

Here I used the anti-commutative relation Eq. (C.118). The second order perturbation matrix is given by,

$$\hat{E}^{(2)} = \begin{pmatrix} 0 & 0 & 0 & 0 \\ 0 & -J & J & 0 \\ 0 & J & -J & 0 \\ 0 & 0 & 0 & 0 \end{pmatrix} = 2 \begin{pmatrix} J/4 & 0 & 0 & 0 \\ 0 & -J/4 & J/2 & 0 \\ 0 & J/2 & -J/4 & 0 \\ 0 & 0 & 0 & J/4 \end{pmatrix} + \frac{J}{2}\hat{I}, \tag{C.123}$$

and we obtain the spin Hamiltonian as,

$$H = 2J\boldsymbol{s}_a \cdot \boldsymbol{s}_b, \tag{C.124}$$

which is the same form as the Heisenberg model but the interaction is antiferromagnetic.

Next, let us consider the case where each magnetic ion has more than two active orbitals but only one electron for each magnetic ion. Then it is useful to introduce the multi-orbital Hubbard model given by,

$$\begin{aligned} H = &- \sum_{<i,j>} \sum_{\alpha,\alpha'} \sum_{\sigma} t_{i\alpha,j\alpha'} \left(c^\dagger_{i\alpha\sigma} c_{j\sigma} + c^\dagger_{j\alpha'\sigma} c_{i\sigma} \right) + \sum_i \sum_\alpha \epsilon_\alpha \sum_\sigma c^\dagger_{i\alpha\sigma} c_{i\alpha\sigma} \\ &+ \sum_i \sum_{\alpha,\alpha'} \sum_{\sigma,\sigma'} \frac{K(\varphi_\alpha, \varphi_{\alpha'}) - \delta_{\sigma,\sigma'} J(\varphi_\alpha, \varphi_{\alpha'})}{2} c^\dagger_{i\alpha\sigma} c_{i\alpha\sigma} c^\dagger_{i\alpha'\sigma'} c_{i\alpha'\sigma'}, \end{aligned} \tag{C.125}$$

where ϵ_α is the energy level of the orbital α.

In the same manner as before, we consider only two magnetic ions and each ion has only two orbitals $\alpha = h, l$ with the energy difference $\epsilon_h - \epsilon_l = \Delta e > 0$, as shown in Fig. The local Hamiltonian is defined as,

$$\begin{aligned} H_{\text{local}} = &- \sum_{\alpha,\alpha'} \sum_{\sigma} t_{\alpha,\alpha'} \left(c^\dagger_{a\alpha\sigma} c_{b\sigma} + c^\dagger_{b\alpha'\sigma} c_{a\alpha'\sigma} \right) + \sum_{i=a,b} \Delta e \sum_{\sigma} c^\dagger_{ih\sigma} c_{ih\sigma} \\ &+ \sum_{i=a,b} \sum_{\alpha,\alpha'} \sum_{\sigma,\sigma'} \frac{K(\varphi_\alpha, \varphi_{\alpha'}) - \delta_{\sigma,\sigma'} J(\varphi_\alpha, \varphi_{\alpha'})}{2} c^\dagger_{i\alpha\sigma} c_{i\alpha\sigma} c^\dagger_{i\alpha'\sigma'} c_{i\alpha'\sigma'}, \end{aligned} \tag{C.126}$$

We use the short hand notation $|A:h, A:l; B:h, B:l\rangle$, e.g. $c^\dagger_{al\uparrow} c^\dagger_{bl\uparrow} |0\rangle = |0, \uparrow; 0, \uparrow\rangle$. The non-perturbative ground states are $|0,\uparrow;0,\uparrow\rangle$, $|0,\uparrow;0,\downarrow\rangle$, $|0,\downarrow;0,\uparrow\rangle$, $|0,\downarrow;0,\downarrow\rangle$ and the first excited states are $|0,\uparrow\downarrow;0,0\rangle$, $|\uparrow,\uparrow;0,0\rangle$, $|\uparrow,\downarrow;0,0\rangle$, $|\downarrow,\uparrow;0,0\rangle$, $|\downarrow,\downarrow;0,0\rangle$ and the symmetric states with respect to swapping A and B. The second perturbative energy is given by,

$$\begin{aligned} H^{(2)}_{\text{F}} &= H^{(2)}_{|0,\uparrow;0,\uparrow\rangle,|0,\uparrow;0,\uparrow\rangle} = H^{(2)}_{|0,\downarrow;0,\downarrow\rangle,|0,\downarrow;0,\downarrow\rangle} = -\frac{2t^2_{h,l}}{\Delta E + K(\varphi_h, \varphi_l) - J(\varphi_h, \varphi_l)}, \\ H^{(2)}_{\text{AF}} &= H^{(2)}_{|0,\uparrow;0,\downarrow\rangle,|0,\uparrow;0,\downarrow\rangle} = H^{(2)}_{|0,\downarrow;0,\uparrow\rangle,|0,\downarrow;0,\uparrow\rangle} = -\frac{2t^2_{l,l}}{K(\varphi_l, \varphi_l)} - \frac{2t^2_{h,l}}{\Delta E + K(\varphi_h, \varphi_l)}, \\ H_{\text{off}} &= H^{(2)}_{|0,\uparrow;0,\downarrow\rangle,|0,\downarrow;0,\uparrow\rangle} = H^{(2)}_{|0,\downarrow;0,\uparrow\rangle,|0,\uparrow;0,\downarrow\rangle} = \frac{2t^2_{l,l}}{\Delta E + K(\varphi_l, \varphi_l)}. \end{aligned} \tag{C.127}$$

If A's l orbital and B's l orbital are completely orthogonal to each other, i.e. $t_{l,l} = 0$, the off-diagonal terms become 0. Then $|0,\uparrow;0,\uparrow\rangle$, $|0,\uparrow;0,\downarrow\rangle$, $|0,\downarrow;0,\uparrow\rangle$, $|0,\downarrow;0,\downarrow\rangle$ remains the eigenstates of the second perturbation Hamiltonian (Eq. (C.127)), i.e. there are no quantum superpositions in the ground states. Thus, we can neglect the quantum effect. The effective exchange interaction between classical spins $\boldsymbol{S}_a$ and $\boldsymbol{S}_b$ is given by,

$$H = J_{\text{eff}} \boldsymbol{S}_a \cdot \boldsymbol{S}_b, \tag{C.128}$$

where

$$J = E^{(2)}_{\text{F}} - E^{(2)}_{\text{AF}} \tag{C.129}$$

and it becomes negative (ferromagnetic) because of Hund's coupling $J(\varphi_h, \varphi_l)$, i.e spins are aligned by the indirect Hund's coupling.

C.5.1 Super-exchange interaction

In materials such as ion crystals, the magnetic ions don't directly coordinate with other magnetic ions but have mediated anions. In this case, the magnetic ions interact with each other via the non-magnetic anions, which is called the super-exchange interaction. Now, we explain this interaction for the case where the magnetic ion is affected by the cubic crystal field. More precisely, we consider the local Hubbard model which is composed of $\alpha = d(xy), d(x^2 - y^2)$ orbitals of two magnetic ions A, B and $\beta = p(x), p(y), p(z)$ orbitals of a mediated oxygen because the other orbitals doesn't overlap to any orbitals. $d(xy), d(x^2 - y^2)$ were called φ_ζ, φ_v in the previous sections. In the ground state, each magnetic ion has one electron and p orbitals of the oxygen are fully occupied. We suppose that Hund's coupling in the oxygen is small enough to be negligible and all p orbitals are completely degenerated. The Hamiltonan is given by,

$$\begin{aligned} H_{\text{local}} = &- \sum_{i=a,b} \sum_{\alpha,\beta} \sum_{\sigma} t_{i:\alpha,o:\beta} \left(c^\dagger_{i\alpha\sigma} c_{o\beta\sigma} + c^\dagger_{o\beta\sigma} c_{i\alpha\sigma} \right) + \sum_{i=a,b} \sum_{\alpha} \Delta e_\alpha \sum_{\sigma} c^\dagger_{i\alpha\sigma} c_{i\alpha\sigma} \\ &+ \sum_{i=a,b} \sum_{\alpha,\alpha'} \sum_{\sigma,\sigma'} \frac{K(\varphi_\alpha, \varphi_{\alpha'}) - \delta_{\sigma,\sigma'} J(\varphi_\alpha, \varphi_{\alpha'})}{2} c^\dagger_{i\alpha\sigma} c_{i\alpha\sigma} c^\dagger_{i\alpha'\sigma'} c_{i\alpha'\sigma'} + \frac{U_o}{2} \sum_{\beta} c^\dagger_{o\beta\sigma} c_{o\beta\sigma} c^\dagger_{o\beta'\sigma'} c_{o\beta'\sigma'}, \end{aligned} \tag{C.130}$$

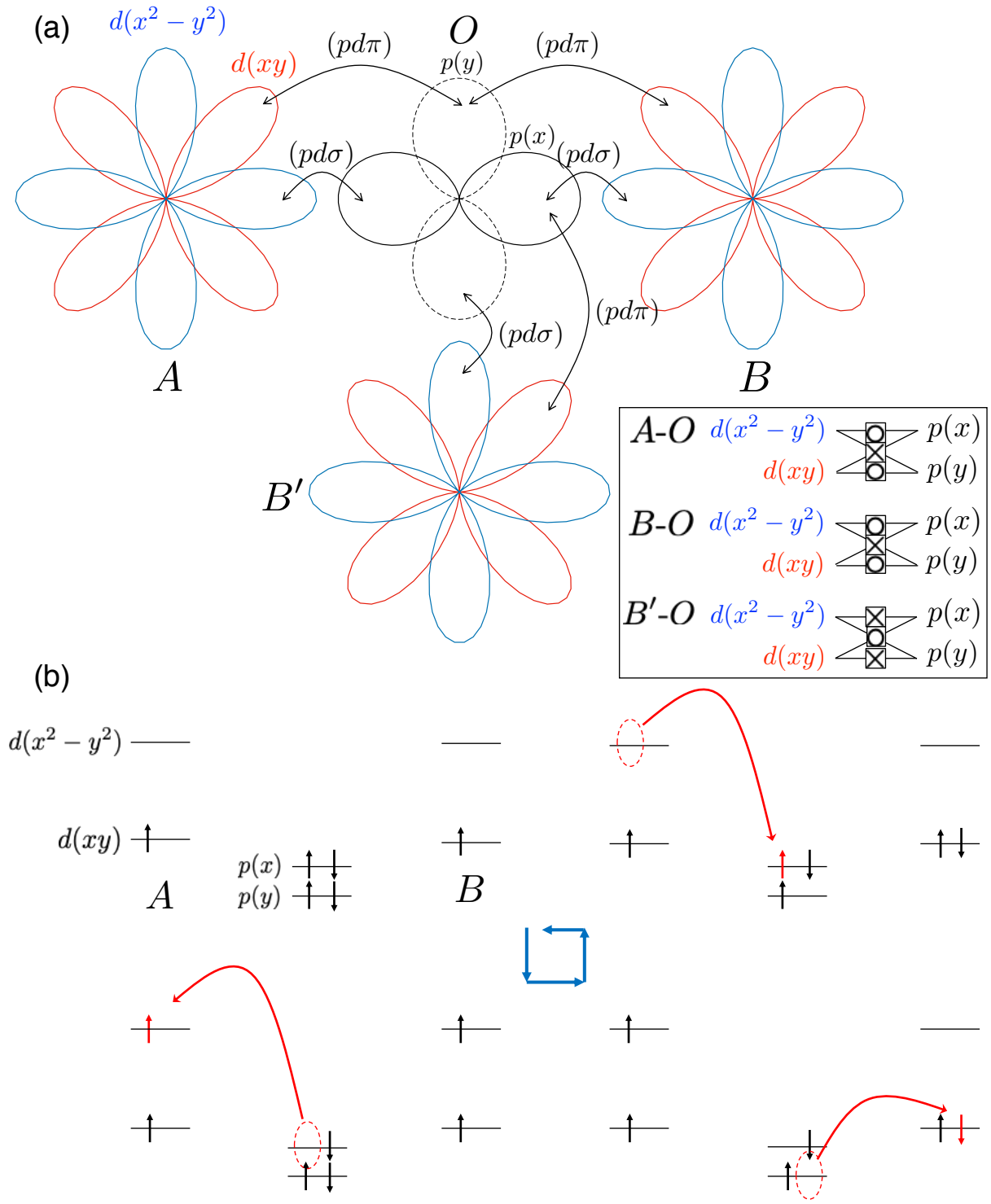

Figure C.8: **Super-exchange interaction**
(a): Schematic picture of A-O-$B(B')$ coordination with the angle $\alpha = 180°(90°)$. The small window shows the overlaps of orbitals. Circle and cross marks correspond to finite and zero overlaps, respectively. (b): An example of the fourth order perturbative process. I omit $p(z)$ orbital of the mediated oxygen ion in both pictures because it is orthogonal to all d orbitals of A and $B(B')$.

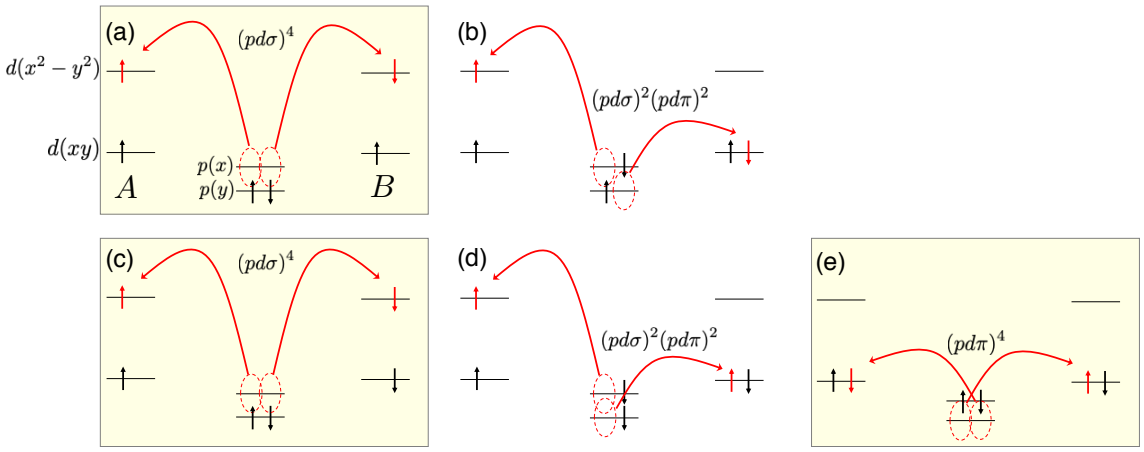

Figure C.9: **All candidates of the second excited state for the case of** 180° **connection** (A-O-B) (a) and (b) arise in the perturbation from the ferromagnetic ground state. (c), (d) and (e) are from the antiferromagnetic ground state.

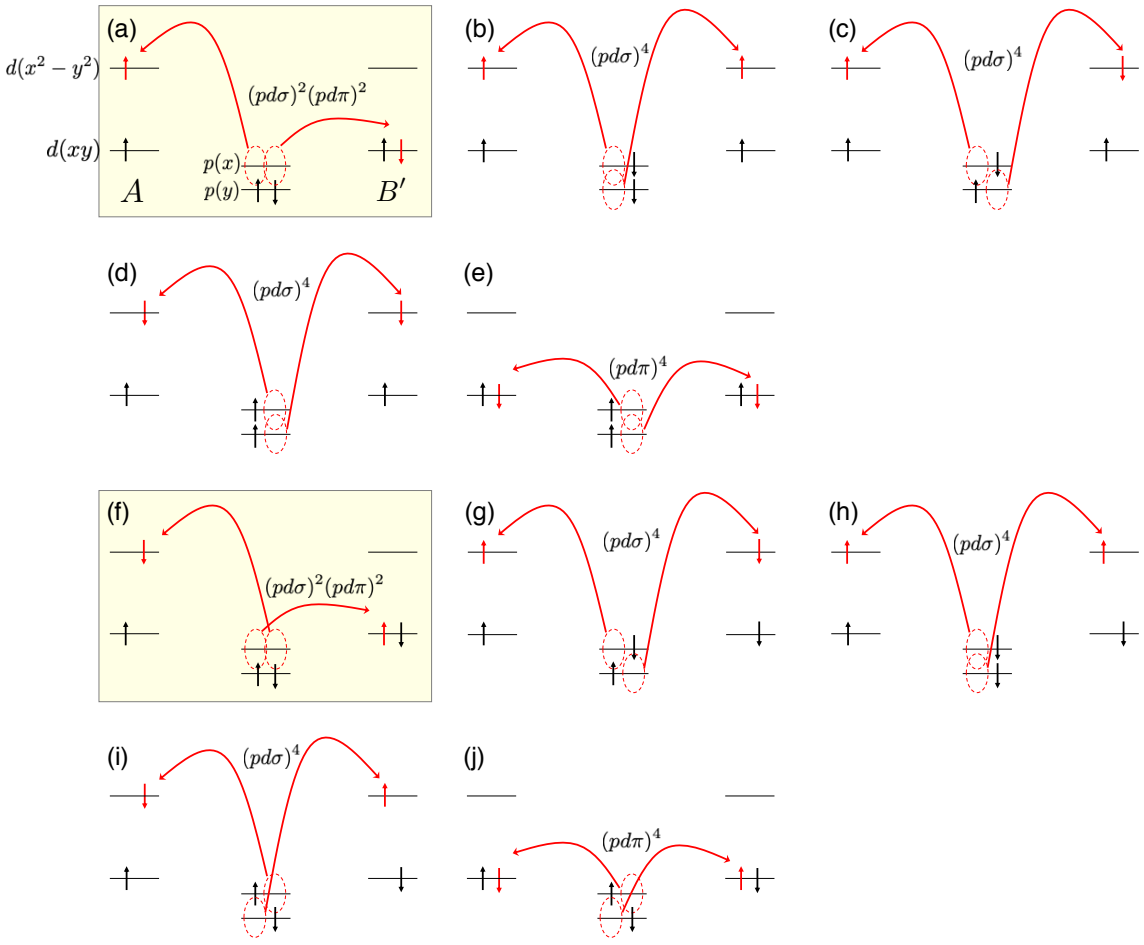

Figure C.10: **All candidates of the second excited state for the case of** 90° **connection** (A-O-B') (a)-(e) arise in the perturbation from the ferromagnetic ground state. (f)-(j) are from the antiferromagnetic ground state.

$-t_{\gamma,\gamma'}(e_x,e_y,e_z)$	Representation by the Slater-Koster parameter
$-t_{x,xy}$	$\sqrt{3}e_x^2e_y(pd\sigma)+e_y(1-2e_x^2)(pd\pi)$
$-t_{y,xy}$	$\sqrt{3}e_y^2e_x(pd\sigma)+e_x(1-2e_y^2)(pd\pi)$
$-t_{z,xy}$	$\sqrt{3}e_xe_ye_z(pd\sigma)-2e_xe_ye_z(pd\pi)$
$-t_{x,yz}$	$\sqrt{3}e_xe_ye_z(pd\sigma)-2e_xe_ye_z(pd\pi)$
$-t_{y,yz}$	$\sqrt{3}e_y^2e_z(pd\sigma)+e_z(1-2e_y^2)(pd\pi)$
$-t_{z,yz}$	$\sqrt{3}e_z^2e_y(pd\sigma)+e_y(1-2e_z^2)(pd\pi)$
$-t_{x,zx}$	$\sqrt{3}e_x^2e_z(pd\sigma)+e_z(1-2e_x^2)(pd\pi)$
$-t_{y,zx}$	$\sqrt{3}e_xe_ye_z(pd\sigma)-2e_xe_ye_z(pd\pi)$
$-t_{z,zx}$	$\sqrt{3}e_z^2e_x(pd\sigma)+e_x(1-2e_z^2)(pd\pi)$
$-t_{x,x^2-y^2}$	$\frac{\sqrt{3}}{2}e_x(e_x^2-e_y^2)(pd\sigma)+e_x(1-e_x^2+e_y^2)(pd\pi)$
$-t_{y,x^2-y^2}$	$\frac{\sqrt{3}}{2}e_y(e_x^2-e_y^2)(pd\sigma)-e_y(1+e_x^2-e_y^2)(pd\pi)$
$-t_{z,x^2-y^2}$	$\frac{\sqrt{3}}{2}e_z(e_x^2-e_y^2)(pd\sigma)-e_z(e_x^2-e_y^2)(pd\pi)$
$-t_{x,3z^2-r^2}$	$e_x[e_z^2-\frac{1}{2}(e_x^2+e_y^2)](pd\sigma)-\sqrt{3}e_xe_z^2(pd\pi)$
$-t_{y,3z^2-r^2}$	$e_y[e_z^2-\frac{1}{2}(e_x^2+e_y^2)](pd\sigma)-\sqrt{3}e_ye_z^2(pd\pi)$
$-t_{z,3z^2-r^2}$	$e_z[e_z^2-\frac{1}{2}(e_x^2+e_y^2)](pd\sigma)+\sqrt{3}e_z(e_x^2+e_y^2)(pd\pi)$

Table C.2: **The transfer integral at general relative positions between p and d orbitals [65]**

where Δe_α represents the energy difference between d and p orbitals. The super-exchange interaction is derived by the fourth order perturbation of the local Hubbard model from the ground state. For instance, one electron of the oxygen ion hops to A ion and another electron hops to B ion and then two electrons return to the original orbitals, as shown in Fig. C.8 (b). The perturbative energy is given by

$$E^{(4)}_{mm'}=-\sum_{l,l',l''}\frac{1}{2}E'_{ml}E'_{ll'}E'_{l'l''}E'_{l''m'}\left(\frac{1}{(E_l-E_m)(E_{l'}-E_m)(E_{l''}-E_m)}+\frac{1}{(E_l-E_{m'})(E_{l'}-E_{m'})(E_{l''}-E_{m'})}\right). \tag{C.131}$$

The transfer integral $t_{i:\alpha,o:\beta}$ depends on the geometry of the overlapping orbitals. If the bond is formed by head-on overlapping like between $d(x^2-y^2)$ of A and $p(x)$ of O in Fig. C.8 (a), the connection becomes the strongest, which is called the σ bond. On the other hand, if the bond formed by doubly overlapping like between $d(xy)$ of A and $p(y)$ of O in Fig. C.8 (a), it is called the π bond. We write transfer integrals where p orbital and d orbital form σ and π bond as $(pd\sigma)<0$ and $(pd\pi)>0$, respectively. The ratio is known as

$$\frac{(pd\sigma)}{(pd\pi)}\simeq -2.17. \tag{C.132}$$

and $(pd\sigma)$ is given by

$$(pd\sigma)=\eta_{pd\sigma}\frac{\hbar^2 r_d^{3/2}}{m r_{ab}^{7/2}}, \tag{C.133}$$

where $\eta_{pd\sigma}\simeq -2.95$ is the universal constant. [64] The parameter r_d called the d-state radius is a length that is characteristic of the ion. r_{ab} represents the distance between centers of two ions. Let (e_x,e_y,e_z) be the direction cosine of the relative vector. The transfer integral between p and d orbitals with an arbitrary angle is given by the linear combination of $(pd\sigma)$ and $(pd\pi)$, which is shown in Table. C.2 and is called the Slater-Koster parameter. [65]

The super-exchange interaction is dependent upon the angle of the A-O-B bond because the transfer integral depends the degree of overlap of orbitals. Now, we consider the two simplest cases, 180° connection

(A-O-B) and 90° connection (A-O-B'), as shown in Fig. C.8 (a). For the case of 180° connection, we find,

$$\begin{aligned} t_{a:d(x^2-y^2),o:p(x)} &= t_{b:d(x^2-y^2),o:p(x)} = (pd\sigma), \\ t_{a:d(xy),o:p(y)} &= t_{b:d(xy),o:p(y)} = (pd\pi) \end{aligned} \tag{C.134}$$

and other transfer integrals are zero. The candidates of the second excited state shown in Fig. C.9, hereafter we call these states $F(a), F(b), AF(c), AF(d), AF(e)$. First, we consider the perturbative process of the ferromagnetic ground state $\left|A : d(xy), d(x^2-y^2); O : p(x), p(y); B : d(xy), d(x^2-y^2)\right\rangle = |\uparrow, 0; \uparrow\downarrow, \uparrow\downarrow; \uparrow, 0\rangle$ and I explicitly write down the perturbative processes going through $F(a)$, for example. There are two possible first excited states (l, l''), $|\uparrow, \uparrow; \downarrow, \uparrow\downarrow; \uparrow, 0\rangle, |0, \uparrow; \uparrow, \uparrow\downarrow; \uparrow, \downarrow\rangle$, and there are 2×2 ways of the fourth perturbation to intermediate $F(a)$. In addition, we have the mirrored process with respect to A and B. The perturbation energy $E^{(4)}_{F(a)}$ is calculated as

$$\begin{aligned} E^{(4)}_{F(a)} = &- \frac{2(pd\sigma)^4}{2K(d(xy), d(x^2-y^2)) - J(d(xy), d(x^2-y^2)) - 9U_O} \\ &\times \left(\frac{1}{K(d(xy), d(x^2-y^2)) - J(d(xy), d(x^2-y^2)) - 5U_O} + \frac{1}{K(d(xy), d(x^2-y^2)) - 5U_O} \right)^2. \end{aligned} \tag{C.135}$$

Here the prefactor 5 and 9 of U_O means the decrease of electron pairs on the oxygen ion, more precisely the oxygen ion of the ground state has ${}_6C_2 = 15$ pairs and decrease 5 pairs by the first hopping and additionally degrease 4 pairs by the second hopping. In the same manner, we can calculate other perturbation energies and the effective is given by

$$J_{\text{eff}} = E^{(4)}_{\text{F}} - E^{(4)}_{\text{AF}} = \left(E^{(4)}_{F(a)} + E^{(4)}_{F(b)} \right) - \left(E^{(4)}_{AF(c)} + E^{(4)}_{AF(d)} + E^{(4)}_{AF(e)} \right) \tag{C.136}$$

if we ignore the quantum spin effect. Note that $E^{(4)}_{F(b)} = E^{(4)}_{AF(d)}$ because they include the same perturbative processes, namely they are completely canceled out. We only take $F(a), F(c), F(e)$ into account (marked up with yellow boxes in Fig. C.9). We can easily find $E^{(4)}_{F(a)} > E^{(4)}_{AF(c)}$ since the spins in A of $F(a)$ have the same direction, i.e. Hund's coupling. In addition, for the ferromagnetic ground state, the process where one electron hops to $A : d(xy)$ and another hops to $B : d(xy)$ is prohibited by Pauli's principle, while it is allowed for the antiferromagnetic ground state. This corresponds to $F(d)$. Therefore $J_{\text{eff}} = E^{(4)}_{F(a)} - E^{(4)}_{AF(c)} - E^{(4)}_{AF(e)}$ is positive, i.e. antiferromagnetic. For the case of 180°, the antiferromagnetic interaction is due to Hund's coupling and Pauli's principle.

Next we consider the case of 90° connection. Similarly to 180° connection, we only take $F(a)$ and $AF(f)$ in Fig. C.10 because the others are completely canceled out. Since there is Hund's coupling, $E^{(4)}_{F(a)} < E^{(4)}_{AF(f)}$ and then the interaction becomes ferromagnetic. The ferromagnetic interaction is generally much smaller than the antiferromagnetic interaction of 180° connection. Thus, the super-exchange interaction is usually antiferromagnetic. The facts which we derived above are well-known as the Goodenough-Kanamori rule [91, 92, 93]. According to this rule, the interaction becomes antiferromagnetic if the angle of A-O-B is 180° and it becomes ferromagnetic if the angle of A-O-B is 90°.

C.5.2 Double-exchange interaction

In above discussion, we only considered the Mott insulator state where the transfer integral t is much smaller than the Coulomb energy U. If t becomes closer to U, the electron hopping frequently happens. Then p orbitals of the mediated anions aren't fully occupied and the magnetic ions can show mixed valency, as shown in Fig. C.11 (a). In this situation, the ferromagnetic alignment is selected because the movement of electron is promoted by Hund's coupling. This is called the double-exchange mechanism.

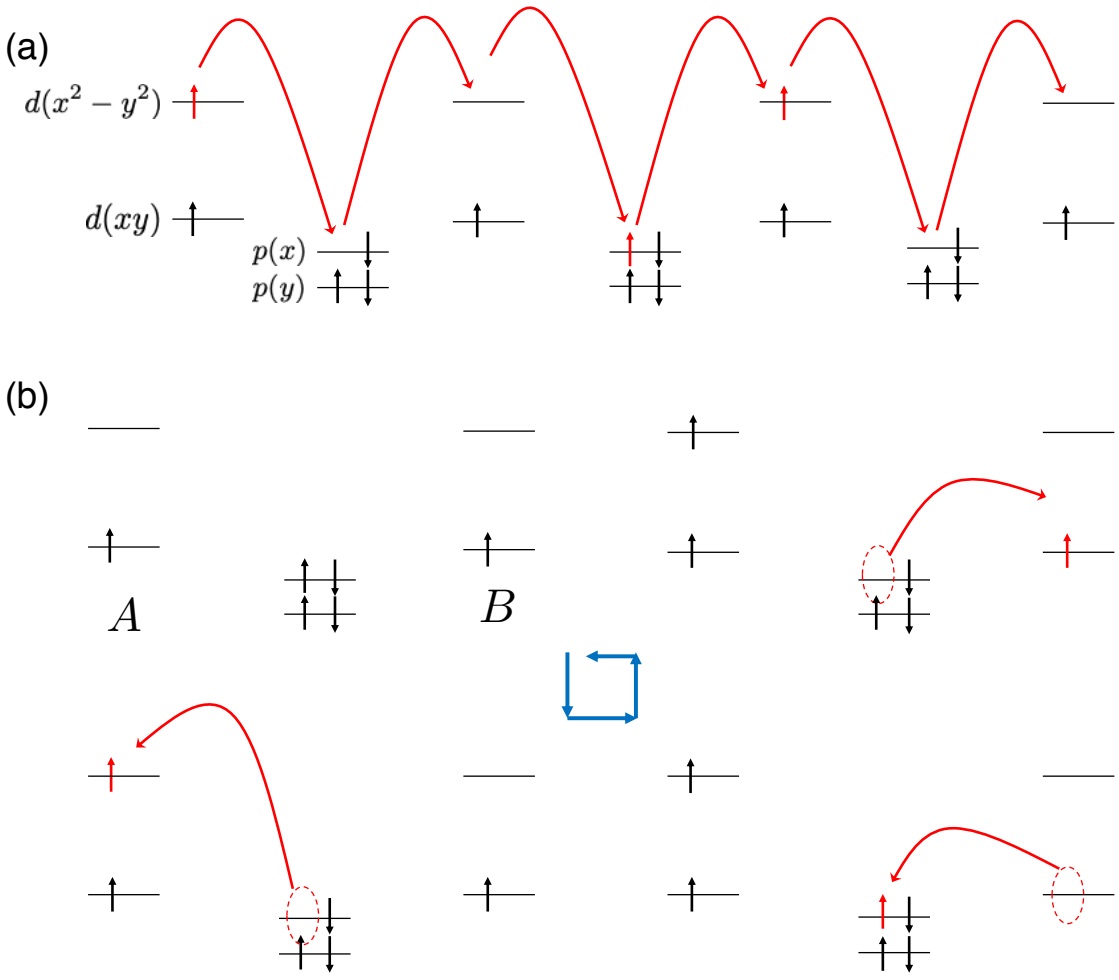

Figure C.11: **Double-exchange interaction**
(a): Schematic picture of double-exchange interaction. (b): Double exchange interaction as the fourth perturbation from the ground state of a Mott insulator.

Actually, the Mott insulator also has a little double exchange interaction which is represented by similar fourth perturbation to the super-exchange interaction. One electron hops from p orbital of the mediated anion to d orbital of a magnetic ion and an electron of another magnetic ion fills the opened p orbital and then they return to the original orbitals. Fig. C.11 (b) shows an example of the double-exchange like process for the case of 180° connection which is used during explaining the super-exchange mechanism in Sec. C.5.1. Here, Hund's coupling also plays an important role and the interaction becomes ferromagnetic.

Appendix D

Elastic energy for $(p-1)$-dimensional simplex

We consider an elastic interaction between two vertices and total energy of one $(p-1)$-dimensional elastic simplex as given by

$$E = \sum_{i<j} V(\sigma_i, \sigma_j) \tag{D.1}$$

with

$$V(\sigma_i, \sigma_j) = k(r_{ij}(\sigma_i, \sigma_j) - 1)^2, \tag{D.2}$$

where ϵ is an energy scale and $r_{ij}(\sigma_i, \sigma_j)$ is a distance between two vertices given by $|\boldsymbol{r}_i(\sigma_i) - \boldsymbol{r}_j(\sigma_j)|$. We assume that each vertex displaces toward or away from the center of simplex, more precisely we define $\boldsymbol{r}_i$ as

$$\boldsymbol{r}_i = \boldsymbol{a}_i - u\sigma_i \hat{\boldsymbol{b}}_i \tag{D.3}$$

where δ is length scale of lattice displacement, $\hat{\boldsymbol{b}}_i = \boldsymbol{b}_i/|\boldsymbol{b}_i|$ is a unit vector from the center of simplex to each vertex and σ_i is a scalar variable. We find

$$\begin{aligned} r_{ij}(\sigma_i, \sigma_j) &= |\boldsymbol{a}_i - \boldsymbol{a}_j - u(\sigma_i \hat{\boldsymbol{b}}_i - \sigma_j \hat{\boldsymbol{b}}_j)| \\ &= \left\{1 + 2u\cos\theta(\sigma_i + \sigma_j) + u^2[(\sigma_i - \sigma_j)^2 + 4\sigma_i\sigma_j\cos^2\theta]\right\}^{\frac{1}{2}}. \\ &= 1 + u\cos\theta(\sigma_i + \sigma_j) + u^2\left[\frac{1}{2}\{(\sigma_i - \sigma_j)^2 + 4\sigma_i\sigma_j\cos^2\theta\} - \frac{1}{8}\{2\cos\theta(\sigma_i + \sigma_j)\}^2\right] + O(u^3), \end{aligned} \tag{D.4}$$

where the $\cos\theta$ is given by

$$\begin{aligned} \cos\theta &= \frac{1}{|\boldsymbol{b}_i|}\boldsymbol{b}_i \cdot (\boldsymbol{b}_i - \boldsymbol{b}_j) \\ &= \sqrt{\frac{p}{2(p-1)}}. \end{aligned} \tag{D.5}$$

We suppose the displacement is small enough ($u \ll 1$). We can rewrite the potential up to the second order of u as

$$V(\sigma_i, \sigma_j) = ku^2\cos^2\theta(\sigma_i + \sigma_j)^2. \tag{D.6}$$

Bibliography

[1] Toshio Taniguchi, Hideo Matsuyama, Susumu Chikazawa, and Yoshihito Miyako. Linear and non-linear susceptibilities in canonical spin glass aufe (1.5 at.% fe). *Journal of the Physical Society of Japan*, 52(12):4323–4330, 1983.

[2] Shoichi Nagata, PH Keesom, and HR Harrison. Low-dc-field susceptibility of cu mn spin glass. *Physical Review B*, 19(3):1633, 1979.

[3] V Cannella and JA Mydosh. Magnetic ordering in gold-iron alloys. *Physical Review B*, 6(11):4220, 1972.

[4] MA Ruderman and C Kittel. *Phys. Rev.*, 96:99–102, Oct 1954.

[5] T Kasuya. *Progress of theoretical physics*, 16(1):45–57, 1956.

[6] Kei Yosida. *Phys. Rev.*, 106:893–898, Jun 1957.

[7] K Yosida. *Phys. Rev.*, 107:396–403, 1957.

[8] LE Wenger and PH Keesom. Calorimetric investigation of a spin-glass alloy: Cumn. *Physical Review B*, 13(9):4053, 1976.

[9] SF Edwards and PW Anderson. *Journal of Physics F: Metal Physics*, 5(5):965, 1975.

[10] Ludovic Berthier and Giulio Biroli. Theoretical perspective on the glass transition and amorphous materials. *Reviews of Modern Physics*, 83(2):587, 2011.

[11] Hans Vogel. The law of the relation between the viscosity of liquids and the temperature. *Phys. Z*, 22:645–646, 1921.

[12] GS Fulcher. Analysis of recent measurements of the viscosity of glasses.ii1. *Journal of the American Ceramic Society*, 8(12):789–794, 1925.

[13] GHJA Tammann and W Hesse. The dependence of viscosity upon the temperature of supercooled liquids. *Z. Anorg. Allg. Chem*, 156:245–257, 1926.

[14] Theodore R Kirkpatrick and Devarajan Thirumalai. p-spin-interaction spin-glass models: Connections with the structural glass problem. *Physical Review B*, 36(10):5388, 1987.

[15] TR Kirkpatrick and PG Wolynes. Connections between some kinetic and equilibrium theories of the glass transition. *Physical Review A*, 35(7):3072, 1987.

[16] Theodore R Kirkpatrick, Devarajan Thirumalai, and Peter G Wolynes. Scaling concepts for the dynamics of viscous liquids near an ideal glassy state. *Physical Review A*, 40(2):1045, 1989.

[17] Jean-Pierre Hansen and Ian R McDonald. *Theory of simple liquids*. Elsevier, 1990.

[18] Patrick Charbonneau, Jorge Kurchan, Giorgio Parisi, Pierfrancesco Urbani, and Francesco Zamponi. Fractal free energy landscapes in structural glasses. *Nature communications*, 5:3725, 2014.

[19] Eric R Weeks and DA Weitz. Properties of cage rearrangements observed near the colloidal glass transition. *Physical review letters*, 89(9):095704, 2002.

[20] Walter Kob and Hans C Andersen. Testing mode-coupling theory for a supercooled binary lennard-jones mixture i: The van hove correlation function. *Physical Review E*, 51(5):4626, 1995.

[21] David Sherrington and Scott Kirkpatrick. Solvable model of a spin-glass. *Physical review letters*, 35(26):1792, 1975.

[22] Giorgio Parisi. Infinite number of order parameters for spin-glasses. *Physical Review Letters*, 43(23):1754, 1979.

[23] Hajime Yoshino. Disorder-free spin glass transitions and jamming in exactly solvable mean-field models. *SciPost Phys*, 4:040, 2018.

[24] JM Kosterlitz, DJ Thouless, and Raymund C Jones. Spherical model of a spin-glass. *Physical Review Letters*, 36(20):1217, 1976.

[25] Elisabeth Gardner. Spin glasses with p-spin interactions. *Nuclear Physics B*, 257:747–765, 1985.

[26] Andrew T Ogielski. Dynamics of three-dimensional ising spin glasses in thermal equilibrium. *Physical Review B*, 32(11):7384, 1985.

[27] Takumi Ogawa, Kazuki Uematsu, and Hikaru Kawamura. Monte carlo studies of the spin-chirality decoupling in the three-dimensional heisenberg spin glass. *arXiv preprint arXiv:1912.02502*, 2019.

[28] Kota Mitsumoto, Chisa Hotta, and Hajime Yoshino. Spin-orbital glass transition in a model frustrated pyrochlore magnet without quenched disorder. *arXiv preprint arXiv:1908.05070*, 2019.

[29] HT Diep et al. *Frustrated spin systems*. World Scientific, 2013.

[30] GH Wannier. Antiferromagnetism. the triangular ising net. *Physical Review*, 79(2):357, 1950.

[31] Jason S Gardner, Michel JP Gingras, and John E Greedan. Magnetic pyrochlore oxides. *Reviews of Modern Physics*, 82(1):53, 2010.

[32] JN Reimers, AJ Berlinsky, and A-C Shi. Mean-field approach to magnetic ordering in highly frustrated pyrochlores. *Physical Review B*, 43(1):865, 1991.

[33] JN Reimers. Absence of long-range order in a three-dimensional geometrically frustrated antiferromagnet. *Physical Review B*, 45(13):7287, 1992.

[34] Ludovic DC Jaubert. *Topological constraints and defects in spin ice*. PhD thesis, 2009.

[35] Linus Pauling. *The Nature of the Chemical Bond...*, volume 260. Cornell university press Ithaca, NY, 1960.

[36] Steven T Bramwell and Michel JP Gingras. Spin ice state in frustrated magnetic pyrochlore materials. *Science*, 294(5546):1495–1501, 2001.

[37] ST Bramwell, MJ Harris, BC Den Hertog, MJP Gingras, JS Gardner, DF McMorrow, AR Wildes, AL Cornelius, JDM Champion, RG Melko, et al. Spin correlations in ho 2 ti 2 o 7: a dipolar spin ice system. *Physical Review Letters*, 87(4):047205, 2001.

[38] Hikaru Kawamura and Seiji Miyashita. Phase transition of the two-dimensional heisenberg antiferromagnet on the triangular lattice. *Journal of the Physical Society of Japan*, 53(12):4138–4154, 1984.

[39] Tsuyoshi Okubo, Sungki Chung, and Hikaru Kawamura. Multiple-q states and the skyrmion lattice of the triangular-lattice heisenberg antiferromagnet under magnetic fields. *Physical review letters*, 108(1):017206, 2012.

[40] HT Diep and H Kawamura. First-order phase transition in the fcc heisenberg antiferromagnet. *Physical Review B*, 40(10):7019, 1989.

[41] Jan N Reimers and AJ Berlinsky. Order by disorder in the classical heisenberg kagomé antiferromagnet. *Physical Review B*, 48(13):9539, 1993.

[42] Berni Julian Alder and Thomas Everett Wainwright. Phase transition for a hard sphere system. *The Journal of chemical physics*, 27(5):1208–1209, 1957.

[43] Hiroaki Ueda, Hiroko Aruga Katori, Hiroyuki Mitamura, Tsuneaki Goto, and Hidenori Takagi. Magnetic-field induced transition to the 1/2 magnetization plateau state in the geometrically frustrated magnet c d c r 2 o 4. *Physical review letters*, 94(4):047202, 2005.

[44] Karlo Penc, Nic Shannon, and Hiroyuki Shiba. Half-magnetization plateau stabilized by structural distortion in the antiferromagnetic heisenberg model on a pyrochlore lattice. *Physical review letters*, 93(19):197203, 2004.

[45] Doron L Bergman, Ryuichi Shindou, Gregory A Fiete, and Leon Balents. Models of degeneracy breaking in pyrochlore antiferromagnets. *Physical Review B*, 74(13):134409, 2006.

[46] Kazushi Aoyama and Hikaru Kawamura. Spin-lattice-coupled order in heisenberg antiferromagnets on the pyrochlore lattice. *Physical review letters*, 116(25):257201, 2016.

[47] NP Raju, E Gmelin, and RK Kremer. Magnetic-susceptibility and specific-heat studies of spin-glass-like ordering in the pyrochlore compounds r 2 mo 2 o 7 (r= y, sm, or gd). *Physical Review B*, 46(9):5405, 1992.

[48] MJP Gingras, CV Stager, NP Raju, BD Gaulin, and JE Greedan. Static critical behavior of the spin-freezing transition in the geometrically frustrated pyrochlore antiferromagnet y 2 mo 2 o 7. *Physical review letters*, 78(5):947, 1997.

[49] SR Dunsiger, RF Kiefl, KH Chow, BD Gaulin, MJP Gingras, JE Greedan, A Keren, K Kojima, GM Luke, WA MacFarlane, et al. Muon spin relaxation investigation of the spin dynamics of geometrically frustrated antiferromagnets y 2 mo 2 o 7 and tb 2 mo 2 o 7. *Physical Review B*, 54(13):9019, 1996.

[50] JE Greedan, Delphine Gout, AD Lozano-Gorrin, Shahab Derahkshan, Th Proffen, H-J Kim, E Božin, and SJL Billinge. Local and average structures of the spin-glass pyrochlore y 2 mo 2 o 7 from neutron diffraction and neutron pair distribution function analysis. *Physical Review B*, 79(1):014427, 2009.

[51] H Kawamura and T Taniguchi. Spin glasses. In *Handbook of Magnetic Materials*, volume 24, pages 1–137. Elsevier, 2015.

[52] TE Saunders and JT Chalker. Spin freezing in geometrically frustrated antiferromagnets with weak disorder. *Physical review letters*, 98(15):157201, 2007.

[53] Hiroshi Shinaoka, Yusuke Tomita, and Yukitoshi Motome. Spin-glass transition in bond-disordered heisenberg antiferromagnets coupled with local lattice distortions on a pyrochlore lattice. *Physical review letters*, 107(4):047204, 2011.

[54] Y Moritomo, Sh Xu, A Machida, T Katsufuji, E Nishibori, M Takata, M Sakata, and Sang-Wook Cheong. Chemical pressure control of exchange interaction in mo pyrochlore. *Physical Review B*, 63(14):144425, 2001.

[55] Y Taguchi and Y Tokura. Magnetotransport phenomena in a metallic ferromagnet on the verge of mott transition: Sm 2 mo 2 o 7. *Physical Review B*, 60(14):10280, 1999.

[56] T Katsufuji, H Y Hwang, and Sang-Wook Cheong. Anomalous magnetotransport properties of r 2 mo 2 o 7 near the magnetic phase boundary. *Physical review letters*, 84(9):1998, 2000.

[57] JS Gardner, BD Gaulin, S-H Lee, C Broholm, NP Raju, and JE Greedan. Glassy statics and dynamics in the chemically ordered pyrochlore antiferromagnet y 2 mo 2 o 7. *Physical review letters*, 83(1):211, 1999.

[58] IV Solovyev. Effects of crystal structure and on-site coulomb interactions on the electronic and magnetic structure of a 2 mo 2 o 7 (a= y, gd, and nd) pyrochlores. *Physical Review B*, 67(17):174406, 2003.

[59] N Hanasaki and et al. *Physical review letters*, 99(8):086401, 2007.

[60] JN Reimers, JE Greedan, and M Sato. The crystal structure of the spin-glass pyrochlore, y2mo2o7. *Journal of Solid State Chemistry*, 72(2):390–394, 1988.

[61] CH Booth, JS Gardner, GH Kwei, RH Heffner, F Bridges, and MA Subramanian. Local lattice disorder in the geometrically frustrated spin-glass pyrochlore y 2 mo 2 o 7. *Physical Review B*, 62(2):R755, 2000.

[62] Peter MM Thygesen, Joseph AM Paddison, Ronghuan Zhang, Kevin A Beyer, Karena W Chapman, Helen Y Playford, Matthew G Tucker, David A Keen, Michael A Hayward, and Andrew L Goodwin. Orbital dimer model for the spin-glass state in y 2 mo 2 o 7. *Physical review letters*, 118(6):067201, 2017.

[63] Hermann Arthur Jahn and Edward Teller. Stability of polyatomic molecules in degenerate electronic states-iorbital degeneracy. *Proceedings of the Royal Society of London. Series A-Mathematical and Physical Sciences*, 161(905):220–235, 1937.

[64] Walter A Harrison. *Electronic structure and the properties of solids: the physics of the chemical bond*. Courier Corporation, 2012.

[65] Allen Nussbaum. Crystal symmetry, group theory, and band structure calculations. In *Solid State Physics*, volume 18, pages 165–272. Elsevier, 1966.

[66] Hiroshi Shinaoka, Yukitoshi Motome, Takashi Miyake, and Shoji Ishibashi. Spin-orbital frustration in molybdenum pyrochlores a 2 mo 2 o 7 (a= rare earth). *Physical Review B*, 88(17):174422, 2013.

[67] Yoshihiko Okamoto, Gøran J Nilsen, J Paul Attfield, and Zenji Hiroi. Breathing pyrochlore lattice realized in a-site ordered spinel oxides ligacr 4 o 8 and liincr 4 o 8. *Physical review letters*, 110(9):097203, 2013.

[68] Roger G Melko, Byron C den Hertog, and Michel JP Gingras. Long-range order at low temperatures in dipolar spin ice. *Physical review letters*, 87(6):067203, 2001.

[69] S Große Pawig and K Pinn. Monte carlo algorithms for the fully frustrated xy model. *International Journal of Modern Physics C*, 9(05):727–736, 1998.

[70] JL Alonso and et al. *Physical Review B*, 53:2537–2545, 1996.

[71] Koji Hukushima and Koji Nemoto. Exchange monte carlo method and application to spin glass simulations. *Journal of the Physical Society of Japan*, 65(6):1604–1608, 1996.

[72] Koji Hukushima. Domain-wall free energy of spin-glass models: Numerical method and boundary conditions. *Physical Review E*, 60(4):3606, 1999.

[73] Marc Mézard, Giorgio Parisi, and Miguel Virasoro. *Spin glass theory and beyond: An Introduction to the Replica Method and Its Applications*, volume 9. World Scientific Publishing Company, 1987.

[74] DS Fisher and DA Huse. *Physical Review B*, 38(1):386, 1988.

[75] H Yoshino and H Takayama. *EPL (Europhysics Letters)*, 22(8):631, 1993.

[76] AJ Bray. *Physical review letters*, 60(8):720, 1988.

[77] Robert Fichtl, Vladimir Tsurkan, Peter Lunkenheimer, Joachim Hemberger, Veronika Fritsch, H-A Krug von Nidda, E-W Scheidt, and Alois Loidl. Orbital freezing and orbital glass state in f e c r 2 s 4. *Physical review letters*, 94(2):027601, 2005.

[78] LDC Jaubert and PCW Holdsworth. *Nature Physics*, 5(4):258, 2009.

[79] Hiroshi Shinaoka, Yusuke Tomita, and Yukitoshi Motome. Effect of magnetoelastic coupling on spin-glass behavior in heisenberg pyrochlore antiferromagnets with bond disorder. *Physical Review B*, 90(16):165119, 2014.

[80] James Hamp, Roderich Moessner, and Claudio Castelnovo. Supercooling and fragile glassiness in a dipolar kagome ising magnet. *Physical Review B*, 98(14):144439, 2018.

[81] Leticia F Cugliandolo, Laura Foini, and Marco Tarzia. Mean-field phase diagram and spin glass phase of the dipolar kagome ising antiferromagnet. *arXiv preprint arXiv:1909.12944*, 2019.

[82] Kota Mitsumoto and Hajime Yoshino. Orientational ordering of closely packed janus particles. *Soft matter*, 14(19):3919–3928, 2018.

[83] Parthasarathi Mondal, Dipten Bhattacharya, and Pranab Choudhury. Dielectric anomaly at the orbital order–disorder transition in lamno3+ δ. *Journal of Physics: Condensed Matter*, 18(29):6869, 2006.

[84] J Rodriguez-Carvajal, M Hennion, F Moussa, AH Moudden, L Pinsard, and A Revcolevschi. Neutron-diffraction study of the jahn-teller transition in stoichiometric lamno 3. *Physical Review B*, 57(6):R3189, 1998.

[85] Y Murakami, JP Hill, Doon Gibbs, M Blume, I Koyama, M Tanaka, H Kawata, T Arima, Y Tokura, K Hirota, et al. Resonant x-ray scattering from orbital ordering in lamno 3. *Physical review letters*, 81(3):582, 1998.

[86] A Moreira Dos Santos, AK Cheetham, T Atou, Y Syono, Y Yamaguchi, K Ohoyama, H Chiba, and CNR Rao. Orbital ordering as the determinant for ferromagnetism in biferroic bimno 3. *Physical Review B*, 66(6):064425, 2002.

[87] T Kimura, S Kawamoto, I Yamada, M Azuma, M Takano, and Y Tokura. Magnetocapacitance effect in multiferroic bimno 3. *Physical Review B*, 67(18):180401, 2003.

[88] Sumio Ishihara, Masanori Yamanaka, and Naoto Nagaosa. Orbital liquid in perovskite transition-metal oxides. *Physical Review B*, 56(2):686, 1997.

[89] G Khaliullin and S Maekawa. Orbital liquid in three-dimensional mott insulator: Latio 3. *Physical review letters*, 85(18):3950, 2000.

[90] Yukito Tanabe and Satoru Sugano. On the absorption spectra of complex ions ii. *Journal of the Physical Society of Japan*, 9(5):766–779, 1954.

[91] John B Goodenough. Theory of the role of covalence in the perovskite-type manganites [la, m (ii)] mn o 3. *Physical Review*, 100(2):564, 1955.

[92] John B Goodenough. An interpretation of the magnetic properties of the perovskite-type mixed crystals la1- xsrxcoo3- λ. *Journal of Physics and Chemistry of Solids*, 6(2-3):287–297, 1958.

[93] Junjiro Kanamori. Superexchange interaction and symmetry properties of electron orbitals. *Journal of Physics and Chemistry of Solids*, 10(2-3):87–98, 1959.